Inductive Wireless Power Transfer for RFID & Embedded Devices: Coil Misalignment Analysis and Design

Kyriaki Fotopoulou

A thesis submitted for the degree of Doctor of Philosophy.
The University of Edinburgh.
November 2008

Acknowledgements

First and foremost I would like to thank my supervisor Dr Brian Flynn for the opportunity he has given me to pursue these studies, for his guidance, advice and constant encouragement through the years. His knowledge of RF never fails to amaze me and his engineering approach to problems has been invaluable to me.

A special thanks goes to my second supervisor Prof. Alan Murray for the enthusiasm he has always shown about this work and the valuable feedback he has provided at critical times.

I am indebted to Prof. Stephen Salter for taking the time to teach an electrical engineer mechanical design. I could not have designed the misalignment apparatus without his help.

Although staying behind the scenes, the technical staff at the School of Engineering and Electronics have offered me significant help with all practical issues I encountered during this project. In particular, I would like to thank Mrs. Susan Kivlin, for her assistance with testing apparatus, the construction of the experimental set-up and for making the long hours in the lab much more enjoyable.

I am truly grateful to the School of Engineering and Electronics for the generous funding I received during my studies, without which this work would have never been realized.

On a more personal note, I wish to thank Nektaria Diamanti and George Moutsopoulos with whom I have shared some of the happiest memories I have from my life in Edinburgh and they have always been there for me with support and advice. In addition, I wish to thank Danilo Blagojevic for his help with all the math related issues I encountered at the start of the PhD and for introducing me to George in the first place.

I must express my deepest gratitude to my family; My parents Petros and Nopi and my sister Katerina whose boundless love supported and motivated me in all my endeavours.

Last but by no means least a very special thanks goes to John Cosgrove for believing in me when I didn't and carrying me through the darkest hours.

Abstract

Radio frequency inductive coupling is extensively employed for wireless powering of embedded devices such as low power passive near-field RFID systems and implanted sensors. The efficiency of low power inductive links is typically less than 1% and is characterised by very unfavourable coupling conditions, which can vary significantly due to coil position and geometry. Although, a considerable volume of knowledge is available on this topic, most of the existing research is focused on the circuital modeling of the transformer action between the external and implanted coils. The practical issues of coil misalignment and orientation and their implications on transmission characteristics of RF links have been overlooked by researchers. The aim of this work is to present a novel analytical model for near-field inductive power transfer incorporating misalignment of the RF coil system.

In this thesis the influence of coil orientation, position and geometry on the link efficiency is studied by approaching the problem from an electromagnetic perspective. In implanted devices some degree of misalignment is inevitable between external and implanted coils due to anatomical requirements. First two types of realistic misalignments are studied; a lateral displacement of the coils and an angular misalignment described as a tilt of the receiver coil. A loosely coupled system approximation is adopted since, for the coil dimensions and orientations envisaged, the mutual inductance between the transmitter and receiver coils can be neglected. Following this, formulae are derived for the magnetic field at the implanted coil when it is laterally and angularly misaligned from the external coil and a new power transfer function presented. The magnetic field solution is carried out for a number of practical antenna coil geometries currently popular in RFID and biomedical domains, such as planar and printed square, and circular spirals as well as conventional air-cored and ferromagnetic solenoids. In the second phase of this thesis, the results from the electromagnetic modeling are embodied in a near-field loosely coupled equivalent circuit for the inductive link. This allows us to introduce a power transfer formula incorporating for the first time coil characteristics and misalignment factors.

This novel power transfer function allows a comparison between different coil structures such as short solenoids, with air or ferromagnetic core, planar and printed spirals with respect to power delivered at the receiver and its relative position to the transmitter. In the final stage of this work, the experimental verification of the model shows close agreement with the theoretical predictions. Using this analysis a formal design procedure is suggested that can be applied on a larger scale compared to existing methods. The main advantage of this technique is that it can be applied to a wide range of implementations without the limitations imposed by numerical modeling and existing circuital methods. Consequently, the designer has the flexibility to identify the optimum coil geometry for maximum power transfer and misalignment tolerance that suit the specifications of the application considered. This thesis concludes by suggesting a new optimisation technique for maximum power transfer with respect to read range, coil orientation, geometry and operating frequency. Finally, the limitations of this model are reiterated and possible future development of this research is discussed.

To my parents Petros and Nopi
and my sister Katerina

Contents

List of figures

List of tables

Acronyms and abbreviations

ASIC	Application Specific Integrated Circuit
BiCMOS	Bipolar CMOS
CMOS	Complementary Metal Oxide Semiconductor
RF	Radio Frequency
RFID	Radio Frequency Identification
FFT	Fast Fourier Transform
IEEE	Institute of Electronics & Electrical Engineers
ISM	Industrial Scientific Medical
NFC	Near-Field Communication
IFF	Identification Friend or Foe
DUT	Device Under Test
LF	Low Frequency
LBS	Biot Savart Law
MF	Medium Frequency
HF	High Frequency
UHF	Ultra High Frequency
VHF	Very High Frequency
VNA	Vector Network Analyzer
SMD	Smart Medical Devices
SoC	System on Chip
EMP	Electromagnetic Powering
EMC	Electromagnetic Compatibility
EMI	Electromagnetic Interference
MRI	Magnetic Resonance Imaging
DCD	Discrete Component Design
EM	Electromagnetic
AC	Alternating Current
SAR	Specific Absorption Rate
ANSI	American National Standards Institute

MPE	Maximum Permissible Exposure
IC	Integrated Circuit
PLL	Phase Lock Loop
TX	Transmitter
RX	Receiver

Nomenclature

Latin Letters

E	Electric Field
H	Magnetic Field
B	Magnetic Flux Density
A	Magnetic vector potential
F	Electric vector potential
J	Current density
$J_0(x)$	Bessel Function of the first kind
Ber	Kelvin Ber function is the real part of $J_0(x)$
Bei	Kelvin Bei function is the imaginary part of $J_0(x)$
$K(m)$	Complete elliptic integral of the first kind
$E(m)$	Complete elliptic integral of the second kind
TX	Transmitter
RX	Receiver
R	Coil separation distance
d	Loop separation distance
R_{TX}	Ohmic losses in the TX coil
R_{RX}	Ohmic losses in the RX coil
R_R	HF resistance per unit length
R_o	Skin effect resistance per unit length
R_{rad}	Radiation resistance
R_{AC}	AC resistance
R_{skin}	Skin effect loss
R_{pe}	Proximity effect loss
R_p	Ohmic resistance per unit length
R_s	Surface impedance of conductor
Q	Quality factor
m_o	Magnetic moment
R_P	Equivalent parallel resistance
R_S	Series resistance of the component

X_P	Shunt reactance
L_{TX}	Inductance of the TX coil
L_{RX}	Inductance of the RX coil
C_m	Mutual capacitance
f	Resonant frequency
a	Radius of transmitter coil
b	Radius of receiver coil
D	Separation distance between the TX and RX Coils
B	Magnetic flux density
H	Magnetic field intensity
K	Loss or Gain in dB between close-field probe and oscilloscope
R	Radial distance
P_{TX}	Transmitted power
P_{RX}	Power received
V_{IND}	Induced voltage across the RX
M	Mutual inductance
C_{TX}	TX Coil
C_{RX}	RX Coil
Z_{in}	Input impedance
Z_s	Source impedance
Z_{Load}	Load impedance
C_m	Distributed capacitance
X_A	Inductive reactance of magnetic loop
X_i	Reactance of loop conductor
I_{TX}	Transmitter current
I_{RX}	Receiver current
I_o	Peak current
N_{TX}	Number of turns of the TX coil
N_{RX}	Number of turns of the RX coil
R_{TX}	Ohmic losses in the TX coil
R_{RX}	Ohmic losses in the RX coil
A_{RX}	Effective area of the RX coil
E_Q	Radiation efficiency

w	Spiral coil track width
s	Interwinding spacing in a spiral coil
t	Conductor track thickness in a spiral coil

Greek Letters

α	Attenuation constant
β	Phase constant
β_o	Phase constant of free space
δ	Skin depth
ϵ	Permittivity
ϵ_r	Relative permittivity
ϵ_o	Permittivity of free space ($8.854 \times 10^{-12} F/m$)
Δ	Lateral displacement distance between the centers of TX and RX coils
γ	Angular misalignment (tilt angle)
σ	Conductivity
μ_o	Free space permeability ($4\pi \times 10^{-7} H/m$)
μ_r	Magnetic permeability of a material
η	Radiation efficiency
η_{link}	Inductive link efficiency
η_s	Link efficiency for series resonant circuits
η_p	Link efficiency for parallel resonant circuits
τ	Power reflection coefficient
κ	Coupling factor
λ	Wavelength
φ	Spiral coil fill factor
ρ	Electrical resistivity of a material
ψ_m	Magnetic flux
ω	Resonant frequency

Chapter 1
Introduction

1.1 RF Wireless Power Transfer - A Novel Concept?

Wireless power transfer is a fascinating field of research which enjoys a long and well established history. The origins of power transmission via radio waves date back to the early work of Heinrich Hertz, [1]. In addition to Hertz's experiments, Nikola Tesla, an acknowledged genius in the area of low-frequency electrical power generation and transmission, conducted pioneering work into this topic at the turn of the 19th century. Tesla became interested in the broad concept of resonance and sought to apply the principle to the transmission of electrical power from one point to another without the aid of wires. By means of alternating surges of current running up and down a mast he strived to set up oscillations of electrical energy over large areas of the surface of the Earth. In this manner Tesla hoped to set up standing waves into which receiving antennas could be immersed at the optimum points. The first attempts of this type were carried out at Colorado Springs, Colorado, in 1899. The famous Tesla coils were resonated at a frequency of 150 kHz with an input power of 300 kW obtained from the Colorado Springs Electric Company, [2]. Unfortunately, there is no clear evidence as to the specific amount of power that could be transfered to a distant point. Tesla's work on high-power transmitters continued after the Colorado Springs in another large installation situated in Long Island 60 miles from New York. However, the unorthodox experimental methods employed by Nikola Tesla and the scale of his ambitious plans resulted in the termination of the project primarily due to the lack of financial resources. Despite the fact that this work was prematurely halted, Telsa managed to produce an impressive number of patents on transmission of electrical energy, [3,4].

In the past few decades, a considerable amount of work has been done in the area of wireless powering. There are two distinct scenarios for wireless powering, namely inductive powering for short ranges in the LF, MF and HF region, and high power density directive radiated powering in the microwave region. The difference between the two wireless powering methods is reflected in the preliminary work of Hertz and Tesla. In the former case of Hertz, radio wave

propagation was employed to transmit power from one point in space to another by propagating electromagnetic waves between antennae. In the latter case, which is the focus of the work described in this thesis, Tesla transfered power via inductive coupling between two resonating coils, [3,4]. With the advantage of historical perspective, one can realise that Tesla's attempts at efficient wireless power transfer were decades ahead of the available technology. It was not until the dawn of the biomedical implants era that the true potential of wireless energy transfer was realised.

The last four decades have witnessed an increasing interest in the area of biomedical engineering and Radio Frequency Identification. The development of the artificial heart in the mid 1950's led the way in the evolution of biomedical implants. More recently, advances in microelectronics and System - on - Chip architectures (SoC) directed the interest of the research community to the implementation of low power biomedical systems for in-vivo diagnostic devices, [5], [6], [7]. Some common applications of implanted devices include biomedical sensors for biometric data measuring, biotelemetry implants, drug delivery systems, transducers, prostheses, artificial organs and neurostimulators to mention a few [8], [6,9–11]. Reliability, safety and size are of prime importance in the design of such systems. Consequently, in designing implantable or autonomous microsystems, the development of a contact-less, wireless powering scheme that is capable of powering a system is a major challenge for biomedical engineers, [12]. Wireless data and power transfer is a very attractive option for such systems as it frees them from wire tethering. The implementation of miniaturised embedded systems is not limited to biomedical applications. Sensors and actuating micro-systems are widely used for environmental monitoring and other industrial applications. Other fields that employ inductive coupling are Radio Frequency Identification (RFID), contact-less smartcards and wireless microelectronic mechanical systems (MEMS). An inductive link between two magnetically-coupled coils is now one of the most common methods for contact-less power transfer from the external world to implantable biomedical devices and sensor systems. A number of factors, such as size constraints, cost, battery lifetime issues, and reliability, forbid the use of an integrated power source. Real-time powering using inductive energy transfer is a favored alternative for such systems.

1.2 Power Supply Options

Recent work in low power wireless communication systems and distributed sensing work has explored two main power supply options, these being batteries and ambient power scavenging. Battery technology is mature, completely self-contained and extensively commercialised. Improvements in the miniaturization and the energy density have been accomplished, with the new generation of primary Lithium cells being a good example. A promising trend in energy-containing devices is in thin-film super capacitors. Despite the advancements in this area, using a battery to power an implant has a clear disadvantage; once the source is exhausted it needs to be replaced using a surgical procedure. Even for relatively large batteries and conservative communication schedules, an optimistic estimate for the mean time to replacement is approximately two years. The problem is significantly aggravated for systems with batteries of more inconspicuous form factors. For example, in RFID scenarios which involve many sensors interacting, integrated batteries will need a replacement every few months. This rate is clearly unsustainable for many applications particularly so for implanted devices.

The alternative is to deliver wireless energy in order to (a) provide on-line power directly to the system or (b) recharge the implanted batteries. This can be achieved by using electromagnetic powering of the system (EMP). EMP includes two main options: (1) Inductive RF coupling of energy using a carrier frequency in the range of a few kHz to a few MHz, depending on the application, and (2) infrared powering, [13]. Infrared powering appears attractive at first, because using photodiodes as receivers rather than coils, results in smaller implants, [14, 15]. However, the process is inefficient, hence non-practical for many implant applications.

Other power sources that have been explored include ambient-power scavenging from sources like thermal and kinetic energy from the body. Moreover, energy harvesting from the external environment as a source of energy, is another possibility. However challenges remain, particularly with ambient power constraints since this technology is still in its infancy. Furthermore, although ambient power sources can be used for wireless communication devices, are unsuitable for implanted systems.

Clearly the most attractive option is near-field coupling which can provide sensor operation in the range of a meter without line of sight. Inductive RF links are currently at the center of attention for short range power transfer and bidirectional data communication. Communication between the implanted device and the outside world can be established through the link by

modulating the RF signal used to power the implant, [16]. The use of inductive coupling can reduce the dimensions of such systems and extend their expected operational life. As such, implanted devices can be cost effective to manufacture and more reliable, a fact that renders inductive RF links very appealing for biomedical and RFID applications. Finally, this type of inductive coupling is advantageous because it avoids the undesirable surgical replacement of implanted power sources. Hence, the possibility of infection where wires would pierce the skin is diminished and patient discomfort is minimised.

1.3 Applications of Inductive Power Transfer

Having established the main advantages of inductive coupling the main applications considered in this thesis should be now introduced in more depth. The main focus of this thesis is on applications involving inductively coupled RFID and biomedical embedded sensor systems. However, the model suggested in this thesis can be employed in any loosely coupled system where a magnetic link is adopted for wireless power transfer, so long as the operation range of the device remains well within the near-field.

Radio Frequency Identification (RFID) is a rapidly developing technology with a wide range of applications in various areas. RFID is an automatic identification method, based on remotely retrieving information via radio waves from miniature electronic circuits called RFID tags. An early work and possibly the first which explored RFID technology was presented by Harry Stockman in a landmark paper given in [18]. By the early 1950's several technologies related to RFID were being pursued. Among the most famous applications of RFID from this era is the long-range transponder systems of *Identification Friend or Foe* (IFF) for aircraft. Although the fundamental principle of RFID was established in the late 1940's, it is only recently that the technology has taken off due to a decrease in the cost and increasing capability, [19].

An RFID system has two main components, a reader and a tag. RFID tags are categorised as either passive or active tags depending on their source of power [22]. A diagram depicting the common ISM frequency bands available to RFID systems is shown in Fig. 1.3. Active RFID tags are autonomous and carry their own power source, usually in the form of an on-board battery. Active tags transmit a stronger signal, and can achieve a larger read range (20-100m) and higher data rates. Active tags operate at higher frequencies - commonly 455 MHz, 2.45 GHz or 5.8 GHz depending on the application and memory requirements [23]. However, their

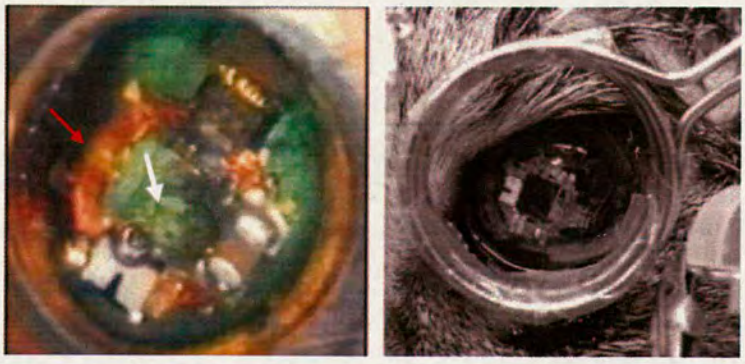

(a) (b)

Figure 1.1: *(a) The receiver unit is shown in the anterior segment of the eye. A microelectrode array for cortical stimulation is placed on the retinal surface, shown by a white arrow, and the RX coil is indicated by the red arrow. (b) view of the transmitter coil in front of the surgical eye and the intraocular receiver unit, [17].*

(a) (b)

Figure 1.2: *(a) The VeriChip implantable RFID tag. The device is 2mm long and 1mm in diameter, comparable to a grain of rice, [20] , (b) X-ray of RFID implants showing the glass ampule style EM4102 tag in the left hand and the Philips HITAG S 2048 in the right arm of the implantee, [21], [20].*

high cost and considerable size are important disadvantages.

When a smaller read range is required and data rate is not critical passive tags offer a desirable alternative [24]. This type of tag is read by intercepting the magnetic field of the reader. Usually passive tags are low power CMOS devices, very compact and inexpensive. The process by which a passive tag is powered is inductive near field coupling and typical read ranges are about 1 meter. Passive RFID systems can be subdivided into low frequency (LF) and high frequency (HF) devices.

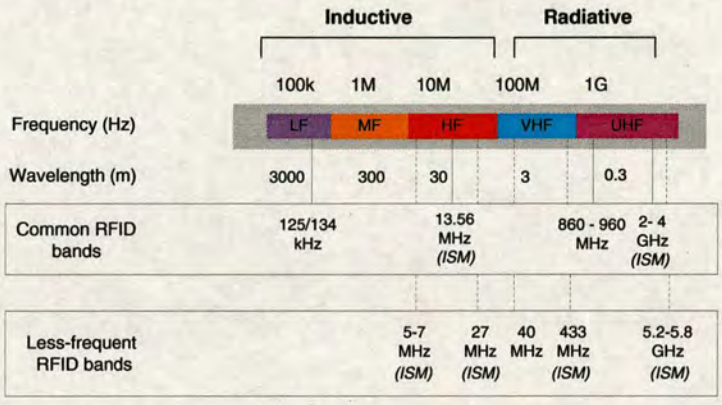

Figure 1.3: *Frequency bands employed in RFID systems.*

In addition, implantable RFID transponders have been used for livestock tracking for many years and they are bridging the gap between the RFID and embedded sensor domain. A recent but increasing development of this technology which evokes enormous interest is the use of RFID in humans. Until a few years ago human RFID implants were limited to the domain of cybernetics provocateurs like Kevin Warwick or hobbyists like Amal Graafstra, see Fig. 1.2(b). However, in 2004, the U.S. Food and Drug Administration approved the first RFID tag for human implantation as a method of accessing and tracking medical records in hospitalised or incapacitated patients, [20]. For example, sensitive information about the identity, physiological characteristics, health and nationality can be easily embedded in a miniaturised but robust transponder about the size of the grain of rice, shown in Fig. 1.2(a). Such a system can be lifesaving for people with chronic conditions and in emergency situations. Despite the advantages of this technology there are serious ethical issues that should be properly addressed such as personal data privacy and security. Nevertheless, with the proliferation of radio-frequency technology the use of embedded RFID devices for human implantation is expected to slowly but steadily increase in the near future.

Additional applications of inductive coupling are emerging from the increasing interest in developing new standards for near-field communications. In recent years, a new principle of Near Field Communication (NFC) has originated from the evolution of more traditional RFID schemes. This technology is targeting simplified, standardized, short-range communication modules similar to the Contact-less Smart Card protocol. The operation of the NFC protocol is based on inductive coupling. This technology opens new applications for the RFID technology, such as automatic payment using mobile phones in close proximity communication as a transaction vehicle. The forecasts for the future development of this technology are promising.

Market researchers anticipate that by the year 2012 twenty percent of the worldwide mobile phone sales will be NFC enabled, [25].

In the biomedical sensors arena inductive coupling is also a major technology. The rapid scaling of CMOS technologies to smaller dimensions has resulted in very high integration densities. This enables circuitry of ever increasing complexity to be implemented on very small chip areas which is very well suited for use in implanted systems. Implanted electronics are used in medical devices for diagnosis as well as treatment. Among the first applications of such systems were pacemakers for cardiac arrhythmia, and cochlear implants for partially restoring the hearing of deaf people. Since the early 1980s the use of such systems has been extensive. According to U.S. Food and Drug Administration 2002 data, it is estimated that approximately 59000 people worldwide have received cochlear implants, [26]. More recently, new applications like intracranial or intraocular systems have become possible. Such devices include deep-brain stimulators for Parkinson's disease, spinal-cord stimulators for control of pain and brain-machine interfaces for paralysis prosthetics, [27]. Ophthalmic applications of embedded devices are also extensive. For instance, devices for monitoring intraocular pressure in Glaucoma patients are common. Other retinal prostheses include visual cortex stimulators where the idea is to restore vision in blind patients by coupling electrodes directly to the visual cortex. An example of the next generation of visual cortex stimulation implants is depicted in Fig. 1.4(a). This system is designed with an integrated planar RX microcoil in order to minimise the size of the overall system. Fig. 1.4(b) illustrates an implanted drug delivery system, developed at the University of Edinburgh, which can be employed in a wide range of treatments such as chemotherapy, and in vivo drug release for conditions like Glaucoma or diabetes.

(a) (b)

Figure 1.4: *(a) Photograph of a retina implant, [26] (b) Photograph of a drug delivery microsystem developed at the University of Edinburgh, [28].*

It follows from the previous discussion that there is a considerable variety of biomedical implanted devices. Although the applications of such systems are diverse their common denominator is that embedded devices need to have low power consumption, be compact, reliable and fully autonomous. Therefore, wireless operation of implantable systems is key to their successful deployment in clinical applications.

1.4 Powering Requirements of RFID and Biomedical Implants

Power consumption is a major concern when designing implantable circuits and RFID systems. Table 1.1 and Table 1.2 give a representative selection of power consumption requirements for several available technologies in industry or reported in the literature. Applications involve biomedical embedded or RFID systems where power is supplied by means of a loosely coupled magnetic power link.

Frequency (Hz)	Consumption	Technology	Application	Reference
1M	1mW	0.5 μm CMOS	Neural Recording	Neihart et al. [29]
2M	90 mW	3μm BiCMOS	Neural Recording	Akin et. al., [30]
24M/40M	0.5mW	2μm BiCMOS	Microtransponder for Biomedical Sensors	Huang et. al., [31]
10 M	22mW	2.5 μm CMOS	Micro-system for Recording Purposes	Parramon et al., [32]
0.5-10 M	5mW	1.2μm CMOS	Artificial Retina Chipset System	Liu et al., [7]

Table 1.1: *Reported power requirements for existing technologies in implanted devices for biomedical applications. The overall power transfer efficiency for these applications is much less than 1%.*

Frequency (Hz)	Consumption	Technology	Application	Reference
134.2k	12.5μW	2μm CMOS	Transponder IC for RFID	Kaiser et. al, [33]
4M	5.61mW	2μm CMOS	Transponder IC for Embedded RFID	Sauer et. al, [34]
50 M	65 μW	CMOS	Capacitive Sensor	Suster et al. [35]
13.56 M	450 μW	CMOS	Passive RFID Label Tag	Philips Semiconductors, [36]

Table 1.2: *Reported power requirements for existing technologies used in RFID devices. Typical values of the coupling coefficient, κ, in the applications listed in this table are between 0.001 and 0.1.*

1.5 Motivation

Wireless inductive power transfer systems are defined as systems where energy is transfered from an external primary TX coil to a secondary RX coil using an alternating magnetic field.

Essentially this principle is very similar to a transformer action. A typical low-power inductive link is illustrated in Fig. 1.5. Although improved designs have emerged in the industry, the electromagnetic modelling of the link efficiency and the optimisation of the coil design has received less attention by researchers. Such systems can be divided into two categories, namely closely coupled and loosely coupled systems.

The efficiency of an inductive link depends on the magnetic coefficient of coupling, κ which is a function of the geometrical parameters of the link such as the coil size and shape and the coil separation distance. The magnetic links of micromodule systems considered in this thesis are loosely coupled systems and are characterised by extremely low coefficients of coupling. The coupling factor, which can be as low as 1%, presents a formidable problem for powering weakly coupled RFID and implanted micromodules.

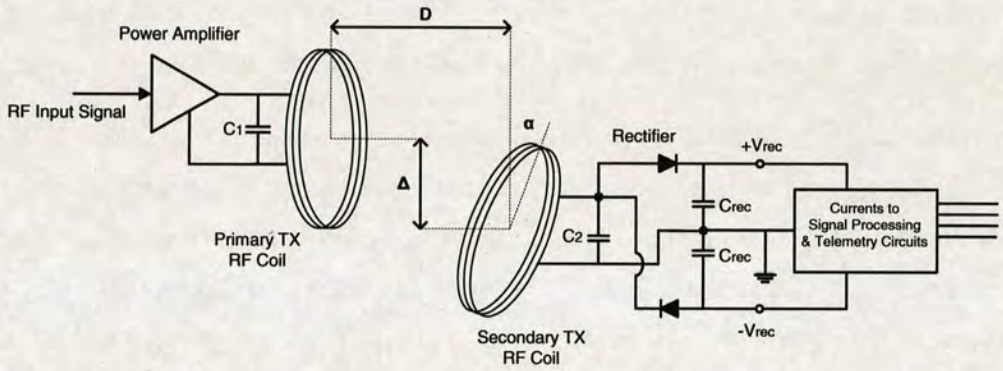

Figure 1.5: *Example of low power inductive link for implanted sensor system illustrating RX coil displacement. D is the coil separation distance, Δ represents lateral misalignment and α is the angular misalignment angle.*

An added complication in the design of an efficient inductive link is the variation of the relative position of the TX and RX coils. The primary or TX coil is located outside the body and is driven by an external transmitter circuit. The secondary or RX coil is implanted with the device and connected to the receiver electronics. A comprehensive study on the topic of injectable electronic identification, monitoring and stimulation systems has been carried out by Troyk which produced a review paper presented in [37]. Referring to this study, in embedded devices such as cochlear or visual prostheses, the coils are separated by a layer of skin and tissues in the region of $2 - 6$cm. Also, a typical implanted micromodule has a diameter of < 3mm whereas an external transmitter coil has a diameter of at least 9cm. Essentially, the external coil dimensions are only restricted by issues related to patient comfort and aesthetic considerations. In fact, external coils can usually be as large as necessary. In an ideal situation the TX and RX

coils are coaxially orientated such that maximum coupling results. However in the biomedical domain, misalignment of the coils can easily occur due to anatomical requirements such as skin mobility and variations in the thickness of subcutaneous fatty tissue.

In addition, coil displacement is common in conventional HF passive RFID devices. In the RFID systems envisaged in this work the reader (TX) and tag (RX) coils are separated by a distance D, typically in the range of a few centimeters, depending on the application and frequency. Often the tag coil is not placed directly on top of the reader coil. This can be easily demonstrated in spatially selective antennas for very close proximity HF RFID applications. Classic examples of this type of RFID systems include contact-less smart cards for access control, e-ticketing, and label item tracking. For these devices, also referred to as *dynamic objects*, the mutual reader-tag alignment can vary drastically. Consequently, for issues like anti-collision, safety and reliability for the user it is critical to be able to predict the misalignment tolerance of such systems and specify geometric boundaries of operation.

There have been several approaches to the analysis and design of inductively coupled transcutaneous links, targeting optimal efficiency in the majority of the cases. However, previous work mainly concentrated on steady-state circuit analysis for coupling optimisation and validation through experiment. Transcutaneous links have been analyzed by Donaldson et al. [38], Galbraith et al. [39], Heetderks et al. [5] and Ko et al. [40]. Although more limited, finite element analysis has been also used for transcutaneous link modelling, [41]. However, the definitive work on the coupling of air-core coils was done by Grover [42] and Terman [43]. It can be demonstrated that the coupling coefficient is related to the mutual inductance M. Earlier research by Soma et al. [44] and Hochmair et al. [45] attempted to present complete analytical solutions for calculation of the mutual inductance M in order determine the effect of misalignment on the coupling factor. Unfortunately, most of the developed solutions so far are semi-analytical and mathematically complex. Furthermore, existing studies usually target a specific design and cannot be universally applied for different coil geometries and orientations.

The aim of this work is to present simplified analytical methods for calculation of the power transfer efficiency under different coil orientations and characteristics. Based on the observation that for loosely coupled inductive links the mutual inductance is very low, the problem can be significantly simplified. This can be achieved by studying the magnetic field of the TX coil and avoiding the involved mathematical treatment of the mutual inductance. Coil dimensions, shape and orientation substantially affect the magnitude of the magnetic field in the near-field.

Since the magnitude of the magnetic field is closely related to the efficiency of the inductive link, it is critical to identify a coil structure that maximises the coupling between the TX and RX.

1.6 Research Objectives & Contribution to Knowledge

This project aimed to explore a simple analytic method for expressing the power transfered between inductively-coupled coils. It was considered vital that the effects of misalignment and coil geometry (circular, square spiral and solenoid coils) be modeled with some accuracy, such that power transfer be optimised in real systems.

Radio frequency inductive links are becoming extensively used in wireless powering of embedded devices such as RFID systems and sensors. The design of RF coils for such links is often empirical and non optimal. A novel analytical model for near field inductive coupling is developed which incorporates misalignment effects on the RF coil system. Formulae are derived for the magnetic field at the tag coil when it is laterally and angularly misaligned from the reader and a new power transfer function presented. For the first time a near-field power transfer formula is suggested incorporating coil characteristics and misalignment factors. This novel power transfer function allows a comparison of different coil structures such as short solenoids, with an air or ferromagnetic core, as well as planar and printed circular and square spirals with respect to power delivered at the RX and its relative position to the TX. It is also possible to define the maximum degree of misalignment permissible in a given application. This analysis allows a formal design procedure to be established in order to identify the optimum coil geometry for RFID tags with respect to read range, angular and lateral coil misalignment, and operating frequency of the system.

The specific objectives of this thesis are listed here:

1. To investigate ways of maximising the power transfer efficiency across a loosely coupled link with a special focus on RFID and embedded sensor scenarios. It is the aim of this work to model the RF link between the TX/reader coil and the RX/tag coil and suggest a method to optimize read range and misalignment tolerance of the system.

2. Study the magnetic near-field of short-solenoid, and planar coils currently employed in the afforementioned applications.

3. Identify the effect of coil geometry on the power transfer, compare different coil structures with respect to the power transfer efficiency and suggest an optimal structure depending on the application.

4. Quantify the effect of the most common coil misalignment configurations on the power transfer efficiency. Lateral displacement and angular tilt of the RX coil with respect to a stationary TX coil are studied.

5. One of the difficulties in the design of loosely coupled inductive links has been the lack of simple, easy to use parameters that combine the performance of the electromagnetic and the circuital design. In this thesis a new analytical set of power transfer functions is derived which attempts to bridge this gap.

6. Design a dedicated experimental system that will test the validity of the proposed model.

7. An optimisation analysis follows for each of the coil geometries. To the author's knowledge there has not been a previous attempt to compare the behaviour of circular and square planar coils with conventional solenoid coils. This work attempts to do this based on the analytic power transfer functions developed.

To accomplish the above objectives a four-phase approach was employed:

- Phase 1: Develop an analytic solution
- Phase 2: Experimental verification
- Phase 3: Comparison of different coil structures and an optimal coil geometry is suggested
- Phase 4: The benefits of the analytic approach are illustrated using an HF passive RFID design example

The original contribution of this thesis is the introduction of a set of novel power transfer functions incorporating misalignment of the RF coils. The analytical expressions for the power transfer allow the designer to optimise the efficiency of the link and predict the effect of coil characteristics, geometry and misalignment on the coupling factor. The analytical approach given in this thesis provides the designer with an in-depth understanding of the problem which is difficult to achieve with numerical methods. Consequently, it is possible to identify the

different parameters and mechanisms affecting the efficiency of loosely coupled inductive links and easily perform optimisation studies. Finally, the optimum coil geometry with respect to the power transfered across the link and insensitivity to misalignment is suggested for a given application.

1.7 Thesis Outline

This chapter provides an overview of the topic of wireless inductive power transfer and discusses the motivation behind this work. A review of the basic applications of wireless power transfer is given. Emphasis is placed on loosely coupled inductive links for low power embedded sensors from the RFID and biomedical domains. Finally the frequency ranges and radio licensing regulations are discussed. This section briefly outlines the contents of the chapters which follow:

Chapter 2: Modelling Near-Field Inductive Coupling. The theory of near-field inductive coupling is discussed in this chapter. A detailed literature review and discussion of the important studies linked to the research introduced in this thesis is presented. The limitations of existing work are addressed and the scope of the current thesis clearly identified. In addition inductive power transfer is introduced from a circuital and electromagnetic perspective.

Chapter 3: Misalignment Analysis. In this chapter the effects of coil orientation, position and geometry on the power transfer efficiency are studied. First, the most popular coil geometries currently employed in RFID and embedded sensor applications are introduced. Expressions for the magnetic field strength at the RX coil when it is laterally or angularly misaligned from the TX or RF source are developed based on the Biot-Savart principle. Then the magnetic field expressions are incorporated into a circuital model of a loosely coupled transformer, which yields a set of novel-power transfer functions describing the power transfer efficiency between several coil geometries such as circular and square printed spiral and conventional short-solenoid coils. In conjunction with air-cored coils, the influence on the power coupling of a ferromagnetic core integrated in the RX coil is also considered. In the case of the embedded sensor application, due to the presence of some conductive tissue between the TX and the implanted RX coil, some of the power transfered across the link will be dissipated as heat due to eddy current in the conductive medium. This chapter concludes by presenting a theoretical treatment in order to quantify the ohmic losses resulting from the presence of biological tissue in the vicinity of

the RX coil.

Chapter 4: Experimental Verification. This chapter describes the experimental verification of the analytical model developed in Chapter 4. This chapter is organised in three sections. The first part introduces the experimental methodology followed in order to characterize the magnetic near-field of the TX coils and measure the power transferred across the inductive link. The second part discusses the calibration of the equipment in addition to the design of the prototype coils used. The design and implementation of a novel misalignment apparatus is introduced. The misalignment jig is very critical since it makes possible field and power transfer efficiency coupling measurements under several coil angular orientations and lateral displacements. In the third part of this chapter the focus is directed to the discussion of the results from the magnetic field and power transfer measurements. Finally, an error analysis is performed and the sources of error are carefully identified and explained. Overall the experimental results strongly support the analytical model of the power transfer functions developed in the previous chapter.

Chapter 5: Optimal Coil Geometry for Efficient Power Transfer. This chapter compares the efficiency of power transfer across the inductive link for short-solenoid, printed circular and square spirals of equal effective areas. The behaviour of the power transfer for different coil structures is investigated for the coaxial coil orientation, lateral and angular coil misalignments by employing the analytical functions for the power transfer developed in Chapter 4. Initially, the magnetic field distribution for the aforementioned coil geometries is discussed. Subsequently, the coupling efficiency for each coil geometry under misalignment is investigated, and trends between quantities in the power transfer functions are identified. In this manner a set of design rules is proposed and an optimisation algorithm is suggested in order to achieve maximum power transfer. The influence of misalignment and coil geometry is determined by adopting the analytic model developed in this thesis. Hence, the analysis presented in this chapter yields an optimum coil geometry which achieves maximum power transfer under different coil orientations.

Chapter 6: RFID Design Example. This chapter demonstrates a practical RFID design example based on the theoretical model developed in this thesis. The power transfer functions derived in Chapter 4 are employed to determine the operating range and sensitivity to misalignment of a HF passive RFID label IC device. Two sets of square and circular planar spiral coils are compared with respect to the power delivered to the device and displacement tolerance of the system. Based on this analysis the optimal coil geometry for efficient power transfer is

suggested.

Chapter 7: Conclusions. The thesis concludes with an overview of the theoretical and experimental work that constitutes this work. The final chapter gives a summary of the main contributions to knowledge of this thesis, reviews the conclusions made in the previous chapters and suggests possibilities for future work.

Chapter 2
Modelling Near-Field Inductive Coupling

2.1 Introduction

In building implantable or autonomous micro-systems, the development of a contact-less or wireless powering scheme that is capable of running the system is one of the challenges encountered by designers. Currently, the preferred method for wireless power and data transfer to implanted electronic devices is magnetic or inductive coupling. A number of parameters need to be considered in the design of such systems. Among these are the size and shape of the coils, location of the implanted device, communication bandwidth, complexity of transmitter (TX) and receiver (RX) circuitry, power consumption, radio frequency regulations and misalignment tolerance of the system. The priority of these factors depends on the specific requirements of each individual application. Consequently, although there are approaches to this problem each methodology targets specific parameters. In spite of the fact that an extensive volume of knowledge is available on this topic, the majority of the studies available attempt to maximise coupling efficiency through the design of the resonant TX and RX circuits. The following sections are a review of studies relevant to this thesis. In this chapter emphasis is given to the modelling of near-field inductive coupling. The reader is introduced to the fundamental principles of this technique and the contribution of this thesis is discussed in detail. The main purpose of this chapter is to establish the fundamental steps taken in the novel approach for modelling wireless power transfer suggested in this thesis. Finally, this chapter concludes by discussing the limitations of the proposed procedure and sets the pace for the more in-depth technical discussion that follows.

2.2 Inductive Coupling and Transformer Action

Recent advances in microelectronics and System - on - Chip architectures (SoC) directed the interest of the research community into the implementation of biomedical systems for in - vivo

diagnostic devices. Currently, there is a proliferation of embedded sensors for a wide range of applications. These vary from biomedical uses such as biometric data measuring, drug delivery and neurostimulation to RFID techniques for security, animal tagging and the recent, but increasing, use of implantable RFID chips in humans. Reliability, autonomy, power consumption and size have been of prime importance in the design of such systems since the very beginning. Currently magnetic or inductive coupling is probably the most widely acknowledged solution for a contact-less powering scheme that meets the requirements of low power devices.

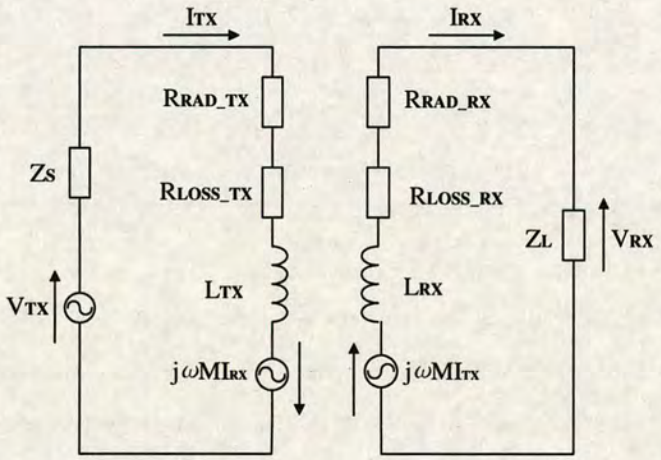

Figure 2.1: *Equivalent circuit of near-field transmission model using the principle of the transformer action, [46].*

An inductive link consists of two weakly coupled resonant circuits with the TX and RX coils forming the primary and secondary windings of a loosely coupled air-cored transformer, illustrated in Fig. 2.1. The inductive term suggests that power transmission takes place in the near-field and transformer action theory is adequate to describe the coupling of energy from the TX to the RX load.

A time-varying current, $I = I_o \sin(\omega_o t)$, circulating in the transmitter coil generates a magnetic field flux which when detected by the receiver a time-varing voltage appears across the inductance of the receiving coil. The magnitude of the e.m.f. induced in the receiver circuit is expressed by Faraday's law as follows:

$$V = M\frac{di}{dt} = \omega_o M I_o \ \sin(\omega_o t + \pi/2) \tag{2.1}$$

A physical representation of an inductive link is shown in Fig. 2.2 where the air-cored primary coil is wired to the transmitter and the pick up coil is incorporated in the receiver unit (RFID tag or Biomedical Sensor). An AC power source excites the primary coil creating the magnetic

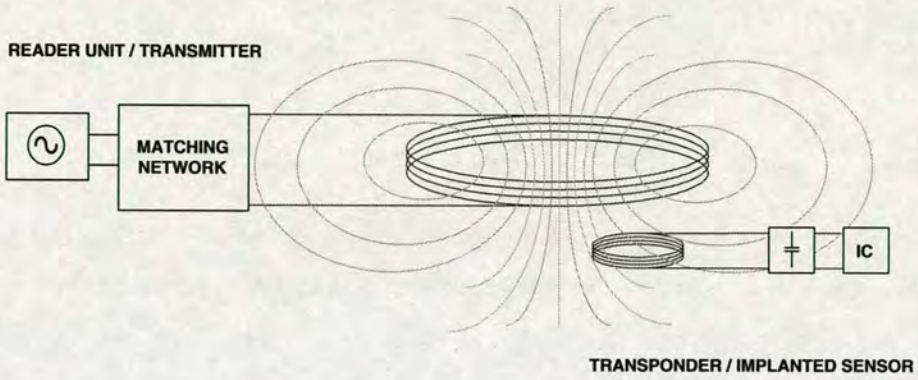

Figure 2.2: *Physical representation of inductive coupled coils.*

field that surrounds the antenna coil. The secondary coil intersects the magnetic field lines created by the transmitter coil and a current is induced in it. This process is prone to power losses with three main categories involved, these being, radiation, ohmic and absorption losses. It should be noted that these losses are critical to the efficiency of the link and they will be discussed in detail later in sections (2.8), (2.9.2) and (2.10) of this chapter.

The associated TX and RX coil resistance introduces some ohmic losses, denoted as $R_{LOSS_{TX}}$ and $R_{LOSS_{RX}}$ respectively. The ohmic losses comprise the most important loss component and are dissipated as heat in the coil. The radiation losses are represented by an additional series resistance, $R_{RAD_{TX}}$ and $R_{RAD_{RX}}$, as shown in Fig. 2.1. It should be noted that the radiation resistance for the applications considered in this work are negligible and can be omitted. In biomedical applications there are some additional losses present due to energy absorption in the tissue. This is mainly caused by the current circulating in the tissue due to the magnetic field. The generated current increases the temperature in the tissue which can be potentially dangerous. Higher frequencies have a smaller skin depth and therefore more radiation is absorbed. Therefore, in order to be able to eliminate this type of loss it is important to work with lower frequencies. The presence of a ferrite cored receiver antenna permits the use of lower frequencies without compromising for range and power transfer efficiency.

Using the equivalent circuit of a transformer as shown in Fig. 2.1 a near-field power transmission model can be developed. The general procedure adopted follows the approach introduced by Yates [47] and Earnshaw [48]. By employing nodal analysis the current and voltage gains can be easily evaluated. Consequently, the power transfered from the transmitter antenna to the receiver can be determined. For simplicity in the following mathematics, the ohmic resistance

and radiation losses can be combined in as follows:

$$\begin{aligned} R_{TX} &= R_{LOSS_{TX}} + R_{RAD_{TX}} \\ R_{RX} &= R_{LOSS_{RX}} + R_{RAD_{RX}} \end{aligned}$$

For the purpose of simplicity any absorption losses will not be included in the circuital modelling at this stage. It follows that the nodal equations can be determined from the equivalent circuit in Fig. 2.1 using Kirchhoff's laws:

$$V_{TX} = (Z_s + R_{TX})I_{TX} + j\omega L_{TX} I_{TX} - j\omega M I_{RX} \tag{2.2}$$

$$V_{RX} = Z_L I_{RX} = j\omega M\, I_{TX} - j\omega L_{RX}\, I_{RX} - R_{RX} I_{RX} \tag{2.3}$$

Thus the current gain can be expressed as:

$$\frac{I_{RX}}{I_{TX}} = \frac{j\omega M}{j\omega L_{RX} + R_{RX} + Z_L} \tag{2.4}$$

The relationship between V_{TX} and V_{RX} can be obtained by algebraic manipulation of the previous expressions. Solving for I_{TX} in (2.3) and substituting in (2.4), it yields:

$$I_{TX} = \frac{j\omega M - \omega^2 M^2 I_{TX}}{(j\omega L_{RX} + R_{RX} + Z_L)\,(Z_S + R_{TX} + j\omega L_{TX})} \tag{2.5}$$

Referring back to equation (2.3) it follows that by multiplying (2.5) by Z_L and rearranging the voltage transfer function can be determined:

$$\frac{V_{RX}}{V_{TX}} = \frac{j\omega M Z_L}{(j\omega L_{RX} + R_{RX} + Z_L)\,(Z_S + R_{TX} + j\omega L_{TX}) + \omega^2 M^2} \tag{2.6}$$

2.3 Resonant Topologies

In order to increase the efficiency of power transmission by inductive coupling, resonant coupled coils are usually utilized in RFID and embedded devices [38, 39, 49–51]. The incentive behind a resonant implementation lies in the following parameters:

- In a tuned TX circuit configuration the current circulating in the antenna coil is maximised. As demonstrated by Galbraith in [39], there are two methods for driving the TX. For a current driven TX a capacitor needs to be connected in parallel in order for the impedance of the circuit to be maximised and the voltage across the inductor coil to resonate. For the voltage driven transmitter the situation is reversed and series resonance

is required to achieve minimum impedance. Both of these techniques optimise the current flow which in return maximises the magnetic field generated by the TX antenna coil [39].

- The second reason for adopting a tuned configuration is justified for impedance matching purposes. Resonance is considered as a means of matching the RX antenna coil to the load introduced by the electronics in the embedded device. The decision to use series or parallel resonance depends on the load resistance as indicated by Vandevoorde in [50]. For low power inductive links studied in this work, the choice between a series or parallel connection is determined by practical considerations regarding the secondary coil inductance and the impedance of the resonant capacitor. It can be argued that the series scenario requires values for the RX coil which are impossible to attain practically. This is especially true for an implanted scheme due to the size restrictions imposed on the embedded coil. It is evident from Fig. 2.3 that both the series and parallel topologies achieve an optimal efficiency but for very different resonant capacitor values. The high values for the RX inductor coil can be explained by the high voltage drop across the series capacitor. Therefore, for low power links a series secondary L-C tank behaving as a voltage source is more suitable.

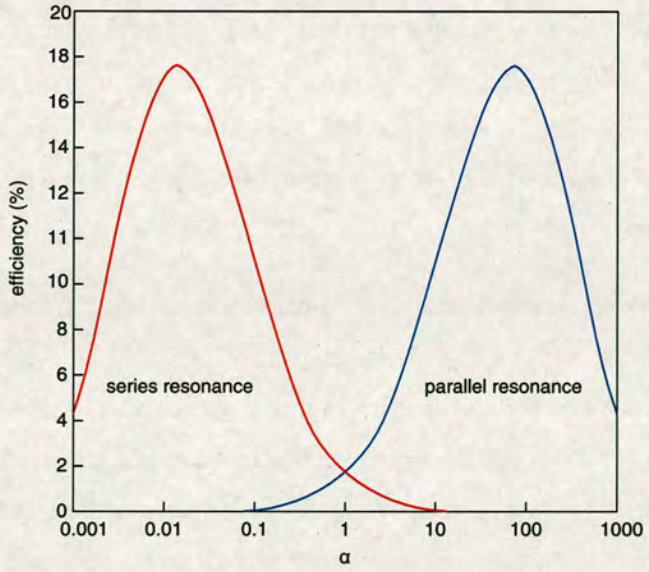

Figure 2.3: *Efficiency versus* $\alpha = \omega C_{RX} R_L$, *[50].*

The value of the tuning capacitor in the series configuration can be computed by the following formula:

$$C = \frac{1}{\omega^2 L} \tag{2.7}$$

However, if parallel resonance is used, expression (2.7) is only valid for an unloaded Q greater than 5. In inductive coupled links there are four possible combinations of series or parallel tuned resonant coils in the transmitter and receiver circuits, as follows:

- Series Resonant TX : Parallel Resonant RX
- Series Resonant TX : Series Resonant RX
- Parallel Resonant TX : Parallel Resonant RX
- Parallel Resonant TX : Series Resonant RX

The equivalent circuit of Fig. 2.1 can equally well represent any one of the four tuned resonant coil topologies. The mutual inductance of the coils can be expressed as:

$$M = \kappa \cdot \sqrt{L_{TX}\ L_{RX}} \tag{2.8}$$

and the unloaded quality factors Q as:

$$Q = \frac{\omega \cdot L_{TX}}{R_{TX}} \tag{2.9}$$

$$Q = \frac{\omega \cdot L_{RX}}{R_{RX}} \tag{2.10}$$

where κ, $(0 < \kappa \leq 1)$, is the coefficient of coupling, [48]. The quality factor Q is defined as the ratio of capacitive or inductive reactance to the resistance. Any distributed *mutual capacitance* denoted as C_m, in Fig. 2.4, is associated with the transmitter and receiver coils coupling. However, for the link analysis described any mutual capacitance will be omitted as it is small enough to be neglected.

The equations expressing voltage and current transfer functions for all four topologies as depicted in Fig. 2.5(a), Fig. 2.5(b), Fig. 2.6(a) and Fig. 2.6(b), can be derived using the same method as the one described previously. However, analysing these topologies using the standard nodal equations is tedious and does not facilitate intuitive insight into the problem studied in this thesis. Although it could be useful to know the voltage and current transfer ratios, the main aim of this work is to suggest a power transfer function which allows a direct comparison between different antenna coils for several possible geometries and orientations.

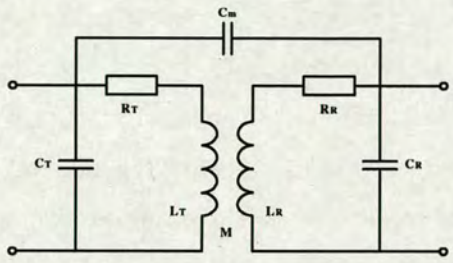

Figure 2.4: *Equivalent Circuit of an Imperfect Inductive Link, [48].*

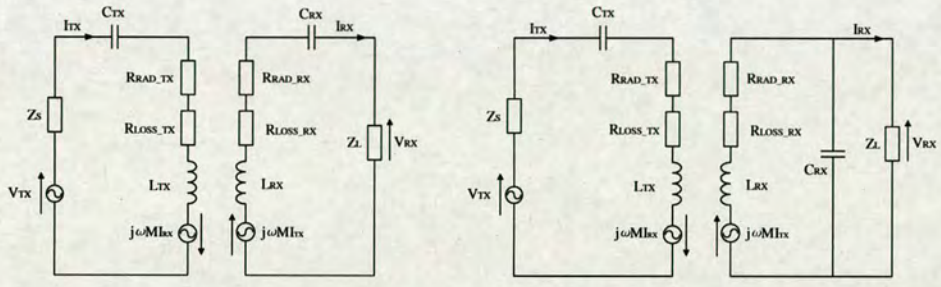

(a) Series (TX) - Series (RX)

(b) Series (TX) - Parallel (RX)

Figure 2.5: *Equivalent circuit for Series resonant TX topology and series or parallel resonant RX configuration.*

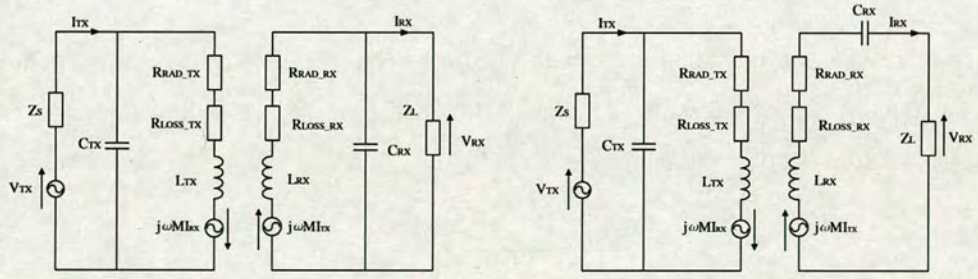

(a) Parallel (TX) - Parallel (RX)

(b) Parallel (TX) - Series (RX)

Figure 2.6: *Equivalent circuit for Parallel resonant TX topology and series or parallel resonant RX configuration.*

2.4 Power Transfer Across a Poorly Coupled Link

The explosion in the development and popularity or RFID technologies and embedded devices has directed the interest of designers for wireless systems to issues such as power consumption and harvesting. Until recently, these parameters have been almost last on the list of specifications with implementations focusing more on reliability and data rate. The importance of

consistent power supply becomes even more pronounced in implanted devices where coupling variations are common and the coils are weakly coupled. Although, it is useful to know the voltage and current transfer functions of the coupled coils, the main objective of this thesis is to introduce a simple power transfer function permitting a direct comparison of different antenna designs for a number of possible antenna orientations. For the applications studied, such a function could be an invaluable aid to the designer as it could provide immediate insight into the problem. In the development of a power transfer function it is critical to define the physical

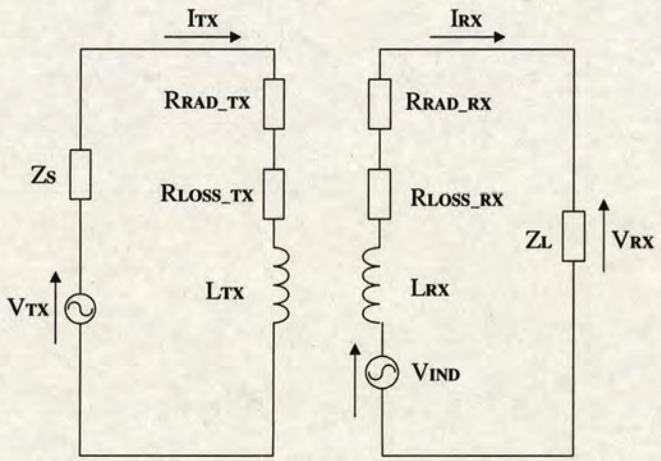

Figure 2.7: *Near-field power transfer model assuming poor coupling.*

meaning of real power transfer. Real power transfer can be identified as the ratio which determines the amount of power dissipated in the TX in order to transfer a specific amount of power across the link to an implanted load, as given below:

$$\frac{P_{RX}}{P_{TX}} = \frac{V_L I_L \cos\phi_L}{V_{TX} I_{TX} \cos\phi_{TX}} \tag{2.11}$$

The real power dissipated in the load is expressed by P_{RX} and P_{TX} represents the power provided by the source driving the TX coil. V_{TX}, I_{TX}, V_L and I_L define the voltage and current amplitude at the resonant TX and RX tuned circuits respectively. The phase differences between the voltage and current signals in the primary and secondary tuned circuits are given by ϕ_{TX} and ϕ_L. It should be noted, that the phase difference does not affect the power transfer function and therefore only the modulus of (2.11) and not the associated argument of the load impedance is of interest. Finally, the efficiency of the link can be defined as:

$$\eta = \left| \frac{V_L I_L}{V_{TX} I_{TX}} \right| \tag{2.12}$$

An equivalent circuit model for a poorly coupled system is depicted in Fig. 2.7, [47]. Using this equivalent circuit a formula expressing the power transfer from transmitter to receiver can be derived, following the method suggested by Yates et al. [47]. On the transmitter side the impedance Z_s is assumed to resonate with the transmitter coil inductance, L_{TX}, enabling the maximum current flow. It follows that:

$$Z_s = \frac{1}{j\omega C} \quad \text{where} \quad C = \frac{1}{\omega^2 L_{TX}} \tag{2.13}$$

The TX coil is exited by a sinusoidal current $I_{TX} = I_o e^{j\omega t}$. The real input power under these conditions is given by:

$$P_{TX} = I^2_{TX_{rms}} \cdot R_{TX} \tag{2.14}$$

On the receiver side the load impedance denoted Z_L in Fig. 2.7, should be conjugately matched to the impedance of the RX coil to achieve maximum power transfer.

$$Z_{LOAD} = R_{RX} - j\omega L_{RX} \tag{2.15}$$

In this case the available real power from the TX that is delivered to the load is given as follows:

$$P_{RX} = \frac{V_L^2}{Real(Z_{LOAD})} \tag{2.16}$$

However, to optimise the power transfer in the radio frequency region it is necessary to use Jacobi's theorem[1]. Consequently, the RX circuit is transformed to a potential divider where:

$$V_L = \left(\frac{Z_L}{Z_L + R_{RX}}\right) \cdot V_{IND} \tag{2.17}$$

Following from (2.16) and (2.17) the received power is expressed in terms of the induced voltage across the RX coil:

$$P_{RX} = V^2_{IND}/4R_{RX} \tag{2.18}$$

The resulting magnetic field vector at the receiver coil can be obtained by integrating Biot-Savart law around the TX loop [52, 53]. Thus, for a short solenoid coil with N turns the magnetic field at the center of the RX coil becomes:

$$\mathbf{H} = \frac{I \cdot N_{TX}}{4\pi} \oint \frac{\mathbf{dl} \times \mathbf{r}}{r^3} \tag{2.19}$$

By Faraday's law, the induced voltage at the receiver antenna is expressed by the rate of change of flux linkage as follows [54]:

$$V_{IND} = \mu_o \, N_{RX} \, A_{RX} \, j\omega \, H \tag{2.20}$$

[1]For a fixed source impedance, maximum power is always transferred into a conjugate matched load

where N_{RX} is the number of turns of the receiver coil, A_{RX} is the loop area ($A_{RX} = \pi \cdot b^2$), b is the radius of the RX loop and μ_o is the permeability of free space.

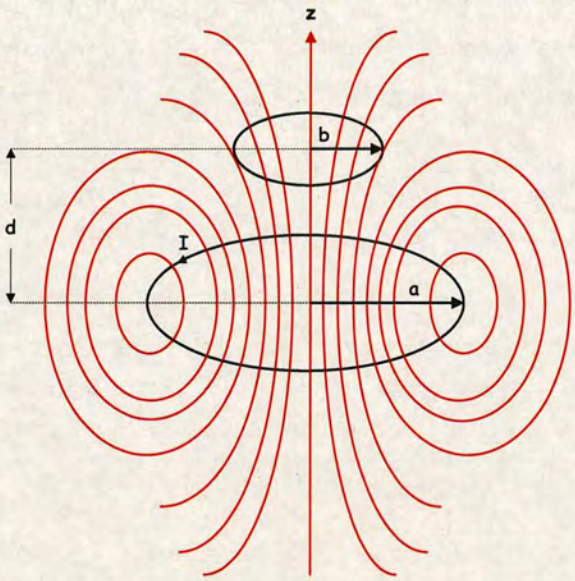

Figure 2.8: *Representation of two inductive coupled coils with figure not drawn to scale. In practice the RX coil is significantly smaller that the TX in order for the field to be uniform across the effective area of the RX.*

Equation (2.20) is valid only for poorly coupled systems. In order for this condition to be true the distance of separation (d) between the TX and RX needs to be much larger than the dimensions of the RX antenna. This is indeed true for biomedical and short range RFID applications where the dimensions of the link are between 1 to 5 cm and the RX coil is usually millimeter and sub-millimeter sized [55]. This condition ensures a uniform magnetic field around the RX such that Faraday's law is applicable.

Combining (2.19) and (2.20), the induced voltage at the RX can be expressed in terms of the transmitter current:

$$V_{IND} = \frac{\mu_o \cdot N_{TX} \cdot N_{RX} \cdot A_{RX} \cdot j\omega \cdot I_{TX_{rms}}}{4\pi} \cdot H_{INT} \tag{2.21}$$

Substituting for V_{IND} and $I_{TX_{rms}}$ in (2.18) and rearranging yields:

$$\frac{P_{RX}}{P_{TX}} = \frac{\mu_o^2 \cdot N_{TX}^2 \cdot N_{RX}^2 \cdot A_{RX}^2 \cdot \omega^2}{16 \cdot \pi^2 \cdot R_{TX} \cdot R_{RX}} \cdot H_{INT}^2 \tag{2.22}$$

where

$$\mathbf{H_{INT}} = \int_0^{\pi} \frac{\mathbf{dl_{TX}} \times \mathbf{r}}{r^3} \tag{2.23}$$

The function derived by Yates et al. is based on an analysis of two identical solenoid coils assumed aligned on a common central axis as depicted in Fig. 2.8. Clearly this scenario represents the ideal case and is not realistic for the applications envisaged in this work. Consequently, it is the objective of this thesis to suggest an extended model for several coil geometries and misalignments. Following, the power transfer expressions introduced in this section, a set of design rules can be formed and the efficiency of the link calculated for several different coil structures and misalignments.

2.5 Radiation Integrals and Auxiliary Potential Functions

Wire loop antennas, are some of the oldest, simplest and most versatile for a variety of applications. It should not come as a surprise to the reader that the review of antenna theory presented in this chapter begins by considering these basic structures. The theory presented here will form the mathematical basis for the analysis of the practical antennas used in wireless power transfer such as the coils structures investigated in this thesis. The coil geometries studied in chapter 3 are the circular, square spiral coils and circular short solenoids usually adopted in RFID and embedded inductive link implementations. As discussed in detail in section 3.4, the loop and dipole antennae are considered the fundamental building blocks in the magnetic field modeling of the more complex structures studied in chapter 3.

In this section the usual procedures used in the analysis of radiation problems are introduced and the method used in this work is justified. A block diagram in Fig. 2.9, depicts the steps used in the computation of radiated fields from electric and magnetic sources. It is common practice to specify the sources and then calculate the fields radiated by the sources. The introduction of auxiliary functions, known as vector potentials, is a valuable aid in the solution of these problems. The solution is often simplified significantly by the introduction of such functions as the magnetic vector potential **A** and the electric vector potential **F**. While the vector potentials may facilitate the solution some additional functions may still be required. Alternatively, it is possible to derive the electric and magnetic field intensities **E** and **H** directly from the source-current densities **J** and **M** or compute the auxiliary potential functions first and then determine the required field intensities, [56]. According to Balanis in [56], in the computation of field intensities two procedures can be identified, as illustrated in Fig. 2.9. A one-step procedure relates the **E** and **H** fields to the **J** and **M**, by integral relations. The two-step procedure, through path 2, associates **A** and **F** potentials to **J** and **M** by integral relations. The electric and magnetic

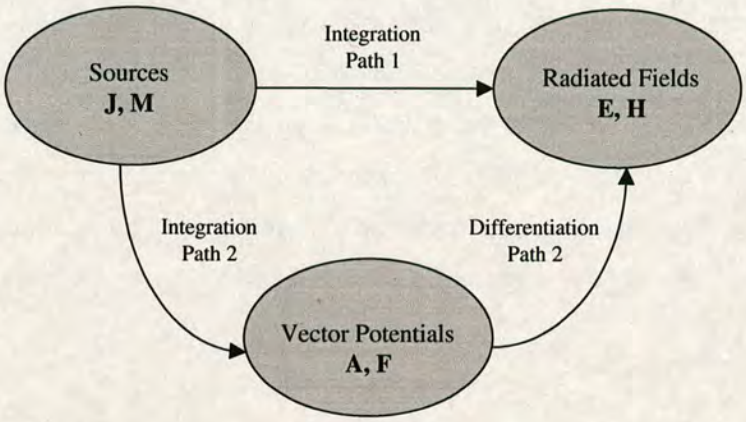

Figure 2.9: *Block diagram for computing radiated fields from electric and magnetic sources.*

field intensities can be simply determined by differentiating **A** and **F**. The one-step process will be adopted in this work as it is less laborious since the integrands appear to be simpler for certain geometries, such as the ones investigated in this work. The integration in the process adopted requires its limits to be determined by the bounds of the sources and the result to be a function of the observation point coordinates. Depending on the situation considered one of the two methods can be employed. The magnetic vector potential approach is more suitable when the radiation pattern of an antenna is required which suggests that it is more suitable for far-field problems.

For many years, the radiation characteristics of loop antennas has an area of interest to researchers. Evidence of this is a substantial body of literature devoted to the subject. An excellent review of research relating to loop antennas is available, among these being King et al. [57], Balanis [56], [58], Kraus [59] and Smith [60]. Literature is readily available for thin circular-loop antennas assuming uniform and nonuniform current distribution and located either in free-space, [61], [62] [63–65] or immersed in layered media [66], [67–69]. As stated and reviewed in [61], [62] and [63], many papers dealt with the radiated fields in the far-field zone generated by circular loops, by applying certain restrictions such as uniform current, sinusoidal current as discussed by Li et al. [64]. Contrary to this, for the near-field zone, only a small amount of work has been reported primarily due to the difficulty in evaluating the integrals of the magnetic vector potential analytically. Werner [61,62] employed the Lommel expansion of Euler's identity in order to evaluate the Hertzian potential integral. This approach involves expressing the electromagnetic components in terms of spherical Bessel and harmonics functions. Some general results are obtained in closed form, with the aid of Fourier Series. In the meantime, Overfelt [63] assumed a constant current distribution in the thin loop

antenna and derived the series form of the Hertzian potential and the radiated near-zone field by means of elliptic integrals. A year later, Li [64] revisited the problem presenting a solution for the electromagnetic fields (EM) for both near and far zones generated by thin circular loop antennas using series in closed form expressions. The results obtained by Werner, Overfelt, Greene and Li although correct, do not appear to be straightforward. Despite the fact that the solutions are analytical and in closed form the use of complex mathematical techniques in the results render them far too complex to be used in practical applications. In addition, the series form solutions presented for the near-field zone converge very slowly and in order to be valid there is a restriction on the observation point. Special cases such as fields due to sinusoidal and uniform current distribution in the circular loop antenna, which are of interest in the applications studied in this work, are presented by Li et al. in [64]. However, for the special case of an electrically small loop antenna which is of interest in this project, the assumption by Li et al., in [64], that uses the first term in the summation in (18) compromises the accuracy of the field calculations for the near-field zone.

On a different note, studies on the field characteristics of polygonal loop antennas are very limited in the literature. In the case of rectangular loop antennas the lack of a circular symmetry seems to complicate a theoretical analysis of the field characteristics. In an early attempt on the problem, King modeled the rectangular loop as a dipole in [66]. Unfortunately, the results presented in this work are extremely complicated. Although this paper provides some information about the circuital properties of the loop the radiation patterns are not given. Another study of rectangular antennas from the same era by Kennedy, [70], presents only experimental techniques and measurements for evaluating the impedance of the antenna. In addition, Balanis and Kraus studied the far-field pattern of a square loop by treating the antenna as a collection of four mutually perpendicular dipoles and superimposing the contributions of each dipole, [56, 71]. In this approach both Balanis and Kraus conclude that the far-field pattern of an electrically square loop of constant current is identical to the far-field characteristics of a small circular loop. On the contrary in the near-field this equivalence does not hold true since the transmitting antenna cannot be modeled based on a source point approximation. However, neither of the aforementioned papers provide any details about the behaviour of the structure in the near-field. It is obvious that in the near-field, the geometry of the loop will influence the field, if the loop is electrically small, but finite in comparison to the observation point. To the author's knowledge there are only two papers available in the literature by Levin, [72], and Lou, [73], that present exact analytic expressions for the field of a square loop. However, these

solutions are mathematically complex. This is attributed to the fact that in the near-field it is difficult to evaluate the integrals involved in the computation of the field.

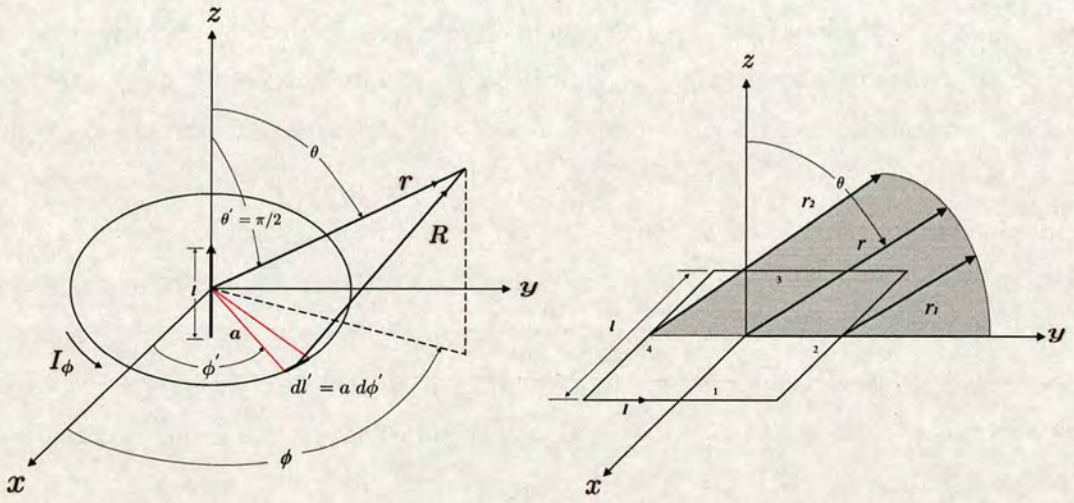

Figure 2.10: *Circular and square loop antennas, [56].*

The previous discussion aims to show that in the magnetostatic case the magnetic field in a circular loop can be easily derived from Biot-Savart law using the one-step process. For the applications envisaged here the loop considered is electrically small and thus the magnetostatic approximation holds well. As a first approach, for the applications envisaged in this work, an electrically small loop antenna is considered. As shown in Fig. 2.10 the loop is thought to be located in an unbounded, homogeneous, isotropic medium consisting of a number of small line elements dl' carrying a current I' and located at the origin of an orthogonal coordinate system (x, y, z). In order to obtain the magnetic field of the current elements along the current path of a constant current $I = I_o e^{j\omega t}$we integrate Ampere's Law over the path:

$$\mathbf{H} = \oint \mathbf{dH} = \oint \frac{I\mathbf{dl} \times \mathbf{R}}{4\pi R^3} \tag{2.24}$$

2.6 Region Separation

The space surrounding an antenna is usually subdivided into three regions: the reactive near-field region, the radiating near-field referred to as Fresnel region and the far-field or Fraunhofer region. These regions are designed to identify the changes in the field structure as the observation point is crossing between boundaries. For an electrically small antenna there are only two

separate regions, the reactive near-field and the radiating field. Energy is stored in the former, whilst energy propagates as electromagnetic waves in the latter. The boundary between the two regions is generally accepted to be at a distance, r, from the antenna:

$$r = \frac{\lambda}{2\pi} \tag{2.25}$$

λ being the wavelength, [46].

In the case of an electrically large antenna a further distinction becomes significant where the radiating field is split into the radiating near field and the radiating far-field regions. There are distinct differences between regions posing a great difficulty in a universal field representation for any point in space. However, approximations can be made to simplify the formulation of the field and yield a closed form solution. At this stage it is very important to introduce the field regions properly and disscuss their influence on the field solution. Over the years various criteria have been established and are commonly used to identify the different field regions. The following definition and quotations are presented by the IEEE, in [74].

The reactive near-field is defined as "that region of the field immediately surrounding the antenna wherein the reactive field predominates". For most antennas, the outer boundary of this region is commonly taken to exist at a distance $R < 0.62\sqrt{D^3/\lambda}$ from the antenna, where λ is the wavelength and D is the largest dimension of the antenna.

The radiating near-field or Fresnel region is defined as "that region of the field of an antenna between the reactive near-field region and the far-field region wherein radiation predominates and the angular field distribution is dependent upon the distance from the antenna". The radial distance R over which this region is defined is $0.62\sqrt{D^3/\lambda} \leq R < 2D^2/\lambda$. In this region the field pattern is, in general, a function of the radial distance and the radial field component may be appreciable.

The far-field (Fraunhofer) region is defined as "that region of the field of an antenna where the angular field distribution is essentially independent of the distance from the antenna". In this region, the real part of the power density is dominant. The radial distance R over which this region exists is $R \geq 2D^2/\lambda$. The outer boundary is situated ideally at infinity. In this region, the field components are essentially transverse to the radial distance, and the angular distribution is independent of the radial distance.

In order to illustrate the difference between the three field regions, as described above, the

magnetic field of a small loop antenna is discussed. At a radial distance r from a small circular loop carrying a sinusoidal uniform current $I = I_o e^{j\omega t}$ two components of magnetic field exist, these being H_θ and H_r, [59]. Due to the circular symmetry of the antenna there is no variation with respect to ϕ. Hence, H_θ and H_r are expressed as follows:

$$H_\theta = \frac{m_o \sin\theta e^{j(\omega t - \beta r)}}{4\pi}\left[-\frac{\beta_o^2}{r} + j\frac{\beta_o}{r^2} + \frac{1}{r^3}\right] \tag{2.26}$$

$$H_r = \frac{m_o \cos\theta e^{j(\omega t - \beta r)}}{2\pi}\left[j\frac{\beta_o}{r^2} + \frac{1}{r^3}\right] \tag{2.27}$$

where m_o is the magnetic moment, equal to $I_o \pi \alpha^2$ and β_o is defined as the phase constant of free-space and is equal to $2\pi/\lambda_o$.

Conventionally, the terms in the magnetic field intensity expressions H_θ and H_r are described as follows:

- $1/r$, radiation component in the far-field
- $1/r^2$, induction component in the radiating near-field
- $1/r^3$, magnetostatic component in the reactive near-field

Solving Maxwell's equations for the fields of a localized oscillating source like an antenna, surrounded by a homogeneous and isotropic material, the field decays proportionally to the terms listed above. For instance, the fields of a source in a homogeneous isotropic medium can be written as a multipole expansion. The terms in this expansion are spherical harmonics, which provide the angular dependence, multiplied by spherical Bessel functions, which support the radial dependence. For large r, the spherical Bessel functions decay as $1/r$ in the radiating far-field. For a distance closer to the source, the reactive near-field dominates and other powers of r become significant. In this case the field strength is proportional to the term $1/r^2$. This term is sometimes referred to as the induction term of the radiating near-field. It can be thought of as the energy stored in the field and returned to the antenna in every half-cycle. For even smaller r, terms proportional to $1/r^3$ become significant; this is sometimes called the magnetostatic field term at regions very close to a loop antenna where the magnetic field dominates. The difference between the field regions can be effectively illustrated using the diagram of Fig. 2.11.

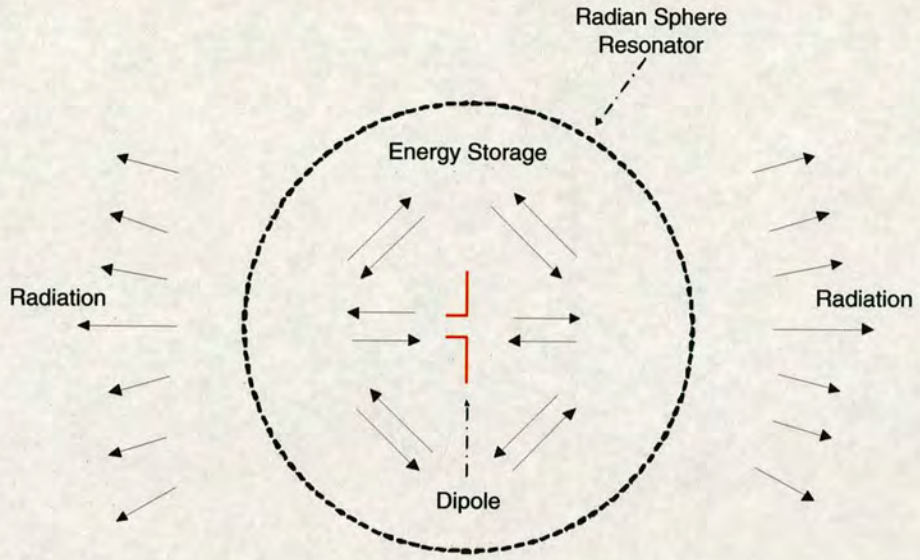

Figure 2.11: *Diagram depicting the analogy between the situation within the near-field with that of a resonator. Inside the radian sphere high-energy is pulsating whereas some leakage is radiated outside the boundary of the near-field.*

2.7 The Infinitesimal Dipole

Let us consider an infinitesimal linear dipole where the length of the conductor is very short compared to the wavelength ($l << \lambda$). The dipole is positioned symmetrically at the origin of a rectangular coordinate system and oriented along the z-axis, as shown in Fig. 2.12. It is of special interest to introduce the infinitesimal dipole and examine the radiation properties of short conductors which can then be applied in the study of more realistic antennas such as rectangular loop structures. Although, infinitesimal dipoles are not very practical structures they can be utilized as building blocks for more complex geometries. In particular, circular or square loop antennas can be considered as consisting of a large number of very short conductors. An infinitesimal dipole is very short ($l \leq \lambda/50$) and of very small ($\alpha << \lambda$) circumference, so the current is assumed to be constant and uniform and is given by:

$$\mathbf{I}(z') = \mathbf{a}_z I_o \tag{2.28}$$

where I_o is constant.

It is important to discuss the field characteristics of an infinitesimal dipole as the square loops studied in this work are considered to be comprised of a series of infinitesimal dipoles. A two step procedure of Fig. 2.9 is implemented. The magnetic vector potential **A** is determined first:

$$\mathbf{A}(x,y,z) = \frac{\mu}{4\pi}\int_C I(x',y',z')\frac{e^{-jkR}}{R}\,dl' \tag{2.29}$$

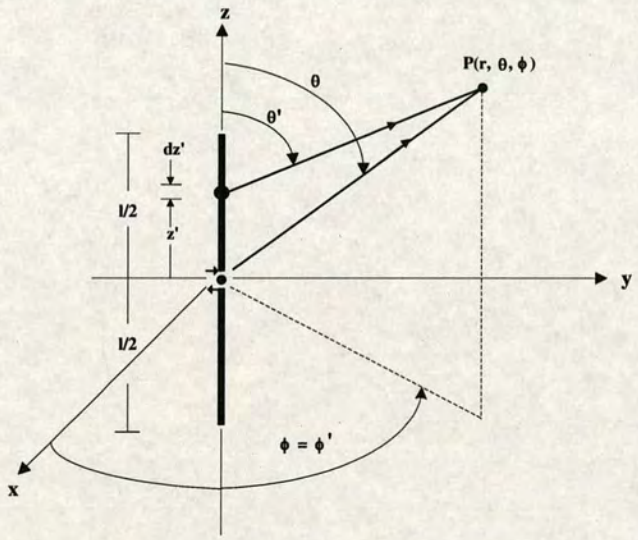

Figure 2.12: *Dipole and Geometry [56].*

where (x, y, z) represent the coordinate system and (x', y', z') represent the coordinates of the source, C is the path of integration along the length of the source. The geometry of the problem can be visualized referring to Fig. 2.12. Since an infinitesimal structure is considered:

- $x' = y' = z' = 0$
- $R = \sqrt{(x-x')^2 + (y-y')^2 + (x-x')^2} = \sqrt{x^2 + y^2 + z^2} = r =$ constant
- $dl' = dz'$

Thus, the magnetic vector potential **A** becomes:

$$A(x, y, z) = \mathbf{a_z} \frac{\mu I_o}{4\pi r} e^{-jkr} \int_{-l/2}^{+l/2} dz' = \mathbf{a_z} \frac{\mu I_o}{4\pi r} e^{-jkr} \tag{2.30}$$

By transforming from rectangular to spherical coordinates and making use of the symmetry of the problem, meaning no variation across the direction of angle ϕ, the field components can be derived using Maxwell's equations as follows:

$$H_\phi = j \frac{k I_o l \sin\theta}{4\pi r} \left[1 + \frac{1}{jkr}\right] e^{-jkr} \tag{2.31}$$

$$E_r = \eta \frac{I_o l \cos\theta}{2\pi r^2} \left[1 + \frac{1}{jkr}\right] e^{-jkr} \tag{2.32}$$

$$E_\theta = j\eta \frac{k I_o l \sin\theta}{4\pi r} \left[1 + \frac{1}{jkr} - \frac{1}{(kr)^2}\right] e^{-jkr} \tag{2.33}$$

The exact derivation of equation (2.30) is illustrated in detail in Balanis [56] and Kraus [59,71]. The terms which determine the variation of the field components in the near and far fields are plotted in the following figure, Fig. 2.13.

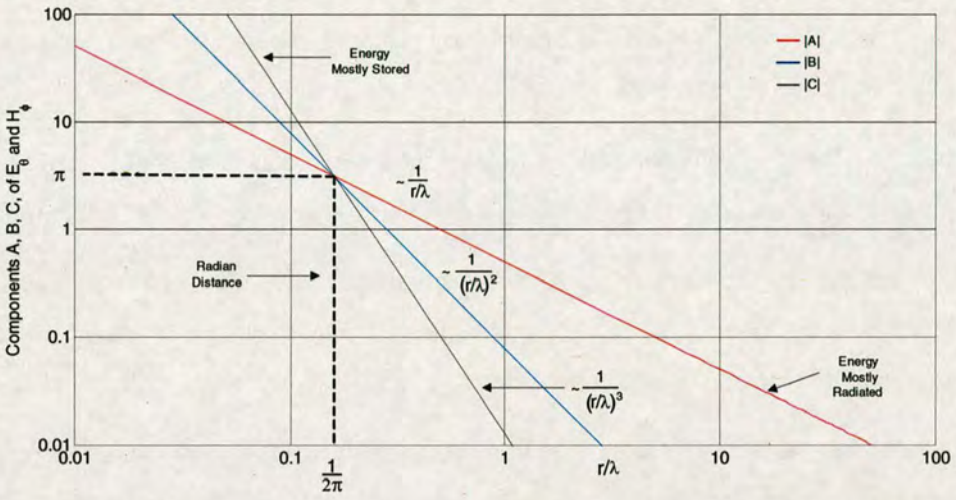

Figure 2.13: *Variation of the magnitudes of the components of E_θ and H_ϕ of a short electric dipole as a function of distance (r/λ). The magnitudes of all components equal π at the radian distance $1/(2\pi)$. At larger distance (far-field) energy is mostly radiated, at smaller distances (near-field) mostly stored, [59].*

2.8 The Importance of the Loop Antenna

The loop antenna is a fundamental and simple antenna and it has received tremendous attention for short-range wireless power transfer and communications. Loop antennas have been used continually since the early days of radio and they have become particularly widespread for applications in the HF band (3-30MHz), due to their small size. Loop antennas are very adaptable structures and except from the widely known circular geometry, they can take many different forms such as rectangle, square, triangle, ellipse. The loop antenna has been identified as being particularly suited to applications where wireless power delivery is required such as the powering of biomedical implants [35], [75], [39] and passive RFID tags [46]. The ability to receive energy wirelessly is essential to these devices since true autonomy is a key factor. Inductive power and telemetry are implemented in a variety of applications where the size of the RFID tag or implant is limited and batteries are not allowed. Currently inductive energy scavenging techniques for ubiquitous computing systems, RFID devices and sensor networks

are receiving extensive attention, [24, 76, 77]. In this section the characteristics of the loop antenna are discussed in order to justify its suitability for the aforementioned applications.

The use of a loop antenna in near-field systems yields several advantages, among these being:

- The relatively non-directional nature of loop antennas can improve the operating range of the device in the near field.
- In the HF band the antenna may be reasonably described as electrically small allowing the assumption of uniform current distribution which significantly simplifies the analysis.
- The effect of any conductive media, such as biological tissue, is decreased using an implantable loop antenna due to the fact that the dominant magnetic near-field suffers less attenuation compared to an electric field.
- A small loop is primarily inductive. In most magnetically coupled systems, resonance is employing using the inductance of the loop antenna in the oscillator resonant tank. In this manner, the loop can operate as a transmitting and receiving antenna, at the specified resonant frequency. This can be demonstrated in simple low power short range transmitters such as those presented in [78], [47].

The loop antenna is a very versatile structure classified into two categories: (a) electrically small and (b) electrically large. A loop antenna is considered to be electrically small if the radius is very small compared to the wavelength ($a << \lambda$) or the overall length (l) is less than one-tenth of a wavelength ($l < \lambda/10$). On the contrary, electrically large loops are those whose circumference (C) is comparable to the wavelength of the operating frequency ($C \approx \lambda$). Most of the formulae presented in this chapter are valid for electrically small coils. As discussed earlier a coil is generally considered to be small if the total conductor length is less than a tenth of the wavelength [56]. Consequently, the range of frequencies over which the analysis presented in this thesis is restricted. Table 2.1 illustrates the maximum frequency in Hz for typical coil dimensions used in biomedical and RFID applications, in order for the coils to be considered electrically small.

2.8.1 Small loop of constant current

A small loop antenna (circular or square) is equivalent to an infinitesimal magnetic dipole whose axis is perpendicular to the plane of the loop. As a result, the fields radiated by an

N/Radius	0.001m	0.005m	0.01m	0.05m	0.10m
1	4.8G	955M	477M	96M	48M
2	2.4G	477M	238M	48M	24M
4	1.2G	238M	119M	24M	12M
6	796M	160M	80M	16M	8M
8	597M	119M	60M	12M	6M
16	298M	60M	30M	6M	3M

Table 2.1: *Maximum Frequency (Hz) for Various Dimensions of Electrically Small Coils.*

electrically small circular or square loop antenna are of the same mathematical form as those radiated by an infinitesimal dipole. A schematic antenna configuration is depicted in Fig. 2.14(a) representing the loop with its self-inductance and resistance and a tuning capacitor in series. In practice an unbalanced feeder is connected via a coupling loop, the magnetic flux of which links the main loop. This principle is represented in Fig. 2.14(b).

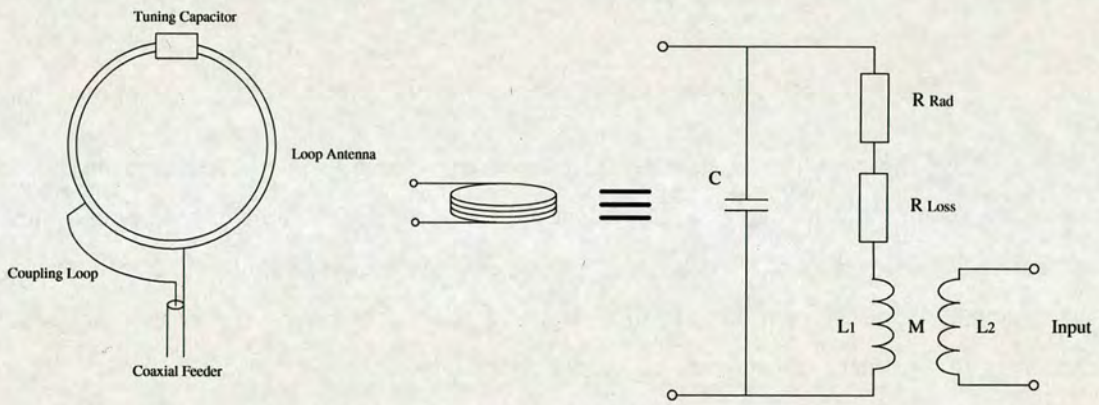

(a) Basic method of driving loop antenna.

(b) Equivalent circuit of multiturn loop antenna using lumped parameter.

Figure 2.14: *L_1 main loop, L_2 coupling loop, M mutual inductance, C resonating capacitance, R_{Loss} loss resistance, R_{Rad} radiation resistance, C resonating capacitor.*

2.8.1.1 The loop in transmitting mode

A small magnetic loop antenna is primarily inductive and can be delineated by a lumped element equivalent circuit as shown in Fig. 2.14(b). The circuital representation of its input impedance when it is employed as a transmitting antenna is shown in Fig. 2.15, which is similar with Fig. 2.14(b). Consequently, the input impedance Z_{in} is represented as follows:

$$Z_{in} = R_{in} + jX_{in} = (R_{Rad} + R_{Loss}) + j(X_A + X_i) \tag{2.34}$$

where:

- R_{Rad} is the radiation resistance
- R_{Loss} is the loss resistance of loop conductor
- X_A is the inductive reactance of magnetic loop antenna, $X_A = \omega L_A$
- X_i is the reactance of the loop conductor, $X_i = \omega Li$

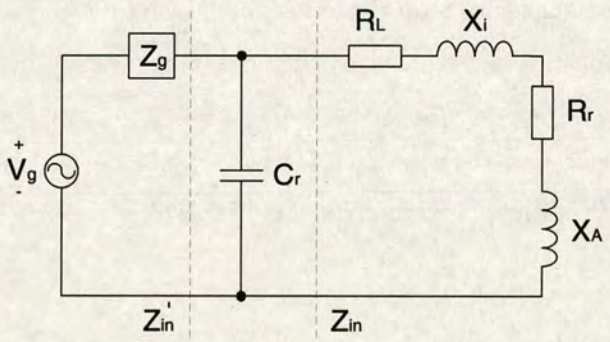

Figure 2.15: *Equivalent circuit of loop antenna in transmitting mode.*

In Fig. 2.15, the capacitor C_r is used to resonate the antenna. In addition, any distributed or interwinding parasitic capacitance present at the loop antenna can be incorporated in the capacitor C_r. The resonant magnetic loop can be employed as a transmitter to transfer energy by means of inductive coupling. In this manner, power can be transfered using transformer action from a primary transmitting coil to the secondary receiving coil, where both coils are tuned resonant magnetic loops at a common frequency. At resonance, the susceptance B_r of the capacitor C_r is chosen in order to cancel the imaginary part of B_i. Hence, at resonance the capacitor value is determined by the following well known expression, [56]:

$$C_r = \frac{B_r}{2\pi f} = -\frac{B_{in}}{2\pi f} = \frac{X_{in}}{2\pi f(R_{in}^2 + X_{in}^2)} \tag{2.35}$$

The equivalent admittance Y_{in} of the capacitor C_r is given as:

$$Y_{in} = G_{in} + jB_{in} = \frac{1}{Z_{in}} = \frac{1}{R_{in} + jX_{in}} \tag{2.36}$$

where

$$G_{in} = \frac{R_{in}}{R_{in}^2 + X_{in}^2} \tag{2.37}$$

$$B_{in} = -\frac{X_{in}}{R_{in}^2 + X_{in}^2} \tag{2.38}$$

Hence, the equivalent input impedance, Z'_{in}, of the resonant magnetic loop antenna is derived as follows:

$$Z'_{in} = R'_{in} = \frac{1}{G_{in}} = \frac{R_{in}^2 + X_{in}^2}{R_{in}} = R_{in} + \frac{X_{in}^2}{R_{in}} \tag{2.39}$$

The losses in the tuned transmitter coil are expressed by R_{Rad} and R_{Loss}. In electrically small loop antennas the radiation losses are negligible, as shown in Fig. 2.16. The radiation resistance of loop antennas with uniform current and dimensions small compared to the wavelength can be easily evaluated using the following well known expression [79], [56]:

$$R_{Rad} = 20\pi^2 N^2 (\frac{l}{\lambda})^4 \Omega \tag{2.40}$$

The proof for the radiation resistance expression (2.40), for an electrically small loop antenna, is attached as an appendix at the end of this Thesis. For an N-turn loop the magnetic field passes through all the loops and the radiation resistance is increased by the term N^2 in (2.40), where l is the circumference of the loop and λ is the wavelength.

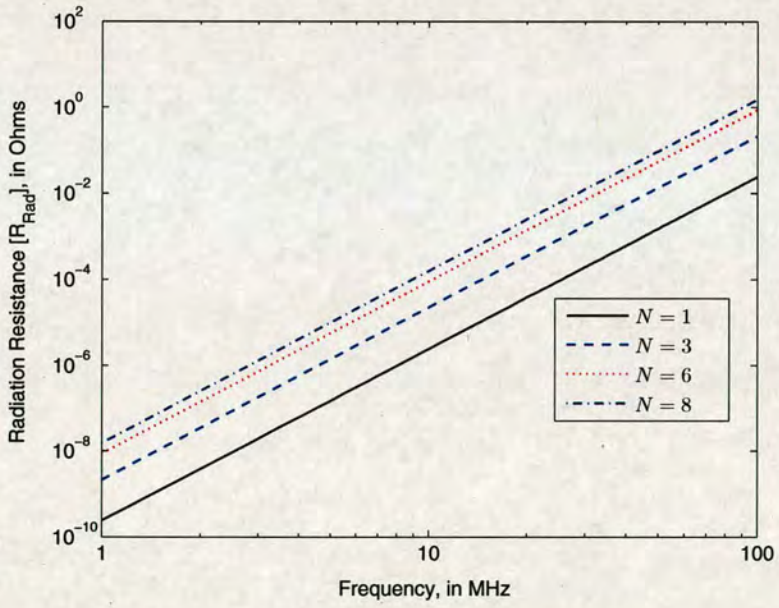

Figure 2.16: *Radiation resistance for a constant current single loop and multi-loop antenna with respect to frequency, based on the approximation of (2.40).*

The radiation and ohmic losses are important parameters in the design of an antenna as they determine the radiation efficiency. In general for the electrically small loop antennas being investigated in this work the loss resistance is generally much larger than the radiation resistance. Therefore, the corresponding radiation efficiency is very low. As a result, small loop antennas are very poor radiators and they are seldom employed in conventional far-field transmission.

The radiation efficiency can be computed based on the two experimental techniques referred to as the *Wheeler method* and the *Q method*, [80]. It should be noted that due to the complexity of the current distribution between the windings of a multi-turn antenna great confidence has not yet been placed in an analytical solution to the radiation efficiency riddle. However, until greater understanding of the theoretical approach to this problem has been established, greater confidence should be placed in the experimental techniques mentioned previously. A detailed discussion of the *Wheeler* (2.41) and *Q* (2.42) methods is given in [80], [81] and [82]. The radiation efficiency as defined by the *Wheeler* method is given by the following expression:

$$\eta = \frac{R_{rad}}{R_{rad} + R_{Loss}} \tag{2.41}$$

The radiation efficiency as defined by the Q method is given below:

$$E_Q = \frac{Q_{RL}}{Q_R} = \frac{power\ radiated}{power\ radiated\ +\ power\ dissipated} \tag{2.42}$$

where Q_{RL}, Q_R are the quality factors of a practical and ideal antennae respectively.

Consequently, the loop antenna is a poor radiator since $R_{Loss} >> R_{rad}$. Therefore, when employing loop antennas magnetic coupling is a more efficient method to transfer energy in the near-field.

2.8.1.2 The loop in the receiving mode

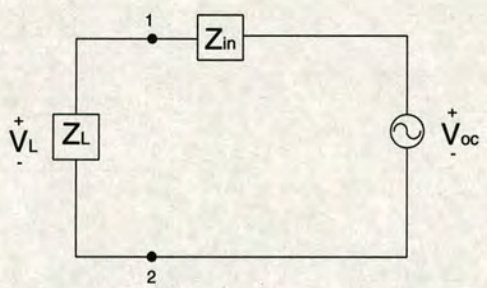

Figure 2.17: *Equivalent circuit of the loop antenna in receiving mode.*

A magnetic loop is often used as a receiving antenna or as a probe to measure magnetic flux density. The Thevenin equivalent circuit of a loop antenna in the receiving mode is depicted in Fig. 2.17. An electrically small loop enclosing an effective area A and placed in a uniform alternating magnetic field can be now considered. Assuming that the axis of the winding is parallel to the field strength vector H and the incident field is uniform over the plane of the

loop, the open circuit voltage for a multiturn loop antenna can be written as, [54], [56]:

$$V_{IND} = j\omega\mu_o NHA \tag{2.43}$$

Close investigation of the previous expression shows that (2.43) is an alternative representation of Faraday's law, where the *emf* across the terminals of the receiving antenna is equal to the time rate of change of magnetic flux through the area of the loop. For the static antenna, [53]:

$$\oint \mathbf{E} \bullet \mathbf{dl} = -\frac{\partial \psi_m}{\partial t} = -\frac{\partial}{\partial t}\int_S \mathbf{B} \bullet \mathbf{dS} \tag{2.44}$$

where the flux ψ_m is found by evaluating the normal component of flux density B over the surface of the loop as shown in Fig. 2.18.

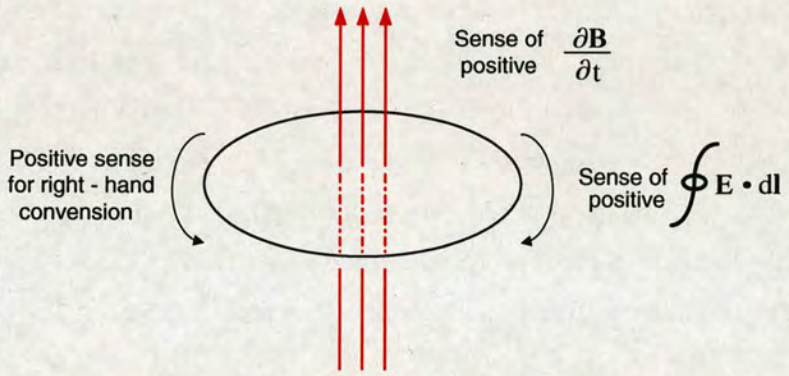

Figure 2.18: *Sense relations for Faraday's law.*

By revisiting the Thevenin equivalent circuit of Fig. 2.17 it is evident that when the load impedance Z_L is connected to the output terminals of the loop, the voltage V_L across the load impedance Z_L is related to the output impedance Z'_{in} and the induced open-circuit voltage of (2.43) as follows:

$$V_L = V_{IND} \cdot \frac{Z_L}{Z'_{in} + Z_L} \tag{2.45}$$

It should be noted that the open circuit voltage of (2.43) is also related to the vector effective length of the loop antenna expressed as:

$$\ell_e(\theta, \phi) = \hat{\mathbf{a}}_\theta l_\theta(\theta, \phi) + \hat{\mathbf{a}}_\phi l_\phi(\theta, \phi) \tag{2.46}$$

However, since the quantity in (2.46), alternatively referred to as the effective height, is a far-field quantity and can be omitted from the near-field induced voltage calculation in (2.43). In

a far-field investigation where the radiation field contributes to the open circuit voltage the following representation is more appropriate:

$$V_{IND} = jk_o A \cos(\psi_i) \sin(\theta_i) \tag{2.47}$$

where the factor $\cos(\psi_i) \sin(\theta_i)$ is introduced as the magnetic flux density component which is normal to the plane and $k_o = 2\pi/\lambda$ is the free space propagation constant. Since the study presented in this thesis is focused on the magnetostatic case in the near-field, Faraday's law can be utilized in the form expressed by (2.43), ignoring any far-field contributions.

Generally, it is common to incorporate ferrite material at the center of a receiver antenna in order to improve signal reception. The advantages of ferrite loaded loop antennas of small volume at HF have been known since the 1940's. Advances in ferrite technologies, have made their use even more attractive. In applications where it is important to minimize the volume occupied by the device, as in remotely controlled biomedical implants, the use of ferrite antennas is desirable. The ferromagnetic material concentrates the magnetic flux lines toward the receiver antenna. Thus, the flux density at the center of the loop is increased by a factor μ_r. The voltage induced cross the terminals of a ferrite antenna can be expressed by [54], [83]:

$$V_{IND_{ferrite}} = j\omega\mu_o\mu_r NHA \tag{2.48}$$

where N is the number of turns, μ_r is the magnetic permeability of the ferromagnetic material.

2.9 Modelling Coil Properties

In the previous sections the radiation characteristics of loop antennas were discussed and the importance of the loop antenna was justified as a device for inductive power transfer in the near-field. Combining the electromagnetic behavior of an electrically small loop antenna with the principle of resonance and the theory of inductively coupled circuits, it is possible to develop a method of expressing the real power transfer between TX and RX antennae. The focus of this section is on the antenna coil properties such as the self and mutual inductance of the coils, as well as discussing the internal impedance and its effect on the power transfer.

2.9.1 Mutual inductance of coupled coils

Following from the circuital analysis of the resonant TX, RX topologies discussed in section 3.2 the concept of mutual induction and its implications to the modelling of near-field power transfer will be discussed in detail. When a variable magnetic field links one part of a circuit to another part an induced voltage is generated according to Faraday's law. This coupling of energy is represented in the circuit by means of a mutual inductor M, as shown in Fig. 2.19. The value of M is defined as the magnetic flux ψ_{12} linking path 1 in Fig. 2.19, divided by the current I_2, as shown in [53]:

$$M = M_{12} = \frac{\psi_{12}}{I_2} \tag{2.49}$$

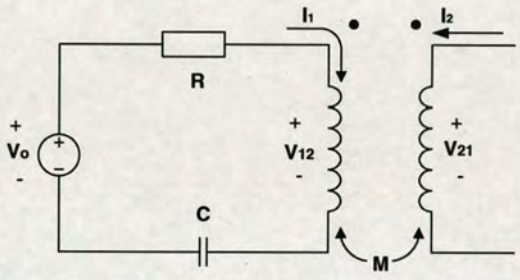

Figure 2.19: *Designation of mutual coupling using the of mutual inductance principle.*

The voltage induced in the first path, depicted on the diagram of Fig. 2.19, is given as:

$$V_{12} = \frac{d\psi_{12}}{dt} = M\,\frac{dI_2}{dt} \tag{2.50}$$

In the same manner, the time varying current circulating in circuit 1, shown in Fig. 2.19, induces a voltage in circuit 2 given as:

$$V_{21} = \frac{d\psi_{21}}{dt} = M\,\frac{dI_1}{dt} \tag{2.51}$$

At this point it should be noted that for isotropic materials there is a reciprocal relation showing that the same M generates a voltage in circuit 2.

The mutual inductance M varies according to the resonant frequency and the inductance of the coils under consideration. However, M is greatly affected by geometrical parameters such as the TX, RX coil proximity, shape and orientation. The mutual inductance as defined previously arises from the induced voltage in one circuit due to current circulating in another circuit. Several approaches to its calculation can be now discussed, some of which will be used to justify the decision of adopting a loosely coupled system.

- **Flux linkages.** The most straight forward approach follows from Faraday's law, finding the magnetic flux linking one circuit related to the current flowing in the other circuit, as in Eq. 2.49. Therefore, for two circuits denoted 1 and 2 the mutual inductance can be written as follows:

$$M_{12} = \frac{\int_{S1} \mathbf{B_2} \cdot \mathbf{dS1}}{I_2} \tag{2.52}$$

where $\mathbf{B_2}$ is the magnetic flux due to current I_2 and integration is over the surface of circuit 1. By reciprocity $M_{21} = M_{12}$, which is true for isotropic materials and as a result the calculation can be done using the inducing current at each circuit. Two parallel coaxial conducting loops can be now considered as pictured in Fig. 2.20. Using Biot-Savart law the magnetic field generated by the current circulating in one loop can be calculated at a point on the axis as given in [46], [71], [53]:

$$B_z\,(0, d) = \frac{\mu\, I_2\, \alpha^2}{2\,(\alpha^2 + d^2)^{3/2}} \tag{2.53}$$

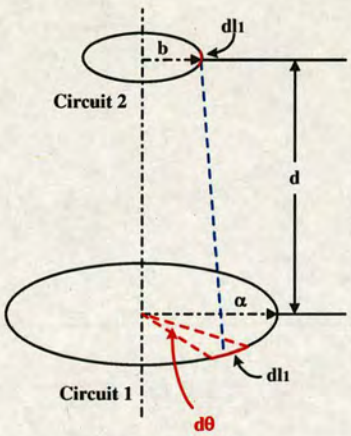

Figure 2.20: *Two parallel coaxial loops.*

For the applications envisaged in this work, such as in the biomedical and RFID domains, loop 2 which acts as the RX is usually small enough compared with the loop spacing d. Thus, the magnetic flux cutting through loop 2 is considered to be relatively constant and uniform over the second loop. In retrospect the relation for the mutual inductance becomes:

$$M = \frac{\mu\pi\alpha^2 b^2}{2(\alpha^2 + d^2)^{3/2}} \tag{2.54}$$

- **Magnetic Vector Potential Approach.** The application of Stoke's theorem to (2.52) yields an equivalent expression in terms of the magnetic vector potential:

$$M = \frac{\int_{S1}(\nabla \times \mathbf{A_2}) \cdot \mathbf{dS_1}}{I_2} = \frac{\oint \mathbf{A_2} \cdot \mathbf{dl_1}}{I_2} \tag{2.55}$$

In cases where the magnetic field is difficult to calculate directly, compared to the vector potential, this form becomes useful. In particular, this is true for problems where the circuit has straight-line segments or can be approximated in such a manner.

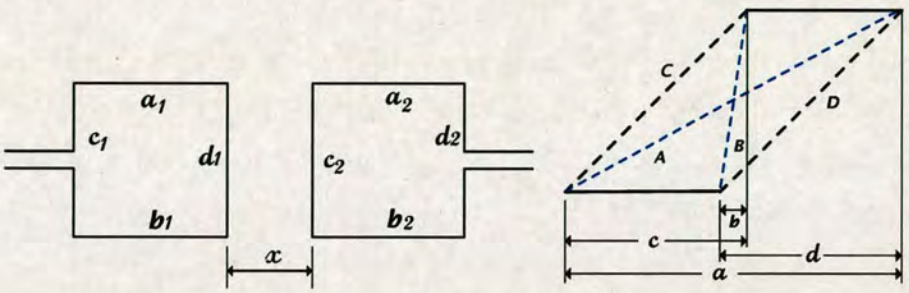

(a) (b)

Figure 2.21: *(a) Two rectangular coupling loops, (b) Parallel current elements displaced from one another.*

- **Neuman's Form.** Another standard technique used in the calculation of mutual inductance of two filamentary conductors is given by Neumann's formula given below. This approach originates from calculating the magnetic vector potential A arising from circuit 2, assuming the current to be in line filaments and neglecting retardation.

$$A_2 = \oint \frac{\mu I_2 \mathbf{dl}}{4\pi R} \tag{2.56}$$

Substitution in (2.56), yields Neumann's formula:

$$M = \frac{1}{I_2} \oint \oint \frac{\mu\, I_2\, \mathbf{dl_1} \cdot \mathbf{dl_2}}{4\pi R} = \frac{\mu}{4\pi} \oint \oint \frac{\mathbf{dl_1} \cdot \mathbf{dl_2}}{R} \tag{2.57}$$

where R is the distance between current element **dl2** and the point at which the magnetic field should be computed.

This standard form is named after Neumann which is used in the derivation of the mutual inductance calculation for a system of parallel coaxial loops as illustrated in Fig. 2.20.

Having presented the most popular methods for the derivation of the mutual inductance, available it is now possible to concentrate on estimating the coupling between the TX and RX coils in the applications we are envisaging using the flux linkage method for the derivation of the mutual inductance for a number of practical antenna coils. An estimate of the mutual coupling will justify the loosely coupled idea adopted in order to simplify the problem of modelling near-field inductive coupling.

Referring back to (2.54) the mutual inductance of two coaxial coils of radius a and b with N_{TX} and N_{RX} number of turns at a distance d is given by:

$$M = \frac{\mu \, \pi N_{TX} \, N_{RX} \, a^2 \, b^2}{2(a^2 + d^2)^{3/2}} \tag{2.58}$$

Figure 2.22 depicts the mutual inductance for a number of TX and RX coil dimensions, representative in biomedical and RFID scenarios. Fig. 2.22 and Fig. 2.23 show that the mutual inductance between coils with radii within practical bounds for the application areas studied, is very low even for larger coils.

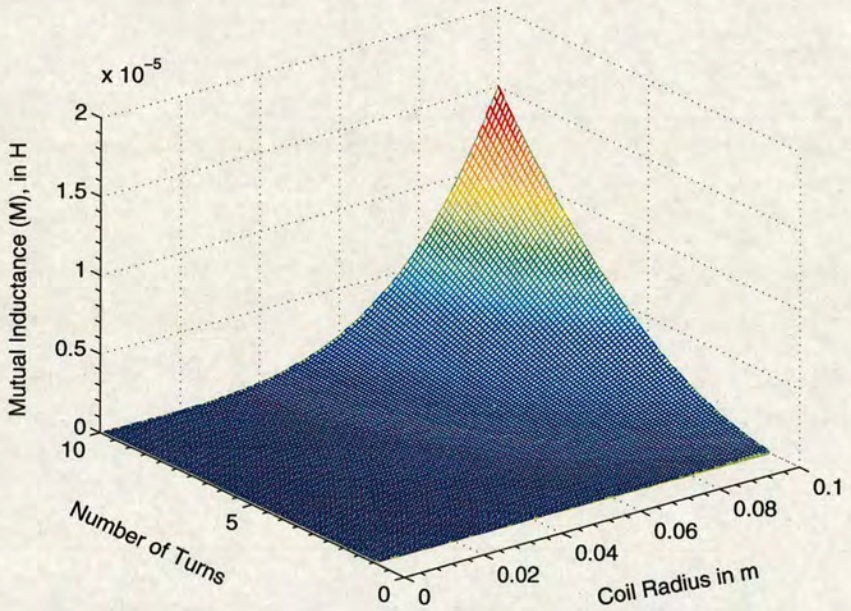

Figure 2.22: *Mutual inductance of TX and RX coils separated by a distance of 0.5m for varying number of turns and coil radius.*

Once the mutual inductance is known the concept of coupling coefficient, k, can be introduced, as it provides a qualitative prediction about the coupling of the conductor loops independent of their geometric dimensions. The following relation applies as referred to in numerous textbooks, [46], [48]:

$$k = \frac{M}{\sqrt{L_1 \cdot L_2}} \tag{2.59}$$

where L_1 and L_2 represent the inductance of the TX and RX coils respectively and the coupling coefficient k always varies between two extreme cases as $0 \leq k \leq 1$.

An analytic calculation for complex antenna structures can be very difficult to achieve. How-

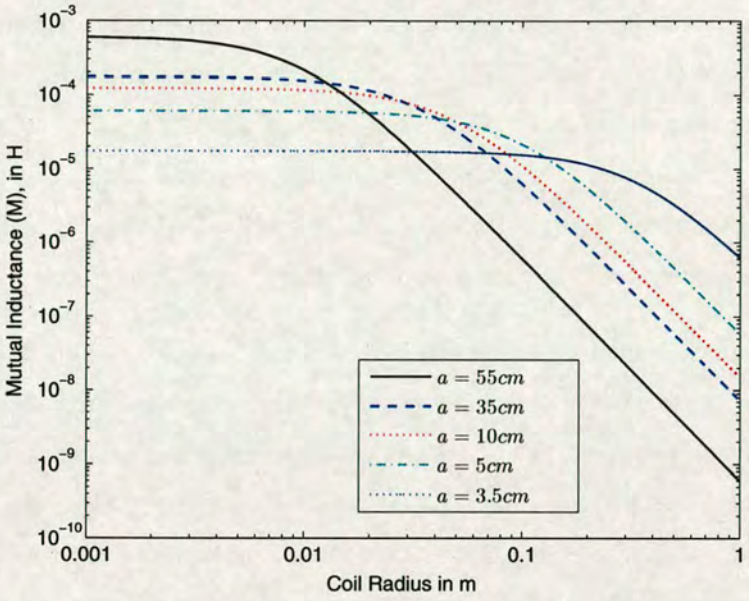

Figure 2.23: *Variation in mutual inductance between the TX and RX antenna coils, for a RX coil radius of 3.5cm, as the distance between the coil increases.*

ever, an approximation for the coupling coefficient for the simple case of two parallel and coaxial circular loops is given in (2.60), [84], [34]. Although this expression does not represent the coupling factor for all the coil configurations investigated in this thesis, it can be used as a first step to approximate the magnitude of the coupling factor:

$$k \approx \frac{a^2 \cdot b^2}{\sqrt{a \cdot b} \cdot \sqrt{d^2 + a^2}^3} \tag{2.60}$$

In implantable devices the external primary or transmitter coil and an implanted secondary coil are separated by a layer of skin and tissues usually not exceeding 1-3cm in thickness. The magnetic link allows the transfer of energy and information, through the biological tissue medium. However, often misalignment of the coils is possible due to skin mobility and variations in the thickness of subcutaneous fatty tissue. Since some degree of misalignment is inevitable between TX and RX coils in transcutaneous RF links, its effect on the mutual inductance needs to be addressed. To the best of the author's knowledge the practical issues of coil misalignment and orientation and their implications on transmission characteristics of RF links has been overlooked by researchers with very few exceptions. Papers presented by Flack et al. [85] and Hochmair [45] consider only the effects of lateral displacement of coils on the mutual inductance. The study by Flack et al. is based on experimental data whereas Hochmair reduces the double integral to a single and implements numerical integration to solve it. Neither of these works take into account the geometric characteristics of the coils and their shape focusing

only on parallel circular loops of zero thickness, these being essentially flat filaments. Almost all designs still depend on an uneasy alliance between the experimental work by Terman [43], empirical data or the extensive data for the self and mutual inductance of coils presented by Grover [42] based on numerical methods. Although these techniques are acceptable they are not applicable unless the actual coil size and shape are specified, which renders them unsuitable for optimization purposes with respect to displacement and angular tolerance of the system.

Any theoretical investigation of the mutual inductance in arbitrary coil configurations is extremely complex due to the lack of symmetry and the tedious work required to solve the double integral in Neumann's formula. The only semi-analytical solution for the mutual inductance for flat loop coils in lateral and angular misalignment is introduced by Soma et al., [44]. In the case of two coaxial loops the computation of the mutual inductance has been treated in detail by numerous textbooks and is given by:

$$M_i = \mu_o \sqrt{ab} \left[\left(\frac{2}{k} - k \right) K(k) - \frac{2}{k} E(k) \right] \tag{2.61}$$

where $K(k)$ and $E(k)$ are the complete elliptic integrals of the first and second kind respectively as shown in Appendix B, and k is the modulus of $K(k)$ and $E(k)$.

Based on the mutual inductance for the ideal coaxial scenario in (2.61), Soma derived upper and lower bounds for the mutual inductance in lateral and angular misalignment and an arithmetic average of these bounds. In the lateral misalignment configuration the lower and upper bounds of the mutual inductance are derived by the following expressions [44]:

$$M_L(min) = \frac{\mu_o ab}{\sqrt{a(b+\Delta)}} G(r_{min}) \tag{2.62}$$

$$M_L(max) = \frac{\mu_o ab}{\sqrt{a(b-\Delta)}} G(r_{max}) \tag{2.63}$$

where

$$r_{min} \equiv \left(\frac{4a(b-\Delta)}{(a+b-\Delta)^2 + d^2} \right)^{1/2} \tag{2.64}$$

$$r_{max} \equiv \left(\frac{4a(b+\Delta)}{(a+b+\Delta)^2 + d^2} \right)^{1/2} \tag{2.65}$$

and $G(r)$ is the bracketed expression in (2.61), denoted as:

$$G(r) \equiv \left(\frac{2}{k} - k \right) K(k) - \frac{2}{k} E(k) \tag{2.66}$$

A closer approximation of the mutual inductance can be evaluated by substituting for the maximum value of $G(r_{max})$ in the lower bound of the mutual inductance as given by (2.62), which

yields:

$$M_{L1} = \frac{\mu_o ab}{\sqrt{a(b+\Delta)}} G(r_{max}) \tag{2.67}$$

In addition an arithmetic mean of the upper and lower bounds is also derived in [44]:

$$M_{L2} = \frac{M_L(min) + M_L(max)}{2} \tag{2.68}$$

In the same manner approximate formulas for the mutual inductance under angular misalignment, expressed by a tilt angle α, are presented as follows:

$$M_{A1} = \frac{\mu_o \sqrt{ab}}{\sqrt{\cos\alpha}} G(\bar{r}) \tag{2.69}$$

$$M_{A2} = \frac{M_i}{\sqrt{\cos\alpha}} \tag{2.70}$$

where:

$$\bar{r} \equiv \frac{r_{max} + r_{min}}{2} \tag{2.71}$$

$$r_{max} = \left(\frac{4ab\cos\alpha}{a^2 + b^2 + d^2 - 2bd\sin\alpha + 2ab\cos\alpha} \right) \tag{2.72}$$

$$r_{min} = \left(\frac{4ab\cos\alpha}{a^2 + b^2 + d^2 + 2bd\sin\alpha + 2ab\cos\alpha} \right) \tag{2.73}$$

Expressions (2.67), (2.68), (2.69) and (2.70) were implemented in MATLAB and plotted for two equal coils with their centers displaced by a distance Δ that does not exceed the radius of the RX coil b and an angular misalignment that does not exceeds 25° respectively. Expressions (2.67), (2.68), (2.69) and (2.70) are illustrated in Fig. 2.36(a) and Fig. 2.36(b) which were produced to test the accuracy of the MATLAB implementation of Soma's model and are identical to Fig.3 and Fig.5 in Soma's paper, [44]. It is suggested in [44] that expression (2.67) evaluating the influence of lateral misalignment tends to underestimate the value of the mutual inductance, whereas (2.68) is computationally efficient and accurate within 10%. Again, according to Soma in the angular misalignment case expression (2.69) tends to underestimate the value of the mutual inductance with an error in the order of 20% compared to the numerical integration results. On the contrary the approximation estimating the mutual inductance given in (2.70) is believed to be correct within 3% of the numerical integration values showing a significantly improved performance with respect to Grover's data even at large misalignment angles.

Consequently, as mentioned above it is critical to note that the analysis presented by Soma in [44] has some limitations as it is based on simplifying the solution of Newman's formula by

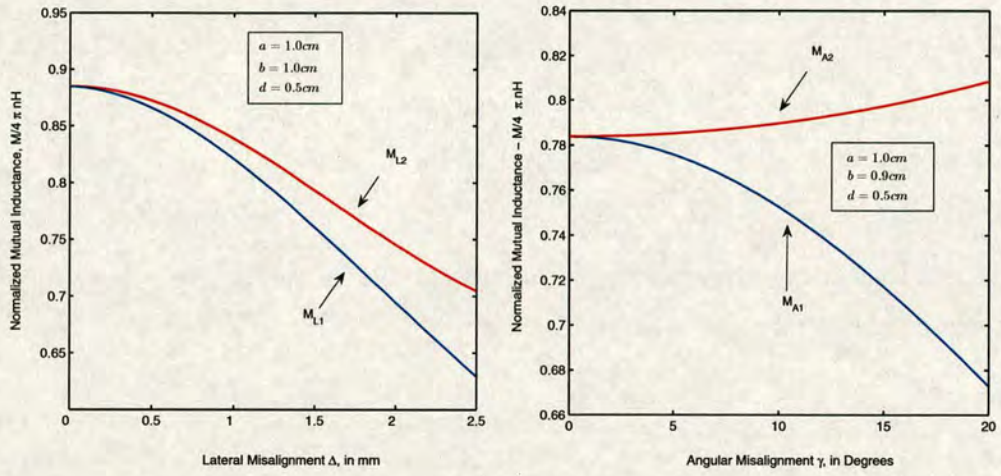

(a) (b)

Figure 2.24: *Mutual Inductance normalized by 4π nH : (a) in lateral misalignment configuration, (b) in angular misalignment configuration.*

evaluating the upper and lower bounds of the double integral. Although the upper and lower bounds for the lateral displacement as expressed by (2.62) and (2.63) can be rather conservative since the integrand in Neuman's formula is not treated as a whole, Soma's method shows good agreement with Grover's data. By utilizing this procedure, formulae for the upper and lower bounds of the mutual inductance in lateral and angular misalignment are given without the need of resorting to numerical integration. However, this method provides only a semi-analytical solution meaning that the expressions evaluating the bounds for the mutual inductance can be valid only for a certain range of misalignment values. In addition, this method overlooks the geometrical parameters of practical coils such as number of turns and shape.

Contrary to these limitations Soma's method has some significant advantages such as it provides simple analytical, computationally efficient and accurate expressions for the mutual inductance under misalignment. Based on the above theoretical considerations this method can be used to investigate the misalignment sensitivity and optimize the design of RF links by utilizing the closed-form derivatives of expressions given in (2.67), (2.68), (2.69) and (2.70).

Soma's cohesive analytical derivation of the mutual inductance for coils under lateral and angular misalignment is utilized here in order to compute the mutual inductance of misaligned coils. Fig. 2.25 and Fig. 2.26 depict the variation of the mutual inductance of two coils in the lateral and angular orientations using the analytic forms of the mutual inductance introduced previ-

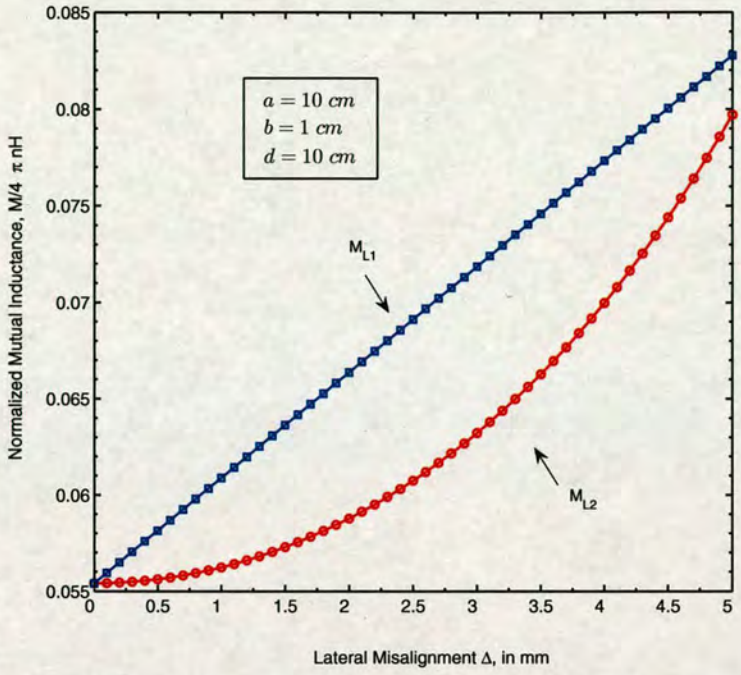

Figure 2.25: *Mutual Inductance versus lateral displacement of the coil centers for TX and RX coils with radii of* 10 *cm and* 1 *cm respectively.*

ously. In the design of transdermal RF magnetic coupling of power for an implant there are a number of different factors that need to be deliberated. Among the most crucial parameters in the design of an RF link is the size and shape of the coils, the location of the implant and the displacement tolerance of the system. Each application has its own unique requirements that influence the priority of these factors. Specifically, in the biomedical scheme the implantable unit should be minimized in order to eliminate patient discomfort and physiological problems. This is in fact reflected in 2.25 and Fig. 2.26 where a realistic value, in the order of 10 ($a/b = 10$), was adopted for the ratio between the TX and the RX coil radii.

In spite of the fact that Fig. 2.25 and Fig. 2.26, represent the mutual inductance between single turn coils based on Soma's method, it is evident that the value of the mutual inductance is very low for realistic coil dimensions and separation distance. Hence, referring to these plots the assumption of weakly coupled coils becomes apparent in the misaligned case. In addition, a MATLAB implementation of (2.68) and (2.70) yields surface plots showing the variation of the mutual inductance with respect to the RX coil size and the separation distance between the coils in both the lateral and angular arrangement, as illustrated in Fig. 2.27, Fig. 2.28, Fig. 2.29, Fig. 2.30.

Referring to Fig. 2.26, Fig. 2.29 and Fig. 2.30 an unexpected increasing trend of the mutual

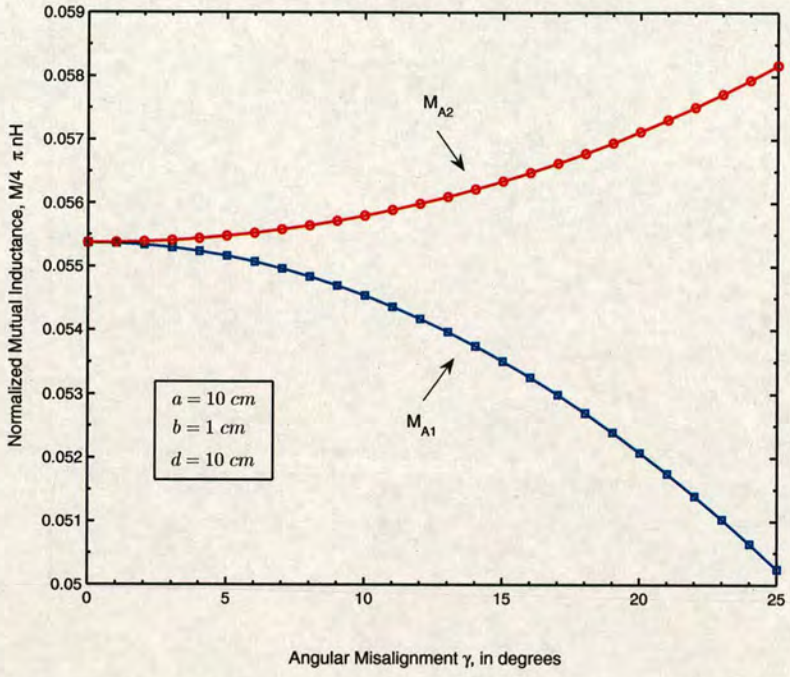

Figure 2.26: *Mutual Inductance versus angular misalignment for TX and RX coils with radii of* 10 *cm and* 1 *cm respectively.*

inductance with the misalignment angle is shown. This behavior might seem surprising at first but it can be easily interpreted as pointed out by Hochmair in [45]:

> *the tilting of the receiver coil brings half of the coil closer to the perimeter of the transmitting coil, and since the magnetic field is maximized at the coil perimeter, we expect increasing coupling, which overcompensates some losses due to the larger distance between the transmitting coil and the other half of the receiving coil.*

Based on this principle, Soma suggests that this behavior is the principal reason behind the error in Grover's data and in the approximation in (2.69).

The results presented in this section support the hypothesis of a weakly coupled system followed in the study presented in this thesis. Accordingly, for the weakly coupled case the mutual inductance is not critical and can be overlooked as a simplification in the analysis of the power transfer under coil misalignment conditions being discussed in detail in the following chapter. Nevertheless, mutual inductance is a key factor in closely coupled systems and for telemetry and communication purposes especially when LSK[2] is employed using the reflected impedance technique of an inductive coupled transformer [86], [87].

[2]Load Shift Keying

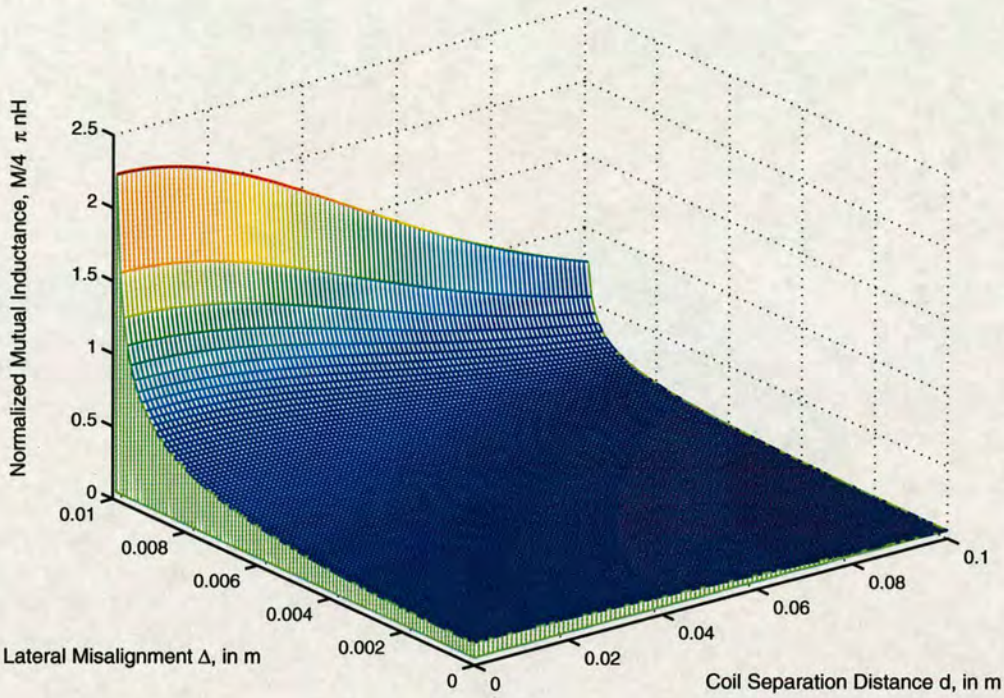

Figure 2.27: *Variation of mutual inductance with respect to lateral misalignment and the vertical distance between the coils for a TX coil radius of* 10 cm *and an implanted RX coil of* 1 cm *in radius.*

2.9.2 Internal Impedance

The input impedance of an antenna is defined as the impedance measured at its input port and can be expressed as $Z_a = R_a + jX_a$. The real part R_a is composed of the radiation resistance and the R_{Loss}. As mentioned earlier the electrically small antenna coil studied in this work can be represented by the equivalent circuit of Fig. 2.14(b), using lumped components and the radiation resistance is negligible.

By definition the internal impedance of a round wire conductor consists of the resistance and the contribution to the reactance introduced by the magnetic flux inside the wire and is a function of frequency. As discussed in sections (2.8.1.1), (2.8.1.2) the loop antenna can be matched to a signal generator and a receiving load reasonably well only over a certain bandwidth. Since the radiating resistance is very low for the frequencies of interest in this work, the transmitted power can be defined as the power dissipated in the resistive losses of the TX coil. In addition, the maximum power received by the RX coil is considered to be the power delivered to the resistive load assuming conjugate matching conditions are met. Maximum power transfer occurs

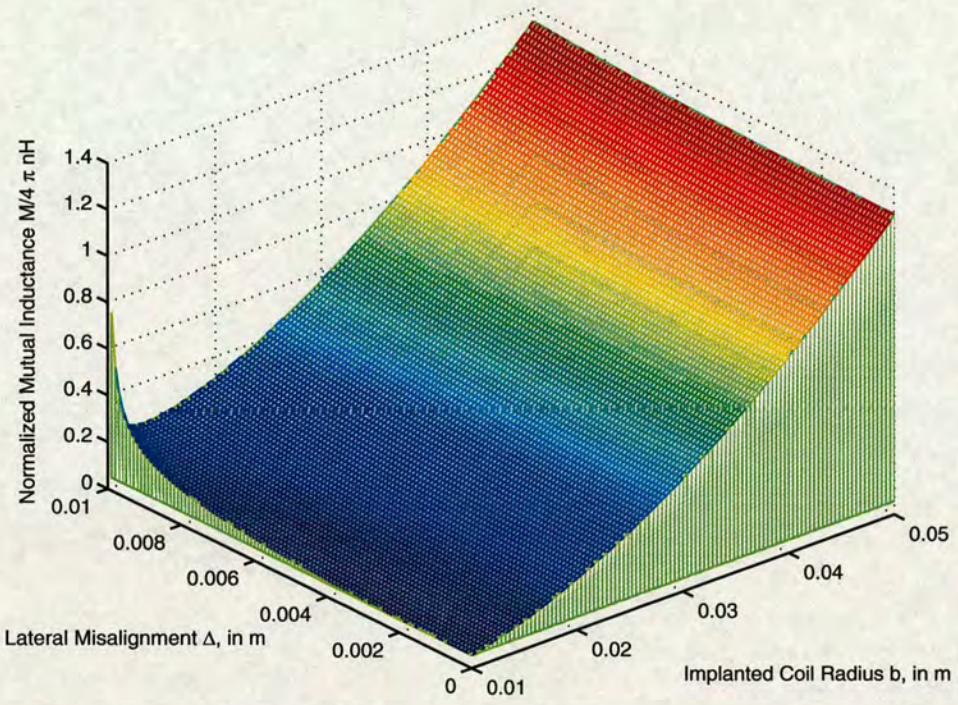

Figure 2.28: *Variation of mutual inductance with respect to lateral misalignment and implanted RX coil radius for a TX coil of* 10 *cm in radius.*

once the resistive component of the antenna coil is equal to the resistance of the load and the reactances canceled out. Based on these facts the ratio of the received power to the transmitted power can be expressed as follows:

$$\frac{P_{RX}}{P_{TX}} = \frac{power\ delivered\ to\ the\ resistive\ component\ of\ the\ load}{power\ dissipated\ in\ the\ ohmic\ losses\ of\ the\ coil} \tag{2.74}$$

Consequently, the importance of the internal impedance is prominent as it serves the dual purpose of defining the power transfer and the controlling the matching so that maximum power is transferred. Therefore, in order to assess the attenuation in the power transfer ratio (2.74) due to the losses in the TX and RX coils denoted as R_{TX} and R_{RX}, these parameters must be defined. These losses in the coil are directly linked with the internal impedance of the conductor in the coil and are represented by the real part of the internal impedance of the conductor [80], [88].

As mentioned before, since the radiation resistance is negligible, for the antenna structure and the frequencies of interest here, the total loss in the process is denoted R_{TX} and R_{RX} is the remaining ohmic loss in the actual coils. The internal impedance of an electrically small single-turn loop can be approximated with that of a straight conductor with length equal to the circum-

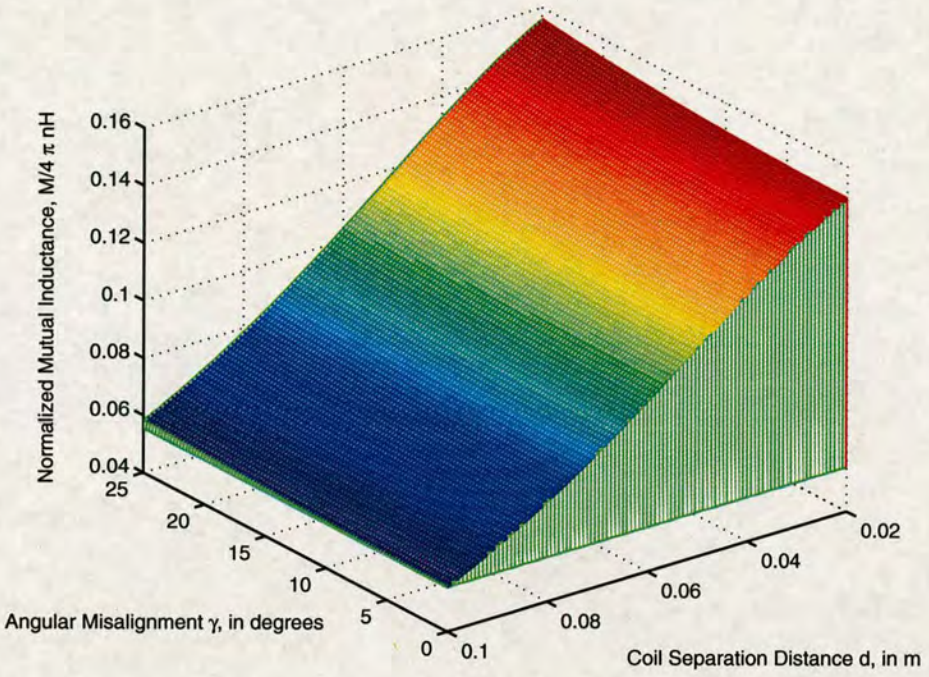

Figure 2.29: *Variation of mutual inductance with respect to angular misalignment and the vertical distance between the coils for a TX coil radius of* 10 *cm and an implanted RX coil of* 1 *cm in radius.*

ference of the loop. However, the internal impedance of a multi-turn loop is more complex in nature and this principle cannot be applied. The current redistribution in a conductor of a multiturn coil as a result of the surface current flow in an adjacent conductor, is known as the proximity effect. The proximity effect contributes to the overall ohmic losses in the coil. At radio frequencies, the penetration of currents and magnetic field distribution in the conductor are governed by the skin and proximity effects and can no longer be considered as uniform. As a result, the skin and proximity effects contribute to the resistive term of the internal impedance of the conductor and both these effects should be considered in electrically small coils. A schematic representation of the skin and proximity effects is depicted in Fig. 2.31.

2.9.2.1 Skin effect

High frequency alternating currents and magnetic flux have the tendency to penetrate into the surface of the conductor only up to a limited depth. In other words the current distribution in a wire carrying AC current concentrates toward the surface of the conductor. This phenomenon is known as the *skin effect*. A very informative paper on the skin effect has been written by

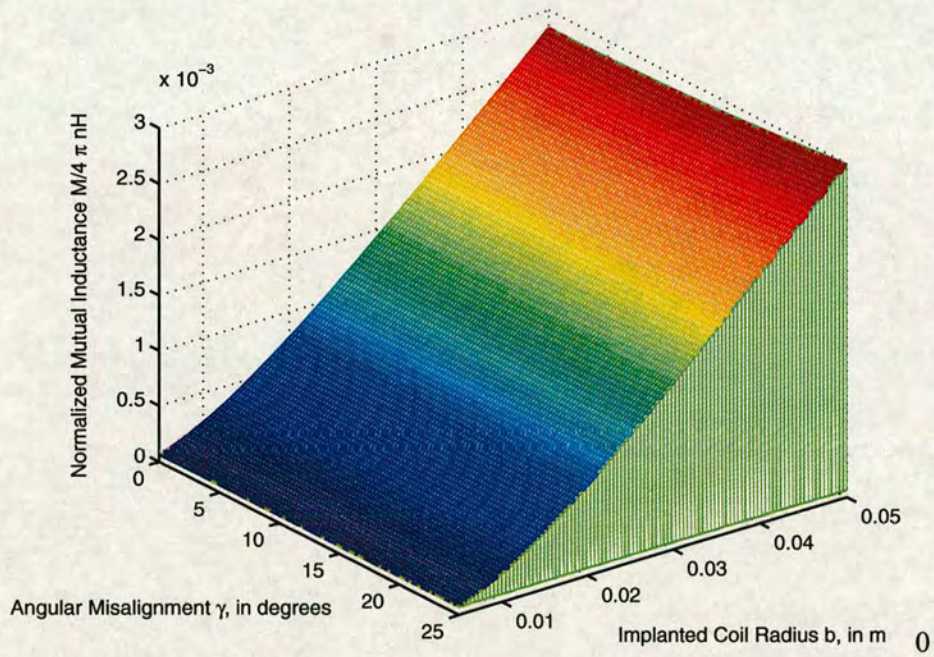

Figure 2.30: *Variation of mutual inductance with respect to angular misalignment and implanted (RX) coil radius for a TX coil of* 10 *cm in radius.*

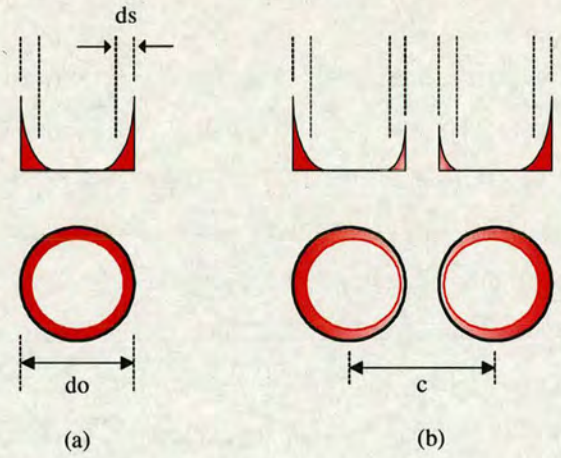

Figure 2.31: *(a) Skin effect in a single conductor. (b) Combination of skin effect and proximity effect in a system of two conductors. The colored area represents the distribution of current on the surface of the wire.*

Wheeler [89], giving simple formulas for the resistance of wires, transmission lines and coils.

The *depth of penetration* of the magnetic field in the wire, alternatively referred to as *skin depth* depends upon the frequency and also on its conductivity, and permeability. The behavior of a circular conductor carrying high-frequency currents can be described as a surface phenomenon

rather than a volume one for a wire with a radius much greater than the skin depth. Thus, the quantity of surface resistance can be defined as the resistance of a conducting surface of equal length and width and is defined as follows:

$$R_s = \frac{1}{\sigma\delta} = \sqrt{\frac{\omega\mu}{2\sigma}} \tag{2.75}$$

where δ is the skin depth, which is given by:

$$\delta = \sqrt{\frac{2}{\omega\mu\sigma}} \tag{2.76}$$

As discussed earlier, the internal impedance of a round wire is defined as the resistance and its contribution to reactance arising from the magnetic flux inside the wire which can be obtained from the total current in the wire and the electric intensity at the surface of the conductor. The total current may be obtained from an integration of current density or from the magnetic field at the surface as follows:

$$I = \oint \mathbf{H} \cdot \mathbf{dl} \tag{2.77}$$

and the magnetic field is derived from the electric field using Maxwell's equations:

$$\nabla \times \mathbf{E} = j\omega\mu\mathbf{H} \tag{2.78}$$

Since for the round wire there are no variations in z or ϕ, only the fields E_z and H_ϕ are present. According to Ramo et al. in [53] and Wheeler in [90] the impedance of the round wire can be derived as the ratio:

$$Z_i = \frac{E_z}{I} \tag{2.79}$$

It follows that the internal impedance per unit length due to the skin effect can be calculated for a round wire using the following equation as presented in [53]:

$$Z_i = R + j\omega L_i = \frac{jR_s}{\sqrt{2}\pi r_o}\left[\frac{Ber(q) + jBei(q)}{Ber'(q) + jBei'(q)}\right] \quad \Omega/m \tag{2.80}$$

where

$$q = \frac{\sqrt{2}r_o}{\delta}$$

Alternatively, the real and complex parts of the internal impedance can be expressed in terms of the ratio of wire radius to depth of penetration as follows, [53]:

$$R = \frac{R_s}{\sqrt{2}\pi r_o}\left[\frac{Ber(q)\,Bei'(q) - Bei(q)\,Ber'(q)}{Ber'(q)^2 + Bei'(q)^2}\right] \quad \Omega/m \tag{2.81}$$

$$\omega L_i = \frac{R_s}{\sqrt{2}\pi r_o}\left[\frac{Ber(q)\,Ber'(q) - Bei(q)\,Bei'(q)}{Ber'(q)^2 + Bei'(q)^2}\right] \quad \Omega/m \tag{2.82}$$

A definition of the Bessel functions with complex argument and their derivatives are given below, see appendix B:

$$\begin{aligned} J_o(j^{-1/2}q) &= Ber(q) + jBei(q) \\ Ber(q) &= \text{real part of } J_o(j^{-1/2}q) \\ Bei(q) &= \text{imaginary part of } J_o(j^{-1/2}q) \end{aligned}$$

and

$$Ber'(q) + jBei'(q) = \frac{d}{dv}(Ber(q) + jBei(q)) = j^{-1/2}J_o'(j^{-1/2}q)$$

where the derivatives $Ber'(q)$ and $Bei'(q)$ are defined in appendix B.

The expression of the internal impedance in (2.80) can be simplified to low and high frequency approximations, as presented in [53]. The low frequency expression of (2.80) is given by:

$$(Z_i)_{lf} \approx \frac{1}{\pi r_o^2 \sigma}\left[1 + \frac{1}{48}\left(\frac{r_o}{\delta}\right)^2\right] + j\frac{\omega\mu}{8\pi} \quad \Omega/m \tag{2.83}$$

and the high-frequency expression is given by:

$$(Z_i)_{hf} = \frac{(1+j)R_s}{2\pi r_o} \quad \Omega/m \tag{2.84}$$

2.9.2.2 The proximity effect

In this section the proximity effect is discussed since it has a significant impact on the ohmic losses in the coil and it is a much more difficult phenomenon to quantify than the skin effect. Although the proximity effect causes an increase in the coil's resistance higher than the skin effect it has received much less attention. Most of the theoretical and experimental work on proximity effect is concerned with systems of two conductors carrying currents of equal magnitudes in opposite directions. The only investigation of the proximity effect with more than two conductors appears to be that done by Butterworth in conjunction with the definition of the Q in an inductance coil [91, 92]. So far this work is considered to be the standard theoretical approach to the problem although the experimental study of Medhurst suggests that at radio frequencies Butteworth's calculations are not valid for a large range of coil parameters, [93, 94]. An error up to 190% was observed for certain coil dimensions. A summary of Butterworth's results is given by Terman [43], where copper losses in single-layer coils are as follows:

$$\frac{AC \text{ resistance}}{DC \text{ resistance}} = H + u(\frac{d_o}{c})^2 G \tag{2.85}$$

where:

- H = resistance due to skin effect
- G = proximity effect factor
- u = constant
- d_o = wire diameter in cm
- c = spacing between centers of adjacent conductors

The values of H and G are tabulated in Terman for values of x which appear as [43] :

$$x = \pi d_o \sqrt{\frac{2f}{\rho}} \tag{2.86}$$

where ρ is the resistivity and f is the frequency in Hz. The constant u also appears in Terman for even number of turns up to 32. Butterworth's formula given in (2.85) allows evaluation of the AC resistance for a large range of parameters. However, there are some limitations for (2.85) such that it is valid for short single-layer coils of a few spaced turns with a ratio $d_o/c \leq 0.6$. In addition, some degree of interpolation is required in order to extract parameters such as H, G and u from the tables given in Terman. However, since the functions $H(x)$, $G(x)$ and $u(N)$ are monotonic, linear interpolation would thus be a simple and adequate solution.

At high frequencies a theoretical analysis has been undertaken by G. S. Smith in [95], to determine the magnitude of the proximity effect. A condition imposed on the theoretical analysis carried out by Smith is that the skin depth is a small quantity compared to the cross-sectional dimension and most of the current is confined to a thin layer in the surface. With more than one conductor present which is the case for a multi-turn coil, the current distribution and external fields for each conductor are no longer rotationally symmetric. In Smith's analysis the current distributions on the surface of the perfect conductors are assumed sufficiently smooth to be represented by a finite number q of cosine Fourier series terms. It follows that in the m^{th} conductor of a multi-turn coil the current can be expressed as:

$$K(\theta) = \frac{I_m}{2\pi a}\left(1 + \sum_{p=1}^{q} a_{mp}\cos(p\theta)\right) \tag{2.87}$$

When all conductors carry the same total current at each cross section, the ohmic resistance per unit length for n parallel wires is expressed as follows:

$$R = \frac{R_s}{2\pi a} \sum_{m=1}^{n} \left(1 + \frac{1}{2} \sum_{p=1}^{q} |a_{mp}|^2 \right) \quad \Omega/m \tag{2.88}$$

where $R_s = \sqrt{\frac{\omega \mu_o}{2\sigma}}$, is the surface impedance of the conductor and a_{mp} are the cosine Fourier coefficients of the current distribution.

Smith computed the normalized additional Ohmic resistance per unit length due to the proximity effect as:

$$\frac{R_p}{R_o} = \frac{R - nR_R}{nR_R} = \frac{1}{2} \sum_{m=1}^{n} \sum_{p=1}^{q} |a_{mp}|^2 \quad \Omega/m \tag{2.89}$$

where:

- $R_R = \frac{1}{2\pi a} \left(\frac{\omega \mu_o}{2\sigma} \right)^{1/2} \Omega/m$, is the high frequency resistance per unit length of a circular conductor
- R_p is the ohmic resistance per unit length due to proximity effect
- $R_o = \frac{N R_s}{2\pi b}$, is the ohmic skin effect resistance per unit length

The ratio R_p/R_o has been numerically evaluated as a function of the spacing c/a and tabulated for up to 8 parallel conductors for $0.91 \leq d_o/c \leq 0.95$. A MATLAB implementation of Smith's analysis yields the plot in Fig. 2.32 which illustrates the importance of taking into account the proximity effect in multi-turn coils and is identical to the figure introduced in [95]. It is evident from Fig. 2.32 that for close spacing the ohmic resistance is twice as large as that in the absence of the proximity effect (R_p/R_o).

Table 2.2 demonstrates the minimum frequency for various wire radii for which Smith's analysis is applicable, by choosing arbitrarily a factor of 10 for the ratio d_s/a, where d_s is the skin depth and a the radius of the conductor.

Conductor Radius/mm	0.1	0.5	1	10
Frequency/Hz	44M	2M	440k	4.4k

Table 2.2: *Minimum Frequency for Smith's proximity effect analysis to be valid for a number of conductor radii.*

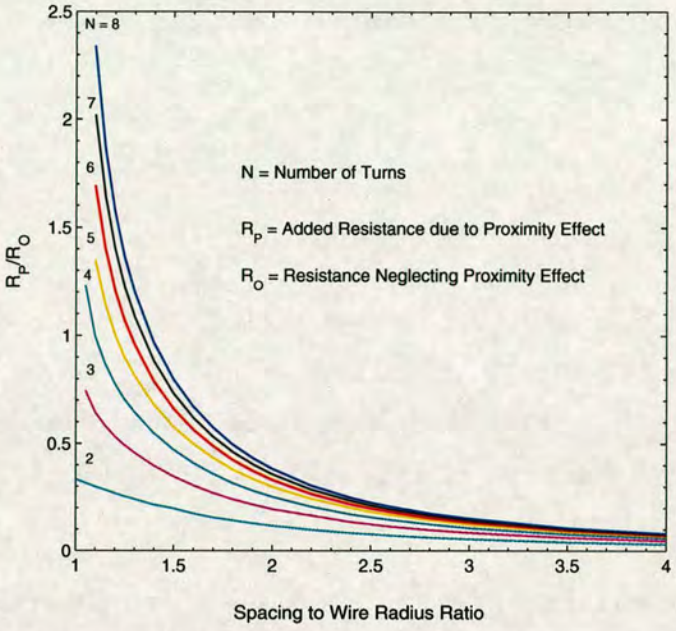

Figure 2.32: *Additional Ohmic resistance per unit length of a system of parallel wires due to the proximity effect.*

Using Smith's work the total ohmic resistance for an n-turn circular loop antenna with wire radius a, loop radius b and loop separation $2c$ is given by [95]:

$$R_{ohmic} = \frac{Na}{b} R_s \left(\frac{R_p}{R_o} + 1 \right) \tag{2.90}$$

The results in Smith's analysis show close agreement with experimental values and they are more accurate than Butterworth's method for a wider range of c/a. However, this analysis is limited to high frequencies and results are valid for conductors with parameters which satisfy the following inequalities as discussed in Terman [43]:

$$\frac{a}{d_s} >> 1, \quad \frac{9(d_s/a)^2}{1 - 9(d_s/a)} << 1 \tag{2.91}$$

These conditions are meet by most wire sizes used in practical antennas, see Table 2.2, operating at frequencies above 1 MHz. Smith's method is accurate for coils up to 8 turns. This is primarily due to the fact that any computation of the current distribution in systems with more conductors becomes too complex as it requires more than six harmonic terms for $K(\theta)$. The plots depicted in Fig. 2.32 are all obtained using less than six harmonic terms (a_{mp}).

For the range of frequencies that this thesis is focused on, 3-30MHz, Smith's analysis can be adopted. However, short range wireless communication systems often use lower frequencies, where Smith's method is not applicable. In such cases Butterworth's approach is a viable alternative in quantifying the proximity effect. Finally, it is important to mention that a limitation

common to both methods evaluating the proximity effect is that they only apply to electrically small antenna coils.

2.10 Power Attenuation in Implanted Devices

In embedded sensors such as biomedical implants and RFID devices, the power transmitted by the external TX coil is inevitably attenuated by the presence of tissue. Any model describing wireless power transfer for these applications would be incomplete without quantifying this effect. In this section these losses are being revisited so that the overall model of near-field power transfer can be extended to account for their effects where needed.

Most inductive telemetry systems operate in air which is a nearly perfect insulating medium. Because of this there is negligible loss due to conduction in the medium. Apart from ohmic losses in the transmitter and receiver coils, attenuation in such systems is due to imperfect coupling between the coils as a result of their relative position and geometry. In power transfer systems for implanted devices the situation is more complicated as the propagation medium is no longer an insulator and is in fact of quite high conductivity. For the case of the human body the conductivity of the tissue and organs may vary between $\sigma = 0.04\ S/m$ for low water content tissue such as fat to $\sigma = 3.30\ S/m$ for higher water content media as stated in [96], [97], [98]. This leads to additional propagation loss due to dissipation of energy in the medium as conduction currents are set up in the medium. The question that arises is how to allow for these losses when modelling the transmission of energy between coupled coils.

Previously some similar research is reported by Bottomley et al. and Ko et al. [99], [100], who studied analytically the RF magnetic field penetration , phase shift and power dissipation in biological tissue and the radiation characteristics from an electrically small circular wire loop in dissipative media. More recently Zborowski et al. revisited the problem by an experimental study of the attenuation of RF pulsed electromagnetic fields in Blood and cortical bone in [101]. Due to the complexity of the problem the work presented in [99], [100] and [101] fails to derive an overall solution. However, most of the existing research on this topic shares a common perspective by approaching the problem as an electromagnetic wave propagating in an imperfect conductor. Taking a step backwards from the biomedical related literature, researchers investigating under water communications in the late 1950s were faced with a problem of a similar nature. Detailed analysis of the effects of surrounding conductive

media on small submerged antennas is reported by Moore et al. [69], King et al. [66], Hansen et al. [68] et al., Fenwick et al. [67] and Dunbar et al. [102], more recently. Additional studies were carried out for antennas immersed in infinite homogeneous and isotropic media. Clearly the situation is a lot different for an implanted antenna in biological tissue where the conductivity varies dramatically between layers of fat and other tissues. A simplified schematic diagram of an implanted sensor depicts this in Fig. 2.33. As a result, a general mathematical treatment of the RF field attenuation can be extremely complicated as the geometry of the human body is irregular, and electromagnetic properties of tissues are heterogeneous. However, a small area of tissue surrounding the antenna is considered for the analysis presented in this thesis. Therefore, the human tissue in which the receiving antenna is located, can be safely considered to be a homogeneous medium with no sharp edges and rough surfaces assuming uniform electric and magnetic properties. This approximation permits the use of the results reported in previous studies, [69], [66], [67], [102]. A similar approach is followed here in order to quantify the effect of the conductive tissue medium on the power transfer.

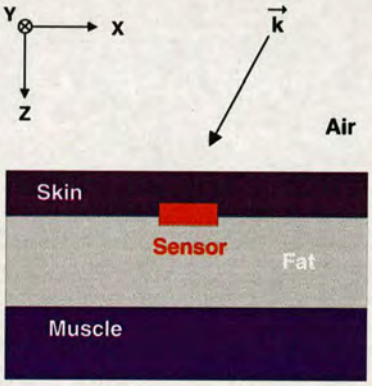

Figure 2.33: *Generic body model as layered tissue depicting and incident plane wave on the skin and the position of the implanted sensor.*

In particular, in the approach followed in this work one transmitting and one receiving antenna are considered, separated by a distance d. An electrically small n-turn loop antenna such as the one discussed in previous sections, is considered in a lossy medium of conductivity σ (S/m), permettivity ϵ (F/m) and permeability $\mu(H/m)$. It follows that at a radial distance r from the transmitting antenna carrying a current $I = I_o e^{j\omega t}$ two components of magnetic field H_θ and H_r exist. As discussed earlier in this chapter there is no variation with respect to θ. The magnetic field components H_θ and H_r in free-space are given as follows, [102]:

$$H_{\theta\,(AIR)} = \frac{m_o \sin\theta\, e^{(j\omega t-\beta r)}}{4\pi}\left[-\frac{\beta_o^2}{r}+j\frac{\beta_o}{r^2}+\frac{1}{r^3}\right] \tag{2.92}$$

$$H_{r\,(AIR)} = \frac{m_o \cos\theta\, e^{(j\omega t-\beta r)}}{2\pi}\left[j\frac{\beta_o}{r^2}+\frac{1}{r^3}\right] \tag{2.93}$$

For the applications envisaged, where inductive coupling is employed, the range of operation is situated well within the near-field. Hence,only the inductive term $1/r^3$ needs to be considered in the magnetic field expressions. In this situation, when the magnetic field is propagating through the conductive tissue the propagation constant γ is complex being a function of both the conductivity and the permittivity of the region. In this case the following conditions apply:

$$\gamma = \alpha + j\beta = j\omega\sqrt{\mu\epsilon\left(1-\frac{j\sigma}{\omega\epsilon}\right)} \tag{2.94}$$

where α is the attenuation constant and β is the phase constant expressed as:

$$\alpha = \omega\sqrt{\frac{\mu\epsilon}{2}\left(\sqrt{1+\left(\frac{\sigma}{\omega\epsilon}\right)^2}-1\right)} \tag{2.95a}$$

$$\beta = \omega\sqrt{\frac{\mu\epsilon}{2}\left(\sqrt{1+\left(\frac{\sigma}{\omega\epsilon}\right)^2}+1\right)} \tag{2.95b}$$

In this situation the exponent of the magnetic field components in (2.92), (2.93) should be modified to account for power transmission through biological tissues, from $j(\omega t-\beta_o r)$ to $(j\omega t-\gamma t)$. In order to simplify the analysis the time variation term ($e^{j\omega t}$) can be omitted. It follows that for near-field conditions expressions (2.92) and (2.93) can now be reduced to:

$$H_{\theta\,(TISSUE)} = \frac{m_o \sin\theta\, e^{-(\alpha+j\beta)r}}{4\pi r^3} \tag{2.96}$$

$$H_{r\,(TISSUE)} = \frac{m_o \cos\theta\, e^{-(\alpha+j\beta)r}}{2\pi r^3} \tag{2.97}$$

Inspection of expressions (2.92), (2.93), (2.96) and (2.97) shows that the only difference between them is the $e^{-\alpha r}$ term which accounts for the loss due to conduction in the medium. In the quasi-static scenario, which is the case for short-range near-field applications, skin effects arising from the resonant RF magnetic field in the biological specimen are primarily due to conduction currents and any associated displacement currents can by neglected. The situation discussed here deals with two coaxial coils where the main variable is the coil separation distance. There is no reason to assume that this only applies to this particular situation and it is

felt that it should still be the case when the coils are off-axis and tilted with respect to each other. This assumption holds true for a small implantation depth compared to the coil separation distance, which is usually the case in biomedical implants, and will be discussed further in section 3.8. Therefore, it is proposed that a useful way of calculating the conduction losses is to multiply the more general expressions that have been derived for coils positioned off-axis and tilted with respect to each other, by the term $(e^{-\alpha r})$, as introduced in the next chapter.

The ratio of the wavelength in a conductive medium, denoted λ_m, to the wavelength in air is a useful quantity given by:

$$\frac{\lambda_m}{\lambda_o} = \frac{\beta_o}{\beta_m} \tag{2.98}$$

Substituting for the phase constants β_o and β_m, in (2.98) and solving for λ_m, it yields that the wavelength in a medium is:

$$\lambda_m \approx \frac{\lambda_o}{\left[\epsilon_r^2 + \left(\frac{\sigma}{\omega\epsilon_o}\right)^2\right]^{1/4}} \tag{2.99}$$

Fig. 2.34 depicts the variation of the wavelength versus frequency in conductive tissue. It is evident that there is consequent phase variation in the magnetic field. However, for power transfer applications only the amplitude variation is of interest. Thus, the focus of this study can now shift to the attenuation constant which models the loss in the biological tissue and can be calculated from the knowledge of the properties of tissue using (2.95a). In order to express the coupling between coils, in a lossy medium, a valid method is to multiply the expressions for the same coils in air by a factor $(e^{-\alpha r})$. This will account for the additional loss due to the conduction currents in the medium. The reciprocal of the attenuation constant is defined as the skin or penetration depth at which the amplitude of magnetic field decreases by a factor of e^{-1}. Using the property of the skin depth the effect of the tissue material on the magnetic field can be visualised. Hence, for powering purposes it is safe to assume that an implantation depth which does not exceed more than half the penetration depth is adequate in order for the implanted sensor antenna to pick up enough energy from the external transmitter.

The skin depth in an arbitrary material varies with frequency and is given by:

$$\delta = \left(\frac{\sqrt{2}}{\omega\sqrt{\mu\epsilon}}\right)\left[\sqrt{1+\left(\frac{\sigma}{\omega\epsilon}\right)^2} - 1\right]^{-1/2} \tag{2.100}$$

for highly conductive materials such as some biological tissue where σ dominates or at low frequencies the following inequality applies:

$$\frac{\sigma}{\omega\epsilon_o\epsilon_r} >> 1 \tag{2.101}$$

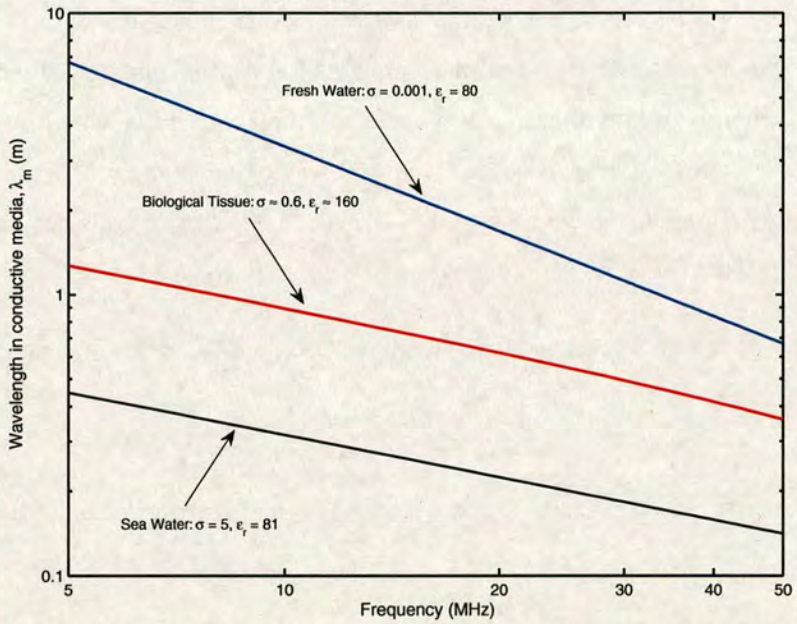

Figure 2.34: *Variation of wavelength with respect to frequency in conductive media.*

so that the expression for the skin depth can be approximated as:

$$\delta = \frac{1}{\sqrt{\pi\sigma\mu f}} \tag{2.102}$$

The difference in the skin depth expressions as given in equations (2.100) and (2.102) is better illustrated in Fig. 2.35.

In order to understand some of the characteristics of radio-frequency propagation within biological material, the dielectic behavior of biological tissues is tabulated in Tables 2.3 and 2.4. The results presented in Tables 2.3 and 2.4 are evaluated based on the data provided by Gabriel et al. and Johnson et al. [96], [103]. The first column lists selected frequencies between 1 MHz and 100 MHz. The frequencies of 6.7 MHz, 13.5 MHz, 27.12 MHz and 40.68 MHZ are specifically selected as they are allocated industrial, scientific and medical (ISM) bands. An implantation depth of $3-10cm$ common in biomedical applications, is inside the skin penetration distance at frequencies of significant interest to this work, as can be seen in column four. As a result, for the frequencies being considered in this thesis the attenuation in the magnetic field is not significant and the method presented in this chapter is adequate to describe the RF field attenuation in biological substances. Power losses increase at higher frequencies with almost all the transmitted energy dispersed in the surface of the conductive media in the form of joule heating. Consequently, the maximum frequency that can be used safely in such applications is considered to be in the range of $30-40\ MHz$ [45].

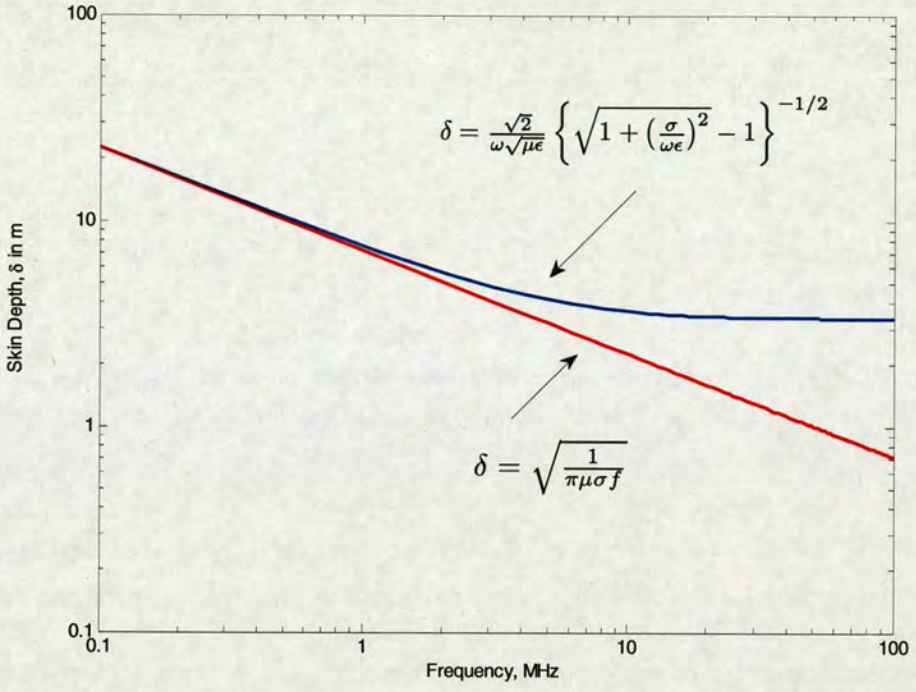

Figure 2.35: *Skin depth in an arbitrary material and approximation expression in conductive media versus frequency, assuming* $\sigma = 0.005S/m$ *and* $\epsilon_r = 10$.

Frequency (MHz)	Wavelength in Air (m)	Relative Permittivity ϵ_r (F/m)	Conductivity σ (S/m)	Wavelength (m)	Skin Depth (cm)
1	300	2000	0.4	347	89
6.7	44.78	300	0.55	115	29
10	30	160	0.625	76	23
13.5	22.22	150	0.615	54	20
27.12	11.06	113	0.612	51	14
40.68	7.38	97.3	0.693	41	11
100	3	71.7	0.889	22.67	6

Table 2.3: *Properties of Electromagnetic Waves in Biological Media for Muscle, Skin and Tissue of High Water Content, based on data provided by Gabriel et al. in [96], and Johnson et al. in [103].*

2.11 Validity of the Poor Coupling Approximation

In section 2.9.1 the mutual inductance of the TX and RX coils for characteristic coil separation distances, orientation and typical coil radii was examined. It follows that the mutual inductance and hence the coupling factor are always small for the specifications of the aimed application areas. This fact simplifies considerably the modelling of the energy coupled across the inductive link. As a result, a simple equation can be derived following the approach suggested by Yates

Frequency (MHz)	Wavelength in Air (m)	Relative Permittivity ϵ_r (F/m)	Conductivity σ (S/m)	Wavelength (m)	Skin Depth (cm)
1	300	-	-	-	-
6.7	44.78	-	-	-	-
10	30	-	-	-	-
13.5	22.22	-	-	-	-
27.12	11.06	20	10.9-43.2	2.14	159
40.68	7.38	14.6	12.6-52.8	1.87	118
100	3	7.45	19.1-75.9	1.06	60.4

Table 2.4: *Properties of Electromagnetic Waves in Biological Media for Muscle, Skin and Tissue of Low Water Content, based on data provided by Gabriel et al. in [96], and Johnson et al. in [103].*

et al. [47], which will enable us to observe the relation of the power transfer on various application parameters and most importantly the impact of misalignment on the link efficiency.

The validity of the poor coupling scenario can be tested against the results presented by Vandevoorde et al., [50] representing the closely coupled situation. According to Vandevoorde the total link efficiency for parallel, η_p, and series resonant, η_s, secondary coils can be written as:

$$\eta_p = \frac{k^2 Q_{TX} Q_{RX}}{(1 + Q_{RX}/\alpha + k^2 Q_{TX} Q_{RX})(\alpha + 1/Q_{RX})} \tag{2.103a}$$

$$\eta_s = \frac{k^2 Q_{TX} \alpha}{(1 + k^2 Q_{TX} + 1/Q_{RX})(\alpha + 1/Q_{RX})} \tag{2.103b}$$

where α is a unit-less constant defined as:

$$\alpha = \omega C_{RX} R_L \tag{2.104}$$

In both equations (2.103a) and (2.103b), Q_{TX} and Q_{RX} express the quality factor of the primary and secondary coils respectively. An analytic calculation of the coupling factor is only possible for very simple antenna configurations. For two parallel conductor loops centered on a single z-axis, as indicated in Fig. 2.8, the coupling coefficient, k, can be approximated by 2.60 according to [84].

In order to achieve maximum power transfer across the link both the primary and secondary circuits are tuned to the same resonant frequency. In addition, in low power inductive links the combination of the receiver coil and capacitor impedance should be matched to the impedance of the implanted device. Hence, expressions (2.103a) and (2.103b) can be combined to repre-

sent the maximum efficiency in both the series and parallel configurations as derived in [50]:

$$\eta_{opt} = \frac{k^2 Q_{TX} Q_{RX}}{\left(1 + \sqrt{1 + k^2 Q_{TX} Q_{RX}}\right)^2} \tag{2.105}$$

and the new optimal value for α, in parallel and series configurations respectively, is given by the following expressions:

$$\alpha_{opt} = \frac{Q_2}{\sqrt{1 + k^2 Q_{TX} Q_{RX}}} \tag{2.106a}$$

$$\alpha_{opt} = \frac{\sqrt{1 + k^2 Q_{TX} Q_{RX}}}{Q_{RX}} \tag{2.106b}$$

In poorly coupled systems the term $k^2 Q_{TX} Q_{RX}$, in the above equations, is usually much smaller than 1 even for coils with high quality factors in the order of 100. It follows that by employing $k^2 Q_{TX} Q_{RX} \ll 1$, expressions (2.105), (2.106a), (2.106b), can be extended to account for poorly coupled systems. Consequently, the maximum efficiency and the constant α in loosely coupled inductive links can be represented using the following formulae:

$$\eta_{opt} = \frac{k^2 Q_{TX} Q_{RX}}{4} \tag{2.107}$$

$$\alpha_{opt} = Q_{RX} \text{ for parallel resonance} \tag{2.108a}$$

$$\alpha_{opt} = \frac{1}{Q_{RX}} \text{ for series resonance} \tag{2.108b}$$

The validity of the poor coupling case can be tested against the modelling of closely coupled coils presented in [50]. This comparison has been performed for maximum link efficiency where expressions 2.105 and 2.107 are plotted against the receiver coil radius. The results are depicted in Fig. 2.36 for a parallel tuned receiver configuration as this is the most common topology currently employed in the applications considered. Referring back to Fig. 2.36 the full lines represent the power transfer taking into account the energy coupled back to the transmitter as calculated by (2.105) whereas the dashed lines show the power transfer as evaluated by (2.107) using the poor coupling theory. It is evident from Fig. 2.36 that the poor coupling approximation indicates a level of deviation at large coil radii in the order of 2dB. However, for a small receiver coil radii the discrepancy is minimal and considered negligible. It could be argued that for a minimum separation distance between the coils of twice the transmitter diameter, the poor coupling approximation is valid up to a receiver radius half that of the transmitter coil. Since in implanted devices the receiver coil is usually much smaller than the transmitter it can be concluded that the range of values over which this methodology is valid is first constrained by other factors in the analysis other than the poor coupling concept.

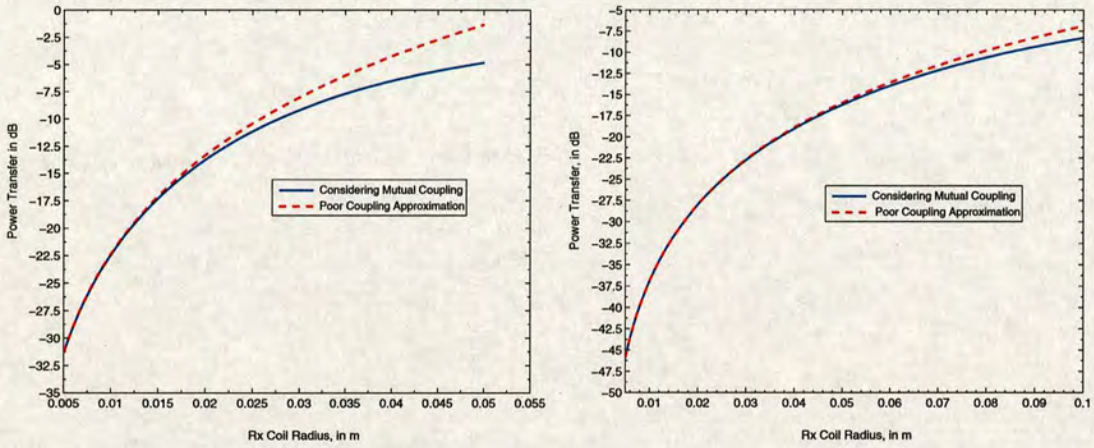

(a) TX coil radius of 5cm and coil separation distance of 20cm, $Q_{TX} = Q_{RX} = 100$

(b) TX coil radius of 10cm and coil separation distance of 0.5m, $Q_{TX} = Q_{RX} = 100$

Figure 2.36: *A comparison of the variation of power transfer with respect to RX radius as predicted for two axial loops using the efficiency models for mutual coupling and poor coupling approximations.*

2.12 Limitations of the Proposed Model

One of the main challenges in this analysis is to define the range of parameters for which this modelling is valid. In an elecromagnetic modelling scenario it is very important to understand where these limitations lie. The assumptions made in the derivation of the model were discussed and verified in this chapter. To reiterate, the boundaries on the inductive power transfer approach presented in this thesis are set by the following conditions:

- Poor Coupling: The tuned TX and RX circuits have little effect on each other and can be treated separately. This requires a RX coil to be much smaller than the TX or a separation distance sufficiently larger than the RX radius.
- Uniform Magnetic Field: A uniform magnetic flux cutting the effective area of the RX coil is necessary in order for Faraday's law to be applicable. This condition is satisfied by the poor coupling criterion.
- Electrically Small Antenna Coils: Both the TX and RX coils need to be electrically small. This suggests a uniform current distribution in the TX coil. Also, the coils can be considered as loop antennas essentially acting as magnetic dipoles. These assumptions simplify significantly the magnetic field computation at the RX coil. It follows that any

radiation losses are negligible and the ohmic resistance of the coils can be easily derived, as operation is believed to be well within the near-field region.

- Near-field Operation: The RX coil needs to be positioned well withing the near-field generated by the TX coil. Operation in the near-field of the TX antenna coil is critical to the approach being followed, as it is synonymous to inductive coupling. All the energy is stored in the near-field, circulating around the TX coil. Hence, energy is transferred to the RX by means of induction.

- Optimal Driving Conditions: Both the TX and RX coils are considered to be resonant at the same frequency. In addition, the source at the TX circuit is regarded to be ideal with zero internal resistance.

- Load Impedance Matching: The load impedance is matched to the tuned RX circuit in order to optimise the power delivered to the implanted device.

- Coil Orientations: Starting from the ideal coil orientation, as illustrated in Fig. 2.8, the model predicting the power transfer from TX to RX will be extended to account for lateral displacement and an angular tilt of the RX coil.

2.13 Chapter Summary

The scope of this chapter was to introduce the reader to the background theory of near-field inductive coupling. In addition, a detailed literature review is included. Initially, the physical principles and the merits behind a resonant TX-RX configuration, in efficient inductive power transfer, were explained. The resonant circuit configurations employed in inductive coupled systems were introduced. The concept of a loosely coupled inductive link, which is central to this project, in conjunction with the loop antenna theory and its suitability for near-field operation were discussed in detail.

Fundamental geometries like the loop and dipole antennas are critical in the modelling of more complex structures which are the focus of this work. Subsequently, the radiation characteristics and field structure of fundamental antennas like the circular loop and dipole antennas were addressed. The decision to model the inductive coupling action based on the magnetostatic scenario, is well justified in this chapter. The mutual inductance of the coils in the ideal and non-ideal orientations was derived using Soma's analysis. The results yield that for the ap-

plications that this work targets the mutual coupling is very low. Hence, the loosely coupled approximation is valid. Finally, the losses present in the power transfer process between two inductively coupled coils are identified. The limitations of existing research are addressed and the scope of this thesis clearly identified. Finally, inductive power transfer is introduced both from a circuital and electromagnetic perspective. This chapter concludes with a summary of the assumptions used in the derivation of the analytical model suggested in this thesis.

Chapter 3
Misalignment Analysis

3.1 Introduction

In a wide range of biomedical and RFID applications involving implanted devices, the energy to power the embedded system is transfered via near-field inductive coupling. This scheme of magnetic coupling is advantageous as it provides true autonomy to the implanted device. Furthermore, it reduces the risk of of infection, by avoiding surgical replacement of embedded power sources. In this type of inductive coupling, misalignment between the external transmitting and implanted receiving coils can easily occur due to anatomic requirements such as skin mobility and variations in the subcutaneous fatty tissue. As an example, in visual prostheses, the TX and RX coils are separated by a layer of skin and tissue, in the range of 1 to 4 cm, where coils are usually misaligned. This misalignment of the coils leads to a change of transmission characteristics and an inevitable reduction in the coupling efficiency of the link.

In this chapter the effects of coil orientation and position as well as geometry are studied, based on the loosely coupled model for the inductive link, discussed in section 2.4. Combining the notion of a loosely coupled transformer action with the quasi-static analytical field study of solenoid and spiral coils, results in the development of novel power transfer functions for each coil type. The model introduced in this chapter can contribute to the design of low power inductive links by predicting the effect of misalignment on the coupling performance for each coil geometry. The analytic power transfer functions derived can form a powerful system analysis tool for optimisation studies in a number of applications which employ inductive near-field power transfer.

3.2 Existing Misalignment Studies

In the analysis and design of inductive links, there is a considerable body of knowledge with several approaches possible to maximise the coupling efficiency. However, existing studies

focus primarily on steady-state circuit analyses and validation through experiment, with geometric considerations on the coupling efficiency often being overlooked. Pioneering work into the misalignment problem was carried out by Flack et al. [85], who provided computer-derived graphs for the mutual inductance of solenoid coils in lateral misalignment. In addition, Ko et al. in [40] suggested a design procedure for the coaxial orientation between solenoid coils with emphasis on the importance of the geometrical parameters of the coils. Donaldson et al. in [38] presented an analysis of resonant solenoid coupled coils for displacement tolerance of the system based on the results of Ko's study mentioned previously. Donaldson et al. considered only a lateral displacement of the RX coil where the RX coil is displaced by a relatively small distance from the center of the TX coil. The results provided by Donaldson are primarily based on experimental measurements and do not provide sufficient information about the behavior of the system under misalignment since no analytical solution is given. Almost all designs still rely on experimental work by Grover [42] and Terman [43], empirical techniques for a specific implementation or numerical evaluations. Consequently, it is difficult to perform an optimisation study based on existing methods.

The most complete study of misalignment effects to date was carried out by Soma et al., [44], and Hochmair, [45]. In theirs papers, discussed in section 2.9.1, Soma and Hochmair attempted to investigate the effects of misalignment on the mutual inductance both from a geometrical and a circuit design standpoint. However, their analysis is focused on closely coupled coils. In [45], Hochmair's approach is focused on a lateral misalignment configuration of planar circular coils, i.e., ideal solenoids with zero thickness. In this paper Hochmair reduces the double integral of Neuman's formula to a single integral and then resorts to numerical integration to compute the mutual inductance between the coils. On the contrary, Soma's work is more complete since both lateral and angular misalignment is considered. However, in this paper Soma provided upper and lower bounds of the mutual inductance between two idealised circular rings of similar dimensions and does not attempt a general solution to Neuman's equation. In order to account for multi-turn coils Soma suggests to use shape correction factors provided by Grover and Terman. This semi-analytic approach although advantageous due to its simplicity it is an uneasy alliance between analytical results and empirical data. Soma in [44] suggests that a straightforward application of Neuman's formula for more complex coil geometries under misalignment is mathematically intractable. This can be easily justified since neither the line integrals or the limits of integration cannot be written in a simple form. Therefore, an exact analysis of the general case of the mutual inductance of arbitrary coils still remains an open

problem. Clearly, for practical coils employed in RFID and embedded sensors often coils are loosely coupled. Therefore, an alternative approach for practical coils under misalignment, which avoids the complications introduced by the mutual inductance calculation is presented henceforth.

3.3 Methods for Computing the Magnetic Field from TX Coils

In section 2.4 the process of power transfer across a poorly coupled inductive link was introduced based on a method suggested by Yates in [47]. The two most important elements of this procedure are the computation of the magnetic field and the induced voltage at the RX coil. It is these two parameters that reveal the adaptive nature of the technique. The magnetic field distribution in the near-field is significantly influenced by the geometrical parameters of the coils. In view of this, the RF inductive link efficiency analysis and coil optimization introduced by Yates et al., in [47], can be extended to take this into account. A detailed study of the magnetic field distribution due to different coil geometries, currently popular in the embedded sensor and RFID domains, is presented in section 3.4 of this chapter. Coil orientation is another important factor that affects the magnetic field strength in the vicinity of the RX coil. As a consequence, the amount of induced voltage at the RX depends on the coil shape and its relative position to the TX coil. Expressing the magnetic field with respect to coil geometrical configurations and incorporating the results into Yates' approach results in a very powerful optimisation technique for the design of RF inductive coupled coils.

In the quasi-static near field, fields strongly resemble the electrostatic fields of a charge dipole for a dipole antenna and the fields of a magnetic dipole for a loop antenna. In chapter 2 the basic theory of infinitesimal dipole and loop antennas was introduced since these structures are critical to the modelling of practical coils used in inductive power transfer. As confusion may arise from insufficient understanding of the difference between an induction field and a radiation field, the distinction between the near and far field was discussed in detail. According to the IEEE Standard Definitions of Terms for Antennas in [74], an antenna is defined as: *that part of a transmitting or receiving system that is designed to radiate or to receive electromagnetic waves*. This definition suggests that the term antenna is appropriate to describe devices operating in the far-field, where radiation is taking place. On the contrary, an inductor is a passive electronic component that stores energy in the form of a magnetic field. In its simplest form, an inductor consists of a wire loop or coil. The inductance is directly proportional to the square

of the number of turns in the coil. Inductance also depends on the radius of the coil and on the type of material around which the coil is wound. Hence, the action of an antenna differs from that of an inductor coil in that the former is due to a propagating electromagnetic wave whereas the latter to a static magnetic field, [104]. However, there is some ambiguity surrounding the use of the term antenna. The term antenna is often encountered in studies examining near-field applications, such as in [105], [106], [107]. Furthermore, the expression "antenna coil" is often erroneously employed to indicate inductive coupling in low power wireless systems and RFID devices, [108], [109]. It follows that the term coil is more suitable for wireless inductive coupling applications in the near-field. Thus, the term coil is adopted henceforth in this thesis in order to avoid any confusion.

Currently, there is a wide and diverse variety of applications for RF coils. Among the most common ones are biomedical devices such as magnetic resonance imaging (MRI), magnetic stimulation and inductive telemetry applications, as well as industrial systems like electromagnets, [110–115]. As RF coils are relatively complicated structures it is difficult and time consuming to analyze them using Maxwell's equations. Nevertheless, for electrically small coils whose size is a small fraction of the wavelength, the so-called equivalent circuit approach can be employed. The basic principle of this method is to establish an equivalent lumped-circuit for the coil by modelling a conductive wire or strip as an inductor, as demonstrated in sections 2.2 and 2.8. Therefore, Kirchhoff's laws are employed to model the transformer action between magnetically coupled RF coils using the aforementioned equivalent circuit. In order to calculate the magnetic field, Biot-Savart law is usually applied. This procedure is highly efficient, reasonably accurate and, as a result, it constitutes a very practical approach to the design of RF coils, [116].

Magnetic field computation is one of the most essential elements in the modelling of RF coils. Several approaches are available for solving a stationary magnetic field problem. Nowadays, there is a variety of numerical codes capable of responding to this problem. One possible solution for the electromagnetic field modelling of implantable telemetry systems involves finite difference time domain (FDTD) and finite element (FEM) methods, [117], [41]. Nevertheless, the use of the above numeric-differential approaches can present some difficulties. Generally, a simulating grid, composed of a large number of discretizing elements, is required, in order to reach a satisfactory simulation result. Moreover, problems may arise with the definition of the boundary conditions depending on the geometric complexity of the system being investigated.

In addition, approximation functions and the choice of the type of the elements can significantly influence the computation time of such numerical codes. Consequently, it is time consuming to guarantee the efficiency of numerical methods and often dedicated hardware tools with computational power are required. It follows that, whenever possible, analytical solutions are favored. Therefore, by limiting the case to a stationary magnetic field analysis of iron free media, an integral approach can offer significant advantages and it is particularly suitable to optimization purposes. In fact, many papers deal with the calculation using the integral method based on Biot-Savart's law [112], [118], [119], [120]. A consistent technique for field computation was introduced by Garrett, who presented a solution based on the complete elliptic integrals of the first, second and third kind, [121]. According to Garrett's method, the conductor cross-sectional area is considered to be negligible and a basic element of winding is employed, practically resembling a cylindrical current layer of infinitesimal thickness. This assumption is know as the *filament* approximation. In a later study Urankar suggests that this approach can be still applied to coils of complex forms by superimposing the filament solutions [122], [123]. The semi-analytical elliptic integral method is particularly docile in situations requiring the self and mutual inductance of a coil system, [53]. Note that the term semi-analytical is used because numerical methods are used in the algorithms computing the elliptic integrals. Although the integral method has been known since Maxwell's time, its practical importance can only be realized today, by the modern computational methods available [124]. However, at present elliptic integrals can be easily and efficiently evaluated by using a mathematical package like Mathematica or MATLAB or by consulting handbook tables, i.e. in [125].

3.4 Coil Structures

The choice of a specific coil geometry for RFID systems and embedded devices depends on the intended application parameters. The two most critical factors influencing coil selection are the frequency of operation and the size restrictions imposed on implanted devices. Low-frequency (LF) passive devices are normally inductively coupled, which implies that the induced voltage is proportional to frequency and number of turns. In LF devices many turns in the range of 10-30 turns are required for sufficient voltage to be induced in the RX. In commercial injectable RFID transponders, used in animal and human identification, the coils used are glass-encapsulated multilayer ferrite cored microcoils, as illustrated in Fig. 3.1(a) for the

VeriChip[1] passive transponder. At higher frequencies (HF) such as 13.5MHz, planar spirals dominate the scene, [126]. Typically square or circular spirals with 5 to 7 turns over a credit card-sized form factor are common. These coils are relatively inexpensive and can be used to provide an operation range in the order of tens of centimeters. HF coils are usually fabricated from copper or aluminum. In the past conductive inks were used in transponder coils, but these have encountered problems with IC adhesion and environmental stability.

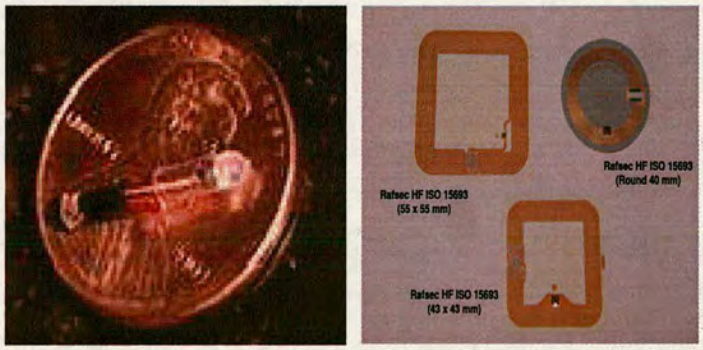

(a) Embedded VeriChip glass-encapsulated transponder, [127].

(b) UPM Raflatac HF RFID tag antenna coils, circular and square spirals, [128].

Figure 3.1: *Photos of types of RFID tags.*

It follows from the previous discussion that the practical coils used in short-range RFID devices fall into two main categories:

- Short Solenoids: a short cylindrical coil has a diameter appreciably larger than its length. Each turn of the coil has the same radius. Short solenoids can have air or ferromagnetic cores.

- Spiral Inductors: the longitudinal thickness of these coils is small compared to the radial thickness and coil radius. Each coil is essentially a flat spiral. Spiral inductors can take many forms such as square/rectangular, circular or polygon. Circular and square printed spirals are the ones studied in this thesis. Spirals can be made from 3D copper enameled or Litz wire or fabricated on PCB or plastic substrates. Printed spirals can be fabricated on top of a ferromagnetic layer to increase their inductance, but this process is usually expensive and prone to parasitic effects degrading the performance of the coil. In

[1] http://www.verichipcorp.com/

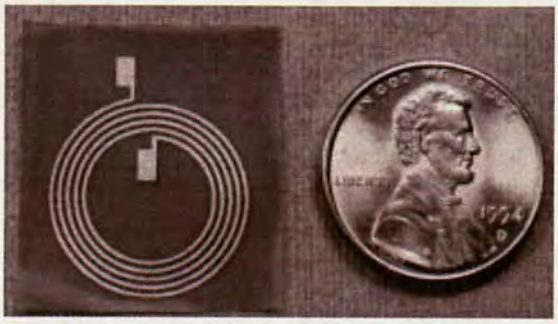

Figure 3.2: *5-turn circular spiral coil, for transcranial telemetry applications, fabricated on a flexible and biocompatible polyimide substrate, with a trace width ($W = S = 313\mu m$) [111].*

practical applications spiral coils are often favored compared to the conventional solenoid coils, as they are more suitable to be built into housings of miniature receivers, Fig. 3.4. Owing to the nature of the embedded application, the transmitting and receiving coils must be very compact, robust and lightweight. Planar spiral structures enjoy most of these qualities. This is a significant advantage over the conventional solenoid structure. The shape and geometry of the coils used in the next generation of implantable devices is very likely to be planar and lithographically defined in one or multiple layers on rigid or flexible substrates similar to printed circuit boards (PCB). Printed spiral coils offer more flexibility with respect to optimising their geometry and aspect ratio, a fact that makes these coils particularly attractive for implantation under the skin or within the epidural space. Likewise, printed spiral coils can easily conform to the outer body or brain surface curvature if fabricated on thin flexible substrates such as polyimide.

Each coil type will be discussed in the following sections. The loosely coupled model introduced by Yates, [47], is revisited in this chapter and extended to account for flat coils and printed spirals which may or may not misalign from the ideal coaxial orientation. It is stated in the literature that the coupling coefficient of an inductive link can be improved by the use of flat coils [129]. The fundamental question examined in this thesis is whether the flat coils and printed spirals are immune to misalignment effects and can improve the displacement tolerance of the inductive link. Using the expressions for the power transfer developed in this chapter, a detailed discussion follows in chapter 6, where the pursuit for the optimal coil geometry continues. Employing the model developed in this chapter, the efficiency of the link, is expressed with respect to lateral and angular misalignments among possible reader/tag coil geometries. A comparison between the received power between different coil shapes will yield the optimum coil type.

3.4.1 The solenoid

The electromagnetic field generated by a current system of any complexity and shape can be evaluated by means of superimposing the field contributions generated by elementary structures. Such structures are infinitesimal current conductors or rings in which a constant current distribution is assumed. Therefore, three-dimensional analytic solutions of the quasi-static magnetic problems have been recently reported for the most elementary conductor geometries, [122], [123]. In view of this, each turn of a closely wound N-turn solenoid coil constructed of circular wire, can be approximated by a collection of vertically stacked equal concentric circular loops which span the length of the solenoid. Such an approximation is valid since, in practice, the diameter of the wire is small in comparison with the solenoid radius a.

Biot-Savart law states that the infinitesimal magnetic field contribution due to an infinitesimal current conductor, denoted $d\ell$, that carries a current I where $\mathbf{r}$ is the displacement vector pointing from the element to the observation point $P(x, y, z)$, is expressed as, [53], [52]:

$$d\mathbf{H} = \frac{I}{4\pi}\frac{d\boldsymbol{\ell}\times\mathbf{r}}{r^3} \tag{3.1}$$

At first glance, the vectorial nature of (3.1) seems to indicate serious difficulties in the computation of simple closed form expressions for the total magnetic field $\mathbf{H}$. However, applying the basic differential form of Biot-Savart law to a finite length of wire of a closed circuit, results in a line integral of the following form:

$$\mathbf{H} = \frac{I}{4\pi}\oint\frac{d\boldsymbol{\ell}\times\mathbf{r}}{r^3} \tag{3.2}$$

where the path of integration is along the wire or loop.

Consequently, Biot-Savart law can be employed in order to compute the magnetic field of the short solenoid at a point $P(x, y, z)$ outside the solenoid. Fig. 3.3, depicts the ideal coaxial orientation, where it is possible to express the magnetic field components by applying a Cartesian frame of coordinates with the origin situated at the center of the TX coil. Hence, referring to Biot-Savart law as expressed in (3.2), the magnetic field at a point O_2 situated at the center of the implanted RX coil can be approximated as:

$$H(\mathbf{r}) = \frac{I}{4\pi}\int_0^{2\pi}\frac{d\boldsymbol{\ell}_{TX}\times\mathbf{r}}{r} \tag{3.3}$$

where $d\ell$ lies on the circumference of the loop.

In most practical cases the embedded coil is much smaller than the external TX coil. Therefore, the magnetic field is considered uniform throughout the effective area of the RX coil. The

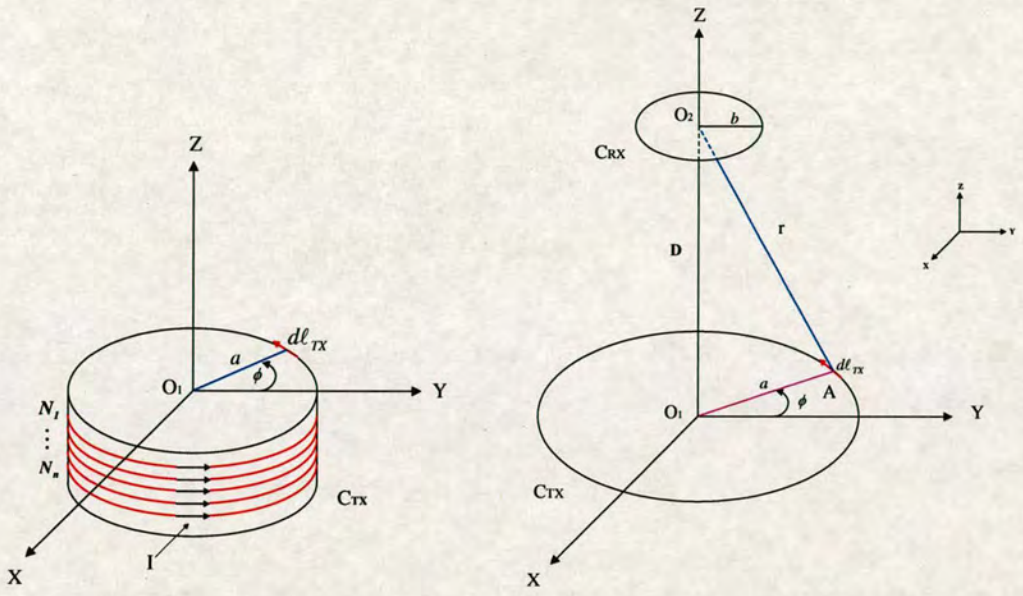

(a) Schematic illustration of the current loops

(b) Coordinate system for the TX, RX coils in the coaxial orientation

Figure 3.3: *Short solenoid representation.*

components of the vectors in (3.3) are obtained by applying vector calculus in the ideal configuration, which is illustrated in Fig. 3.3. The distance r is the magnitude of the vector $\mathbf{r}$ between a point A on the circumference of the TX and point O_2 at the center of the RX coil, that is:

$$\mathbf{r} = \mathbf{O_1O_2} - \mathbf{O_1A} \tag{3.4}$$

Referring to Fig. 3.3 the vectors $\mathbf{O_1A}$ and $\mathbf{O_1O_2}$ are defined below:

$$\mathbf{O_2} = D\mathbf{z}$$

$$\mathbf{O_1A} = (-a\sin\phi)\,\mathbf{x} + (a\cos\phi)\mathbf{y}$$

Hence, from (3.4) the vector is given here:

$$\mathbf{r} = (a\sin\phi)\,\mathbf{x} + (-a\cos\phi)\,\mathbf{y} + D\mathbf{z} \tag{3.5}$$

and the magnitude of $\mathbf{r}$ is defined as

$$|\mathbf{r}| = \sqrt{(a\sin\phi)^2 + (-a\cos\phi)^2 + D^2} = \sqrt{a^2 + D^2} \tag{3.6}$$

It is evident from Fig. 3.3(a) that the inner product of infinitesimal current conductor $d\boldsymbol{\ell}$ with the vector $\mathbf{O_1A}$ is zero, because these vectors will always be perpendicular to each other. Thus,

the element $d\boldsymbol{\ell}$ is defined vectorially as:

$$d\boldsymbol{\ell} = \frac{d\mathbf{O_1A}}{d\phi} \cdot d\phi \tag{3.7}$$

Substituting for the vector $\mathbf{O_1A}$ in the previous expression (3.7) yields:

$$d\boldsymbol{\ell} = (-a\cos\phi\, d\phi)\,\mathbf{x} + (-a\sin\phi\, d\phi)\,\mathbf{y} \tag{3.8}$$

It should be noted that the unit vectors $\mathbf{x}$, $\mathbf{y}$, and $\mathbf{z}$ from the given orthogonal coordinate system satisfy the following equalities:

$$\mathbf{x}\times\mathbf{y} = \mathbf{z} \qquad \mathbf{y}\times\mathbf{z} = \mathbf{x} \qquad \mathbf{x}\times\mathbf{z} = \mathbf{y}$$

Following the vector definition in (3.5) and (3.7), the cross product at the numerator of expression (3.3) is given as:

$$d\boldsymbol{\ell}\times\mathbf{r} = \begin{vmatrix} \mathbf{x} & \mathbf{y} & \mathbf{z} \\ -a\cos\phi & -a\sin\phi & 0 \\ a\sin\phi & -a\cos\phi & D \end{vmatrix} \tag{3.9}$$

Evaluating the determinant yields:

$$d\boldsymbol{\ell}\times\mathbf{r} = (-aD\sin\phi\, d\phi)\,\mathbf{x} + (-aD\cos\phi\, d\phi)\,\mathbf{y} + \left(a^2\, d\phi\right)\mathbf{z} \tag{3.10}$$

Substituting the cross product, as evaluated in (3.10) above, in the numerator and the magnitude of the vector $\mathbf{r}$ in the denominator of expression (3.3), the Cartesian magnetic field components can be evaluated by the following integrals:

$$\mathbf{H}_x = 2\,\frac{I}{4\pi}\int_0^{\pi} \frac{-a\,D\sin\phi}{\sqrt{a^2+D^2}^3}\, d\phi \tag{3.11a}$$

$$\mathbf{H}_y = 2\,\frac{I}{4\pi}\int_0^{\pi} \frac{-a\,D\cos\phi}{\sqrt{a^2+D^2}^3}\, d\phi \tag{3.11b}$$

$$\mathbf{H}_z = 2\,\frac{I}{4\pi}\int_0^{\pi} \frac{a^2}{\sqrt{a^2+D^2}^3}\, d\phi \tag{3.11c}$$

It is clear from the above expressions, (3.11), that the line integrals formulating the x and y magnetic field components are zero. This is indeed justified due to the circular symmetry of the RX coil so that the x and y components cancel out at the center of the coil. This suggests that the z component of the field dominates at the center of the RX coil. Solving the integral

in expression (3.11) yields the well-known text book expression for the z component of the magnetic field on the axis of the TX circular loop, [71]:

$$\mathbf{H}_z = \frac{Ia^2}{2\pi\sqrt{a^2+D^2}^3}\int_0^{\pi} d\phi = \frac{\mu_o I a^2}{2\sqrt{a^2+D^2}^3} \tag{3.12}$$

Subsequently, from the previous expression (3.12), the magnetic field at the center of the circular TX coil when the separation distance between the TX and RX coil is zero ($D = 0$) is

$$\mathbf{H}_z = \frac{I}{2a} \tag{3.13}$$

and at a large distance from the TX coil ($D >> a$) the z field component becomes:

$$H_z = \frac{I\,a^2}{2D^3} \tag{3.14}$$

Therefore, the resulting magnetic field, from an N-turn circular short solenoid illustrated in Fig. 3.3(a), at the RX coil can be obtained from Biot-Savart law as described previously:

$$H_z = \frac{I_{TX}\,N_{TX}\,a^2}{2\left(a_{TX}^2 + r^2\right)^{3/2}} \tag{3.15}$$

Once the magnetic field is defined, the induced voltage at the RX coil can be described as the rate of change of flux linkage based on Faraday's law, [54]:

$$V_{IND} = N_{RX}\mu_o A_{RX} \cdot j\omega H_z \tag{3.16}$$

where A_{RX} is the loop area and N_{RX} is the number of turns.

The modelling of the magnetic coupling between the circular and square TX and RX coil geometries discussed in sections 3.4.2 and 3.4.3 comprises of two parts. The first part in sections 3.4.2 and 3.4.3 is focused on the evaluation of the magnetic field generated by the TX. In the second part of sections 3.4.2 and 3.4.3 the induced voltage across the RX, due to the presence of the alternating magnetic flux generated by the resonant TX coil, is computed. In this section the coils are assumed to be aligned on a common central axis as depicted in Fig. 3.3(b). This is known as the perfect alignment or coaxial configuration. This configuration signifies the simplest scenario and is considered here in order to establish some mathematical conventions, which will be used in comparison with the non-ideal topologies studied in section 3.5.

3.4.2 The circular spiral

For most practical spiral structures, the spacing between adjacent turns and the trace width are often small compared to the inductor size. In the special case of a planar spiral coil of

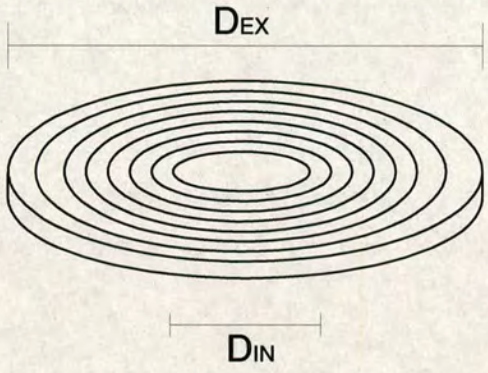

Figure 3.4: *A schematic representation of a circular spiral inductor.*

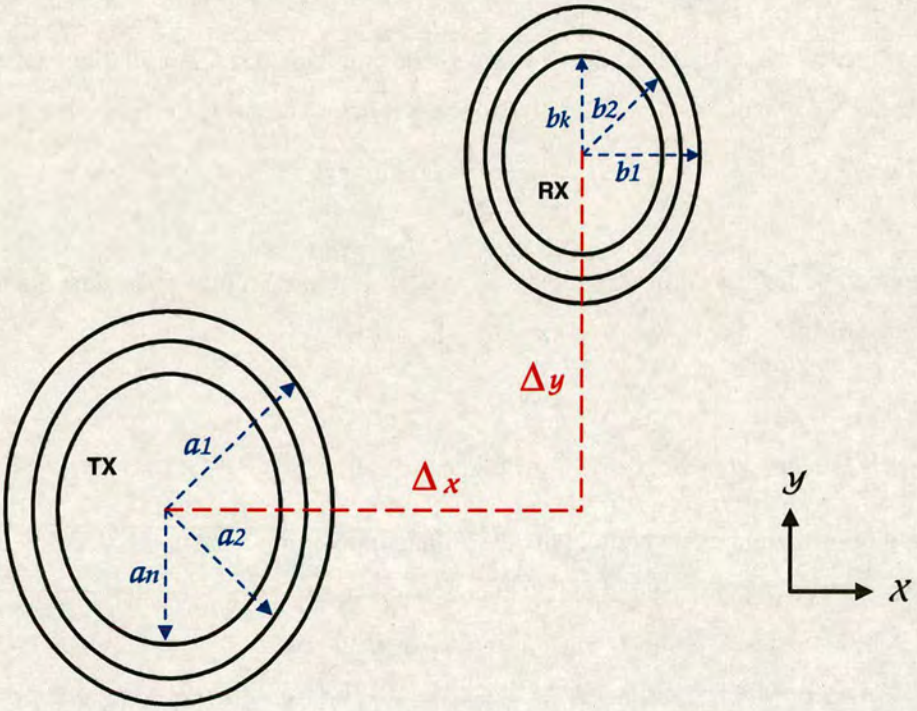

Figure 3.5: *Geometric arrangement and notation for TX and RX circular spiral coils represented by a number of concentric circular loops.*

circular conductor, the diameter of the wire is considerably smaller than the dimensions of the spiral and the wavelength at the operating frequency. The outer diameter of the spiral, D_{EX}, is not significantly larger than the the inner one, D_{IN}, as shown in Fig. 3.4. Therefore, for a circular spiral coil satisfying the above conditions, the approximation of having closed turns has a negligible effect on the results. Consequently, a typical circular spiral coil can by represented as a collection of n closed concentric circular loops with decreasing radii, $a_i (i = 1, 2, \cdots, n)$, from the circumference to the center of the coil. It follows that for the benefit of simplicity each

loop represents one winding of the coil, as illustrated in the diagram of Fig. 3.5. In the special case of closely spaced turns it is essential to replace the n-turn spiral with n concentric circles in order to evaluate analytically the integral expressing the magnetic field of the spiral. This important physical observation, which is employed in this section, is a powerful tool commonly used in the modelling of two-dimensional spiral inductors, [130].

Fig. 3.5 shows the top-view of the equivalent idealized diagram of the TX and RX circular spiral coils consisting of n-turn planar windings situated in a homogeneous and isotropic medium such as air. In this planar system assuming that the current is distributed uniformly across the conductor cross section, the total magnetic field generated by the TX coil can be computed using the Biot-Savart law based on the superposition principle [131], [132]. The direction of the current is assumed to be equal in all the turns of the circular spiral coil. Referring to Fig. 3.5 we can express the magnetic field at the center of the RX coil as the total field generated by the number of loops comprising the TX coil. Starting from the perfect alignment case, the dominant H-field component is H_z as discussed earlier. Thus, the z component of the H-field in the ideal coplanar orientation generated by a TX spiral of n turns is given by the following expression:

$$H_z = \sum_{i=1}^{n} \frac{I_{TX} \cdot a_i^2}{2\left(a_i^2 + D^2\right)^{3/2}} \tag{3.17}$$

At the receiving end of the inductive link, the total induced emf across the RX spiral can be expressed using Faraday's law as the sum of emf induced in each concentric loop. Considering the geometry depicted in Fig. 3.5, the RX coil is being approximated as a number k of concentric loops with different radii $b_j (j = 1, 2, \cdots, k)$, in a similar manner with the approach adopted for modelling the TX coil. Hence, the resulting emf, denoted V_{IND}, is given as:

$$V_{IND} = j\, \mu_o\, \omega\, H_z \cdot \sum_{j=1}^{k} \pi\, b_j^2 \tag{3.18}$$

3.4.3 The square spiral

The advantages of spiral coils make the use of square spirals attractive in small-sized devices, especially in RFID, near-field communication systems as well as implanted sensors. Thus, a comprehensive analysis of their performance in the near-field is essential. It is known that the far-field components in the plane of an electrically small square loop coincide with the field components of a circular loop antenna of the same area, [59], [66]. However, the behaviour

of a square loop in the near-field varies significantly from that of the circular loop. Regarding electrically small square loops, but finite in comparison with the distance to the observation point, it is evident that in the inductive near-field the loop shape will influence the field. The near-field of a circular loop is studied in a limited number of papers, as discussed in section (2.5). In the antenna literature, research focusing on the near-field of a square loop is even more limited with the exception of a paper written by Levin, [72].

In the square spiral case a three-axis square loop transmitter-receiver model is employed, as shown in Fig. 3.6(a), in order to investigate the theoretical magnetic field strength in the near-field where the RX coil is situated. Consequently, based on Faraday's law an equation that calculates the corresponding induced voltage at the RX due to the presence of the induction field is derived.

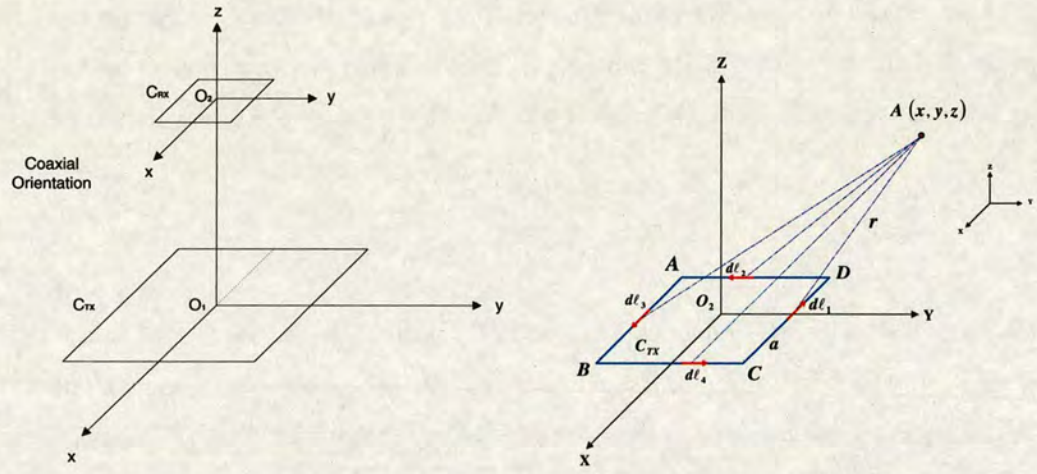

(a) Transmitter and receiver coaxial orientation.

(b) Geometry of the square loop under consideration.

Figure 3.6: *Schematic representation of square loop geometry employed in the modelling of square spiral coils.*

The space between adjacent turns and the trace width are typically small compared to the spiral inductor size, as shown in Fig. 3.8. Therefore, the approximation of having closed turns holds, hence the transmitter-receiver square spiral coil model can be approximated as shown in Fig. 3.7. The approach taken in this section is to divide the spiral into a collection of segments, partitioned as four linear elements, with lengths $a_i\,(i = 1, 2, \cdots, n)$ and $b_j\,(j = 1, 2, \cdots, k)$ representing the TX and RX coils respectively. Closed-form expressions for the field from each

segment are then applied to find the total field at the point of interest, $A(x, y, z)$, where the center of the RX coil is located.

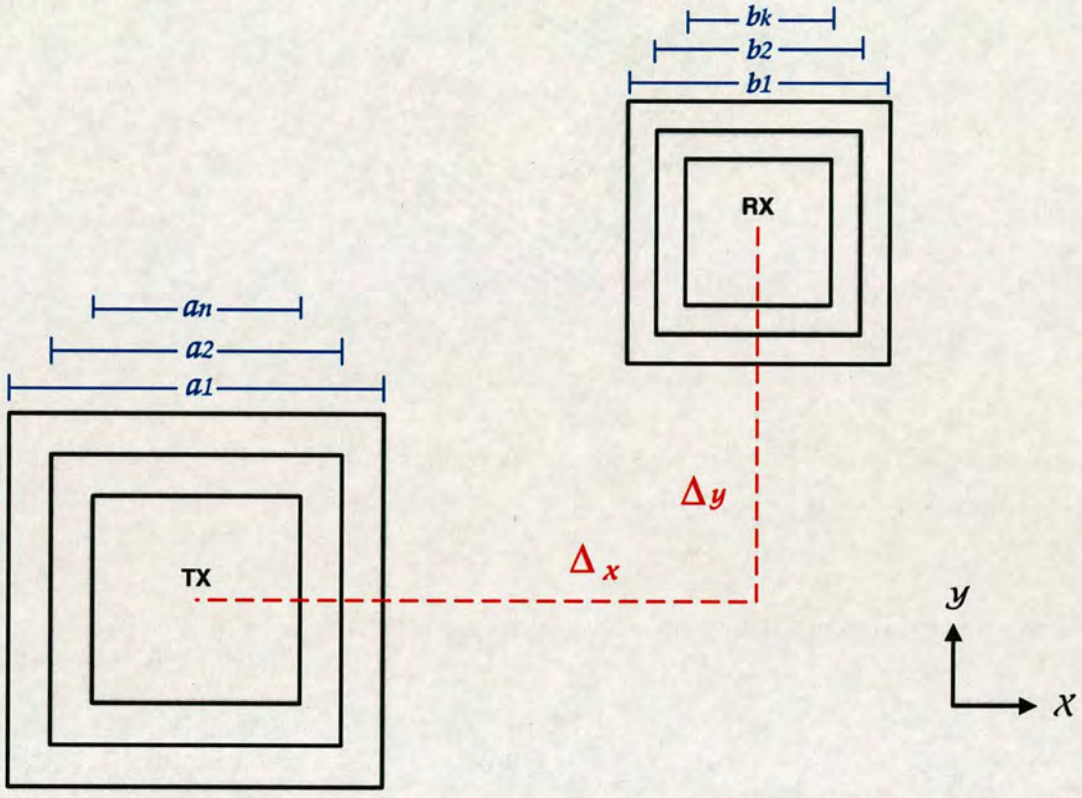

Figure 3.7: *The closed turn approximation for TX and RX square spiral coils represented by a number of concentric square loops.*

The scheme of a square loop is represented in Fig. 3.8 below. The center of the loop is located on the $x - y$ plane, at the origin of a Cartesian coordinate system (x, y, z). It is assumed that the loop is electrically small, that is, the side length a is much smaller than the wavelength λ, $(a << \lambda)$. Hence, in the same manner as with the circular loop considered previously, the amplitude and phase of the current along the loop conductor is though to be constant.

Starting with the magnetic field $\mathbf{H}$ generated by a square loop $ABCD$ as depicted in Fig. 3.6(b), Biot-Savart law (LBS) is employed as expressed in (3.2). In this form of LBS I is the uniform current circulating in the windings of the spiral coil, and $\mathbf{d}\ell$ is the infinitesimal current conductor situated on the side of the square loop.

The square loop can be treated as four short linear dipoles. In this way we can compute the

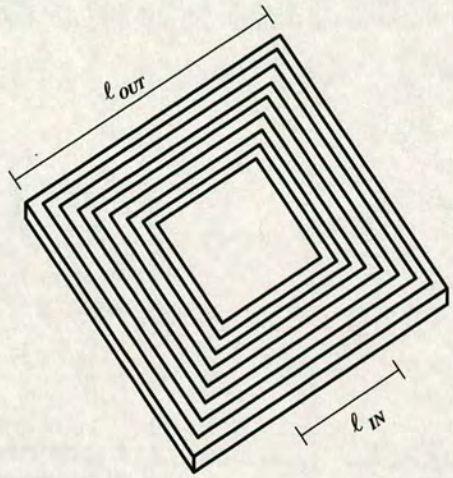

Figure 3.8: *A schematic representation of a square spiral inductor.*

magnetic field $\mathbf{H}$ generated by each dipole and add the resulting expressions. Applying LBS for the dipole CD yields:

$$\mathbf{H_{CD}} = \frac{I}{4\pi}\int_C^D \frac{\mathbf{d}\ell \times \mathbf{r}}{r^3} \tag{3.19}$$

Starting with the vector definition in the integrand of the LBS, as given in (3.19),

$$\ell = \left(-\frac{a}{2}t, \frac{a}{2}, 0\right) \tag{3.20}$$

$$\mathbf{d}\ell = -\frac{a}{2}(1,0,0) \tag{3.21}$$

$$\mathbf{r} = \left(x + \frac{a}{2}t, y - \frac{a}{2}, z\right) \tag{3.22}$$

The cross product of vectors $\mathbf{d}\ell$ and $\mathbf{r}$ is given by their determinant:

$$\mathbf{d}\ell \times \mathbf{r} = \begin{vmatrix} \mathbf{x} & \mathbf{y} & \mathbf{z} \\ -\frac{a}{2} & 0 & 0 \\ x + \frac{a}{2}t & y - \frac{a}{2} & z \end{vmatrix} = \frac{a}{2}\left(z\mathbf{y} - (y - \frac{a}{2})\mathbf{z}\right) = \left(0, \frac{a}{2}z, -\frac{a}{2}(y - \frac{a}{2})\right) \tag{3.23}$$

Substituting in (3.19) it follows that:

$$\mathbf{H_{CD}} = \frac{I}{4\pi}\int_{-1}^{1} \frac{\frac{a}{2}z\,\mathbf{y} - \frac{a}{2}(y - \frac{a}{2})\,\mathbf{z}}{\left[(x + \frac{a}{2}t)^2 + (y - \frac{a}{2})^2 + (z)^2\right]^{3/2}}\, dt \tag{3.24}$$

This integral can be simplified by an appropriate substitution. Now, let $t' = \frac{a}{2}t$ in the integrand of (3.24). Immediately this yields $dt' = \frac{a}{2}dt$ and the new limits of integration are $-a/2, a/2$. Consequently, by substituting for $t' = \frac{a}{2}t$ and dt in (3.24) the new integral becomes:

$$\mathbf{H_{CD}} = \frac{I}{4\pi}\int_{-a/2}^{a/2} \frac{z\,\mathbf{y} - (y - \frac{a}{2})\,\mathbf{z}}{\left[(x + t')^2 + (y - \frac{a}{2})^2 + (z)^2\right]^{3/2}}\, dt' \tag{3.25}$$

In the same manner, applying LBS for to the dipole DA:

$$\mathbf{H_{DA}} = \frac{I}{4\pi}\int_{D}^{A}\frac{\mathbf{d}\ell \times \mathbf{r}}{r^3} \tag{3.26}$$

Starting with the vector definition in the integrand of the LBS as given in (3.26)

$$\ell = \left(-\frac{a}{2}, -\frac{a}{2}t, 0\right) \tag{3.27}$$

$$\mathbf{d}\ell = -\frac{a}{2}(0,1,0) \tag{3.28}$$

$$\mathbf{r} = \left(x+\frac{a}{2}, y+\frac{a}{2}t, z\right) \tag{3.29}$$

The cross product of vectors $\mathbf{d}\ell$ and $\mathbf{r}$ is given by their determinant:

$$\mathbf{d}\ell\times\mathbf{r} = \begin{vmatrix} \mathbf{x} & \mathbf{y} & \mathbf{z} \\ 0 & -\frac{a}{2} & 0 \\ x+\frac{a}{2} & y+\frac{a}{2}t & z \end{vmatrix} = -\frac{a}{2}\left(z\mathbf{x} - \left(x+\frac{a}{2}\right)\mathbf{z}\right) = \left(-\frac{a}{2}z, 0, \frac{a}{2}\left(x+\frac{a}{2}\right)\right) \tag{3.30}$$

Substituting in (3.26) it follows that:

$$\mathbf{H_{DA}} = \frac{I}{4\pi}\int_{-1}^{1}\frac{-\frac{a}{2}z\,\mathbf{x} + \frac{a}{2}(\frac{a}{2}+x)\,\mathbf{z}}{\left[(x+\frac{a}{2})^2 + (y+\frac{a}{2}\,t)^2 + (z)^2\right]^{3/2}}\,dt \tag{3.31}$$

By applying the substitution $t' = \frac{a}{2}t$, the integral in (3.31) becomes:

$$\mathbf{H_{DA}} = \frac{I}{4\pi}\int_{-a/2}^{a/2}\frac{-z\,\mathbf{x} + (\frac{a}{2}+x)\,\mathbf{z}}{\left[(x+\frac{a}{2})^2 + (y+t')^2 + (z)^2\right]^{3/2}}\,dt' \tag{3.32}$$

Applying LBS for the dipole AB:

$$\mathbf{H_{AB}} = \frac{I}{4\pi}\int_{A}^{B}\frac{\mathbf{d}\ell \times \mathbf{r}}{r^3} \tag{3.33}$$

Starting with the vector definition in the integrand of the LBS as given in (3.33)

$$\ell = \left(\frac{a}{2}t, -\frac{a}{2}, 0\right) \tag{3.34}$$

$$\mathbf{d}\ell = \frac{a}{2}(1,0,0) \tag{3.35}$$

$$\mathbf{r} = \left(x-\frac{a}{2}t, y+\frac{a}{2}, z\right) \tag{3.36}$$

The cross product of vectors $\mathbf{d}\ell$ and $\mathbf{r}$ is given by their determinant:

$$\mathbf{d}\ell \times \mathbf{r} = \begin{vmatrix} \mathbf{x} & \mathbf{y} & \mathbf{z} \\ \frac{a}{2} & 0 & 0 \\ x-\frac{a}{2}t & y+\frac{a}{2} & z \end{vmatrix} = -\frac{a}{2}\left(z\mathbf{y} - \left(y+\frac{a}{2}\right)\mathbf{z}\right) = \left(0, -\frac{a}{2}z, +\frac{a}{2}\left(y+\frac{a}{2}\right)\right) \tag{3.37}$$

Substituting in (3.33) it follows:

$$\mathbf{H_{AB}} = \frac{I}{4\pi}\int_{-1}^{1} \frac{-\frac{a}{2}z\,\mathbf{y} + \frac{a}{2}(y+\frac{a}{2})\mathbf{z}}{\left[(x-\frac{a}{2}t)^2 + (y+\frac{a}{2})^2 + z^2\right]^{3/2}}\,dt \tag{3.38}$$

By applying the substitution $t' = \frac{a}{2}t$, the integral in (3.38) becomes:

$$\mathbf{H_{AB}} = \frac{I}{4\pi}\int_{-a/2}^{a/2} \frac{-z\,\mathbf{y} + (y+\frac{a}{2})\mathbf{z}}{\left[(x-t')^2 + (y+\frac{a}{2})^2 + z^2\right]^{3/2}}\,dt' \tag{3.39}$$

Applying LBS for the dipole BC:

$$\mathbf{H_{BC}} = \frac{I}{4\pi}\int_{B}^{C} \frac{\mathbf{d}\ell \times \mathbf{r}}{r^3} \tag{3.40}$$

Starting by the vector definition in the integrand of the LBS as given in (3.40)

$$\ell = \left(\frac{a}{2}, \frac{a}{2}t, 0\right) \tag{3.41}$$

$$\mathbf{d}\ell = \frac{a}{2}(0,1,0) \tag{3.42}$$

$$\mathbf{r} = \left(x - \frac{a}{2}, y - \frac{a}{2}t, z\right) \tag{3.43}$$

The cross product of vectors $\mathbf{d}\ell$ and $\mathbf{r}$ is given by their determinant:

$$\mathbf{d}\ell \times \mathbf{r} = \begin{vmatrix} \mathbf{x} & \mathbf{y} & \mathbf{z} \\ 0 & \frac{a}{2} & 0 \\ x-\frac{a}{2} & y-\frac{a}{2}t & z \end{vmatrix} = \frac{a}{2}\left(z\mathbf{x} - \left(x-\frac{a}{2}\right)\mathbf{z}\right) = \left(\frac{a}{2}z, 0, -\frac{a}{2}\left(x-\frac{a}{2}\right)\right) \tag{3.44}$$

Substituting in (3.40) it follows that:

$$\mathbf{H_{BC}} = \frac{I}{4\pi}\int_{-1}^{1} \frac{\frac{a}{2}z\,\mathbf{x} - \frac{a}{2}(x-\frac{a}{2})\mathbf{z}}{\left[(x-\frac{a}{2})^2 + (y-\frac{a}{2}t)^2 + z^2\right]^{3/2}}\,dt \tag{3.45}$$

In a similar manner to the previous square sections, substituting for $t' = \frac{a}{2}t$ in (3.45) becomes:

$$\mathbf{H} = \frac{I}{4\pi}\int_{-a/2}^{a/2} \frac{z\,\mathbf{x} - (x-\frac{a}{2})\mathbf{z}}{\left[(x-\frac{a}{2})^2 + (y-t')^2 + z^2\right]^{3/2}}\,dt' \tag{3.46}$$

The integrals in (3.25), (3.32), (3.39), (3.46) can be evaluated based on the integration by substitution technique which can simplify the integrand until it resembles an expression that is

integrable. In this manner the expressions for the magnetic field due to each side of the square loop can be represented by the following general form:

$$H_{INT} = \int_{-a/2}^{a/2} \frac{ds}{\left[(u-s)^2 + c^2\right]^{3/2}} \tag{3.47}$$

Careful inspection of the above integral, (3.47) yields that by a double substitution the integral can be evaluated analytically. Initially a substitution of the form $v = s - u$, where u is a constant and $dv = ds$ can take place in the denominator of the integrand in (3.47) resulting in:

$$H_{INT} = \int_{-\left(\frac{a}{2}+u\right)}^{\left(\frac{a}{2}-u\right)} \frac{dv}{\left[v^2 + c^2\right]^{3/2}} \tag{3.48}$$

It is critical to notice that the limits of integration change with each successive integration. A further substitution of the form $v = c \cdot w$, where c is a constant and $dv = dw$, returns

$$H_{INT} = \int_{-\left(\frac{a}{2}+u\right)/c}^{\left(\frac{a}{2}-u\right)/c} \left(\frac{c\, dw}{c^3 \left[w^2+1\right]^{3/2}} \right) = \frac{1}{c^2} \int_{-\left(\frac{a}{2}+u\right)/c}^{\left(\frac{a}{2}-u\right)/c} \left(\frac{dw}{\left[w^2+1\right]^{3/2}} \right) \tag{3.49}$$

Applying a trigonometric substitution of the form $w = \tan g$ and $dw = \dfrac{1}{\cos^2 g}\, dg$, in (3.49), gives:

$$\begin{aligned} H_{INT} &= \frac{1}{c^2} \int_{-\tan^{-1}\left(\left(\frac{a}{2}+u\right)/c\right)}^{\tan^{-1}\left(\left(\frac{a}{2}-u\right)/c\right)} \left(\frac{1/\cos^2 g}{1+\tan^2 g}\, dg \right) \\ &= \frac{1}{c^2} \int_{-\tan^{-1}\left(\left(\frac{a}{2}+u\right)/c\right)}^{\tan^{-1}\left(\left(\frac{a}{2}-u\right)/c\right)} \left(\frac{1/\cos^2 g}{1/\cos^3 g}\, dg \right) \\ &= \frac{1}{c^2} \int_{-\tan^{-1}\left(\left(\frac{a}{2}+u\right)/c\right)}^{\tan^{-1}\left(\left(\frac{a}{2}-u\right)/c\right)} (\cos g\, dg) \end{aligned} \tag{3.50}$$

The final integral in (3.50) is a standard cosine integral which can now be solved, giving the following expression:

$$\frac{1}{c^2} \left[\sin\tan^{-1}\left(\left(\frac{a}{2}+u\right)/c\right) + \sin\tan^{-1}\left(\left(\frac{a}{2}+u\right)/c\right) \right] \tag{3.51}$$

Employing the following trigonometric identities, the expression given in (3.51) can be algebraically manipulated in order to return a simpler solution that does not involve trigonometric

functions. Initially, the Pythagorean identity can be written as follows:

$$\begin{aligned}\cos^2 h + \sin^2 h = 1 \ \text{(divide left and write by } \sin^2 h) &\Rightarrow \frac{1}{\sin^2 h} = 1 + \frac{1}{\tan^2 h} \\ &\Rightarrow \sin^2 h = \frac{\tan^2 h}{\tan^2 h + 1} \\ &\Rightarrow \sin h = \frac{\tan h}{\sqrt{1 + \tan^2 h}} \end{aligned} \tag{3.52}$$

Thus, substitution of (3.52) into the expression (3.51), yields the solution of the integral (3.47) in the form:

$$H_{INT} = \frac{1}{c^2}\left[\frac{\frac{a/2-u}{c}}{\sqrt{\left(1+\frac{(a/2-u)^2}{c^2}\right)}} + \frac{\frac{a/2+u}{c}}{\sqrt{\left(1+\frac{(a/2+u)^2}{c^2}\right)}}\right] \tag{3.53}$$

Finally, by algebraic simplification of the previous expression, the solution to the integral of (3.47) is:

$$H_{INT} = \frac{1}{c^2}\left[\frac{\left(\frac{a}{2}-u\right)}{\sqrt{\left(\frac{a}{2}-u\right)^2 + c^2}} + \frac{\left(u+\frac{a}{2}\right)}{\sqrt{\left(u+\frac{a}{2}\right)^2 + c^2}}\right] \tag{3.54}$$

Therefore, the total magnetic field due to the square current loop $ABCD$ shown in Fig. 3.6(b) can be expressed by superimposing the contributions of each linear dipole that compose the four sides of the square. The total field denoted H_z is thus:

$$\begin{aligned} H_z = \frac{I}{4\pi}\Bigg[&\int_{-a/2}^{a/2} \frac{-\left(y-\frac{a}{2}\right)\mathbf{z}}{\left[(x+t')^2 + (y-\frac{a}{2})^2 + z^2\right]^{3/2}}\,dt' + \\ &\int_{-a/2}^{a/2} \frac{\left(\frac{a}{2}+x\right)\mathbf{z}}{\left[(x+\frac{a}{2})^2 + (y+t')^2 + z^2\right]^{3/2}}\,dt' + \\ &\int_{-a/2}^{a/2} \frac{\left(y+\frac{a}{2}\right)\mathbf{z}}{\left[(x-t')^2 + (y+\frac{a}{2})^2 + z^2\right]^{3/2}}\,dt' - \\ &\int_{-a/2}^{a/2} \frac{\left(x-\frac{a}{2}\right)\mathbf{z}}{\left[(x-\frac{a}{2})^2 + (y-t')^2 + z^2\right]^{3/2}}\,dt'\Bigg] \end{aligned} \tag{3.55}$$

Consequently, the integral function (3.55) is composed of the individual contributions of the four sides of the square loop, each being an integral of the general form shown by (3.47). The solution to this integral was evaluated earlier in this section and the result is shown in (3.54). The substitution of the u and c term in (3.54) for each integral term in (3.55) leads to the analytic expression for the magnetic field of the square spiral. For example, the first integral

term in (3.47), representing the magnetic field strength due to the contribution from one side of the square loop, is:

$$\int_{-a/2}^{a/2} \frac{\left(y-\frac{a}{2}\right)\mathbf{z}}{\left[(x+t')^2+(y-\frac{a}{2})^2+z^2\right]^{3/2}}\,dt'$$

where u is $-x$, as $(x+t')^2=(-x-t')^2$ and c^2 represents $\left(y-\frac{a}{2}\right)+z^2$.

$$\begin{aligned}
H_z = \frac{I}{4\pi}\Bigg\{ & \frac{-\left(y-\frac{a}{2}\right)}{\left(y-\frac{a}{2}\right)^2+z^2}\left[\frac{\frac{a}{2}+x}{\sqrt{\left(\frac{a}{2}+x\right)^2+\left(y-\frac{a}{2}\right)^2+z^2}}\right.\\
& \left.+\frac{\frac{a}{2}-x}{\sqrt{\left(\frac{a}{2}-x\right)^2+\left(y-\frac{a}{2}\right)^2+z^2}}\right]\mathbf{z}\\
& +\frac{\left(\frac{a}{2}+x\right)}{\left(x+\frac{a}{2}\right)^2+z^2}\left[\frac{\frac{a}{2}+y}{\sqrt{\left(\frac{a}{2}+y\right)^2+\left(x+\frac{a}{2}\right)^2+z^2}}\right.\\
& \left.+\frac{\frac{a}{2}-y}{\sqrt{\left(\frac{a}{2}-y\right)^2+\left(x+\frac{a}{2}\right)^2+z^2}}\right]\mathbf{z}\\
& +\frac{\left(y+\frac{a}{2}\right)}{\left(y+\frac{a}{2}\right)^2+z^2}\left[\frac{\frac{a}{2}-x}{\sqrt{\left(\frac{a}{2}-x\right)^2+\left(y+\frac{a}{2}\right)^2+z^2}}\right.\\
& \left.+\frac{\frac{a}{2}+x}{\sqrt{\left(\frac{a}{2}+x\right)^2+\left(y+\frac{a}{2}\right)^2+z^2}}\right]\mathbf{z}\\
& -\frac{\left(x-\frac{a}{2}\right)}{\left(x-\frac{a}{2}\right)^2+z^2}\left[\frac{\frac{a}{2}-y}{\sqrt{\left(\frac{a}{2}-y\right)^2+\left(x-\frac{a}{2}\right)^2+z^2}}\right.\\
& \left.+\frac{\frac{a}{2}+y}{\sqrt{\left(\frac{a}{2}+y\right)^2+\left(x-\frac{a}{2}\right)^2+z^2}}\right]\mathbf{z}\Bigg\}
\end{aligned} \tag{3.56}$$

Referring back to the model of the square spiral, illustrated in Fig. 3.7, the coil is approximated by a number of n concentric square loops. The integral equation method described above for the square loop can be employed here to solve the three dimensional magnetic field problem for the square spiral. The algorithm in (3.56) computes the dominant z component of the magnetic field generated by the square loop of Fig. 3.6(b). Applying this algorithm to each consecutive loop in Fig. 3.7 and summing the results yields the z component of the induced field due to the

TX square spiral coil as:

$$H_z = \frac{I}{4\pi}\sum_{i=1}^{n}\left\{\frac{-\left(y-\frac{a_i}{2}\right)}{\left(y-\frac{a_i}{2}\right)^2+z^2}\left[\frac{\frac{a_i}{2}+x}{\sqrt{\left(\frac{a_i}{2}+x\right)^2+\left(y-\frac{a_i}{2}\right)^2+z^2}}+\frac{\frac{a_i}{2}-x}{\sqrt{\left(\frac{a_i}{2}-x\right)^2+\left(y-\frac{a_i}{2}\right)^2+z^2}}\right]\mathbf{z}\right.$$
$$+\frac{\left(\frac{a_i}{2}+x\right)}{\left(x+\frac{a_i}{2}\right)^2+z^2}\left[\frac{\frac{a_i}{2}+y}{\sqrt{\left(\frac{a_i}{2}+y\right)^2+\left(x+\frac{a_i}{2}\right)^2+z^2}}+\frac{\frac{a_i}{2}-y}{\sqrt{\left(\frac{a_i}{2}-y\right)^2+\left(x+\frac{a_i}{2}\right)^2+z^2}}\right]\mathbf{z}$$
$$+\frac{\left(y+\frac{a_i}{2}\right)}{\left(y+\frac{a_i}{2}\right)^2+z^2}\left[\frac{\frac{a_i}{2}-x}{\sqrt{\left(\frac{a_i}{2}-x\right)^2+\left(y+\frac{a_i}{2}\right)^2+z^2}}+\frac{\frac{a_i}{2}+x}{\sqrt{\left(\frac{a_i}{2}+x\right)^2+\left(y+\frac{a_i}{2}\right)^2+z^2}}\right]\mathbf{z}$$
$$-\frac{\left(x-\frac{a_i}{2}\right)}{\left(x-\frac{a_i}{2}\right)^2+z^2}\left[\frac{\frac{a_i}{2}-y}{\sqrt{\left(\frac{a_i}{2}-y\right)^2+\left(x-\frac{a_i}{2}\right)^2+z^2}}+\frac{\frac{a_i}{2}+y}{\sqrt{\left(\frac{a_i}{2}+y\right)^2+\left(x-\frac{a_i}{2}\right)^2+z^2}}\right]\mathbf{z}\left.\right\} \quad (3.57)$$

3.4.3.1 Coil sensitivity

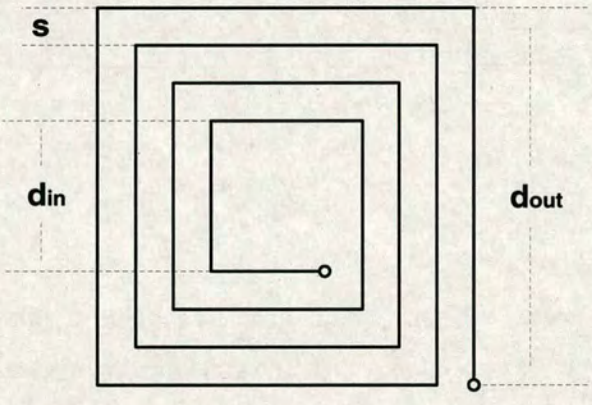

Figure 3.9: *Planar view of square spiral coil.*

The sensitivity of the RX square spiral coil is determined by the induced voltage across the terminals of the coil. The induced voltage is proportional to the flux captured by the cross-

sectional area of the coil. Hence, in the case of the square spiral coil, as shown in Fig. 3.9, the effective area of the coil can be derived by summing the area of each turn in the coil. An alternative technique is applied for the computation of the effective area of the coil, following an expression for the area of a square spiral coil suggested by Lee, [133]. The simple formula adopted offers the advantage that it does not involve the cumbersome summation technique used in the circular spiral case. The effective area of a square spiral coil is estimated as, [133]:

$$A = \frac{2}{3}s^2N(N-1)(2N-1) + d_{in}^2N + 2d_{in}sN(N-1) \tag{3.58}$$

where s is the spacing between each successive turn, d_{in} is the size of the innermost turn which is equal to the internal diameter of the spiral and N is the number of turns. In addition, the outside dimension of the coil, also referred to as the external diameter, is defined as twice the sum of all the turn spacings and the internal diameter of the coil. Hence, the external diameter of the coil denoted d_{out}, is given by:

$$d_{out} = 2(N-1)s + d_{in} \tag{3.59}$$

In a similar manner to a circular coil the induced voltage across the receiver square spiral coil is given by Faraday's law as follows:

$$V_{IND} = \mu_o \cdot A_{RX} \cdot j\omega H_z \tag{3.60}$$

where A_{RX} is the effective area of the square spiral coil given by (3.58), and H_z is the magnetic field strength at the center of the RX coil as expressed by equation (3.57) derived earlier.

3.5 Geometric Configurations for TX, RX Topologies

Coil orientation is a key parameter in the design of magnetically coupled devices. In particular, embedded devices using inductive coupling to receive power from an external resonant coil, will receive maximum power when the external TX and the implanted RX coils are coaxially orientated. The coaxial orientation is depicted in Fig. 3.3(b) and Fig. 3.6(a) for a circular and square loop coils respectively. In the coaxial orientation, also referred to as the ideal case in this thesis, the magnetic field lines associated with the TX are orthogonal to the RX coil hence, best coupling results. Contrary to the perfect alignment position of the coils, no coupling is expected when the RX coil is situated at a right angle with respect to the TX. In this position no magnetic flux lines are intersecting the RX coil and so, no energy will couple across the link.

Table 3.1 specifies the coil and configuration parameters used in the formulation of the model presented in this chapter. The majority of these factors appear in the power transfer functions developed in section 3.6.

In this thesis two cases of misalignment which occur commonly in most practical cases will be studied, listed here:

1. *Lateral Misalignment* - In the lateral misalignment case Fig. 3.10 the TX, RX coils are situated in parallel planes and their centers are displaced by a distance Δ.

2. *Angular Misalignment* - In the angular misalignment case Fig. 3.11, the plane of the RX coil is tilted to form an angle γ and the axis of one coil passes through the center of the other coil.

A general misalignment case which incorporates both a lateral and angular displacement of the RX coil is not considered in this thesis. This decision is supported by the fact that there is no

FACTORS	SYMBOL
Transmitter (TX), Receiver (RX) Coils	C_{TX}, C_{RX}
TX Circular/Square Coil Radius/Length	a [m]
RX Circular/Square Coil Radius/Length	b [m]
TX Circular Spiral	$a_1 \cdots a_n$
RX Circular Spiral	$b_1 \cdots b_k$
TX Square Spiral	$a_1 \cdots a_n$
RX Square Spiral	$b_1 \cdots b_k$
TX, RX Number of Turns	N_{TX}, N_{RX}
Transmitter Excitation Current	I_{TX} [A]
Coil Vertical Separation Distance	D [m]
Lateral Misalignment Distance	Δ [m]
Angular Misalignment Angle	γ [degrees]
Series Ohmic Losses in the TX Coil	R_{TX}[Ohm]
Series Ohmic Losses in the RX Coil	R_{RX}[Ohm]
Transmitter Input Power	P_{TX} [Watt]
Receiver Power dissipated at the Load	P_{RX} [Watt]
Complete Elliptic Integral of the First Kind	$K(m)$
Complete Elliptic Integral of the Second Kind	$E(m)$
Modulus of Elliptic Integrals K, E	m
Magnetic Permeability of Free-Space	$\mu_o = 4\pi 10^{-7}$ [H/m]
Magnetic Permeability of Core Material	μ_r
Resonant Frequency	$\omega = 2\pi f$ [rad/s]
magnetic Field Strength at the RX coil	H_z [A/m]

Table 3.1: *Coil and Configuration Parameters.*

strong interaction between the two misalignment effects as demonstrated by Soma in [44]. At small lateral misalignments the angular effect dominates and at large lateral misalignments the lateral effect prevails. Hence, the two displacement configurations can be studied independently which is advantageous from an optimisation point of view. In this manner, separate upper bounds for the maximum permissible angular and lateral displacements can be set according to the specified application.

3.5.1 Lateral misalignment

In the lateral misalignment case we can neglect the x and y components of the magnetic field vector since they are parallel to the RX plane and do not contribute to the flux lines cutting through the RX coil. The expression for the magnetic field as a function of misalignment distance, Δ, of the RX coil from a stationary TX coil can be obtained by computing the magnetic field strength at the center of the RX coil as shown in Fig. 3.10(a) and Fig. 3.10(b) for the circular and square geometries respectively.

First, the circular coil geometry is considered, and the magnetic field at the center of the RX coil is evaluated by Biot-Savart law as expressed in equation (3.2). The main difference from the coaxial case is the definition of the vector components $d\boldsymbol{\ell}$ and $\mathbf{r}$ in Biot-Savart law. Referring to Fig. 3.10(a), the vector $\mathbf{r}$ can be derived from the vectorial subtraction of $\mathbf{O_1A}$ from $\mathbf{O_1O_2}$, which yields:

$$\mathbf{r} = (a\sin\phi)\,\mathbf{x} + (\Delta - a\cos\phi)\,\mathbf{y} + D\mathbf{z} \tag{3.61}$$

and the magnitude of the vector $\mathbf{r}$ is defined as:

$$r = \sqrt{a^2 + \Delta^2 + D^2 - 2a\Delta\cos\phi} \tag{3.62}$$

In this case, the vector $d\boldsymbol{\ell}$ can be evaluated as follows:

$$d\boldsymbol{\ell} = -\,(a\cos\phi\,d\phi)\,\mathbf{x} - (a\sin\phi\,d\phi)\,\mathbf{y} \tag{3.63}$$

Then the cross product $\mathrm{d}\ell \times \mathbf{r}$ is expressed as:

$$d\boldsymbol{\ell} \times \mathbf{r} = \begin{vmatrix} \mathbf{x} & \mathbf{y} & \mathbf{z} \\ -a\cos\phi\,d\phi & -a\sin\phi\,d\phi & 0 \\ a\sin\phi & \Delta - a\cos\phi & D \end{vmatrix} \tag{3.64}$$

Manipulating the determinant in (3.64) provides the numerator at (3.2):

$$d\boldsymbol{\ell} \times \mathbf{r} = -\left(aD\sin\phi\, d\phi\right)\mathbf{x} - \left(aD\cos\phi\, d\phi\right)\mathbf{y} + \left[\left(a^2 - a\Delta\cos\phi\right) d\phi\right]\mathbf{z} \tag{3.65}$$

Consequently, the field components can be defined as:

$$H_x = \frac{I}{4\pi}\int_0^{2\pi} \frac{-aD\sin\phi}{\left(a^2+\Delta^2+D^2-2a\Delta\cos\phi\right)^{3/2}}\, d\phi \tag{3.66a}$$

$$H_y = \frac{I}{4\pi}\int_0^{2\pi} \frac{-aD\cos\phi}{\left(a^2+\Delta^2+D^2-2a\Delta\cos\phi\right)^{3/2}}\, d\phi \tag{3.66b}$$

$$H_z = \frac{I}{4\pi}\int_0^{2\pi} \frac{a^2-a\Delta\cos\phi}{\left(a^2+\Delta^2+D^2-2a\Delta\cos\phi\right)^{3/2}}\, d\phi \tag{3.66c}$$

It is evident from the geometry depicted in Fig. 3.10(a) that the H_z component dominates as it is the only component which vertically intersects the plane of the RX coil and can be recognized as a standard elliptic integral. A solution for an integral of this form is available by Good, [134] and in the extensive collection of elliptic integrals and special functions compiled by Byrd and Friedman in [135]. A close investigation of (3.66) reveals that the z - component of the magnetic field intensity at the center of the circular misaligned RX coil, involves the following integral expressions:

$$\int_0^{\pi} \frac{1}{\left(c\pm\cos\phi\right)^{3/2}}\, d\phi = \frac{m}{2-2m}\sqrt{2m}E \tag{3.67a}$$

$$\int_0^{\pi} \frac{\pm\cos\phi}{\left(c\pm\cos\phi\right)^{3/2}}\, d\phi = \sqrt{2m}K(m) - \frac{2-m}{2-2m}\sqrt{2m}E(m) \tag{3.67b}$$

where the functions $K(m)$ and $E(m)$ are the complete elliptic integrals of the first and second kind respectively, defined in appendix B, and m is the modulus of K and E expressed as:

$$m = \frac{2}{1+c}, \quad 0 < m < 1 \tag{3.68}$$

One can then identify that H_z in (3.66) involves the expressions given in (3.67a), (3.67b) above. Hence, H_z can be written as:

$$H_z = \frac{I\cdot a}{2\pi}\left\{\int_0^{\pi} \frac{a\, d\phi}{\left[\left(D^2+\Delta^2+a^2\right)-2a\Delta\cos\phi\right]^{3/2}} + \int_0^{\pi} \frac{-\Delta\cos\phi\, d\phi}{\left[\left(D^2+\Delta^2+a^2\right)-2a\Delta\cos\phi\right]^{3/2}}\right\} \Rightarrow \tag{3.69}$$

$$H_z = \frac{I\cdot a}{2\pi\left(2a\Delta\right)^{3/2}}\left[a\cdot\left(\frac{m}{2-2m}\sqrt{2m}E\right) + \Delta\cdot\left(\sqrt{2m}K - \frac{2-m}{2-2m}\sqrt{2m}E\right)\right] \tag{3.70}$$

An algebraic manipulation of the previous expression reveals that the z-component of the magnetic field intensity at the center of the RX coil can be expressed in terms of the lateral misalignment distance Δ as:

$$H_z = \frac{I}{2\pi\Delta}\left(\frac{m}{4a\Delta}\right)^{1/2}\left(\Delta K + \frac{am-(2-m)\cdot\Delta}{2-2m}\cdot E\right) \tag{3.71}$$

where Δ is the lateral misalignment on the y-axis and m is the modulus of the elliptic integrals expressed as:

$$m = \left[\frac{4a\Delta}{(a+\Delta)^2+D^2}\right] \tag{3.72}$$

It should be noted that due to the circular symmetry of the TX coil, expression (3.71) can equally well describe the variation of the magnetic field intensity due to a RX coil translation anywhere on the x-y plane, with Δ being essentially a radial displacement from the center of the TX coil. Interestingly, expression (3.71) is derived by Smythe in [52] by adopting the more complicated approach of the magnetic vector potential.

Of course, it is evident that expression (3.71) describes the magnetic field generated by a single circular loop TX coil. Therefore, the z-component of the magnetic field generated by short solenoids and circular spiral TX coils can be evaluated by superimposing the contributions of the individual loops that constitute these more complex TX geometries. Consequently, the z-component of the radial magnetic field produced by a short solenoid TX coil of N-turns is given by:

$$H_z = \frac{I\cdot N}{2\pi\Delta}\left(\frac{m}{4a\Delta}\right)^{1/2}\left(\Delta K + \frac{am-(2-m)\cdot\Delta}{2-2m}\cdot E\right) \tag{3.73}$$

where the modulus m of the elliptic integrals can be expressed by equation (3.72).

Finally, for a circular spiral TX coil the z-component of the magnetic field at the center of a radially displaced RX coil can be derived in a similar manner to the coaxial orientation demonstrated in section 3.4.2. Therefore, the z component for the magnetic field generated by a circular spiral TX coil, H_z, is expressed as:

$$H_z = \frac{I}{2\pi\Delta}\sum_{i=1}^{n}\left(\frac{m_i}{4a_i\Delta}\right)^{1/2}\left(\Delta K + \frac{a_i m_i-(2-m_i)\cdot\Delta}{2-2m_i}\cdot E\right) \tag{3.74}$$

In this case the modulus of the elliptic integrals K and E varies for each concentric loop. Hence, it is more appropriate to define m_i as follows:

$$m_i = \left[\frac{4a_i\Delta}{(a_i+\Delta)^2+D^2}\right] \tag{3.75}$$

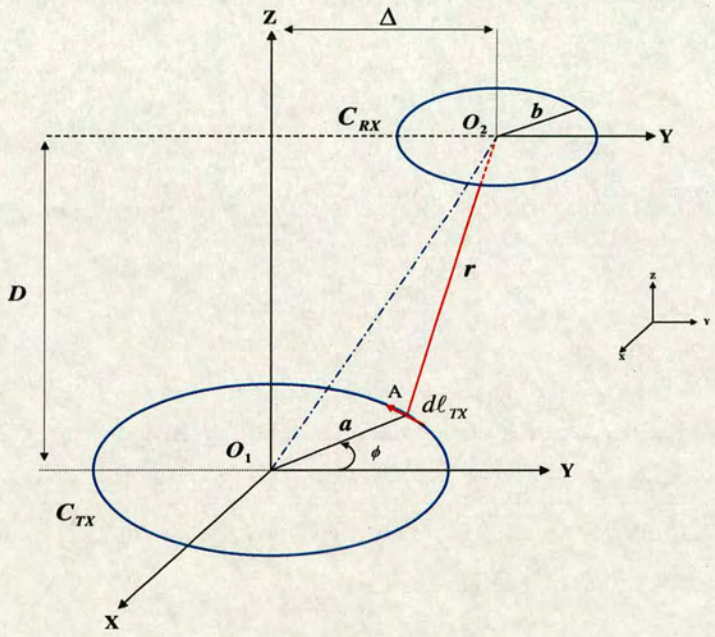

(a) Circular geometry representing the solenoid and the circular spiral coils

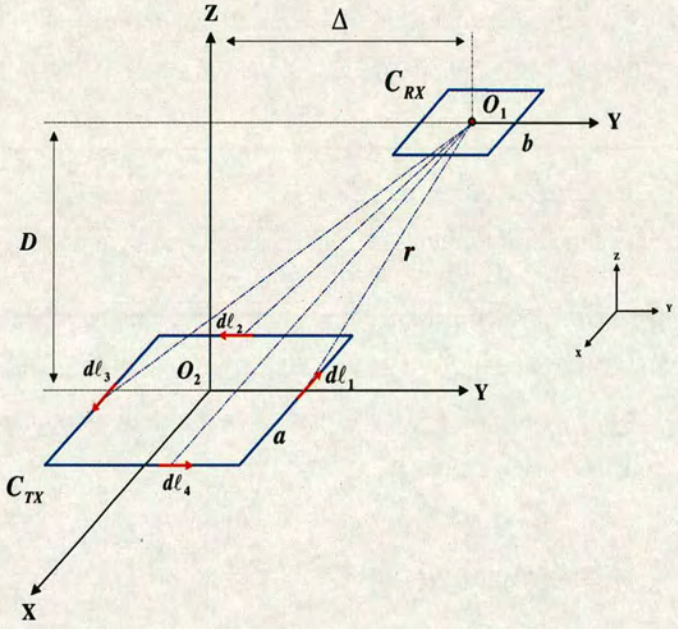

(b) Square geometry representing the square spiral coils

Figure 3.10: *Lateral Misalignment Configuration of the TX, RX Coils.*

where a_i is the radius of each concentric loop.

Revisiting the square coil geometry, it is clear that equation (3.57) is adequate to express the z-component of the magnetic field denoted H_z, generated from a square spiral TX coil at any point situated on the x-y plane and at a distance z from the level of the TX spiral. Clearly, for a laterally misaligned RX coil as indicated in Fig. 3.10(b), the z-component of the magnetic field can be expressed at the center of the RX coil by (3.57). In this expression, (3.57), the constants x and y represent the lateral displacement of the center of the RX coil on the x-axis and y-axis respectively and z is the separation distance of the TX, RX coils. The square spiral TX coil is thought to be stationary with the center of the structure located at the origin of a Cartesian coordinate system (x, y, z) as shown in Fig. 3.10(b).

At this point it is important to stress that symmetry is also relevant for the square spiral structure. Ultimately it is possible to take advantage of this and predict the magnetic field intensity at the vicinity of the RX when it is laterally misaligned either on the x or y axis. Due to the square geometry, a translation on the x-axis is identical to a translation on the y-axis. Therefore, this significantly simplifies the computation of expression (3.57) and the variation of the magnetic field strength on the x-axis can be mirrored to reflect the trend on the y-axis.

3.5.2 Angular misalignment

The 3-D problem of a tilted RX coil of an arbitrary shape above a stationary TX coil is shown in Fig. 3.11(a) and Fig. 3.11(b) for circular and rectangular TX geometries respectively. The main challenge is to compute the magnetic field strength at the region of the tilted RX coil, which is defined by the shape of the TX coil. The basic loop configuration depicted in Fig. 3.11 can be employed in order to compute the magnetic field generated by a short-solenoid, circular and square spiral coils, by employing the principle of superposition addressed earlier for each coil geometry. The z-axis of a Cartesian coordinate system lies along the centerline of the TX coil, as indicated in the diagrams of Fig. 3.11, and the $x - y$ plane where $z = 0$ coincides with the conductor surface. In this case, the calculation of the magnetic field can be significantly accelerated by the use of Biot-Savart law and the coordinate transformations that account for the tilt, [136]. Although this approach seems to be appropriate for more complex coil geometries and a TX coil rotation, it is not necessary for the configuration depicted in Fig. 3.11. Bearing in mind the applications considered in this work, a small RX coil is assumed which supports the condition of a uniform field distribution over the surface of the RX. Subsequently, this

allows the reference point for the field calculation to be located at the center of the RX coil. At the center of the RX coil the circular symmetry reduces dramatically the computational effort required.

In the angular misalignment case, depicted in Fig. 3.11, the x and y components of the magnetic field vector cancel out due to the circular and square symmetry at the center of the RX coil. Consequently, the z-component of the magnetic field dominates and it will be solely considered hereinafter.

However, as the coil is tilted by an angle γ, the component of the field which is vertical to the plane of the tilted coil, denoted here as ($H_{z\,AM}$), can be determined by the dot product of the unit vector ($\mathbf{n}$) vertical to the plane of the rotated coil and the z magnetic field vector component, given by $H_{\mathbf{z}}$, at the center of the RX prior to the rotational displacement. As the RX coil is rotated with respect to the x-axis, the unit vector $\mathbf{n}$ is defined as $\mathbf{n} = (0, \sin\gamma, \cos\gamma)$. Angle γ defines the degree of angular misalignment and is positive for a clockwise rotation and negative for an anticlockwise rotation. Therefore, the component of the magnetic field vertical to the RX that produces flux through the RX is given as follows:

$$H_{z\,AM} = \mathbf{n} \cdot H_{\mathbf{z}} \tag{3.76}$$

It should be stated at this point that, due to symmetry, a rotation about the x-axis is equivalent to a rotation about the y-axis for a RX coil located vertically above the TX coil as illustrated in Fig. 3.11. Based on the previous discussion, the magnetic field expressions derived earlier for short-solenoid, circular and square spirals can be now extended to account for the rotation by multiplying (3.15), (3.17) and (3.57) with a rotational misalignment factor $\cos\gamma$.

3.6 Power Transfer Expressions

In inductive links coil misalignments drastically reduce the coupling factor, hence the purpose of the analytical model presented in this thesis is to predict accurately the impact of geometrical parameters on the link efficiency. Coil dimensions and shape substantially affect the magnitude of the magnetic field in the inductive near-field as shown in sections 3.4.1, 3.4.2 and 3.4.3 for coils of circular and square geometries. Since the magnitude of the magnetic field is closely related to the efficiency of the inductive link, it is critical to identify a coil structure that maximises the coupling between the TX and the RX. The contribution of this section is the introduction of

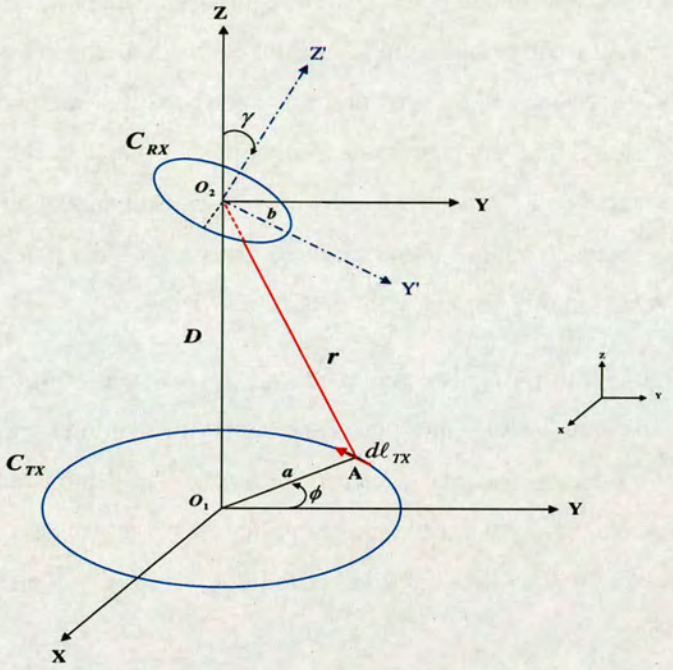

(a) Circular geometry representing the solenoid and the circular spiral coils

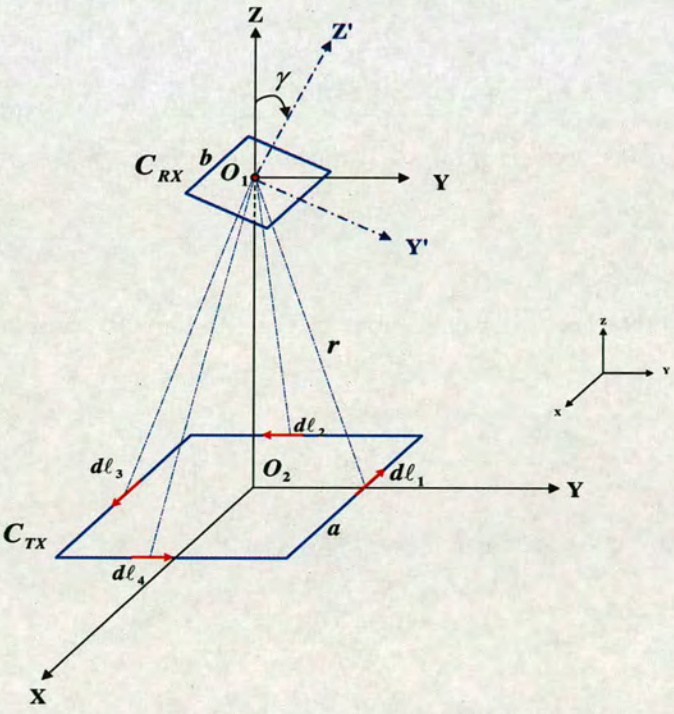

(b) Square geometry representing the square spiral coils

Figure 3.11: *Angular Misalignment Configuration of the TX, RX Coils.*

a set of novel power transfer functions incorporating misalignment of the RF coils, for circular and square structures, currently popular in RFID and embedded sensor technologies. The expressions for the power transfer introduced in this section constitute a powerful design tool for inductive RF links. Based on the power transfer functions presented in this chapter it is possible to predict the effect of coil characteristics, position and misalignment on the coupling factor and develop a link efficiency optimisation technique. In chapter 5 the potential applicability of the modelling suggested in this chapter will be discussed in detail.

A general equivalent circuit for a poorly coupled system is shown in Fig. 3.12. Adopting this approach significantly simplifies the analysis of the transformer action for the applications considered in this thesis, since the mutual inductance is very small as demonstrated in section 2.9.1. Therefore, it is possible to derive a formula expressing the power transfer from transmitter to receiver in an inductive link as illustrated in section 2.4. This methodology is revisited here with reference to Fig. 3.12.

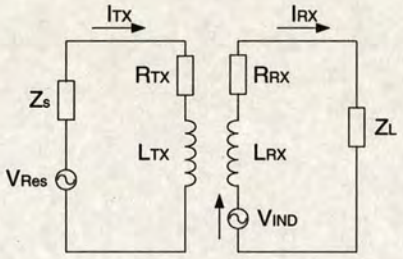

Figure 3.12: *Equivalent circuit of a loosely coupled transformer representing an inductively coupled RF link.*

Initially, the transmitter and receiver sections of Fig. 3.12 are assumed to be resonating at a common frequency where:

$$Z_s = \frac{1}{j\omega C_{TX}}, \quad \text{and} \quad C_{TX} = \frac{1}{4\pi^2 f^2 L_{TX}} \tag{3.77}$$

Under these conditions the real input power, P_{TX}, can be expressed as:

$$P_{TX} = I_{TX}^2 \cdot R_{TX} \tag{3.78}$$

where R_{TX} represents the ohmic losses of the transmitter coil.

On the receiver side the load impedance denoted Z_L in Fig. 3.12, should be conjugately matched to the impedance of the RX coil to achieve maximum power transfer. Therefore,

the available real power from the TX that is delivered to the load, denoted P_{RX}, is given as follows:

$$P_{RX} = \frac{V_{IND}^2}{Real(Z_L)} \tag{3.79}$$

The current I_{TX} circulating in the TX coil produces a magnetic field **H**. Assuming a relatively uniform magnetic field over the area of the small effective area of the receiver coil, then the voltage induced across the RX coil is given by Faraday's law:

$$V_{IND} = -\int_s \frac{\partial \mathbf{B}}{\partial t} \cdot d\mathbf{s} \tag{3.80}$$

where the magnetic field vector is related to the magnetic flux density by the equation $\mathbf{B} = \mu \cdot \mathbf{H}$. According to (3.80) the total induced emf at the receiver coil is equal to the normal component of the rate of change of the flux density **B** integrated over the surface bounded by the RX coil. An alternative representation of (3.80) can be written as:

$$V_{IND} = \mu_o A \cdot j\omega H_z \tag{3.81}$$

where A is the effective area of the loop and H_z is the z-component of the magnetic field which is normal to the plane of the RX coil. Equation (3.81) relates to the time harmonic case in which $e^{j\omega t}$ is the implicit time factor ($\partial/\partial t \equiv j\omega$). It is possible to express the induced voltage at a receiver coil irrespective of its geometry by applying formula (3.81) and substituting for the effective area of the coil's geometry in place of A. This is demonstrated in equations (3.16), (3.18) and (3.60) for a short-solenoid coil, circular and square spiral coils respectively. In addition, the expression for the magnetic field component normal to the plane of the RX coil represented by H_z in (3.81) has been derived for the three main TX geometries studied in this thesis by evaluating Biot-Savart law for the short solenoid, circular and square spirals. By substituting for the magnetic field as given by Biot-Savart law for each TX geometry in (3.81), the induced open circuit voltage at the RX coil can by expressed in terms of the real input power at the TX side, according to equation (3.78). Hence, substituting for V_{IND} and I_{TX} in (3.79) for the received power across the inductive link and rearranging yields a power transfer function expressed as a ratio of the received power over the real input power at the TX coil as $(\frac{P_{RX}}{P_{TX}})$. This can be better demonstrated by the following ratio:

$$\frac{P_{RX}}{P_{TX}} = \frac{\mu_o^2 \, A_{RX}^2 \, \omega^2}{4 \, R_{RX} \, R_{TX} \, I_{TX}^2} \, H_z^2 \tag{3.82}$$

It should be noted that the majority of the factors in expression (3.82) depend on the geometry of the TX and RX coils except from the resonant frequency ω and the current I_{TX} circulating

in the TX coil. The parameters involved in the expressions introduced in the following section are listed in Table 3.1.

3.6.1 Power transfer for coils in perfect alignment

The power transfer functions developed in this section provide insight to the design of inductively coupled embedded sensor systems with respect to a number of important parameters for design engineers. Among these are the implantation depth and operational range distance, frequency and losses of the TX and RX coils as well as size and shape of the coils and of course misalignment conditions mostly overlooked until now. The mutual inductance and the coupling factor are always small over the range of operation and the coil dimensions suitable for the aimed applications. Hence, it is possible to simplify the problem and converge to analytical expressions for the power transfer ratio. This will enable the designer to evaluate the dependence of the power transfered on the various application parameters. Continuing from expression (3.82) this section presents the power transfer functions for two coaxial coils.

Short solenoid, TX, RX coils

The simplest scenario of two coaxial solenoid coils is considered fist. Starting from the general expression (3.82) and substituting for the magnetic field H_z generated by a short solenoid TX coil, as given by (3.15), yields the following equation:

$$\frac{P_{RX}}{P_{TX}} = \frac{\mu_o^2\,\pi^2\,N_{TX}^2\,N_{RX}^2\,a^4\,b^4\omega^2}{16R_{TX}\,R_{RX}\,\left(a^2+D^2\right)^3} \tag{3.83}$$

Circular spiral, TX, RX coils

In a similar manner, for the perfect alignment configuration the power transfer function describing the coupling between reader and tag circular spiral coils is given by:

$$\frac{P_{RX}}{P_{TX}} = \frac{{\mu_o}^2\,\pi^2\,\omega^2}{16\,R_{TX}\,R_{RX}} \cdot \left(\sum_{i=1}^{n} \frac{{a_i}^2}{\left(\sqrt{{a_i}^2+D^2}\right)^3}\right)^2 \cdot \left(\sum_{j=1}^{\kappa} b_j^2\right)^2 \tag{3.84}$$

In this case the dominant magnetic field component H_z, in the general power ratio expression (3.82), is evaluated for the circular spiral TX coil geometry by equation (3.17).

Square Spiral, TX, RX coils

Finally, the square spiral coil structure is considered, where the magnetic field component H_z

in (3.82) is evaluated by expression (3.57). Substituting for H_z in (3.82) and rearranging yields the power transfer function for a set of loosely coupled square spiral coils:

$$\frac{P_{RX}}{P_{TX}} = \frac{\mu_o^2\,\omega^2\,A_{RX}^2}{64\,\pi^2\,R_{TX}\,R_{RX}} \cdot \left\{ \sum_{i=1}^{n} \frac{2a_i^2}{\left(\frac{a^2}{4} + D^2\right)\sqrt{\frac{a^2}{2} + D^2}} \right\}^2 \tag{3.85}$$

where A is the effective area of the square spiral RX coil expressed as:

$$A = \frac{1}{3}\,s^2 N(N-1)(2N-1) + \frac{d_{in}^2}{2}\,N + d_{in}\,s\,N(N-1) \tag{3.86}$$

3.6.2 Power transfer for coils laterally displaced

This section presents the power transfer functions, for each coil geometry, in the lateral misalignment configuration. The magnetic field in the lateral configuration is discussed in section 3.5.1.

The same principle applies when the coils are lateral misaligned. Three expressions are derived for each coil geometry by substituting for the magnetic field H_z in (3.82). The magnetic field component H_z strength at the center of the RX coil varies for each geometry studied and it also depends on the position of the RX with respect to the TX coil. The configurations studied are illustrated in Fig. 3.10 and Fig. 3.11.

Short solenoid, TX, RX coils

For the sort-solenoid coils in the lateral misalignment case, H_z is computed by (3.73) and the power transfer function becomes:

$$\frac{P_{RX}}{P_{TX}} = \frac{\mu_o^2\,N_{TX}^2\,N_{RX}^2\,b^4\,\omega^2\,m}{64\,a\,R_{TX}\,R_{RX}\Delta^3} \cdot \left(\Delta K + \frac{am - (2-m)\cdot\Delta}{2-2m} \cdot E\right)^2 \tag{3.87}$$

Circular spiral, TX, RX coils

For circular spiral coils laterally misaligned, H_z is computed by expression (3.74) and the power transfer function becomes:

$$\frac{P_{RX}}{P_{TX}} = \frac{\mu_o^2 \cdot \omega^2}{16\,R_{RX}\,R_{TX}\,\Delta^2} \cdot \left[\sum_{i=1}^{n} \left(\frac{m_i}{(2\,a_i\Delta)}\right)^{1/2} \cdot \left(\Delta\,K + \frac{a_i\,m - (2-m_i)\Delta}{2-2\,m_i} \cdot E\right)\right]^2 \left(\sum_{j=1}^{\kappa} b_j^2\right)^2 \tag{3.88}$$

where m_i represents the modulus of the elliptic integral and is given by equation (3.75).

Square Spiral, TX, RX coils

Finally, for the square spiral coils the magnetic field at the RX coil is computed by expression (3.57), where x and y represent the lateral displacement of the RX from the center of the TX coil across the x and y-axis respectively:

$$\begin{aligned}\frac{P_{RX}}{P_{TX}} = \frac{\mu_o^2 A_{RX}^2 \omega^2}{64\,\pi^2\,R_{TX}\,R_{RX}} \Bigg(\sum_{i=1}^{n} \Bigg\{ & \frac{-\left(\Delta_y - \frac{a_i}{2}\right)}{\left(\Delta_y - \frac{a_i}{2}\right)^2 + D^2} \Bigg[\frac{\frac{a_i}{2} + \Delta_x}{\sqrt{\left(\frac{a_i}{2} + \Delta_x\right)^2 + \left(\Delta_y - \frac{a_i}{2}\right)^2 + D^2}} \\ & + \frac{\frac{a_i}{2} - \Delta_x}{\sqrt{\left(\frac{a_i}{2} - \Delta_x\right)^2 + \left(\Delta_y - \frac{a_i}{2}\right)^2 + D^2}} \Bigg] \\ & + \frac{\left(\frac{a_i}{2} + \Delta_x\right)}{\left(\Delta_x + \frac{a_i}{2}\right)^2 + D^2} \Bigg[\frac{\frac{a_i}{2} + \Delta_y}{\sqrt{\left(\frac{a_i}{2} + \Delta_y\right)^2 + \left(\Delta_x + \frac{a_i}{2}\right)^2 + D^2}} \\ & + \frac{\frac{a_i}{2} - \Delta_y}{\sqrt{\left(\frac{a_i}{2} - \Delta_y\right)^2 + \left(\Delta_x + \frac{a_i}{2}\right)^2 + D^2}} \Bigg] \\ & + \frac{\left(\Delta_y + \frac{a_i}{2}\right)}{\left(\Delta_y + \frac{a_i}{2}\right)^2 + D^2} \Bigg[\frac{\frac{a_i}{2} - \Delta_x}{\sqrt{\left(\frac{a_i}{2} - \Delta_x\right)^2 + \left(\Delta_y + \frac{a_i}{2}\right)^2 + D^2}} \\ & + \frac{\frac{a_i}{2} + \Delta_x}{\sqrt{\left(\frac{a_i}{2} + \Delta_x\right)^2 + \left(\Delta_y + \frac{a_i}{2}\right)^2 + D^2}} \Bigg] \\ & - \frac{\left(\Delta_x - \frac{a_i}{2}\right)}{\left(\Delta_x - \frac{a_i}{2}\right)^2 + D^2} \Bigg[\frac{\frac{a_i}{2} - \Delta_y}{\sqrt{\left(\frac{a_i}{2} - \Delta_y\right)^2 + \left(\Delta_x - \frac{a_i}{2}\right)^2 + D^2}} \\ & + \frac{\frac{a_i}{2} + \Delta_y}{\sqrt{\left(\frac{a_i}{2} + \Delta_y\right)^2 + \left(\Delta_x - \frac{a_i}{2}\right)^2 + D^2}} \Bigg] \Bigg\} \Bigg)^2 \end{aligned} \tag{3.89}$$

3.6.3 Power transfer for tilted coils

This section presents the power transfer functions, for each coil geometry, in the angular misalignment configuration as discussed in section 3.5.2.

Short solenoid, TX, RX coils

It is evident from section (3.5.2), that in the angular misalignment the magnetic field component H_z should be modified to account for the angular tilt of the RX coil based on expression (3.76). Thus, the power transfer function for the solenoid coils in the angular misalignment

case becomes:

$$\frac{P_{RX}}{P_{TX}} = \frac{\mu_o^2\, N_{RX}^2\, N_{TX}^2\, \omega^2\, b^4\, a^4\, \pi^2\, \cos\gamma^2}{16 R_{TX}\, R_{RX}\, (a^2 + D^2)^3} \tag{3.90}$$

Circular spiral, TX, RX coils

In a similar manner, for the circular spiral structures the efficiency of the link is given by the following expression:

$$\frac{P_{RX}}{P_{TX}} = \frac{\mu_o^2\, \omega^2\, \pi^2\, I_{TX}^2}{16 R_{RX} R_{TX}} \left(\sum_{i=1}^{n} \frac{a_i\, \pi\, \cos\gamma^2}{\sqrt{a_i^2 + D^2}} \right)^2 \cdot \left(\sum_{j=1}^{\kappa} b_j^2 \right)^2 \tag{3.91}$$

Square Spiral, TX, RX coils

Last, for the square structure the efficiency of the inductive link comprising of two square spiral coils is expressed by the following equation:

$$\frac{P_{RX}}{P_{TX}} = \frac{\mu_o\, \omega^2\, A^2\, \cos\gamma^2}{16\, \pi^2\, R_{TX}\, R_{RX}} \cdot \left\{ \sum_{i=1}^{n} \frac{2 a_i^2}{\left(\frac{a^2}{4} + D^2\right) \sqrt{\frac{a^2}{2} + D^2}} \right\}^2 \tag{3.92}$$

It should be noted that in the angular misalignment case only a tilt angle is considered. Hence, the x and y components in (3.57) are equated to zero, and the remaining expression is modified according to (3.76).

3.7 Ferrite Cored RX Coils and Power Efficiency.

The analysis presented in this chapter is not limited to air-cored coils. The analytical expressions for the energy transfer across an inductive link introduced in section 3.6, can be extended to account for the effect of a ferromagnetic core in the RX coil.

Magnetic cores are extensively used to augment the effective area of the RX coil and concentrate the magnetic flux in its vicinity, essentially creating a much more sensitive coil. The ferrite material enhances the performance of the winding, thus reducing the dimensions of the coil. Ferrite antennas are readily employed in communication applications to reinforce signal strength. In the last few years ferrite cores are increasingly being used in inductively coupled systems such as RFID and sensors. In particular the use of ferrite materials is advantageous in spacially selective antennas for very close proximity HF RFID applications and on transponders mounted on metallic surfaces. In biomedical applications optimised planar microcoils with

magnetic layers for energy transfer in telemetric systems are becoming more common. This type of coil offers significant advantages due to the reduction in the size without compromising the efficiency of the link, [137].

Currently there is a variety of ferrite materials and shapes that target applications such as embedded sensors as opposed to the more traditional power electronic uses of ferrites. The theory of cylindrical ferrite cores is well known in literature, (see Snelling [54], [138]). Although the following treatment is based on the use of cylindrical cores it applies in principle to cores of any cross section. Referring to Fig. 3.13 when a magnetic field is applied to a soft magnetic material, the resulting flux density is composed of that of free space plus the contribution of the aligned domains such as:

$$\mathbf{B} = \mu_o \mathbf{H} + \mathbf{J} \quad \text{or} \quad \mathbf{B} = \mu_o(\mathbf{H} + \mathbf{M}) \tag{3.93}$$

The total flux density in the solenoid is given by (3.93) where **J** is the magnetic polarization or intrinsic magnetic flux density.

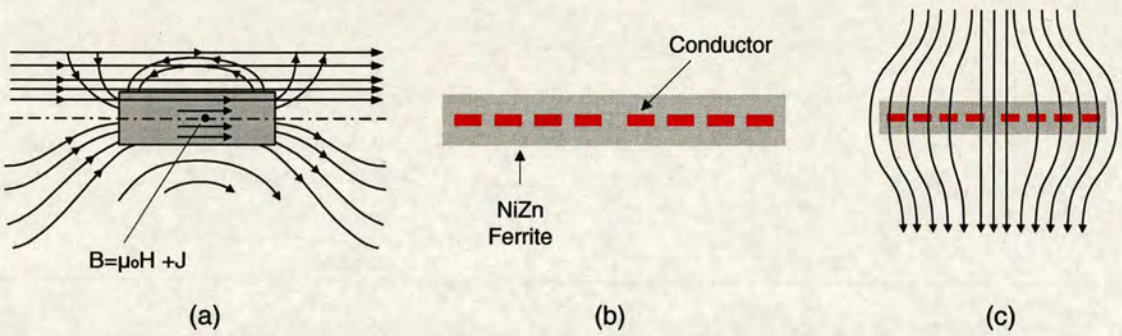

Figure 3.13: *(a) A short ferromagnetic cylinder immersed in uniform magnetic field: upper half of the diagram shows component fields; lower shows resultant field, (b) cross sectional view of planar inductor integrated in ferromagnetic material, (c) planar coil integrated in a disk of magnetic material placed in a homogeneous magnetic field.*

Initially a short circular winding of N-turns representing a short-solenoid coil enclosing an effective area A_N is considered. In the presence of a uniform alternating magnetic field where the axis of the winding is parallel to the field strength vector H an e.m.f. (V_{IND}) is induced in it, expressed by the induction equation:

$$V_{IND} = \mu_o \, \omega \, H \, A_N \, N \tag{3.94}$$

Incorporating a ferrite core into the aperture of the winding in the form of a long ferrite cylinder coaxial with the winding and having its center coinciding with the center of the winding the flux

density at the center of the winding will be increased by a factor μ_{core}. If the cross sectional area of the ferrite core is A_{core} then the total flux linking the winding is given by $\mu_o \mu_{core} HAN$ and neglecting any flux that passes through any area difference between A and A_{core}, as shown by Snelling and Pettengill in [54, 83]. The resultant field distribution due to the presence of the field is depicted in Fig. 3.13(a). Withing the ferrite rod the magnetic flux distribution varies from a maximum in the center to a minimum at the ends. In the case of a short solenoid coil in a coaxial arrangement to the ferrite core, immersed in a uniform external field, a uniform flux can be assumed throughout the entire length of the coil. Consequently, the induced voltage in a ferrite cored short-solenoid receiver coil is given by the following expression:

$$V_{IND} = \mu_o \mu_{core}\, \omega\, H\, A\, N \tag{3.95}$$

Usually a longer ferrite core is employed to ensure uniform flux density along the length of the solenoid. For longer solenoids an empirical averaging factor F_A is used to describe the variation of the field along the axis of the coil as discussed in [57], [54].

In conjunction to short-solenoid coils, planar inductors are often used in implanted sensors, [139]. The challenge in the design of planar inductors is to reduce the size of structure and at the same time achieve a high enough inductance to operate the coil at the HF range. A solution to this problem is to embed the planar inductor into a magnetic material disk as shown in Fig. 3.13(b), [140], [141]. The behaviour of a planar microcoil in a magnetic disk placed in a homogenous magnetic field is illustrated in Fig. 3.13(c). The field lines are now displaced due to the demagnetization factor of the disk. The value of the demagnetization factor N depends on the geometry of the core and to a lesser extent on the permeability. The flux density varies along the length of the ferrite core immersed in a uniform magnetic field according to a dimensional ratio m defined as $Length/diameter$ of the core. According to Snelling in [54], as $m \rightarrow 0$ the flux density will become uniform along the axis. Therefore, for a short circular ferrite disk enclosing a RX planar coil and situated inside the uniform magnetic field region generated by a resonant TX coil the open circuit e.m.f. induced across the RX coil can be expressed by equations (3.18), (3.60) multiplied by the magnetic permeability of the ferrite disk, μ_{core}.

3.8 The Influence of Conductive Media

In inductive coupled embedded devices the effect of the RF magnetic field penetration in tissue has a direct consequence on the power transfer efficiency of the link. The power attenuation in

implanted devices has been discussed in detail in section 2.10 where an approach for quantifying this effect is proposed based on the attenuation constant principle.

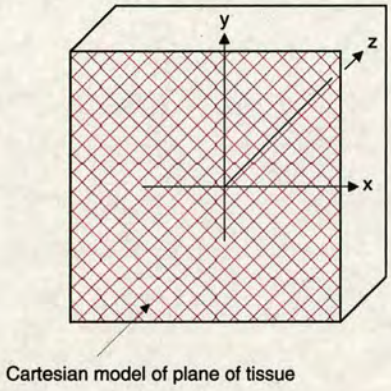

Figure 3.14: *Cartesian coordinate system used in the semi-infinite planar model.*

A complete analytical description of power attenuation due to the presence of conductive tissue between the TX and the RX is a very difficult task. It can be argued that it is not possible to converge to a general model for implanted devices due to the wide range of applications associated with embedded devices. Each implementation involves unique parameters and a complete mathematical treatment becomes quickly too convoluted to be easily incorporated in the power transfer functions developed earlier in this chapter. Therefore, a general mathematical conduct of the RF field in biological media can be extremely complicated. This is attributed to the fact that the quasi-static approximation cannot be assumed as the frequency increases, and Maxwell's wave equation must be employed. In addition, the geometry of the biological specimen can be very irregular, and electromagnetic properties of tissues heterogeneous. Hence, a simple but accurate solution, easily tractable for design optimisation purposes, asks for a set of clear and specific boundaries to the problem. This can be achieved by limiting the analytical solution to the HF passive RFID domain frequency range which does not exceed 30MHz according to [46]. Clearly, this implies that for the electrically small RX coils employed in these frequencies in near-field conditions the magneto-static approximation can be applied. In other words, there is no radiative contribution to the power attenuation of the RF field and the magnetic field can be studied independently of the electric field. The electrical properties of biological tissue linked with induction effects are the conductivity, σ, and the dielectric constant, ϵ, of the medium. For all practical purposes the permeability μ can be considered equal to that of free space. The attenuation and phase constant α and β given in (2.95a) and (2.95b) respectively, are determined by the frequency and the material constants of the medium. In the

limit of HF passive RFID frequencies and for the material characteristics of biological tissues illustrated in Table 2.3 and Table 2.4, $\omega\epsilon_r\epsilon_o << \sigma$. Subsequently, the conduction currents greatly predominate over the displacement currents, [53].

Initially, the RX coil is considered to be an electrically small coil with dimensions significantly smaller than a TX antenna for the loosely coupled approximation to be valid. Hence, a small volume of tissue surrounding the RX coil is considered in the current approach. Therefore, it is now possible to assume a linear, homogeneous and isotropic medium in which the RX coil is embedded. The uniform magnetic flux density generated by the resonant TX coil must satisfy the wave equation, as given by Bottomley et al. [99]:

$$\nabla^2\mathbf{B} - \epsilon\mu\frac{\partial^2\mathbf{B}}{\partial t^2} - \frac{\mu\partial\mathbf{B}}{\rho\partial t} = 0 \tag{3.96}$$

where ϵ is the permittivity, μ is the permeability and ρ the resistivity of the medium. The solution to equation (3.96) which describes the behaviour of a sinusoidal time-varying magnetic induction field in a plane of conducting material is the same as that which describes the propagation of plane electromagnetic waves in conducting media. It follows that if the embedded device which occupies a region $z \geq 0$ in the conductive tissue is subjected to a uniform magnetic induction field expressed as:

$$B = B_o e^{j\omega t}\mathbf{z} \tag{3.97}$$

then within the medium the magnetic flux density is given by:

$$\mathbf{B}(z \geq 0) = B_o e^{-\alpha z + j(\omega t - \beta x)}\mathbf{z} \tag{3.98}$$

where the attenuation constant α is the reciprocal of the distance over which the amplitude of the field on the surface is attenuated by a factor $1/e$ which corresponds to about 36.9%. The phase constant β describes the change in phase with position in the material and it is not being considered since only the magnitude of the magnetic field is important for inductive power transfer. Bottomley et al. adopted the *semi-infinite solid* approximation to model the conductive tissue as illustrated in Fig. 3.14 above. Essentially, in this approach the biological media is described as filling a half-space $z > 0$ in a rectangular coordinate system with the $x-y$ plane coinciding with the boundary of the conductive tissue. In spite of the infinite nature of this model it can be applied in the case of a finite region of conductive tissue since the depth of implantation where the RX is situated is very small compared with the total volume of the biomedical specimen. It follows from the previous discussion that for an implantation depth d

which is much smaller than the separation distance between the TX and RX coils ($d << D$) the magnitude of the magnetic field at the center of the receiver antenna is given by:

$$H_{\text{media}} = H_o e^{-\alpha\, d} \tag{3.99}$$

In expression (3.99) above, the magnetic field intensity at the surface of the conductive medium given by H_o corresponds to the H_z dominant magnetic field component derived in this chapter for each coil geometry and orientation.

3.9 Chapter Summary

In this chapter, a novel analytical model expressing the power transfered across a loosely coupled inductive link was derived for maximum link efficiency. More specifically, in this model the power transfer gain ($\frac{P_{RX}}{P_{TX}}$) is expressed as a function of coil geometry, orientation, and misalignment, as well as resonant frequency and ohmic losses in the process. In the design of inductively coupled systems, these parameters are very critical. The novel scheme introduced in this chapter incorporates both the geometric characteristics of the link and circuital parameters of the resonant TX and RX circuits such as load impedance. The approach adopted here is valid for all four resonant TX and RX circuit configurations. The principal aim of the analytical approach presented is to convey a better understanding of the physical operation of a loosely coupled inductive link. Consequently, this methodology provides the designer with a spherical view of the problem both from a circuital and electromagnetic standpoint. In addition, the effect of a conducting medium, present between the TX and RX coils, on the coupling efficiency has been studied. It was shown that for the inductive near-field the magnetostatic approximation is valid. Hence, the attenuation constant is adequate to describe the effect the presence of the conductive volume poses on the overall link efficiency. An analytical model incorporating all the aforementioned parameters which was not previously available was introduced in this chapter. The analytical solution given for the power transfer function provides a concise preview of the behavior of a loosely coupled inductive link, that cannot be easily obtained with a numerical solutions. Therefore, the analytical scheme presented is particularly suited to optimisation studies for each of the parameters involved in the power transfer equations.

Chapter 4
Experimental Verification

4.1 Introduction

In chapter 3 a novel near-field model incorporating misalignment effects in the TX/RX coil system has been proposed. The magnetic field at the RX antenna was expressed for different TX, RX coil geometries and topologies as the RX misaligns from the optimal coaxial position. Integrating the model introduced in chapter 3 with the notion of near-field inductive coupling, power transfer functions were formulated for two inductively coupled coils positioned in non-optimal orientations.

In the current chapter a thorough examination of the experimental techniques used in the verification of the theoretical model is presented. The experimental methodology as well as the calibration of the equipment and the design of the misalignment apparatus used in the experimentation are described. In addition, the experimental results from the magnetic field measurements and power coupling tests for the coil structures studied in this thesis, are introduced. Finally, a detailed discussion of the obtained results indicates a close correlation between the analytical model and the experimental data which justifies the validity of the proposed model.

4.2 Experimental Methodology

The experimental work that is presented in this chapter is based on the following two types of measurements:

- Investigation of the magnetic field strength around the RX coil structure, in a rectangular coordinate system (x, y, z).
- Detecting the level of the induced voltage across the resistance R_{Load} which represents the equivalent resistive load introduced by the embedded device at the RX end.

4.2.1 Measuring the magnetic field strength

In wireless power transfer via inductive coupling, the power delivered at the RX coil depends principally upon the magnetic field distribution and strength created by the TX coil. Therefore, it is essential to characterize the magnetic near-field in the close vicinity of the TX coil, which in this section is denoted as the RF source. An accurate characterization of the field pattern generated by the TX coil in the near-field zone requires consistent measurement of the magnetic field strength. As reported by Iskra et al. in [142], magnetic near-field measurements are potentially subject to large error due to the extremely non-uniform spatial variation of the near-field components and the proximity of the measurement instrument to the RF source. The aim of this section is to introduce the adopted experimental procedure and describe the apparatus employed in magnetic field strength measurements.

The field characterization for the TX coil strength is based on techniques employed for the development of near-zone field strength standards, for the evaluation of hazards due to high-level electromagnetic radiation, over the range 150kHZ to 30MHz. Electromagnetic field measurements have been the subject of intense investigation since the 1960's, due to their importance in a wide range of applications. Among these are EMC testing, ascertaining exposure hazards and the definition of new standards including the characterization of antennas and mobile devices. It is beyond the scope of this thesis to provide a detailed analysis of the existing methods and techniques since they are well known in literature, [74, 143–149].

For the HF coil antennas considered in this work, the general dividing line between the near-field and far-field regions occurs at $r = \lambda/2\pi$, where r is the radial distance from the DUT and λ is the free-space wavelength. As discussed in section 2.6, up to that distance the inductive $(1/r^3)$ and quasi-static $(1/r^2)$ terms dominate. As an example, for the case of a 3MHz electrically small loop antenna in free-space, the near-field to far-field boundary is located at 16m from the DUT, well beyond the range of operation of conventional HF passive RFID systems. It is crucial to remember that since no loop is truly infinitesimal, a source point singularity does not physically exist as $r \rightarrow 0$. Hence, the magnetic field at short distances to the source should be computed using the magnetostatic Biot-Savart Law. This approach is followed in chapter 3 to determine the field strength generated by short solenoid, circular and square spiral coils. The value of the field predicted by the analysis presented in the previous chapter will be compared to the measured magnetic field strength in order to validate the model proposed in this thesis.

In the near-field region, the magnetic and electric fields cannot be unambiguously determined from one another as their ratio is dependent on the type and orientation of the source with respect to the measurement sensor, [142]. However, in the near-field the transverse wave impedance ($Z = E/H$) is very small for the electrically small TX coil source, since it primarily generates magnetic fields. According to [150] the steps listed in Fig. 4.1 should be

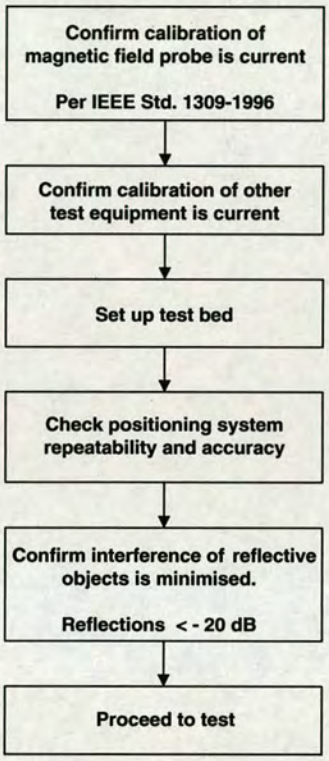

Figure 4.1: *TX coil near-field measurement pre-test flowchart, [150].*

performed before the near-field test is performed. In order to comply with consistent and good laboratory practices, such functions were executed periodically throughout the course of the experimentation. However, these tests need not be performed before every measurement. Certain aspects of the flow chart on Fig. 4.1, such as the calibration and the positioning of the probe, will be discussed in sections 4.2.1.1 and 4.3.1 that follow.

4.2.1.1 Measurement Sensor

An accurate characterization of the field pattern in the near-field requires the use of small sensors in order to provide both high degree of spatial resolution and small perturbation errors introduced by the presence of the sensors themselves. In an ideal case, the measuring probe

would consist of an infinitesimal sensor for a point measurement of the desired electromagnetic field component [151], [152], [153]. A loop antenna probe in reality measures both the magnetic field and the electric field components present. The undesired contribution due to capacitive coupling is more pronounced, with an increase in frequency. However, the use of a smaller loop with respect to the device under test (DUT) and an improved design, such as the split-shield loop antenna, provides effective isolation from any electric field components [154], [155], [156].

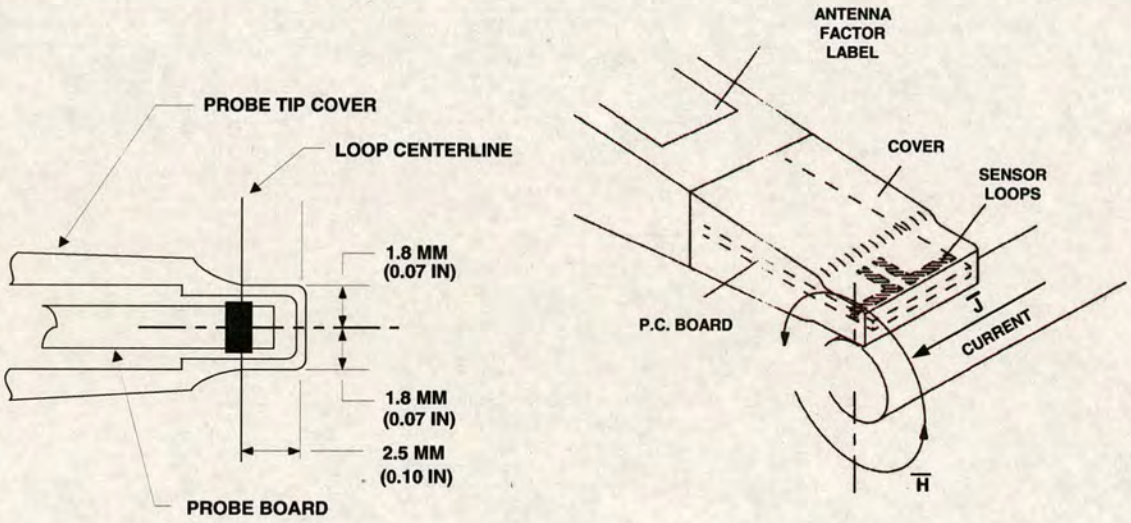

Figure 4.2: *HP 11941A near-field probe schematic diagrams: (a) Probe tip detail side view and (b) Testing a coaxial cable with HP 11941A, [157].*

In general, shielded magnetic field loop antennas are considered a standard tool for field-strength measurements. Usually, the antenna factor is reported for both magnetic and electric field strength, despite the fact that the shielded loop is expected to be insensitive to electric fields. Closer inspection reveals that the electric field antenna factor for most loop sensors is equivalent to the magnetic field antenna factor, modified by the free-space wave impedance.

The dominant magnetic field component H_z from the TX coil antenna was measured using the close-field hand-held electromagnetic sensor which is illustrated in Fig. 4.2(a) and Fig. 4.2(b). The HP11941A is optimised for Electromagnetic Interference (EMI) detection in electronic equipment. The field probe is calibrated for use between 9kHz and 30MHz. Fig. 4.3 illustrates

the characteristic frequency response of the HP 11941A and the magnetic field orientation for maximum coupling.

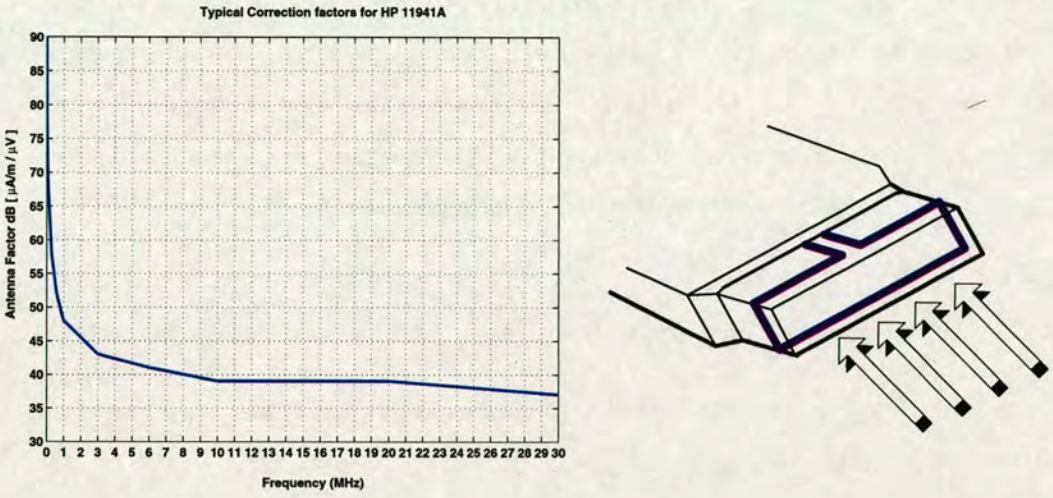

(a) (b)

Figure 4.3: *HP 11941A near-field probe: (a) antenna factors and (b) magnetic field orientation for maximum coupling, [157].*

The HP 11941A is a magnetic field sensor that provides an output voltage proportional to the strength of the magnetic field strength at the center of its sense loop. Fig. 4.2(a) details the relationship between the probe tip cover and the probe loop centerline. Signals from a magnetic field source couple directly to the probe and generate an output voltage. Due to the construction of the probe not all radiated electric fields produce an output voltage . The probe is designed to be held very close to potential radiating points. The plane of the probe loops must be perpendicular to the radiating magnetic field as illustrated in Fig. 4.3. Once connected to a spectrum analyzer, the HP 11941A measures only the field component that is perpendicular to the loop at its tip as indicated in Fig. 4.3. Hence, based on its directional nature of the probe, it is possible to distinguish between the H_x, H_y and H_z magnetic field components. The following equation is used to measure the magnetic field strength at an arbitrary point from a magnetic field source:

$$\bar{H} - \text{Magnetic Field Strength } \left(dB\frac{\mu A}{m} \right) = V_{SA} + AF \tag{4.1}$$

where V_{SA} is the voltage measured on the spectrum analyzer in $dB\ \mu V$ and AF is the antenna factor in $dB\ \frac{\mu A/m}{\mu V}$. A plot of the characteristic antenna factors for the HP 11941A near-field

probe is shown in Fig. 4.3, [157].

The probe termination effect is also significant for the sensitivity achieved in a practical case. According to Joseph et al. in [154] in near-field measurements one should strive to achieve a disturbance of the measured field quantity lower than 5% and at the same time enhance sensitivity. In such a situation the termination of the measuring probe plays an important role. To achieve this target the probe is loaded with a 50-Ω resistance since the measurements are performed with a spectrum analyzer with an imput impedance of 50-Ω.

4.2.2 Power transfer function verification

In order to test the power transfer model developed and discussed in the previous chapter, the equivalent circuit of the loosely coupled transformer in Fig. 4.4 was used.

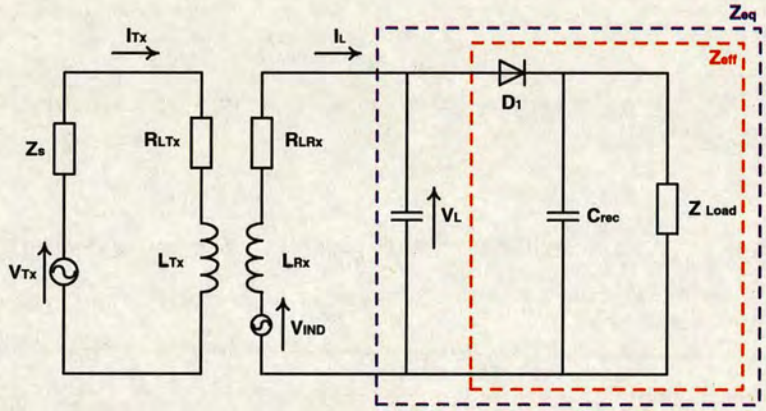

Figure 4.4: *Equivalent circuit of the loosely coupled transformer used in the current experimental set-up.*

The rectifier is by definition a non-linear device. Despite its non-linear nature, according to [158], [159] the rectifier can be represented as an effective resistive load R_{rec} across the RX tank circuit. In essence, this means that the tank circuit is damped by an equivalent resistance R_{rec}, equal to 81% of the load added by the embedded device, indicated as R_{Load}. Consequently, the rectifier can be substituted by its equivalent resistive component as given by the following expression, [160], [161], [159]:

$$R_{\text{rec}} = \frac{8}{\pi^2} \cdot R_{\text{Load}} \tag{4.2}$$

A proof of equation (4.2) is available in [159].

It is critical to determine the equivalent resistance presented by the rectifier. In low power links, studied in this thesis, the combination of the rectifier and load determine the impedance of the RX coil in an optimal design strategy for maximum power transfered to the load. Furthermore, as illustrated in Fig. 4.4 a Schottky diode has been selected to eliminate the high frequency losses in the rectifier attributed to the finite switching time of the diode. Schottky barrier diodes are fabricated using metal-semiconductor junction technology. This type of device exhibits a low potential barrier across the junction with a forward voltage typically in the order of 0.3 volts, much lower than that of a conventional p-n junction. It is this characteristic that gives Schottky diodes their superior RF performance.

4.2.3 RX antenna coil matching

In order to verify the model for near-field power transfer we need to match the RX antenna coil to the equivalent impedance presented by the electronics of the embedded device. In order to do so, the series resistance of the RX coil R_S, needs to be transformed to a parallel one denoted R_P, as illustrated in Fig. 4.5. In a lossless resonant circuit, the impedance seen across the circuits terminals at resonance is infinite. In practice, due to component losses, there exists some finite equivalent parallel resistance. Once the value of R_S is known the rectifier and the load impedance associated with the implanted electronics can be matched to the impedance of the resonant RX coil.

The resistance (R_S) and its associated shunt reactance (X_S) can be found from the following equations if the Q of the antenna coil is greater than 10:

$$R_P \approx Q^2 \cdot R_S \tag{4.3a}$$

$$X_P \approx X_S \tag{4.3b}$$

where R_P is the equivalent parallel resistance and R_S is the series resistance of the component. This transformation is frequency dependent because it involves a component reactance which varies with frequency. A series to parallel transformation is carried out for all the RX coils used in the experimental process. As an example a series to parallel transformation is performed below for a short-solenoid RX coil C:

- Inductance of coil C - $L_c = 8.18\ \mu$H

- Series Loss Resistance $R_S = 2.297\ \Omega$

The Q of this coil at 6.7 MHz is,

$$Q = \frac{X_S}{R_S} = \frac{j\omega L}{R_S} = 150 \tag{4.4}$$

Thus, since the Q of the component is greater than 10, we can use equation (4.3a):

$$R_P = Q^2 \cdot R_S = 51.7\ \text{k} \tag{4.5}$$

As the coil has a high Q we can neglect the change in the inductor value required by the transformation, see expression (4.3b). Once the transformation is complete we can connect a resistive load equal to the transformed equivalent parallel losses, $R_{\text{Load}} = R_P$, across the resonant circuit as illustrated in Fig. 4.7.

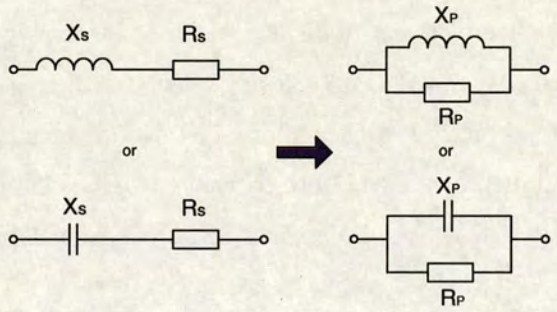

Figure 4.5: *A series to parallel transformation.*

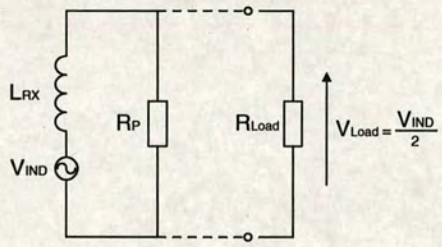

Figure 4.6: *Matching the tuned circuit to the equivalent resistance of the rectifier and the implanted device, $R_{Load} = R_P$.*

The rectifier/load circuit is approximated by a single resistor element, R_{rec}, as given by (4.2), where R_{Load} is the real load resistance. This is implemented in an attempt to avoid the complications caused by the non-linear behaviour of the rectifier circuit as discussed earlier. Once the equivalent parallel resistance of the receiving electronics, R_{eq} shown in Fig. 4.4, is known the

parallel resistance of the coil R_P should be made equal to this value for impedance matching as follows:

$$R_{eq} = \frac{R_{\text{rec}} \cdot R_{\text{Load}}}{R_{\text{rec}} + R_{\text{Load}}} \approx R_P \tag{4.6}$$

Substituting for R_P and R_{rec} in equation (4.6) and rearranging for R_{Load} we derive an expression for R_{Load} as:

$$R_{\text{Load}} = \frac{R_P \cdot (\pi^2 + 8)}{8} \tag{4.7}$$

Using (4.7) the necessary values for matching the RX coil to the embedded electronics can be computed.

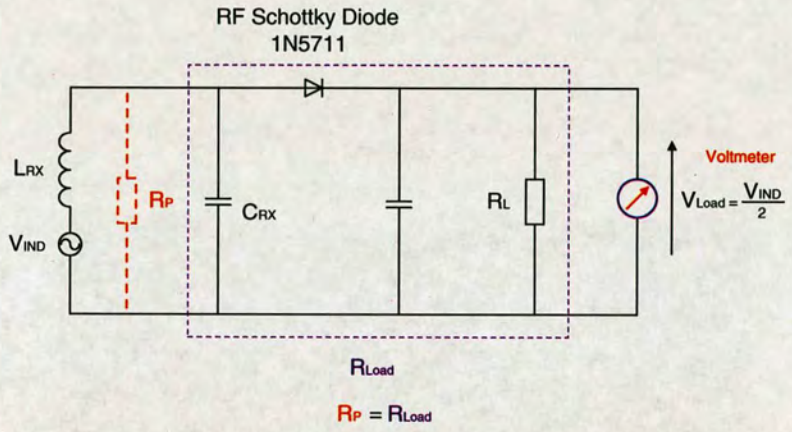

Figure 4.7: *Equivalent receiver circuit diagram depicting voltage multimeter.*

4.3 Experimental Setup

This section describes the experimental configuration used in the near-field measurements and the power coupling testing between the TX and RX coils. The experimental methodology described in this chapter is comprised of two parts. In the first part, which consists of the magnetic near-field measurements, the procedure followed can be demonstrated with reference to the block diagram of Fig. 4.8 showing the experimental configuration adopted. In addition, a photograph of the experimental set-up used for the magnetic near-field measurements is depicted in Fig. 4.10. Finally, the power transfer experimental set-up is shown in Fig. 4.11.

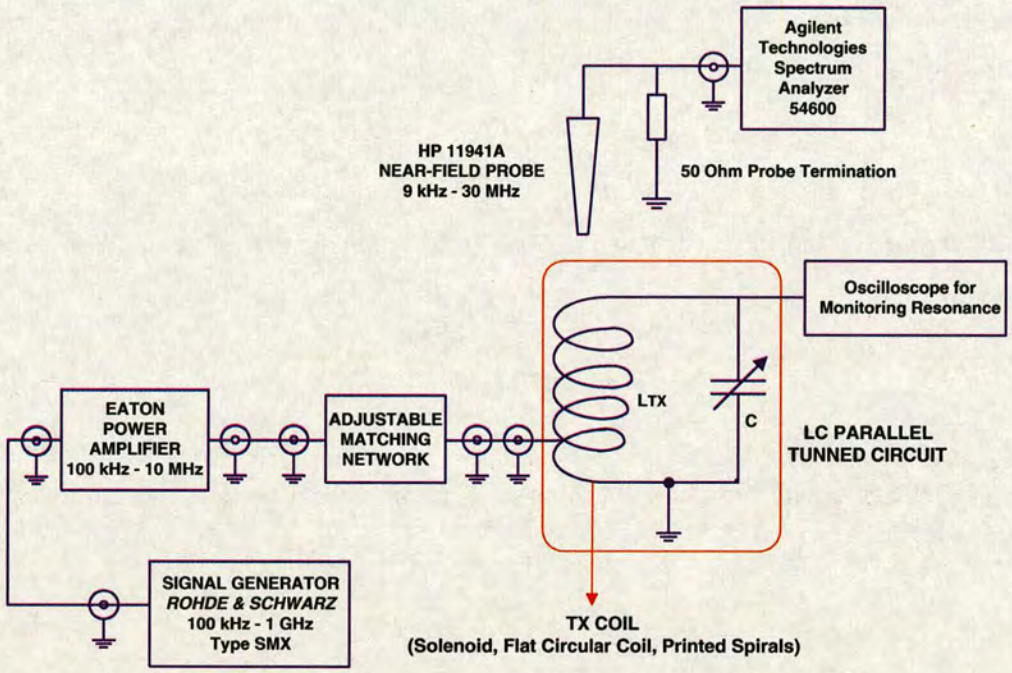

Figure 4.8: *Block Diagram of the Experimental Set-up.*

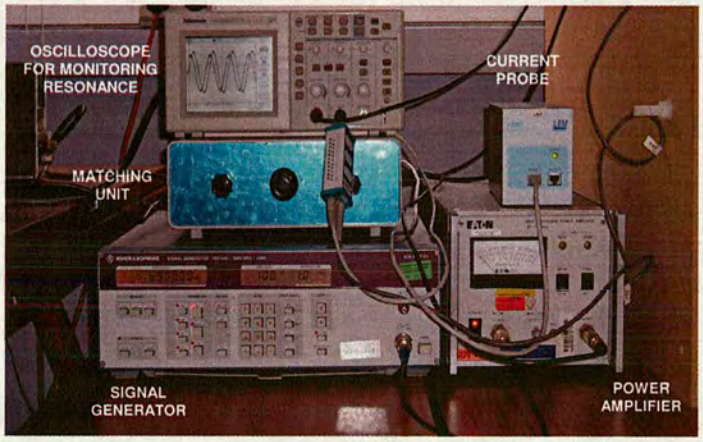

Figure 4.9: *Photograph of the experimental Set-up for near-field measurements.*

4.3.1 Mechanical aspects of DUT positioning

For the experimental verification of the analytical model discussed in the previous chapter, field and power transfer measurements were carried out for the coil geometries listed in tables 4.5 and 4.6. During the experimental procedure, the transmitting coil was mounted at the center of the misalignment apparatus and placed on a table at a height of 70 cm. In field measurements, the 3cm in diameter shielded loop sensor of the HP11941A near-field probe was placed 1m

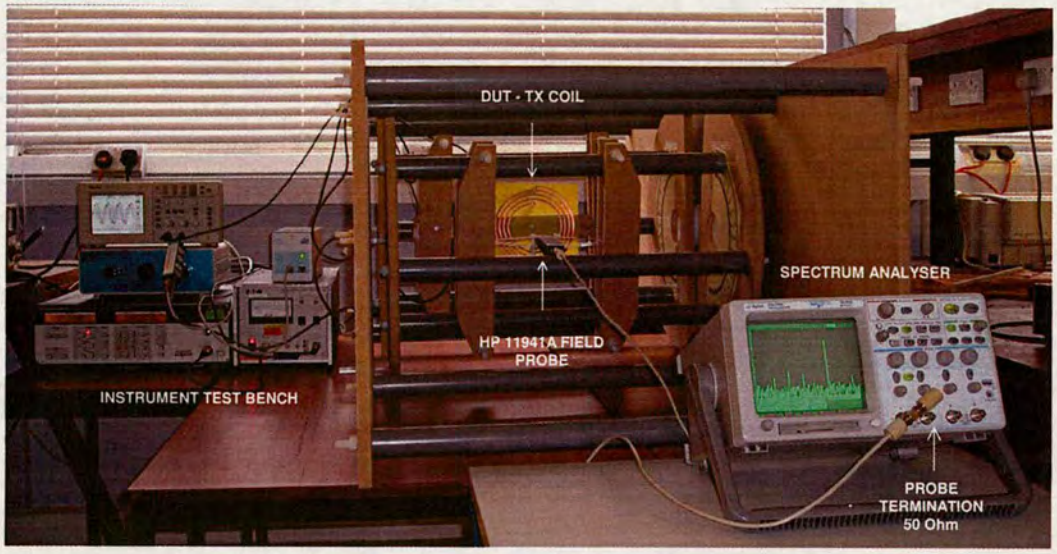

Figure 4.10: *Photograph of the Experimental Instrumentation Test Bench.*

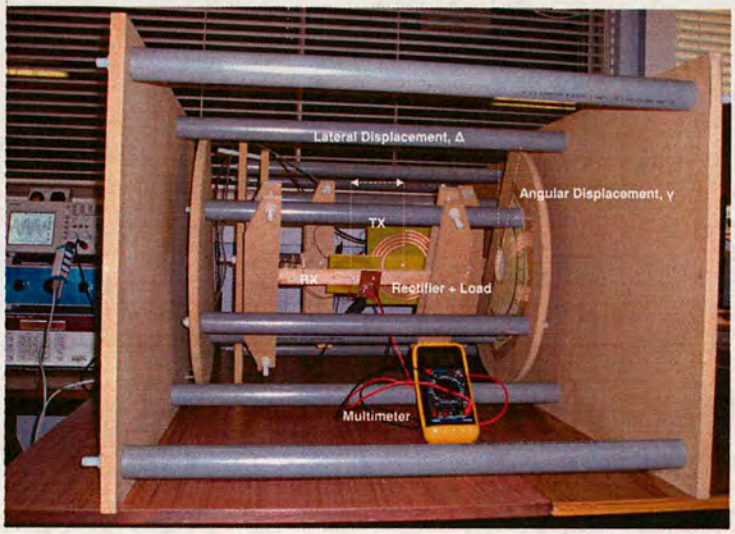

Figure 4.11: *Photograph of the experimental configuration employed in power transfer measurements.*

from the floor level pointing towards the direction of the source, as shown in Fig. 4.10. In the case of power coupling measurements, the sensor probe was replaced by the TX coil. The dominant inductive magnetic field component H_z and the voltage across the RX coil were measured at progressively larger distances from the TX source for the axial, radial and angular orientations discussed in chapter 3. The effects of impedance coupling and perturbation of the field due to the measurement sensor or pick-up coil must be minimised so that the accuracy of the experimental data is not compromised. Therefore, according to Brunett et al. in [152],

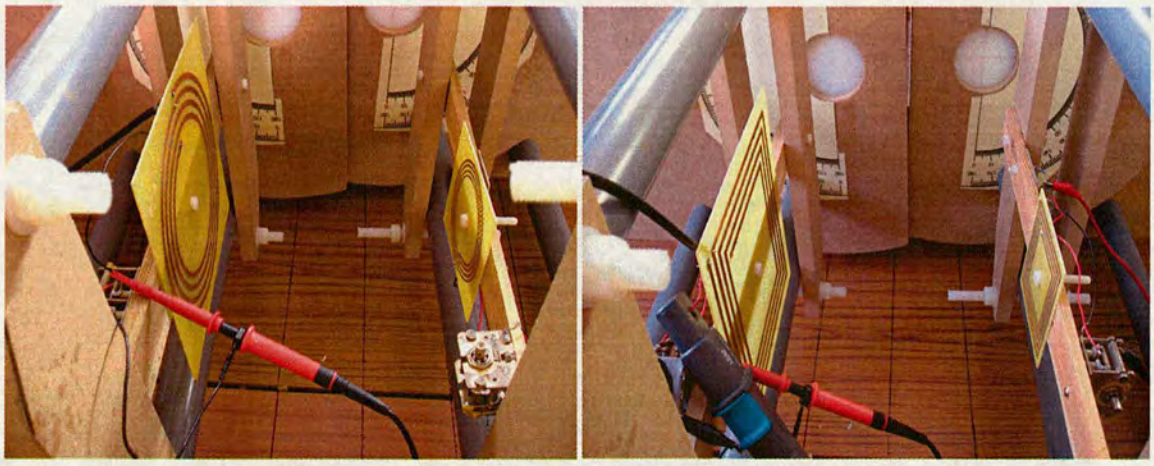

(a) (b)

Figure 4.12: *Photograph of the coupled TX and RX printed spiral coils, mounted on the misalignment apparatus: (a) Circular spiral coils, (b) Square spiral coils.*

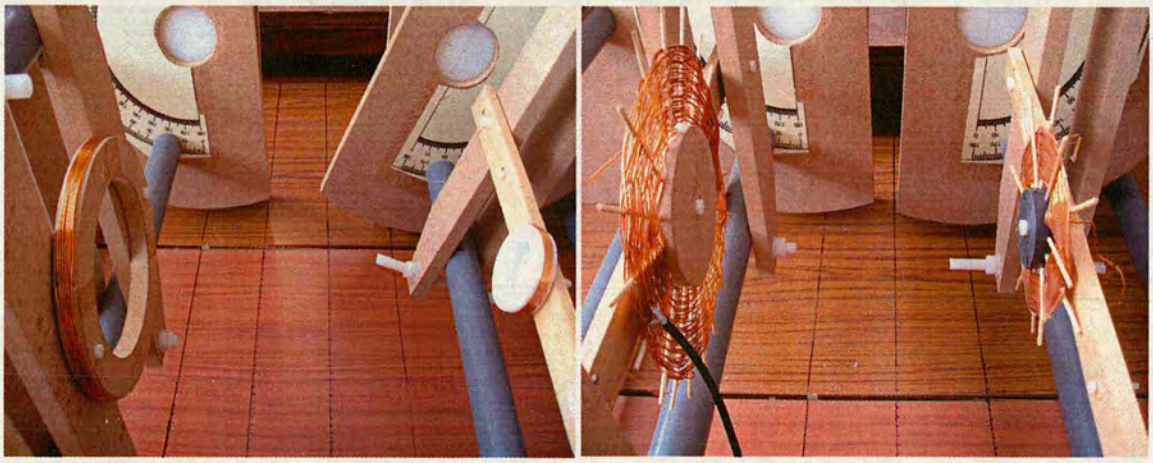

(a) (b)

Figure 4.13: *Photograph of the coupled TX and RX coils, mounted on the misalignment apparatus: (a) short-solenoid coils, (b) flat spiral coils.*

no measurements should be performed within a distance of the DUT, in this case the TX coil, shorter than 10 times the radius of the largest TX loop in use. However, such a configuration is clearly not realistic for measurements focused on HF passive RFID and embedded sensor applications, where the RX coil is usually situated in the close vicinity of the TX coil. Due to the small effective area of the RX coil usually employed in embedded applications, very sensitive

instrumentation is essential to detect the low power levels coupled across the inductive link. Therefore, it would have been technically challenging to test the field and power transfer by adopting the scale of the TX, RX coils that are typically used in embedded RFID applications. Consequently, to ensure a high degree of accuracy in the experimental measurements with the available instrumentation, an alternative approach was selected as discussed in the following paragraphs.

Firstly, for magnetic field measurements instead of placing the field sensor at a large distance from the TX coil, to eliminate the possibility of the sensor distorting the field, a larger TX coil was used. This permits measurements close to the source with negligible field perturbation. In addition, a significantly larger coil than the ones used in practice was selected for the power transfer measurements. Nevertheless, the ratio of the radii of the TX-RX coils was kept similar to the RFID embedded scenarios. In essence, an increase in the size of the RX coil means a larger coil effective area. As a result, a larger RX coil is a more sensitive RX-pick up coil. Hence, more voltage is induced across a larger coil, which can be easily measured by a standard multimeter without compromising the accuracy of the measured data. However, a larger receiver coil is prone to load and detune the TX when the coil separation distance is less than one TX coil diameter. In order to overcome this problem a larger TX coil which is less likely to be affected by the RX has been used. The scaling of the coils permitted measurements very close to the TX coil and at the same time the effect of impedance coupling was minimised.

Photographs of the instrumentation test bench and the measurement set-up are shown in Fig. 4.9 and Fig. 4.10 respectively. For the near-field measurement system illustrated in the block diagram of Fig. 4.8, an electrically small magnetic field probe, with respect to the wavelength of the TX resonant frequency such as the HP 11941A, is suitable for measuring the magnetic field strength without significantly perturbing the field. According to IEEE Std C95.3-1991, [162], in order to avoid measurement errors associated with the probe disturbing the measured field generated from the TX coil, the probe should not be placed closer than a distance equal to three times the length of the active elements of the probe. The coil test fixture, also referred to as the misalignment apparatus, is employed as a method of holding into position and rotating the H-field probe as required by the magnetic field measurements. In addition, the misalignment structure keeps the coils aligned in parallel planes and it allows the RX to misalign laterally and rotate angularly with respect to the TX for the testing of the coil coupling discussed in 4.2.2. The rationale behind this mechanism is that the system needs to be capable of sufficient

accuracy and repeatability in position so as to guarantee a minimum measurement uncertainty. It can be argued that the use of an automated movement system, such as robotic arms or three-axis positioners, should be favored, as it can provide superior probe placement accuracy and placement repeatability. A manual placement system was preferred and the system was verified as having the required placement accuracy.

The mechanical implementation of the misalignment apparatus has proven to be a challenging task as the nature of the experiments carried out prohibited the use of any conductive materials in the assembly of the misalignment structure. In addition, the misalignment mechanism should be a lightweight and robust structure capable of providing three degrees of freedom for the RX coil. The set of independent displacements for the RX coil achieved using this structure are an axial displacement across the z-axis, a translation on the y-axis and a rotation about the y-axis. In order to achieve this, the misalignment system consists of two parts: one being stationary and housing the TX coil and a moving section for the RX coil. The overall system was assembled in the laboratory and the detailed drawings of the mechanical design for the apparatus are provided in appendix C. The misalignment jig including all parts of the probe holding and movement mechanism were designed and built using RF-transparent or non-magnetic materials. The end panels of the misalignment structure, the rotating end disks, the coil bobbins as well as the support plates for the coil former are made of medium-density fibreboard (MDF). The cone bearing and the fasteners used for adjusting the rotation movement of the end plates are fabricated from polytetrafluoroethylene (PTFE) and nylon respectively. The fasteners used are manufactured from tough, lightweight nylon, which offers excellent electrical insulating properties and is non-corrosive and non-magnetic. Finally, plastic tubing and washers, nylon threaded rod studding and fasteners are utilized for fixing the support of the end plates and the rotating disks. Holes were drilled through the rotating discs every 5° to allow angular displacement measurements every 5° by securing the rotated disc into position at the required angle using a nylon rod. The radial displacement necessary for lateral misalignment measurements was achieved by a translation of the moving section of the apparatus on the table surface at a parallel plane to the stationary part. The coaxial measurements were carried out by gradually increasing the separation distance of the TX and RX sections of the misalignment apparatus with their centers situated on the z-axis.

It is apparent from the previous discussion that the only conductive material present in the test volume is the brass chassis of the air-spaced tuning capacitors. The chassis of the air-spaced

capacitor was fixed using nylon screws on the former of the coil. Placing the capacitor further away from the coil requires the use of longer wires thus adding some unwanted capacitive coupling. The effect of capacitive coupling was rather pronounced throughout the experimental procedure so every effort was made to keep the wires as short as possible. Although eddy currents are undoubtedly formed in the metal plates of the capacitor, and the conducting elements might have introduced some reflections, the measurement accuracy is believed not to be significantly compromised. This is justified since the size of the capacitors used (3cm $\times$ 3cm $\times$ 3cm) is much smaller in comparison to the wavelength of the highest resonant frequency used. Therefore, it was estimated that the magnitude of any reflections established is below the permitted limit of -20dB of the measured signal. In order to establish the influence that nearby conducting objects, such as the the tuning capacitors and the metallic supports of the experimental table, have on the field measurements, a sheet of copper plate with dimensions (60cm $\times$ 60cm) was placed behind the TX coil. The presence of the copper screen did not produce any measurable change on the signal level displayed on the spectrum analyzer which represents the field level detected with the HP near-field probe. This test was repeated for all the prototype coil structures tested and any variation in the signal strength remained below the noise floor of the spectrum analyzer. The results of this test indicate that possible reflections from nearby conductive objects are below 20dB of the measured signal and can be classified as negligible at the frequencies of operation.

4.3.2 Instrumentation and calibration

Table 4.1 lists the instrumentation used during testing. Prior to any experimental data acquisition, all equipment listed in Table 4.1 was calibrated and verified for correct operation to minimise experimental errors. Most of the equipment used during the experimental procedure were firmware calibrated from the manufacturer and a three year recertification cycle was recommended. In view of this, field-site precision recalibration of the equipment used was not possible. This is especially true for the antenna factor calibration of the HP 11941A probe, which requires the use of a calibrated magnetic field that cannot be reproduced in the lab. However, operation verification tests are suggested by the manufacturer which are designed to detect damage in the circuitry rather than provide an accurate recalibration methodology for the system in question. In the absence of a precise calibration technique, any systematic error contribution due to the instrumentation will be accounted in section 4.6.

INSTRUMENT	TYPE
Digital Oscilloscope	Agilent 54624A, 200Msa/s - deep memory
Digital Oscilloscope	Tektronix TDS 210
Near-field Probe	Hewlett-Packard HP 11941A
Current Probe	LEM LS50 dc/ac probe
Network Analyzer	Hewlett-Packard HP 8753C, 300kHz - 3.0GHz
S-Parameter Test Set	Hewlett-Packard HP 85046A, 300kHz - 3.0GHz
Signal Generator	Rohde & Schwarz, 100kHz-1000MHz SMX
Broadband Power Amplifier	EATON 5001, 0.01-10MHz
Power Meter	Hewlett-Packard HP 435A
Multimeter	Fluke 77
Multimeter	Rapid 318 DMM

Table 4.1: *Table of the instrumentation used during the experimental verification of the proposed model.*

In the case of the Hewlett-Packard HP 8753C vector network analyser (VNA) calibration is of the utmost importance for reflection measurements used in the characterization of the impedance of the prototype coils. Accuracy in network analysis is greatly influenced by factors external to the network analyser. As an example, parts of the measuring setup such as interconnecting cables and test sets may introduce variations in magnitude and phase, which in return can mask the actual performance of the DUT. As mentioned previously, the purpose of calibration is to remove systematic errors in the test setup. These can be described in three major categories as follows, [163]:

- Frequency Response
- Leakages
- Mismatch

The HP 8753C has several techniques available for measuring and compensating for these errors. Greater flexibility is available to the user to perform a measurement calibration procedure depending on the required measurement accuracy. For S11-parameter and impedance measurements carried out in this work a one-port calibration is adequate. This calibration routine removes all three of the systematic error terms seen from a single input port for a reflection measurement. The VNA was calibrated for a frequency range of 1kHz to 15MHz by connecting a standard open, short and 50 Ohms load to the S11 port. Each load is measured in turn, and the results are stored in memory. Upon completion, the analyzer determines the contribution of each of the three error terms and removes any impact they introduce on the data acquired.

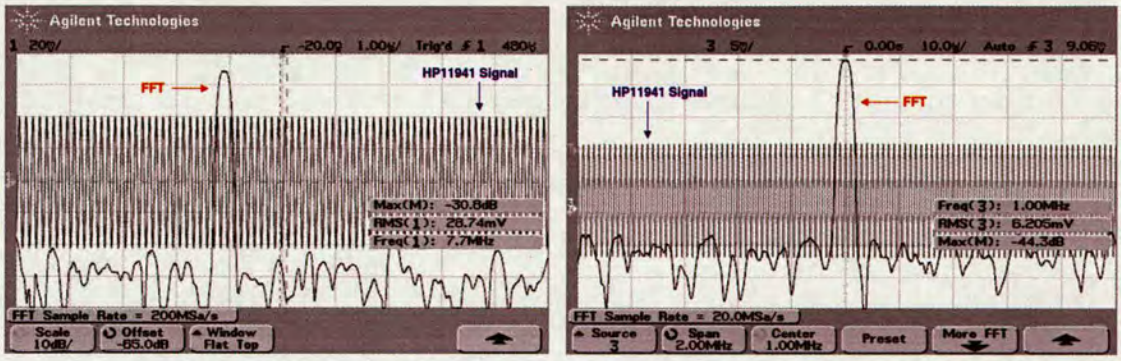

(a) (b)

Figure 4.14: *Agilent 54624A FFT screen shots for magnetic near-field measurements. (a)PSS1 spiral TX coil. 2 Watts of input power in the TX coil, 80V p-t-p resonance across the coil. The near-field probe is situated on the z-axis at 7.5cm from the center the source. (b) FSC1 spiral TX coil. 2 Watts of input power in the TX coil, 2.56kV p-t-p resonance across the coil. The near-field probe is situated on the z-axis at 30cm from the center of the source.*

The functionality of the digital oscilloscopes used was tested based on automatic pre-installed self-calibration utilities and by checking that the 5V peak to peak calibration signal provided by the oscilloscopes is accurately displayed on the screen. In addition to an oscilloscope for checking the resonance in the TX coil, the Agilent 54624A digital oscilloscope was used as a spectrum analyzer due to its integrated FFT function. The spectrum analyzer facility was used to detect the signal from the HP 11941A near field-probe as illustrated in Fig. 4.14 for a printed square spiral coil (PSS1) and a flat circular spiral coil (FSC1).

4.4 Coil Calculation and Construction

This section addresses the issues associated with the design and construction of the primary and secondary coupled coils used in the experimental procedure discussed in this chapter. One of the primary concerns in the design of inductive coupled links is optimising the coils to ensure that the TX coil generates a maximum magnetic field and power losses in the RX coil are minimised. In order to satisfy the above criteria, the inductance and the resistance of the coupled coils are among the most important parameters that need to be addressed during the coil design phase. The scale of the experimental set-up required the use of much larger coils than the ones employed in practical applications. In view of this, although every effort was made to optimise the coils, the prototype coils were designed to be primarily functional. Furthermore,

the coils were designed to satisfy the weakly coupled assumption in the theoretical model. Consequently, for all the prototype coils pairs constructed, the TX coil was designed to be twice the size of the RX to satisfy the loosely coupling scenario as addressed in section 2.11. The construction of the prototype coils was governed by the geometric constrains introduced by the loosely coupled approximation. Therefore, in order to accommodate for this, the size of the coils was decided first. Once the geometrical parameters were set, the challenge was to calculate the impedance of the coils so that they can be efficient at the operating resonant frequency.

4.4.1 Coil materials and construction

Fig. 4.15 depicts the four sets of prototype TX and RX coils built for the experimental verification of the model proposed in this thesis. The key idea is to measure the magnetic field from a short-solenoid coil, flat spiral, printed circular and square coils, and compare the results with the analytic expressions of chapter 4. Once the magnetic field expressions have been verified, the power transfer between the TX and RX coils is tested using the sets of short-solenoids, flat and printed spirals shown in Fig. 4.15. Tables 4.5 and 4.6 list the geometric and electrical characteristics for all the prototype coils used.

The simplest coil structure, namely a short solenoid of round insulated copper wire, is investigated first. The final design for the solenoid coils consists of 7 to 8 turns of 18 and 19 SWG copper-enameled wire. The decision to use 18 and 19 SWG wire is well justified since a conductor with larger cross sectional area is required to minimise the internal resistance of the coil and at the same time provide a flexible enough conductor for hand winding of a solenoid coil. In addition, the number of turns was chosen to provide enough inductance where the length ℓ of the coil remains significantly smaller than its radius a, ($\ell \ll a$), to conform with a short-coil structure. Construction of a short-solenoid coil requires a form or bobbin on which to wrap and support the turns. For the TX coil and the coil used for field measurements, rings of MDF material were cut on a lathe. A hollow ring form was adopted to reduce the weight of the coil form. This proved to be very practical for the later attachment of the coil to the misalignment structure. The MDF bobbins were designed to fit the turns of the coil, with extra space allowed for errors in hand winding. In addition, the inside surface of the form ring provided extra room for attaching the variable tunning air-spaced capacitors. All the coils were wound on the forms by hand, keeping the wire under tension on a vice and slowly rotating the form to achieve a

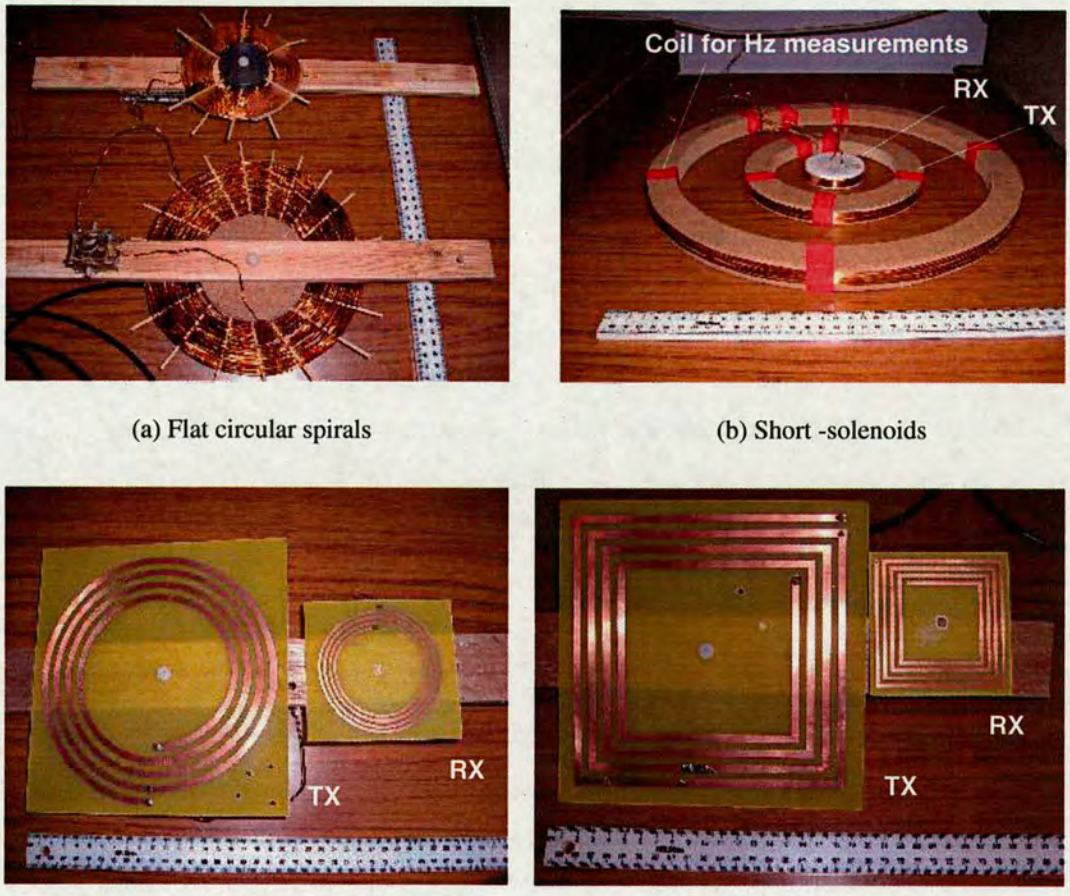

(a) Flat circular spirals

(b) Short -solenoids

(c) Printed circular spirals

(d) Printed square spirals

Figure 4.15: *Photographs of the TX, RX constructed coils used in the verification of the theoretical model.*

closely spaced winding of 7 to 8 turns. A plastic PTFE disk was selected as a bobbin for the RX coil C and a hole of approximately 10mm was drilled down the center for later attachment of the coil to the misalignment jig using a nylon M5 screw. Once the coils were wound, the turns were glued on the former using epoxy resin. In the closely wound approach, adjacent turns are touching to ensure that the ratio of the spacing between adjacent conductors and the wire radius is $c/a = 1$. Of course, this takes a very optimistic view of the precision of wire placement in a hand-wound coil. Nevertheless, it is obvious from the close-up photograph of the winding for the RX solenoid C, as depicted in Fig. 4.16 below, that the c/a ration is in fact very close to unity. The same spacing ratio was applied for the TX coil B and for coil A used in the magnetic field measurement. It is of interest to note that in the absence of the proximity effect, the skin effect resistance would be minimised as the radius of the conductor increases.

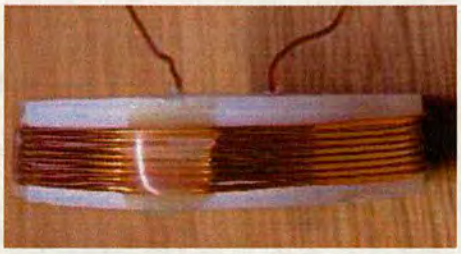

Figure 4.16: *Short solenoid RX coil windings close up.*

On the contrary, for the frequencies of 3 and 6.7MHz, where the short-solenoid coils are resonant, the proximity effect cannot be neglected. Clearly, in this case a larger wire diameter has the opposite effect on the losses of the coil by increasing the proximity effect resistance. According to Smith in [95], in a system of parallel conductors, such as the windings of a short solenoid investigated here, an optimum minimum resistance point is reached when the increase in proximity loss is counterbalanced by the decrease in the skin effect loss. Hence, it is of interest to identify the wire radius a or wire spacing c/a for which the resistance of the coil is minimum. In the same paper Smith, introduces a dimensional quantity $2\pi\ell R/NR^s$ which is proportional to the total ohmic resistance per unit length of the system of parallel conductors. In Fig. 6 of [95] Smith provides plots of this quantity versus the normalized wire radius a/ℓ where the point of the minimum resistance is shown. The results of this analysis are also listed with respect to conductor spacing c/a. Smith's table is reproduced below.

Number of Turns (N)	a/ℓ	c/a	$2\pi\ell R/R^s$
2	0.250	1.00	5.33
3	0.148	1.19	10.41
4	0.098	1.37	16.07
5	0.071	1.50	22.01
6	0.056	1.59	28.10
7	0.046	1.66	34.30
8	0.039	1.71	40.57

Table 4.2: *Conductor spacing for minimum resistance, [95].*

Table 4.2 indicates that a turn spacing of 1.66 and 1.71 is required in order to minimise the losses in coils C and B, A respectively. However, it is difficult to achieve such a spacing with hand wound coils. Although a choice of $c/a \approx 1$ is a slight compromise on the resistive losses of the coil, it ensures that the theoretical representation of a short-solenoid adopted in the previous chapter, where the coil is modeled as a number of stacked loops is valid. On the other hand, closely spaced turns increase the inter-winding stray capacitance of the coil. This distributed

capacitance may be replaced by a single capacitance shunted across the coil terminals. This equivalent capacitance is called the self-capacitance of the coil, and causes the coil to exhibit parallel resonance effects. According to Grandi et al. in [164] the self capacitance, C_{self}, for closely wound short-solenoid coil is given as:

$$C_{self} = \frac{\pi^2 D \epsilon_o}{\ln(F + \sqrt{F^2 - (1 - t/r)^{2/\epsilon_r}})} \tag{4.8}$$

where F in the above expression is defined as:

$$F = \frac{p/2r}{(1 + t/r)^{1-1/\epsilon_r}} \tag{4.9}$$

In equations (4.8) and (4.9) t is the insulation thickness of the wire, p is the coil pitch, D is the coil diameter and r is the conductor radius.

The following Table 4.4.1 lists the distributed capacitance and self-resonant frequencies of the prototype short solenoid coils A, B, C. For the coils employed in this work their operation was confined to frequencies below the self-resonant frequency. The impedance operator of an inductor is given as:

$$Z = R_S + jX_S \tag{4.10}$$

where R_S is the effective series resistance and X_S is the effective series reactance. Clearly, at frequencies below the self-resonant frequency the circuit is inductive when $X_S > 0$. In this case, the impedance approximates to:

$$Z = R_S + j\omega L \tag{4.11}$$

Refocusing at the planar spiral coil structures in Fig. 4.15, the design of the prototype spiral inductors is now discussed in more detail. Printed spirals were fabricated on single-sided copper clad epoxy glass (FR4) boards. The geometric features of the coil were directly transfered on the board by etching the exposed copper cladding using a ferric chloride solution. The board thickness is 1.6mm, where copper is the conducting material of content in the order of 305g per

Coil	C_{self}	f_{self}
A	37pF	3.1MHz
B	18pF	6.5MHz
C	6.5pF	15.5MHz

Table 4.3: *Distributed capacitance and self-resonant frequency of prototype short-solenoid coils.*

square meter. In a similar manner to the solenoid coils, a 10mm hole is drilled at the center of each spiral and the prototypes are fixed to the misalignment apparatus using a M5 nylon screw as illustrated in Fig. 4.13. Although the structure for a spiral inductor coil appears to be simple, the design of such a coil is a rather complex task. Coil geometry is an important factor in the design of the spiral configuration as it has a direct effect in the electrical characteristics of the coil. The electrical characteristics of both square and circular spiral coils are discussed in detail in the following section 4.4.2 based on a lumped-element circuit model. All the prototype spiral coils of strip conductor used in this work were implemented using PCB technology due to the fact that it is a relatively fast and cost effective approach for the dimensions of coils required. However, the suitability of PCB technology in embedded systems is questionable due to the potential of delamination. Thus, in practice the technology of choice for such applications is thick film or ceramic.

In addition to the printed spiral coils, conventional wire-wound flat spirals were constructed using 18 and 19 SWG copper-enameled wire. The technique implemented during the construction of the flat spiral coil depicted in Fig. 4.15 made of circular wire is known as basket coil winding. The coil former consists of a circular disk of MDF or plastic material and 17 and 11 wooden radials for the TX and RX coils respectively. In order to attach the radials to the central disk, 5mm holes were drilled evenly around the circumference of the coil former where the wooden spokes are push fit inserted, to form a star like formation depicted in Fig. 4.15. Using this structure as a basic frame, the flat spiral coil windings were alternated over the radials in a basket-weave fashion starting from the center and extending towards the outside, keeping the windings close together. This resulted in two very neat and high Q coils. Such a winding method combines simplicity of construction and mechanical rigidity. It should also be possible to stabilize the coil and remove the radial supports for even higher quality coils. In practice, the turns of the prototype coils are close wound and bonded by embedding the coils in a layer of epoxy as shown in Fig. 4.16. Nevertheless, extra attention is required when constructing the coil to ensure that the windings do not overlap and are kept nicely tight at all times.

4.4.2 Electrical properties of coils

The electrical properties of the coils can be now discussed as they are key in the optimisation of the inductive link. This section includes an analysis of the electrical characteristics for the coil geometries considered in this thesis. In an RFID system, the inductively coupled transmitting

and receiving coils are tuned to resonate at a particular frequency. In most cases, the operating resonant frequency is determined by the combination of the coil and the capacitor values in the resonant or tank circuit. The losses associated with the resonant circuit can be described by the losses of the coil and the capacitor. Capacitive losses were kept to a minimum by adopting air-spaced variable capacitors, which present minimum resistive losses, [165]. Hence, the resonant circuit losses can be solely attributed to the losses of the coil. It is critical to determine the impedance of the transmitting and receiving coils in order to drive the TX coil, match the RX to the implanted electronics and tune both transmitting and receiving ends to the specified frequency, so as to optimise power transfer across the link. The complex impedance of the coil yields both the resistive losses in the coil and its inductance. The real part represents the ohmic losses and the reactive part determines the inductance of the coil. Once the inductance of the coil is determined, it can be used to calculate the necessary capacitor value in order to tune the coil at the specified resonant frequency, based on the well-known formula:

$$f = \frac{1}{2\pi\sqrt{L\,C}} \tag{4.12}$$

Also of interest is the quality factor (Q) of the TX and RX coil which defines the amount of energy a coil inductor can store relative to the amount dissipated as heat. The relationship between the coil Q, coil inductance (L) and the series losses of the coil denoted R_S can be defined as, [166]:

$$Q = \frac{\omega \cdot L}{R_S} \tag{4.13}$$

An alternative representation of the quality factor Q, is given with reference to the equivalent parallel resistance R_P, which represents the losses in the coil. Hence, the relationship between the coil Q, coil inductance L, and the parallel loss resistance R_P is given as, [165, 166]:

$$Q = \frac{R_P}{\omega \cdot L} \tag{4.14}$$

It is of interest to note that the relationship between R_S and R_P is defined as, [165]:

$$R_P = R_S \cdot (Q^2 + 1) \tag{4.15}$$

This expression is simplified for high quality coils where $Q^2 >> 1$ and $R_P = Q^2 \cdot R_S$. Expressions (4.13), (4.14) and (4.15) are very important for impedance matching of the receiving coil to implanted device as discussed previously in section 4.2.3. It follows that in order to characterise the coils used, the following parameters are required. These are the coil impedance, inductance, operating frequency and loss resistance R_S or R_P.

Having explained the importance of the electrical characteristics of the coils, the inductance of the coils used is evaluated here for each structure defined in section 3.4. There is an extensive range of inductance calculation techniques available in the literature, which range from semi-analytical and approximation techniques to handbook methods. Included below is a brief review of some of the most important inductance estimation references available for inductance estimation of finite-length solenoids, flat planar spirals and disc coils. Classical inductance calculation methods are developed for solving for the inductance of structures in closed form. Such analytical techniques were first introduced by Maxwell in his seminal work, presented in [167]. More recently, Smythe covered classical field and inductance calculation in his great work given in [52]. It is possible to compute the inductance of a simple structure such as a toroid, an infinitely long solenoid, with the aid of analytical tools based on the magnetostatic limit of Maxwell's equation and by setting appropriate boundary conditions. Some of the most popular analytical tools available are the brute force calculation method, the energy method and the magnetic circuit analysis [168]. In the solution for the inductance of magnetic field structures, it is important to identify which of the above tools to use. Alternatively, computation methods such as the Biot-Savart law, the magnetic vector potential or finite element analysis can deliver a solution when the other methods fail. However, for more complex structures like disk coils, finite-length solenoids and flat planar spirals, which do not easily lend themselves to closed form solutions, approximation techniques and handbook methods are more appropriate, [169]. An excellent reference for inductance calculation is given by Frederick Grover in [42]. In this book there is an extensive list of inductance calculations for different kinds of wire loops. In the same book Grover gives correction factors to account for high frequency operation, which is especially useful in the current work, and other effects such as the insulation thickness of wires. In close collaboration with Grover, Bashenoff developed an accurate set of inductance calculation formulae for the inductance of single-turn close form antennas of many shapes and the results are reported in these two papers, [170], [171]. Another good source of inductance calculations is the *Radio Engineer's Handbook* in [43], edited by Terman. In this reference, the inductance calculation formulae are presented for many different coil shapes such as single -turn loops, rectangles, multiple-layer coils and solenoids.

4.4.2.1 Inductance Calculation

Short-solenoid. In the case of a finite-length solenoid with radius a and length ℓ made of round wire, the inductance can be calculated with good accuracy by using one of the Wheeler formula

given as follows, [172, 173]:

$$L \approx \frac{10\pi\mu_o N^2}{9a + 10\ell} \text{ microhenries} \tag{4.16}$$

The accuracy of this expression is better than 1% if the length of the solenoid is larger than $0.8a$. However, for a short-solenoid coil the accuracy of the above expression (4.16) is compromised. Therefore, an alternative approach for the inductance of a short-coil is required based on Nagaoka's formula. Nagaoka's solution supports the inductance calculation on the well-established method for the inductance of a cylindrical current sheet of infinite length and applies a correction to take into account the effect of the ends. Nagaoka's formula is expressed below, [42]:

$$L = 0.004\pi^2 \left(\frac{a^2}{\ell}\right) N^2 K \text{ microhenries} \tag{4.17}$$

K is defined as a reduction factor which depends only on the shape of the coil and takes account of the effect of the ends. Tables for values of the constant K as a function of the shape ratio $\frac{2a}{\ell} = \frac{\text{diameter}}{\text{length}}$ are reproduced by Grover and Roza in [42] and [174] respectively. The theoretical formula for K for a short coil is given as follows, [175]:

$$K = \ln(1 + \pi a/\ell) + 0.4347 \tag{4.18}$$

Based on this modification, a much more accurate formula is suggested by Wheeler in [175]:

$$L = \mu_o N^2 a \left(\ln(1 + \pi a/\ell) + \frac{1}{2.3 + 1.6\ell/a + 0.44(\ell/a)^2}\right) \text{ microhenries} \tag{4.19}$$

It is reported in the same paper by Wheeler that the above expression for the inductance of a short solenoid (4.19) produces a relative error less than 0.001.

It is also suggested by Grover that the interpolation of the tabulated values for K becomes uncertain for very short coils. Consequently, the reader is encouraged to use the following alternative series expression in order to derive values of K:

$$K = \frac{2\beta}{\pi}\left[\left(\ln\frac{4}{\beta} - \frac{1}{2}\right) + \frac{\beta^2}{8}\left(\ln\frac{4}{\beta} + \frac{1}{8}\right) - \frac{\beta^4}{64}\left(\ln\frac{4}{\beta} - \frac{2}{3}\right) + \frac{5}{1024}\beta^6\left(\ln\frac{4}{\beta} - \frac{109}{120}\right) - \cdots\right] \tag{4.20}$$

where $\beta = \ell/2a$. For values of β as large as $\frac{1}{4}$ three terms will suffice for an accuracy better than one part in a thousand.

Flat spiral coil of round wire. Planar spiral coils constructed of round wire have been ex-

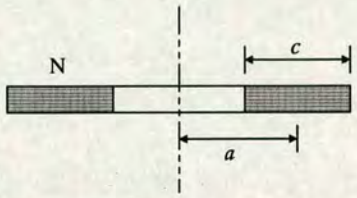

Figure 4.17: *Cross section for a pancake flat circular spiral.*

tensively used in inductive coupling and in biomedical telemetry applications since the early 1960's. The self-inductance of such coils, also known as pancake coils, can be computed based on Wheeler's formula:

$$L = 31.33\mu_o N^2 \frac{a}{8a + 11c} \text{ microhenries} \tag{4.21}$$

where a in this case is the coil mean radius and c is the thickness of the winding. Wheeler states that the formula is correct to within 5% for coils with $c > 0.22a$ as shown in Fig. 4.17. This formula was adopted to calculate the inductance of the flat spiral coils depicted in Fig. 4.15. Wheeler's formula (4.21) is accurate for closely-wound coils of many turns, which is true for the coils used during the experimental phase of this work.

Printed spiral coils. Technological advancements in the areas of microwave integrated circuits and miniature power electronic components resulted in an increasing use of on-chip planar spiral coils. Especially in the RFID domain, printed spiral antenna coils are used in an ever-increasing extent. Due to the fact that spiral inductors are fundamental components for a wide range of applications, the study of their electrical properties has received a lot of attention from many researches, see e.g. [137, 139, 176–181]. A number of methods are available for the computation of the inductance of a round spiral coil. Starting with Grover's formula, the self-inductance of a circular spiral of strip conductor is given as:

$$L = \frac{15\mu_o}{\pi} aPN^2 \text{ microhenries} \tag{4.22}$$

where a is the mean coil diameter in meters and P is the form factor depending on $c/2a$, where c is the thickness of the winding as stated before. However, this equation is applicable if the inner and outer radii of the coil are not too different as for example in a hollow inductor, which is clearly not the case for the coil shown in Fig. 4.15. Alternatively, for coils with windings spread over the area of the coil, Schieber [182] calculates the inductance based on the following expression:

$$L = 1.748 \times 10^{-5} \mu_o \pi d_{out} N^2 \text{ Henries} \tag{4.23}$$

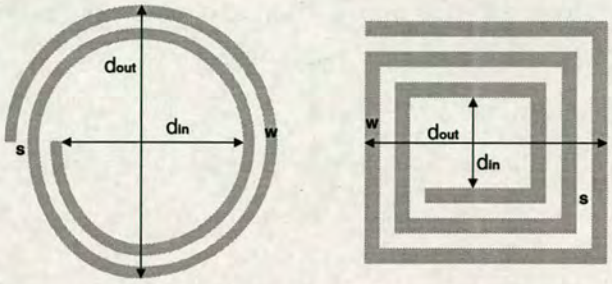

Figure 4.18: *Realization of circular and square printed spiral inductor coils.*

In the case of the printed square spiral coils, the inductance is more difficult to calculate analytically. This is due to the fact that it is more complex to quantify the effect of mutual coupling for the square geometry. In conjunction to Wheeler, Terman and Grover, detailed inductance calculations for square planar spirals are given in references by Greenhouse , [181], and Mohan et al., [176]. These papers are particularly interesting as they compare methods of calculation of planar spiral coils with experimental and numerical results. Based on these references, two simple and accurate expressions for the inductance of printed square spiral coils are given below. According to Greenhouse, Bryan's method suggests that the inductance of a flat square coil is of the form:

$$L = 0.024aN^{5/3}\ln[8(a/c)] \text{ microhenries} \tag{4.24}$$

for dimensions expressed in centimeters. The constants in (4.24) above are defined as follows:

$$a = \frac{d_{in} + d_{out}}{4} \tag{4.25}$$

$$c = \frac{d_{in} + d_{out}}{2} \tag{4.26}$$

and N is the number of turns. Simple analytic approximate expressions as the one given in (4.24) are known to produce errors in the region of 20%. Alternatively, Greenhouse suggests a method based on Grover's work on the inductance of a rectangle of round wire. Although accurate, this technique is cumbersome for initial coil design and optimisation. Therefore, in order to design the square spiral coils used in this work, a much more accurate approximation given by Mohan et al. is adopted:

$$L = K_1\mu_o\frac{N^2 d_{avg}}{1 + K_2\varphi} \tag{4.27}$$

where φ defines the fill ratio of the coil expressed as $\varphi = (d_{out} - d_{in})/(d_{out} + d_{in})$ and the average diameter is $d_{avg} = 0.5(d_{out} + d_{in})$. K_1 and K_2 are layout dependent coefficients equal

to 2.34 and 2.75 respectively. Derived from a modified Wheeler expression, expression (4.27) yields a typical error in the order of 2% to 3% and qualifies for the design purposes of this work. An alternative simple and accurate expression for the inductance of planar spirals is suggested by Mohan et al. which is obtained by approximating the sides of the spirals by symmetrical currents sheets of equivalent current densities. Based on this principle the following expression is introduced, [176]:

$$L_{gmd} = \frac{\mu N^2 d_{avg} c_1}{2} \left[\ln(\frac{c_2}{\varphi}) + c_3\varphi + c_4\varphi^2 \right] \tag{4.28}$$

In the previous formula (4.28), the coefficients c_1, c_2, c_3 are layout dependent and values are provided in Table II of [176]. For the circular spiral geometries these coefficients are reproduced here: $c_1 = 1.00$, $c_2 = 2.46$, $c_3 = 0.00$ and $c_4 = 0.20$. Note that for typical integrated spiral inductors with $s \leq w$ expression, (4.28), exhibits a typical error in the region of 8%. Subsequently, for the applications studied in this work (4.28) is sufficiently accurate.

In addition to the calculated value, the coil impedance was measured for both the TX and RX coils used and the results are summarized in Tables 4.5 and 4.6.

4.4.2.2 Coil resistance calculation

The notion of coil impedance was first introduced in chapter 3 and is revisited here for the prototype coils fabricated in this work. A major challenge in the design of magnetic storage elements that operate at high frequencies is the difficulty to account for all the parasitic effects completely and accurately. In an attempt to predict the impedance of the air-cored coils designed in this work, a simple lumped parameter equivalent circuit model is adopted, shown in Fig.4.19.

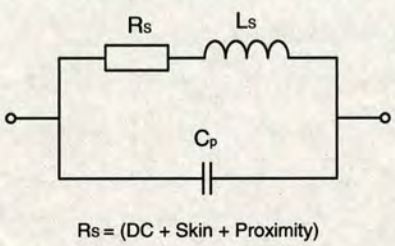

Figure 4.19: *Equivalent circuit for air-core spirals. R_S is the frequency dependent winding resistance, L_s represents the inductance of the spiral, and C_p is the distributed capacitance.*

Expressions for inductance calculation for all the prototype coils employed in this work were

discussed in the previous sections. The focus now shifts from the imaginary to the real part of the impedance of the coil, representing the series resistance in the lumped circuit model. The calculation of the resistance in a coil operating at high frequencies necessitates three additive resistive effects to be considered. These components are defined as the DC resistance R_{DC}, the skin effect R_{SE} resistance and the proximity effect R_{PE} resistance, [91,92]. Both the DC and the skin effect resistance are well-defined in the literature, see e.g. [53,58]. On the contrary, the proximity effect is a much more complicated phenomenon. The classical proximity effect occurs when an external magnetic field intersects a current carring conductor, creating eddy currents which introduce additional losses. Since the proximity effect is more pronounced for closely wound coils such as the ones used in this work, it should be considered. Consequently, the total resistive losses can be expressed as:

$$R_S = R_{DC} + R_{SE} + R_{PE} \tag{4.29}$$

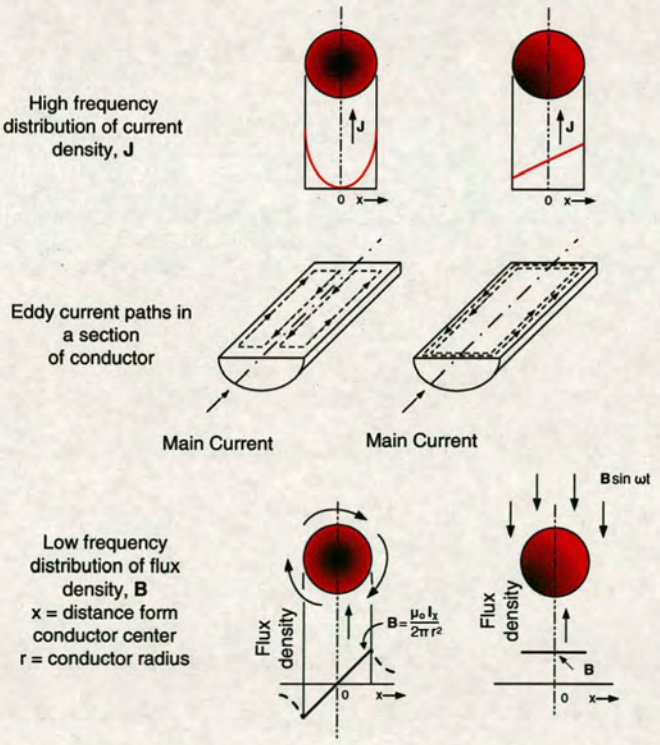

Figure 4.20: *Skin and proximity effects in round conductors, [54].*

Short-solenoid. The AC resistance of the short solenoid coil is studied first. A comprehensive analysis of solenoid losses was presented by Medhurst in [93,94]. This work forms the basis of AC resistance calculations since. Prior to the publication of Medhurst's work, the calculation of

the coil resistance was based on the theoretical work of Butterworth, [91,92]. However, Butterworth's results are seriously flawed for short coils with closely-spaced turns. This inaccuracy is attributed to Butterworth's false assumption of a uniform current distribution in the conductor. On the other hand, Medhurst's method provides an accuracy better than 3% provided the ratio of skin depth to wire diameter is less than $1/10$. In this context, referring to Table. 4.4 Medhurst's regime is applicable in the HF operation of wires whose diameter is 0.5m or larger. This is the case for the 18 and 19 SWG conductor used.

Frequency (f) MHz	Skin depth (δ) μm
1	66.6
3	38.49
6.7	25.75
7.78	23.90
13.5	18.14

Table 4.4: *Skin depth δ for copper wire ($\sigma = 5.7 \times 10^7\ S/m$) at 25° Celcius.*

The AC resistance of a short-solenoid with less than 30 turns is given by Medhurst as follows, [93,94]:

$$R_{AC} = \frac{R_{DC}\ \Xi\ \Phi\ (N-1)}{N} \tag{4.30}$$

The AC resistance as expressed by (4.30) can be perceived as the DC resistance of the inductor, denoted R_{DC}, multiplied by a skin effect factor Ξ. The DC resistance is given by, [53]:

$$R_{DC} = \frac{\rho \ell_w}{A_w} \tag{4.31}$$

where ρ is the resistivity, ℓ_w is the length of the conductor, $A_w = \pi d^2/4$ is the cross sectional area of the wire, d is the diameter of the wire and finally Ξ is defined as follows:

$$\Xi = d^2[4(d\delta - \delta^2)] \tag{4.32}$$

where δ is the skin depth at the frequency considered.

Medhurst derived equation (4.30) by applying a tentative but plausible end-correction factor at long solenoid coils. The end correction factor $(N-1)/N$ has no effect for a long solenoid with a large number of turns N. Therefore, expression (4.30) can equally well describe the AC losses of both long and short solenoid coils. Medhurst's table of Φ values for various solenoid length/diameter and wire spacing/diameter ratios is reproduced in appendix G.

Printed spiral coils. The computation of the series resistance in a spiral coil is a much more complex task. A detailed discussion on the design of integrated spiral inductors is given in

two papers published by Yue et al., [178, 179]. In these papers the resistance of the coil is treated as a parasitic effect. The reason is that, since an inductor is primarily a magnetic energy storage device, the inevitable presence of resistance and capacitance degrade the performance of the coil and are thus considered parasitics. In a similar manner to the solenoid coils, the resistance of a printed spiral inductor is frequency dependent due to skin and proximity effects. The mechanism behind this phenomenon is the fact that, as frequency departs from a DC value, the current density in the wire becomes non-uniform. This is explained due to the formation of eddy currents in the conductor which manifest themselves as skin and proximity effects. It follows that eddy currents generate a magnetic field which opposes the original field according to Lenz's law. In view of this, the time-varying magnetic field induces eddy currents in the conductor it-self for the skin effect case. However, it is the influence of a neighbouring time-varying field, produced by an adjacent conductor, that causes the proximity effect. Irrespective to whether a conductor carries a current or not, once the proximity effect takes place, eddy currents are induced in this conductor due to cross-coupling of the adjacent turns in a coil. The presence of eddy currents reduces the net current flow in the conductor, which results in an increase of the AC resistance. Consequently, the total eddy current contribution can be accounted by superimposing the contributions due to the skin and proximity effects.

Compact modelling expressions that account for the skin and proximity effects in printed spiral inductors are limited in the literature. Most of the existing tools for modelling eddy current losses in spiral coils are based on finite-element techniques involving computationally intensive algorithms, [180]. The only available analytical model known to the author, which describes the proximity and skin effects in spiral coils, is introduced from Talwalkar et al. in [180]. In this paper, Talwalkar models a single-turn spiral as a sum of two orthogonal transmission lines. However, the results describe the substrate losses rather than the resistance in the conductor itself. On the other hand, Yue et al. in [179], suggests the following expression for the series resistance of planar spirals:

$$R_S = \frac{\rho \cdot \ell}{w \cdot t_{eff}} \tag{4.33}$$

where ρ and ℓ represent the resistivity and the length of the wire respectively and w is the track width. In order to account for the skin effect Yue et al. introduces the term t_{eff} in (4.33), which accounts for the effective thickness of the wire expresses as follows:

$$t_{eff} = \delta \cdot (1 - \exp^{-t/\delta}) \tag{4.34}$$

where t is the physical thickness of the conductor listed in Table 4.6 for the prototype coils

used. According to Wheeler, [183], it is difficult to determine analytically the significance of the mutual eddy current and the resulting increase in resistance caused by the proximity effect. Yue in [179] investigated this problem by using an electromagnetic field solver based on the finite element method. In the results of this analysis reported in the same paper, Yue et al. dismiss the proximity effect on coplanar turns of the spiral coil as negligible at the frequency of 1GHz. In the intermediate frequency range where this work is focused at, it is the opinion of the author that the proximity effect is a more significant contributor to the losses of the coil than the skin effect. This can be justified with reference to Table. 4.4 where the skin depth at the frequencies of interest is much greater than the conductor track thickness of $35\mu m$. Therefore, for the design of the printed spiral coils used in this work, the drawback in the above expression (4.33) is that it does not take into account the proximity effect. However, in the absence of a more accurate analytic expression, (4.33) was adopted as a first approach to estimate the series resistance of the prototype coils. The results of the calculated losses are tabulated in Table 4.6. A comparison between the measured and calculated results in Table 4.6 reveals that expression (4.33) underestimates the series resistance for the TX square spiral coil. It is worth remembering that Yue's model is developed to describe parasitics on integrated inductors. Since the coils designed for this work are significantly larger some degree of error is expected. Consequently, the expressions used for the derivation of the ohmic losses in the coil were used to provide an indication of the value to be expected. For practical impedance matching purposes, discussed in section 4.2.3, the measured value of the series resistance (R_S) for all the prototype coils used was employed in the series-to-parallel transformation calculation.

In the printed circular spiral case Pettenpaul et al. in [184] suggest the following technique for the derivation of R_S based on experimental data published by Haefner, [185]. The series resistance of a circular printed spiral according to the previous references is given as:

$$R = \frac{\ell}{\sigma \cdot w \cdot t}\left[\frac{0.43093 \cdot x_w}{1 + 0.041(\frac{w}{t})^{1.19}} + \frac{1.1147 + 1.2868 \cdot x_w}{1.2296 + 1.287 \cdot x_w^3} + 0.0035 \cdot \left(\frac{w}{t} - 1\right)^{1.8}\right] \quad (4.35)$$

for $x_w \geq 2.5$. Alternatively, for the spirals PSC1 and PCS2 in Table 4.6 where $x_w \prec 2.5$, $x_w = (2 \cdot f\sigma \cdot \mu \cdot w \cdot t)$ being a normalised frequency, the above expression simplifies as follows:

$$R = \frac{\ell}{\sigma \cdot w \cdot t}\left[1 + 0.0122 \cdot x_w^{(3+0.01 \cdot x_w^2)}\right] \quad (4.36)$$

where ℓ is the length of the conductor and σ is the conductivity of the conductor. In addition, w

and t stand for the width of the conductor and thickness of the metallization of the copper track respectively. The accuracy of (4.36) suffers for the dimensions of the prototype coils fabricated for the experimental phase of this work. The expressions mentioned previously, (4.35,4.36), are originally intended for integrated inductor spirals with $w/t \prec 12$ and $x_w \prec 20$ where an accuracy of 3% is reported. In order to achieve better accuracy, sophisticated numerical methods need to be consulted, which is beyond the scope of this work. The exact calculation of the frequency dependent resistance of a metallic conductor with rectangular cross section is a very demanding task. Therefore, an approximate formula of equation (4.36) was employed here to provide an estimate of the parasitic effects. The results of the calculation using this method for the two circular printed spiral coils used in this work are listed in Table 4.6.

Flat spiral coils. Finally, an expression for the total resistance of close wound air-core spirals of copper enameled wire, such as coils FCS1 and FCS2, is given by Rodriguez et al. in [130]. In this paper the total effective AC resistance of the coils considering the contributions of the skin and proximity effects expressed in (4.29) can be written as:

$$R = \frac{2\rho}{a^2}\sum_{i=1}^{N} b_i \left(1.25 + \frac{a}{2}\sqrt{\frac{\pi f \mu_{int}}{\rho}}\right) + \frac{(\pi \mu_{ext} f)^2 a^4}{2\rho}\sum_{j=1}^{N} b_j \left(\sum_{i=1}^{N}\left[\frac{K(k_{ij})}{b_i + b_j} + \frac{E(k_{ij})}{b_i - b_j}\right]\right)^2 \quad (4.37)$$

In the above expression (4.37) μ_{int} represents the permeability of the conductor, μ_{ext} is the permeability of the surrounding media, b_i is the radius of the i^{th} loop, ρ the resistivity and a is the radius of the wire. Also, the functions $K(k_{ij})$ and $E(k_{ij})$ are the elliptic integrals of the first and second kind as defined in appendix B and $k(i,j)$ is the modulus of the elliptic integrals expressed as:

$$k_{ij} = \frac{2\sqrt{b_i b_j}}{b_i + b_j} \quad (4.38)$$

In expression (4.37), Rodriguez considers the contribution of the skin and proximity effects on the DC resistance of the spiral. However, although in principle this approach is correct (4.37), it tends to overestimate significantly the resistance of the inductor in comparison to the measured value shown in Table 4.6. The proximity effect is evaluated by Rodriguez as the power loss in a single wire due to the presence of an external uniform magnetic field across the conductor, based on the proximity effect loss given by Snelling, [54]:

$$P_{PE} = \frac{\pi^3 f^2 B^2 \ell a^4}{2\rho} \quad (4.39)$$

where a is the wire radius, ℓ is the wire length and B is the magnetic flux density.

The error in (4.37) can be accounted to the fact that the field induced at the center of each turn is computed by Rodriguez to be a summation of the individual contributions of all the other turns. This result is considered to be the value of B in the loss formula (4.39). Considering an N turn spiral the effect the N^{th} turn has on the first, although present, is negligible compared to the influence of the adjacent turns.

Therefore, an alternative approach for the computation of the AC resistance of the flat spiral coils FSC1, FSC2 was adopted. Starting from the RF resistance of round copper wire, as evaluated by Ramo et al. in [53], the result can then be multiplied by the total length of the wire in the spiral-loading coil to yield the overall resistive losses. It follows from the discussion in section 2.9.2 that the high frequency impedance of a round conductor is given by the following expression:

$$R = \frac{R_S}{\sqrt{2}\pi r_o}\left[\frac{Ber(q)\,Bei'(q) - Bei(q)\,Ber'(q)}{Ber'(q)^2 + Bei'(q)^2}\right] \tag{4.40}$$

In (4.40) above, the surface resistance of the conductor R_S, can be derived by expression (2.75) as shown in chapter 2. In addition, r_o is the conductor radius and the constant q can be computed by equation (2.9.2.1).

Hence, the AC resistance of a spiral coil made of round wire, denoted as R_{FS}, can be approximated as follows:

$$R_{FS} = \ell \cdot R \tag{4.41}$$

where ℓ is the total length of the conductor in the coil computed by:

$$\ell = \pi \frac{d_{out}^2 + d_{in}^2}{8\, r_o} \tag{4.42}$$

where d_{in} and d_{out} are the internal and external diameter of the spiral coil respectively.

The computed AC resistance of spirals FSC1, FSC2 is listed in Table 4.6. It is evident that the latter approach underestimates the resistance of the coils as it does not include the contribution of the proximity effect. However, in the absence of a more accurate formula, this method provided a closer estimate compared to the Rodriguez method.

4.4.3 Driving the coils

In order to maximise the power transfer between the two coils it is necessary to maximise the current in the TX coil. One way of achieving this is to employ resonance so that a large alter-

nating current is induced in the coil for a relatively small driving power. The main disadvantage of this method is that the impedance of a parallel resonant tank circuit goes to infinity at resonance, making it difficult to match power into it. One solution to this is to tap the coil at a low impedance point (a small number of turns above ground on the coil) and feed power in at that point. This can give a reasonable match to a 50 ohm generator. A further refinement is to add a variable matching unit to tapping point of the coil. This can consist of either a variable T network of an inductor and two capacitors, or a π network consisting of an inductor and two capacitors. Once this is adjusted to minimise reflected power at the power amplifier, the power fed to the coil is maximised. This arrangement is illustrated in Fig. 4.21 below.

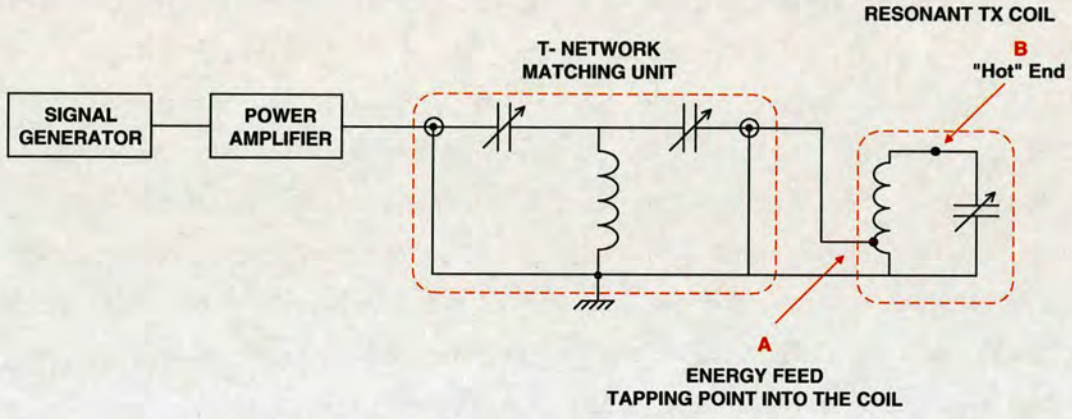

Figure 4.21: *Block Diagram of Matching Process.*

It is probably worth considering what happens in the LC tank circuit. The power delivered to the resonant TX tank is actually only delivered into the losses in the coil/capacitor and any energy coupled into other RX circuitry. At this stage it is worth noting that the L and C are reactive components and if both components were truly lossless the voltage across them and the current through them would go to infinity. In practice the losses in the circuit limit both the voltage and the current. The delivered power is dissipated in the losses of the coil in the form of heat. The disadvantage of using resonance to drive the coil current is that the system will have an inherently narrow bandwidth, which is not a problem in power transfer applications but could be a drawback in communication applications involving wideband data. A further problem in the embedded sensor scenario is that immersion of the RX tank circuit in a conducting medium such as biological tissue would introduce considerable losses to the tuned circuit. It follows that this could also cause a considerable change in the stray capacitance associated with the coil resulting in detuning.

4.4.4 Resonant TX, RX loop antenna coils

This section describes the TX, RX coils being used in the experimental verification. The electrical parameters of the prototype coils were calculated during the design phase. The methods used to calculate these parameters are described in section 4.4.2. The calculated electrical parameters where used in the design phase to estimate the inductance and resistance of coils for the frequencies of interest and coil dimensions selected. Once constructed, all the prototype coils where characterised using the HP 8753C Network Analyzer and HP 85046A S-Parameter Test Set. The measured values for the inductance and resistance were used for calculating the capacitance required to resonate the coils at the specified frequency. In addition, measured values were also used for matching the RX to the rectifier and dummy load in power transfer measurements. Smith chart plots generated by the VNA are given in Figures 4.24, 4.25, 4.26, 4.27, and represent impedance measurements of the prototype coils. The amount of power reflected from a device is directly related to the impedance of both the coils being measured and the measuring system of the NVA. In fact, each value of the reflection coefficient (Γ) uniquely defines a coil impedance. A reflection coefficient of $\Gamma = 0$ can only occur when the device being measured and test set impedance are exactly the same. On the other hand, a short circuit exhibits a reflection coefficient of $\Gamma = 180°$. Every other value for Γ corresponds to a specific complex device impedance, according to the equation, [163], [186], [71]:

$$Z_n = \frac{1+\Gamma}{1-\Gamma} \tag{4.43}$$

where Z_n is the DUT impedance normalized to 50 Ohms, which is the default VNA characteristic impedance. The impedance value for the prototype coils can be extrapolated from the Smith chart plots. At the frequency of interest a marker displays the impedance value in the $R + j\ X$ format, where R is the resistive component and X is the reactive component of the coil's complex impedance. The geometric characteristic as well as the measured and calculated electrical characteristics of the coils are included in Tables 4.5 and 4.6 given below.

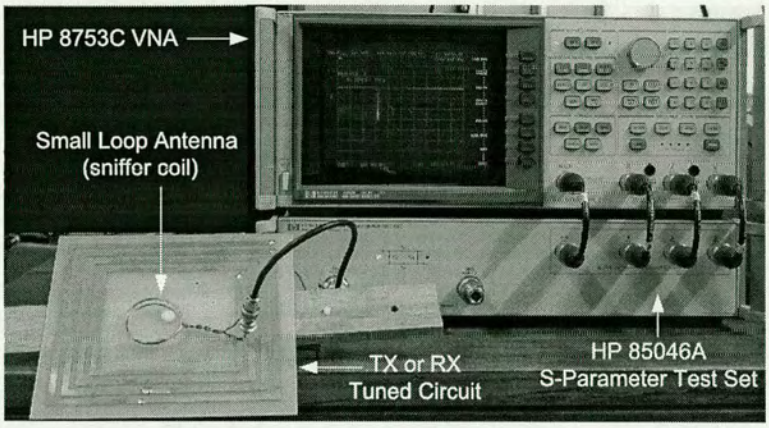

Figure 4.22: *Photograph depicting the S11 reflection measurements setup used in order detect the precise resonant frequency of the TX, RX parallel tank circuits.*

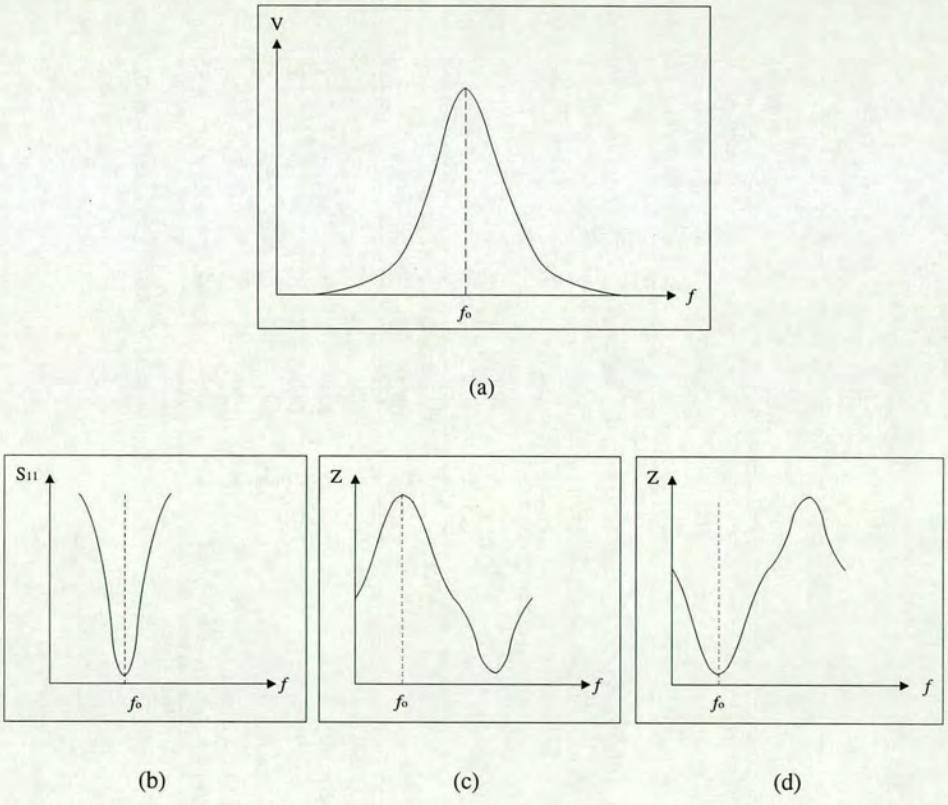

Figure 4.23: *Frequency responses for resonant circuit topologies: (a) Voltage versus frequency for resonant circuit, (b) S11 Response, (c) Impedance Response for a Parallel Resonant Circuit, (d) Impedance Response for a Series Resonant Circuit.*

Coil Type	SWG	a	ℓ	N	Z_{meas}	L_{cal}	L_{meas}	Rs^{*}_{cal}	$Rs^{\star}_{cal}$	f	Q
-	-	Radius/mm	Length/mm	Turns	(ohms)	(μH)	(μH)	(Ohms)	(Ohms)	(MHz)	-
A (Short Solenoid)	18	200	10	8	$65.25 + j1.99k$	73.598	105.26	7.72	4.81	2.7	30
B (Short Solenoid)	18	100	10	8	$103.75 + j2.3k$	32.6	54.8	5.69	3.59	6	22
C (Short Solenoid)	19	34	8	7	$2.297 + j344.7$	16.16	8.18	3.41	2.20	6	150

Table 4.5: *Short Solenoid Coil Characteristics. Column Rs^{*}_{cal} presents the ohmic AC resistance calculated based on Medhurt's formula whereas $Rs^{\star}_{cal}$ shows the results based on Smith's method.*

Coil Type	SWG	d_{in} (mm)	d_{out} (mm)	N -	w (mm)	s (mm)	t (μm)	L_{cal} (μH)	L_{meas} (μH)	Z_{meas} (Ohms)	Rs_{cal} (Ohms)	f MHz	Q -
FCS1 (Circular Spiral)	19	95	200	40	-	-	-	141	348.6	$-32.375 + j2.19k$	1.72	1	68
FCS2 (Circular Spiral)	18	60	120	20	-	-	-	46.22	44.2	$1.938 + j277.7$	0.85	1	143
PCS1 (Printed Circular Spiral)	-	105	180	4	5	5	35	3.22	3.611	$1.172 + j152.04$	0.2268	6.7	130
PCS2 (Printed Circular Spiral)	-	65	90	4	2	2	35	2.13	2.15	$0.734 + j90.59$	0.3417	6.7	123
PSS1 (Printed Square Spiral)	-	105	170	4	5	5	35	3.92	4.074	$1.734 + j199.15$	0.4258	7.78	115
PSS2 (Printed Square Spiral)	-	45	80	4	2	2	35	1.66	1.86	$0.879 + j90.906$	0.5175	7.78	103

Table 4.6: *Flat and Printed Spiral Coil Characteristics*

The TX and RX circuits must both be tuned to the same resonance frequency to ensure maximum power transfer and read range. In order to test the tuning of the TX and RX circuits two methods were used, as suggested by Youbok in [187].

A voltage measurement method was used to tune the TX and an S-Parameter reflection measurement using a Network Analyzer was preferred for the RX circuit. The two techniques are described as follows: *Voltage Measurement Method for TX coil, Fig. 4.21:*

- Tune signal generator at the resonance frequency
- Connect to the tap in the coil, point A
- Connect the Tektronix TDS 210 oscilloscope to the "hot" end of the tank circuit
- Tune the capacitor or the coil while observing the signal amplitude on the oscilloscope
- The circuit is resonating once the maximum voltage is reached

S-Parameter Return Loss Measurement Method for either TX or RX coils:

- Set up an S-Parameter Test Set (Network Analyzer) for S11 measurement, and do a calibration
- Measure the S11 for the resonant circuit
- Reflection impedance or reflection admittance can be measured instead of the S11
- Tune the capacitor or the coil until a null (S11) occurs at the resonance frequency, f_o. For the impedance measurement, the maximum peak will occur for the parallel resonant circuit, and minimum peak for the series resonant circuit as illustrated in Fig. 4.23.

All the prototype coils used in this work exhibit very sharp resonances due to their high quality factors as shown in Tables 4.5 and 4.6. Therefore, in order to fine tune the resonant circuits, the return loss measurement method is preferred. The inductance of the coils was calculated using approximate formulas as discussed in section 4.4.2, which allowed the capacitor value to be estimated in order to tune the LC circuits in the TX and RX ends. The resonant frequency and quality factor of the tuned coils were measured using the HP 8553C VNA and a small loop sniffer coil. The same procedure was implemented for fine tuning the RX ensemble as shown

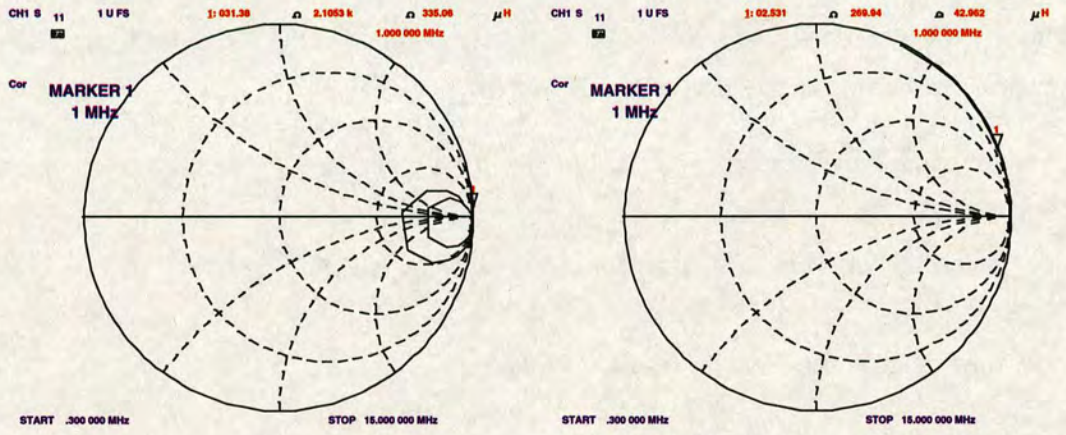

(a) (b)

Figure 4.24: *HP8753C Network Analyzer Screen Capture - S11 Smith Chart Impedance Characteristics at 1MHz: (a) FCS1 Circular Spiral Coil, (b) FCS2 Circular Spiral Coil.*

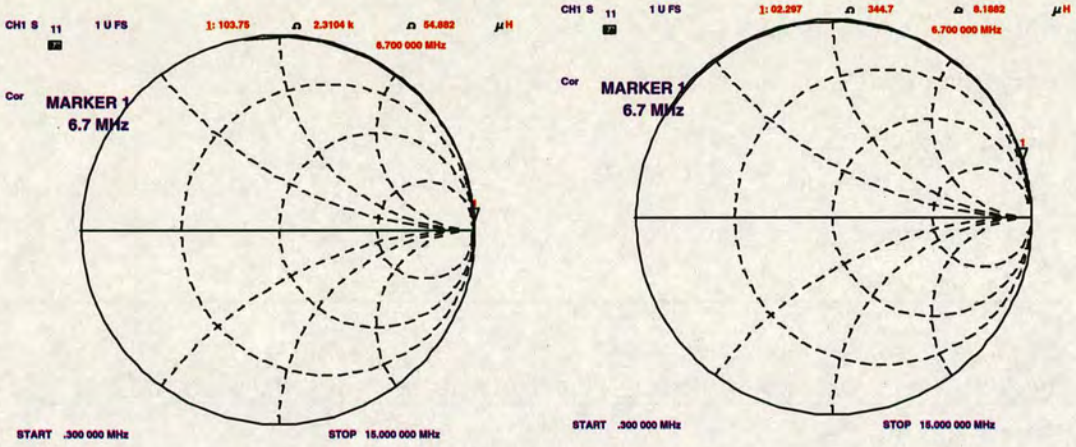

(a) (b)

Figure 4.25: *HP8753C Network Analyzer Screen Capture - S11 Smith Chart Impedance Characteristics at 6.7 MHz: (a) B Small 8-turn loop Antenna Coil, (b) C Small 8-turn loop Antenna Coil.*

in Fig. 4.22. Screen captures of the S11 reflection measurements conducted using the method described previously are given in Fig. 4.29.

In Fig. 4.23, the null at the resonant frequency represents a minimum input reflection at the resonance frequency. This means that the tuned circuit absorbs the signal at the resonant frequency and other frequencies are reflected back. In Fig. 4.23(c), the impedance curve exhibit a peak

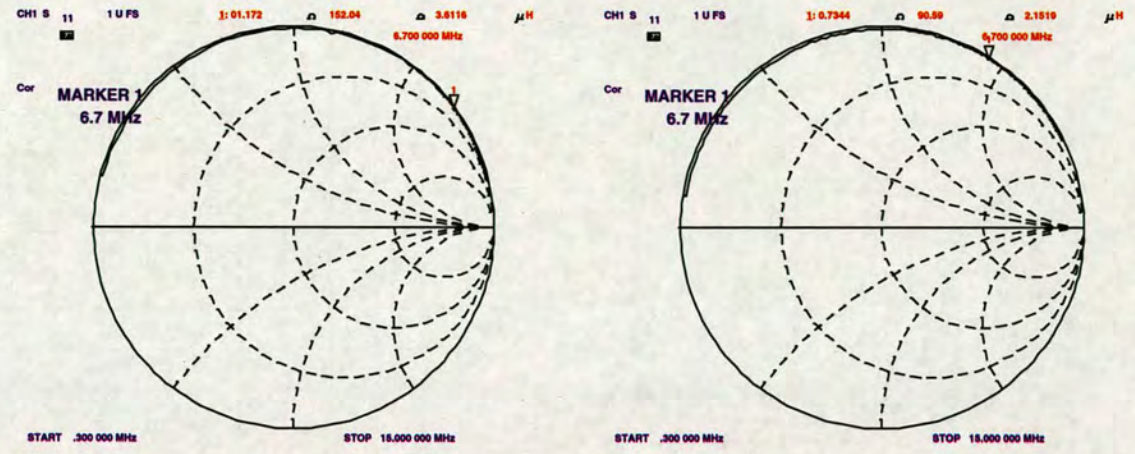

(a) (b)

Figure 4.26: *HP8753C Network Analyzer Screen Capture - S11 Smith Chart Impedance Characteristics at 6.7MHz: (a) PCS1 Circular Spiral Coil, (b) PCS2 Circular Spiral Coil.*

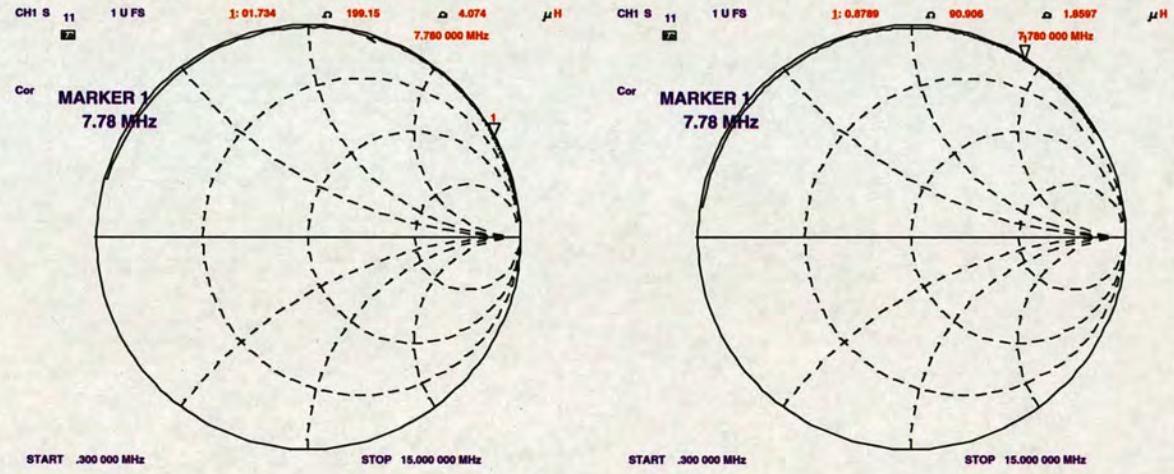

(a) (b)

Figure 4.27: *HP8753C Network Analyzer Screen Capture - S11 Smith Chart Impedance Characteristics at 7.78MHz: (a) PSS1 Square Spiral Coil, (b) PSS2 Square Spiral Coil.*

at the resonant frequency. This is due to the behaviour of the parallel resonant circuit which shows a maximum impedance at resonance. On the other hand, Fig. 4.23(d) shows the response of a series resonant circuit. Since the series resonant circuit has a minimum impedance at the resonant frequency, a minimum peak occurs at the resonant frequency.

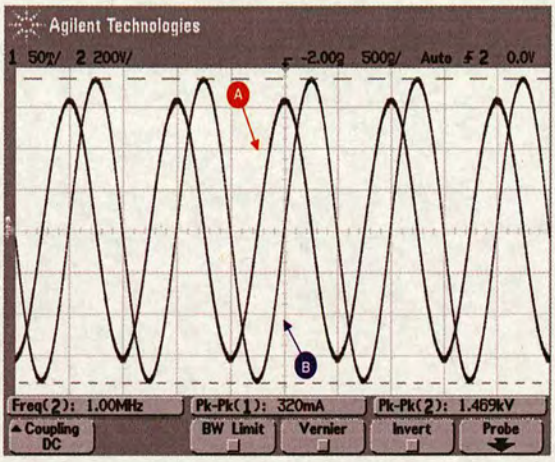

(a) Resonance in flat spiral coil.

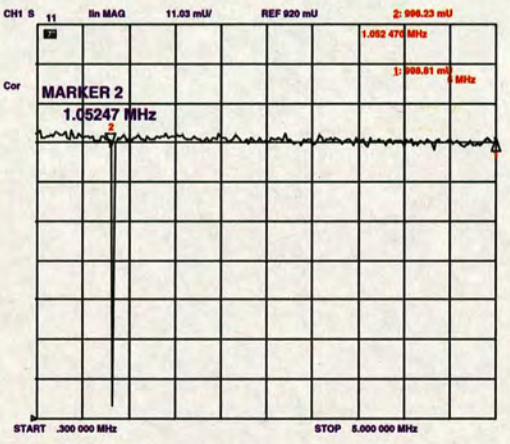

(b) S11 measurement for flat spiral coil.

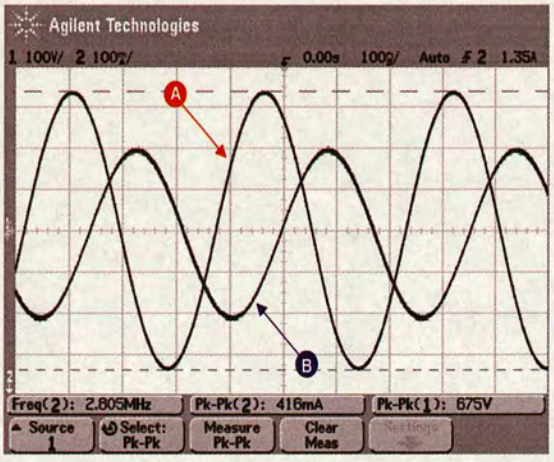

(c) Resonance in solenoid coil.

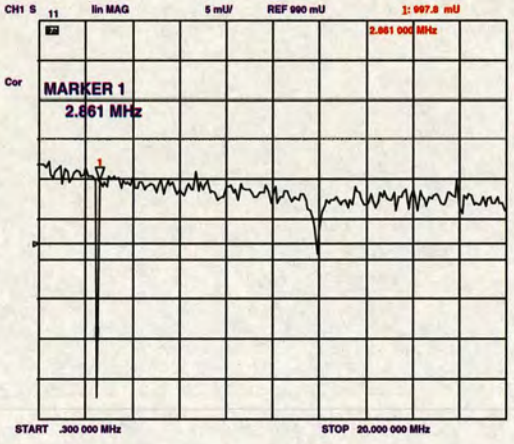

(d) S11 measurement for solenoid coil.

Figure 4.28: *The screenshots on the left ((a), (c)) represent the current (A) and voltage (B) waveforms in the TX coils at resonance. The screenshots on the right ((b), (d)) represent the S11 measurements for the flat spiral coil and solenoid TX coils respectively.*

4.5 Experimental Results

The following paragraphs present the experimental findings for the magnetic field measurements and the power coupling between the solenoid, flat circular spirals, printed circular and square spiral coils. The results presented below show close correlation with the analytical expressions for the power transfer functions developed in chapter 4. The trend of the experimental results follows closely the analytical model. However, the presence of some degree of error

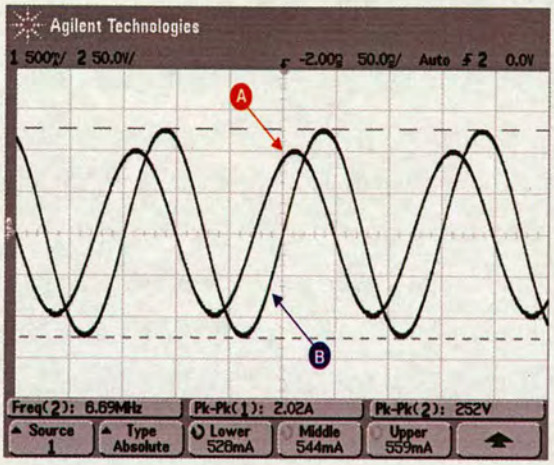

(a) Resonance in printed circular spiral coil.

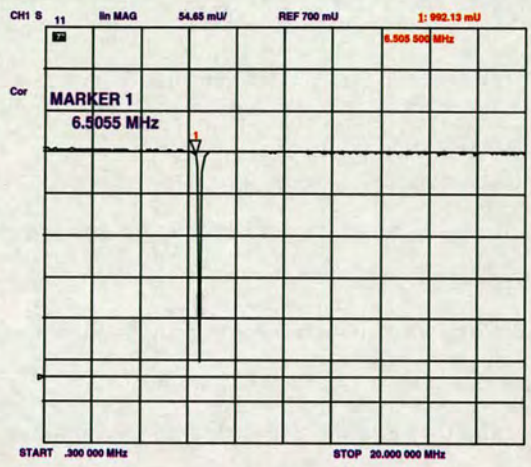

(b) S11 measurement for printed circular spiral.

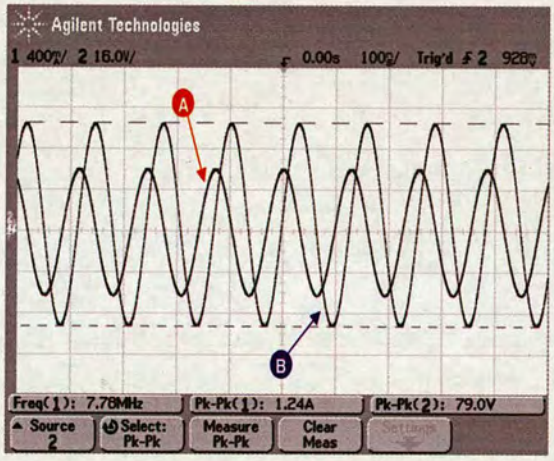

(c) Resonance in printed square spiral coil.

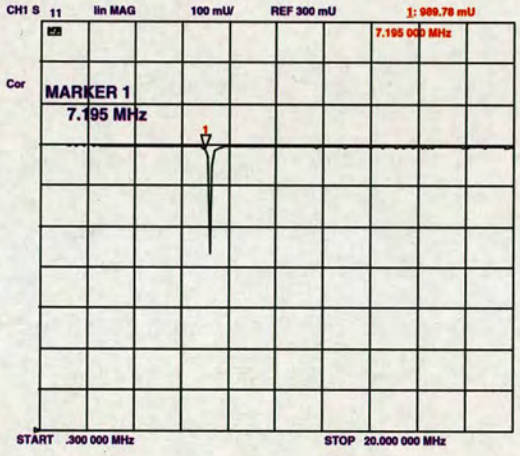

(d) S11 measurement for printed square spiral coil.

Figure 4.29: *The screenshots on the left ((a), (c)) represent the current (A) and voltage (B) waveforms in the TX coils at resonance. The screenshots on the right ((b), (d)) represent the S11 measurements for all the printed circular and square spiral TX coils respectively.*

between the measured and analytical results is inevitable and will be fully addressed and quantified in section 4.6. The agreement is quite reasonable in view of the thin-wire approximation used in the mathematical modelling presented in chapter 3.

4.5.1 Results of the magnetic near-field measurements

This section presents the results from the magnetic near-field measurements for the coil geometries discussed in this chapter. To verify the model discussed in chapter 3, magnetic field measurements of four different coil sources above level ground, that of a solenoid, round wire spiral and printed circular and square spiral coils, were performed. The findings of the field tests are explained below for each individual coil geometry. The agreement between theoretical and experimental data is reasonable given the detailed differences between the coil construction and the thin-wire approximation used in the mathematical modelling. A detailed comparison of the true and measured H_z field component is given in this section. The relative percentage error present is determined by the relative deviation of the field component measured by the probe with the true field as follows:

$$e_r = \left[\frac{X_{\text{Measured}} - X_{\text{Analytical}}}{X_{\text{Analytical}}}\right] \cdot 100 \tag{4.44}$$

with X being the rms value of H_z.

Conversion to a decibel value requires the following formula for the field strength:

$$e_r(\text{dB}) = 20 \cdot \log\left[\frac{100 + e_r}{100}\right] \tag{4.45}$$

A detailed error analysis is included in section 4.6. The possible error sources are determined and discussed in detail and finally an error budget is introduced for measurements carried out in each orientation. In a near-field electromagnetic environment, measurement of magnetic field strengths is subject to potentially large error due to a number of factors such as nonuniform spatial variation of the electromagnetic field components, the influence of the measuring probe itself and interactions between the source and nearby objects. The aforementioned parameters are some of the factors that have a significant adverse effect on the measurement accuracy. Recognizing this, it is essential to introduce and discuss in detail these effects in order to estimate the measurement uncertainty for both tests discussed in this chapter. Hence, the validity of the presented results, for the near-field measurements and the power transfer evaluation, is quantified.

4.5.1.1 Magnetic near-field measurements for solenoid coil A.

The results of the magnetic field measurements from the short-solenoid source coil A are presented first. Fig. 4.30 depicts the measured and calculated magnetic field strength generated

from the short-solenoid coil A. The solid red and dotted blue lines represent the calculated and experimental data for the field strength of the dominant H_z magnetic field component respectively.

The results from the field measurements from all three orientations studied are shown in Fig. 4.30. The discrepancy between the predicted field strength and the measured value is very low for the short-solenoid source. In Fig. 4.31 the relative percentage error and the dB error is given. In the coaxial orientation the relative percentage error is in the order of 8% for the coaxial orientation, 4% for the lateral displacement and 7% for the angular misalignment. Subsequently, the measured magnetic field attenuation with increasing misalignment correlates well with the theoretical predictions. The small error observed can be attributed to the fact that the 20 cm radius coil source is much larger than the dimensions of the measurement sensor. Hence, the effects of impedance coupling were insignificant. To guarantee that the influence of the sensor dimensions are minimised, no measurements can be performed in the close vicinity of the source. It is interesting to note that it was possible to overcome this problem by employing a larger TX coil which was less likely to be loaded by the measurement probe itself. It is clear from the experimental results shown in Fig. 4.30 and Fig. 4.31 that this method was succesfull.

4.5.1.2 Magnetic near-field measurements for Flat Circular Spiral FCS1.

In the same manner for the flat circular spiral coil source FCS1 the results from the magnetic field measurements are shown in Fig. 4.32. It is evident that in the coaxial and lateral orientations the measured data follow closely the theoretical predictions. In Fig. 4.33 the relative percentage and dB error is plotted separately for measurements in each orientation. It should be noted that the maximum percentage error in the coaxial scenario is in the order of 8% whereas in the lateral misalignment the relative percentage error is in the order of 15%. In both the coaxial orientation and lateral or radial measurements, the accuracy of the measurement results is very good. The dimensions of the 20cm external diameter spiral FCS1 coil source are still significantly larger than the 3.5cm diameter HP 11941 probe. Therefore, the accuracy of the measurements is not compromised by the presence of the sensor probe. However, in the angular orientation the relative percentage error is much larger in the order of 40%. The increased percentage error in this case is ascribed to errors in the winding of the spiral. In practice the turns of the spiral are not perfect circles as expected by the theory. Hence, it was not possible to accurately place the probe at the center of the spiral. Alternatively, the probe was positioned

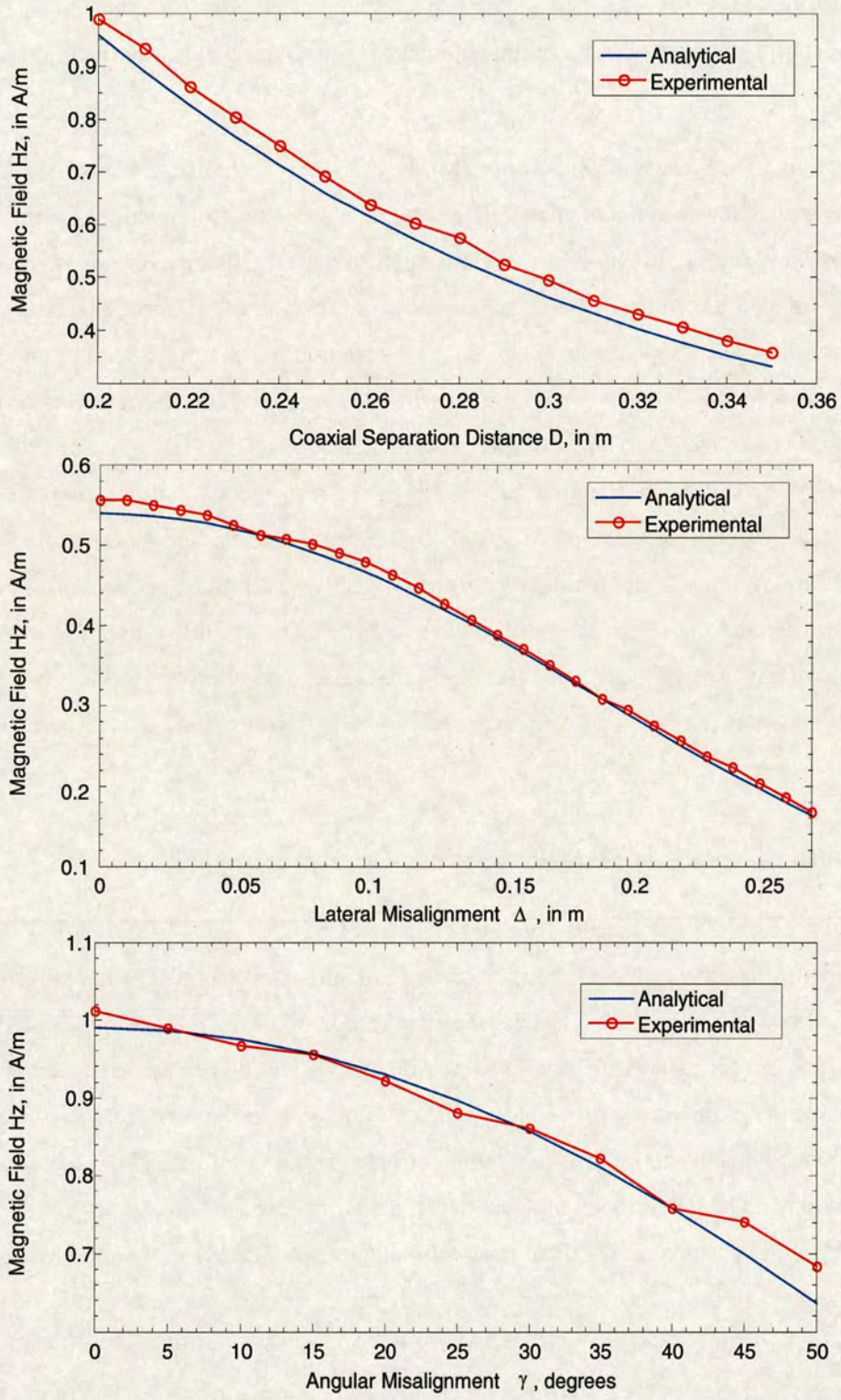

Figure 4.30: *H_z magnetic field component, measured by the HP 11941A probe, in the coaxial orientation, lateral and angular misalignments, as generated by a short-solenoid TX coil. The current I_{TXrms} in the TX coil is 160mA.*

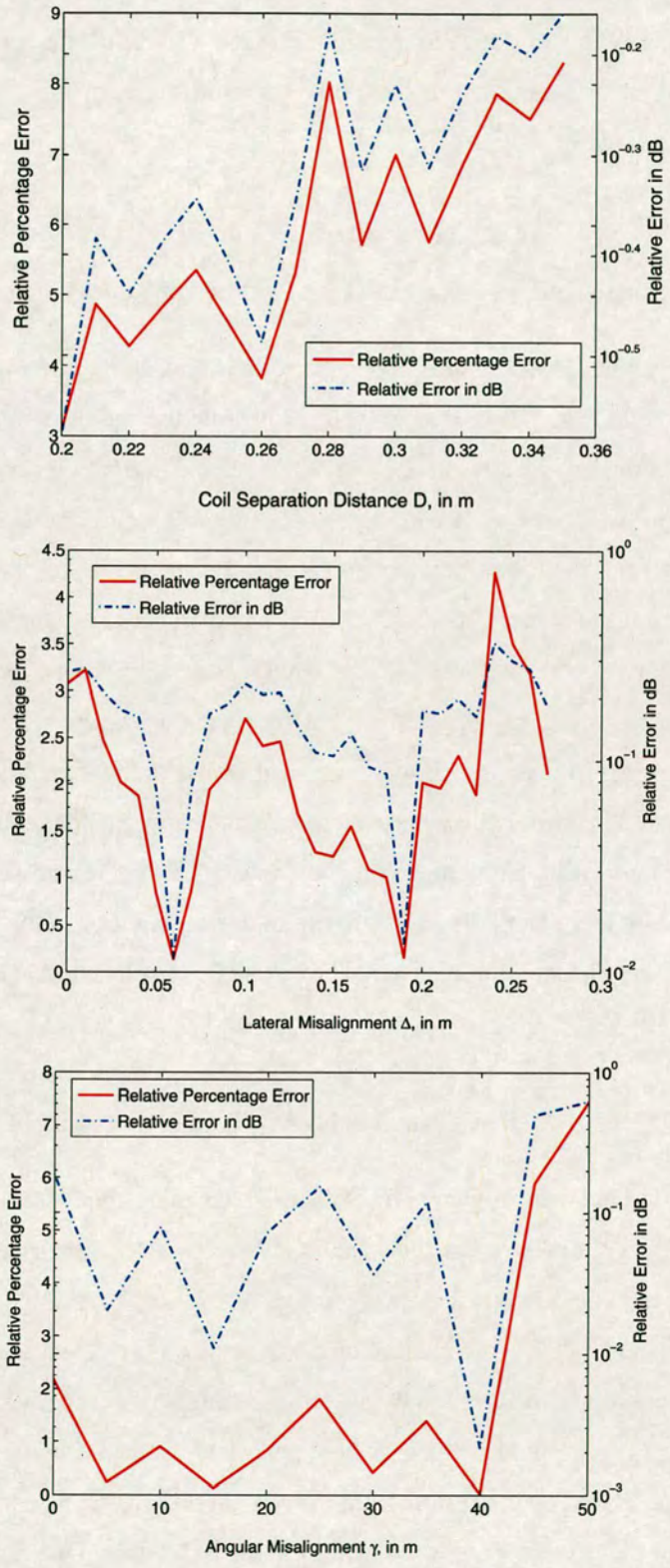

Figure 4.31: *Relative percentage and dB error for the H_z magnetic field component, measured by the HP 11941A probe, in the coaxial orientation, lateral and angular misalignments, as generated by a short-solenoid TX coil.*

approximately at the center of the source which ultimately introduced some added error. Although, this type of error cannot be neglected the trend of the experimental data still follows closely the theoretical curve in Fig. 4.32.

4.5.1.3 Magnetic near-field measurements for Printed Circular Spiral PCS1.

In the case of a printed circular spiral coil source the trend of the measured results follow the theoretical curve in Fig. 4.34. However, for this structure the error in all orientations is more pronounced compared to the solenoid coil since the source coil is smaller and therefore more easily affected by the sensor probe. In the coaxial orientation the only apparent significant mismatch between theory and measurement is the decrease in the field attenuation rate at great distance from the source. This effect can be explained as the receiver probe reaches the noise-floor, adding to the measured field strength. An attempt was made to resolve this issue by adding an instrumentation amplifier between the measurement probe and the spectrum analyzer. However, this approach was soon abandoned as the signal was being distorted by the amplifier and the additional wires required were introducing some unwanted capacitive coupling. Another interesting phenomenon is the crossing of the theoretical and experimental curves at a distance of 35cm from the source in the coaxial orientation. This is further evidence that the near-field probe is detuning the source coil at distances close to the coil.

4.5.1.4 Magnetic near-field measurements for Printed Square Spiral PSS1.

The results of the H_z field measurements from the printed square spiral coil PSS1 are conveyed in Fig. 4.36. The degree of error in this case is analogous to the error seen for the printed circular spiral source. The relative percentage and dB error is given in Fig. 4.37. Referring to Fig. 4.37 it can be shown that in the coaxial measurements the percentage uncertainty is 40%, 20% in the lateral configuration and finally 30% for the angular arrangement. The uncertainty in the measurements is attributed to the effect the near-field probe has on the impedance of the resonant coil source. Based on the results from the coaxial orientation measurements, shown in Fig. 4.36, it is clear that as the probe approaches closer to the source the discrepancy between the measured and calculated results is more pronounced. In an attempt to minimise the distortion due to the field probe no measurements where carried out at a distance smaller than 20cm from the source in both the lateral and angular configurations.

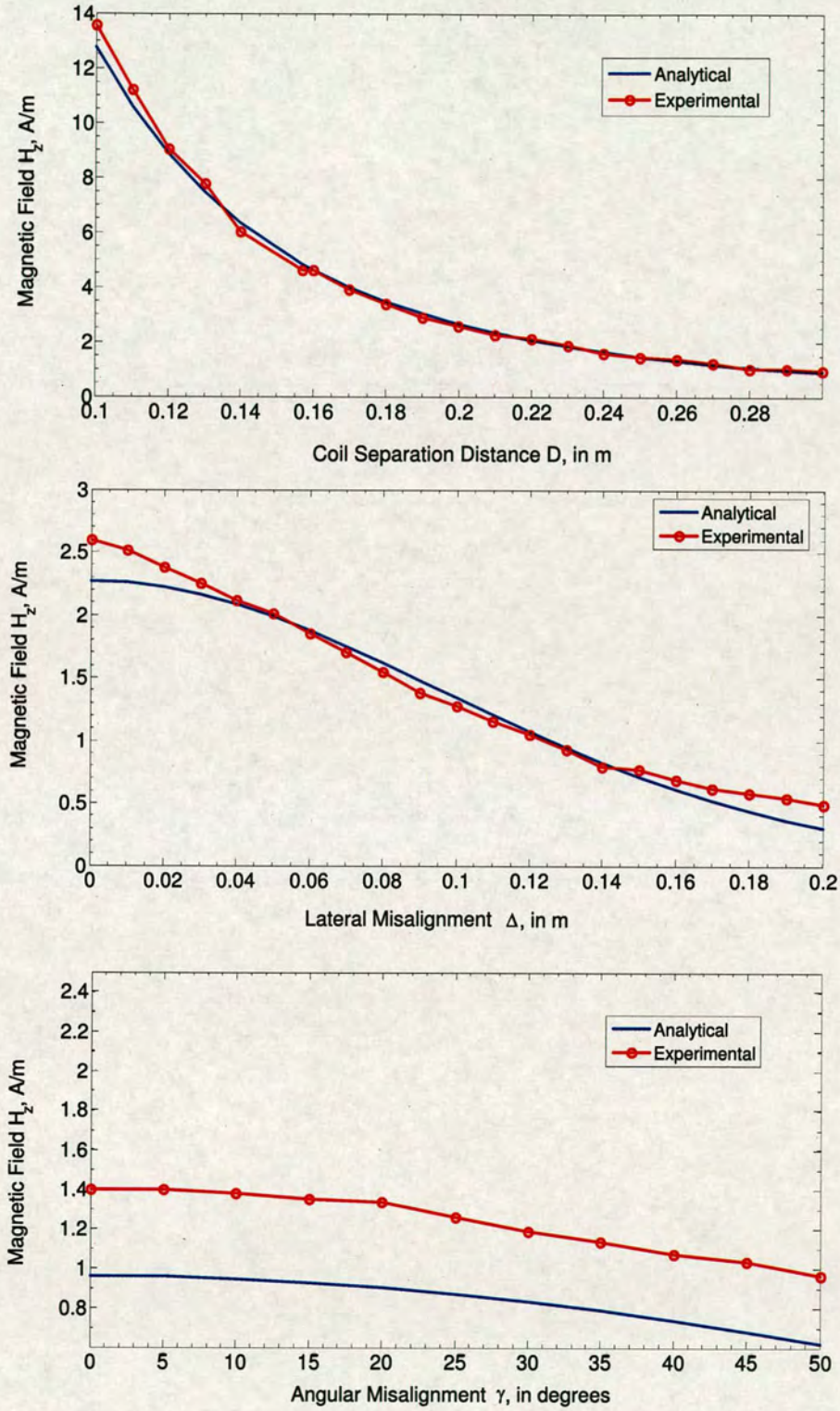

Figure 4.32: *H_z magnetic field component, measured by the HP 11941A probe, in the coaxial orientation, lateral and angular misalignments, as generated by the FCS1 printed circular spiral TX coil. The current I_{TXrms} in the TX coil is 300mA.*

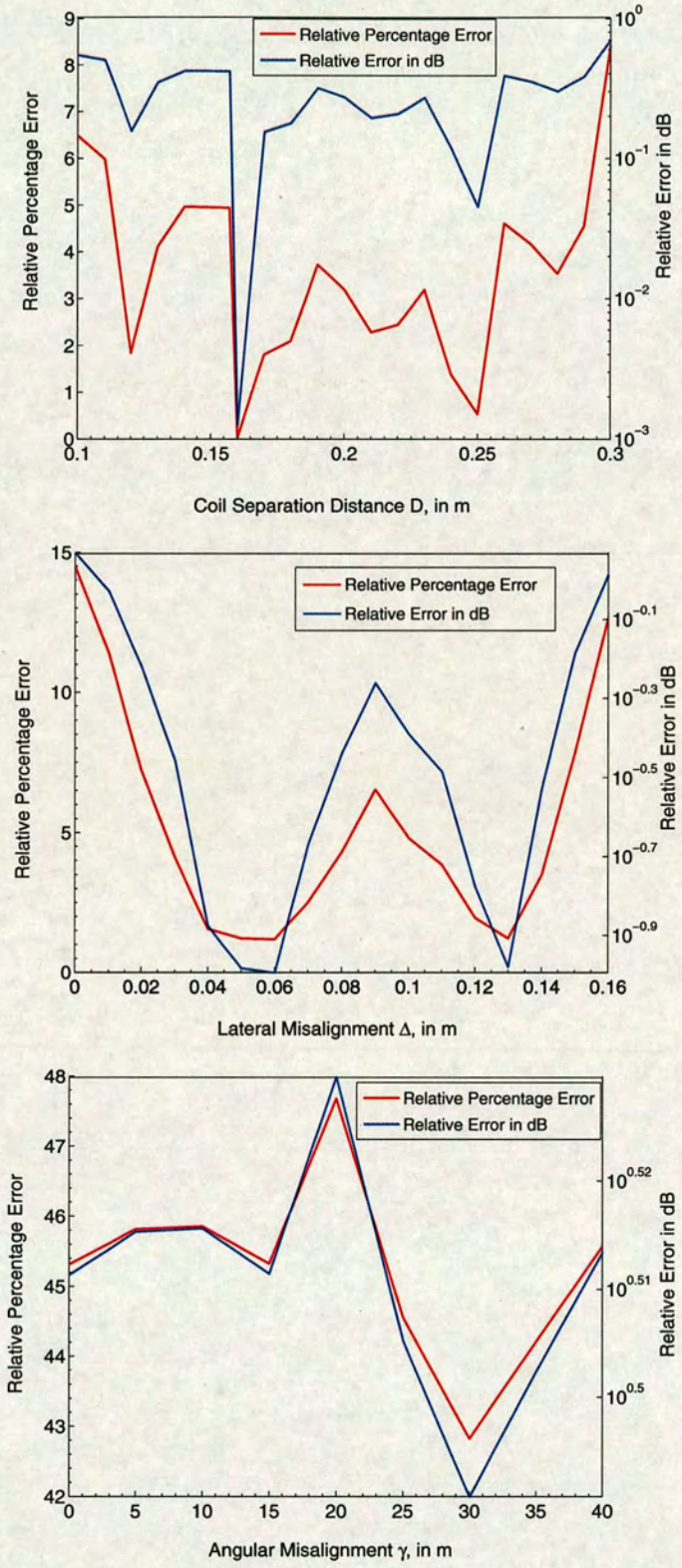

Figure 4.33: *Relative percentage and dB error for the H_z magnetic field component, measured by the HP 11941A probe, in the coaxial orientation, lateral and angular misalignments, as generated by the flat spiral TX coil FCS1.*

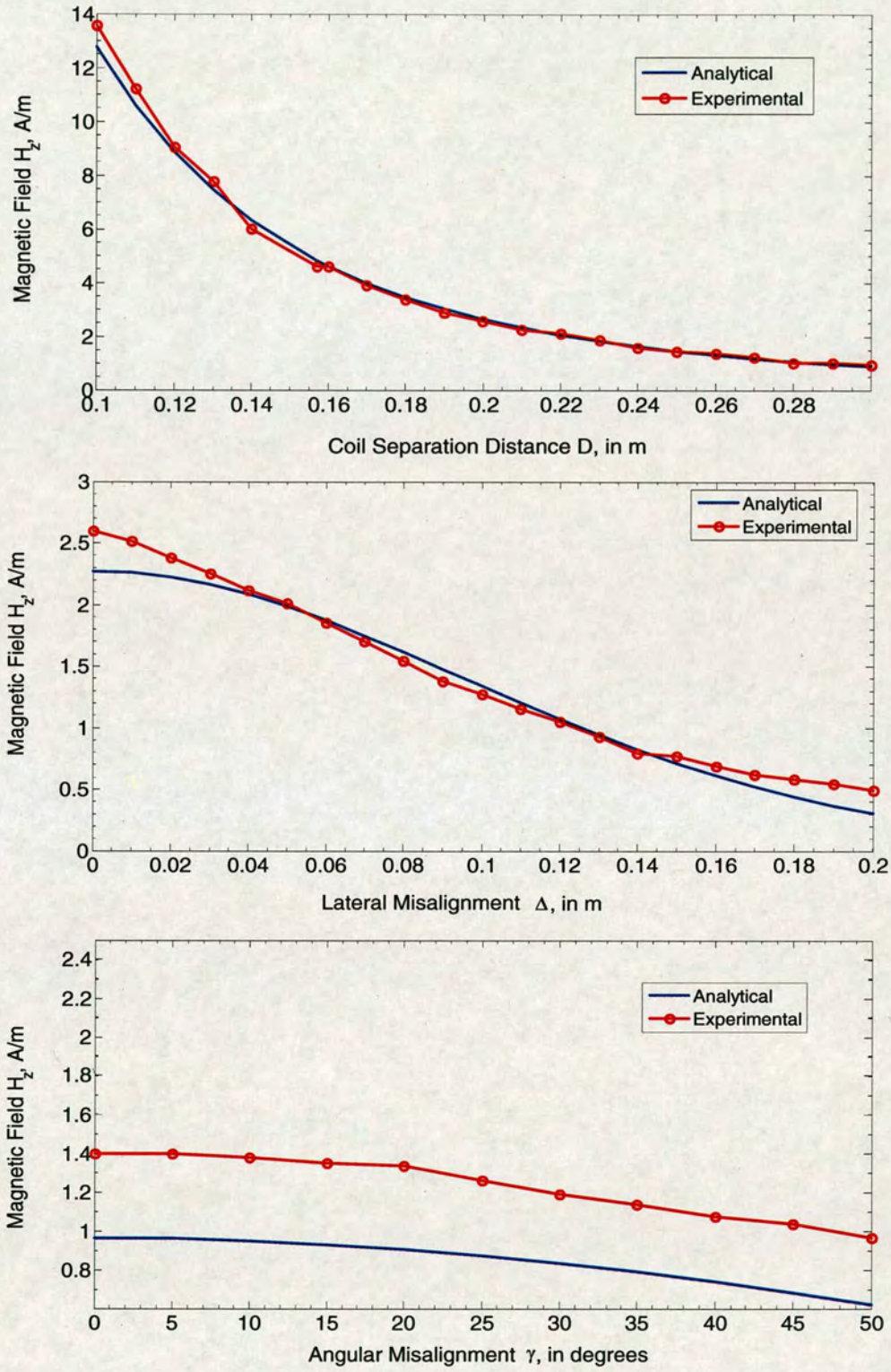

Figure 4.34: *H_z magnetic field component, measured by the HP 11941A probe, in the coaxial orientation, lateral and angular misalignments, as generated by the PCS1 printed circular spiral TX coil. The current I_{TXrms} in the TX coil is 1.4A.*

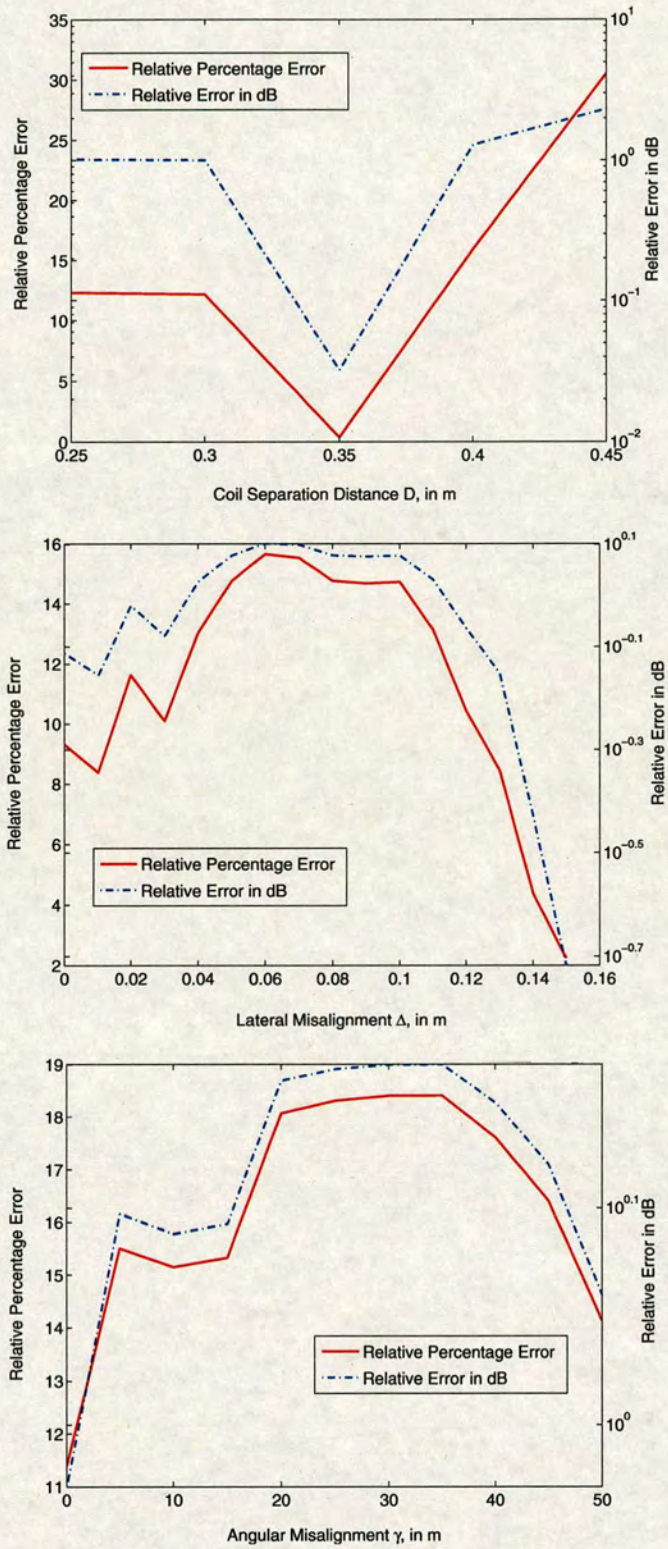

Figure 4.35: *Relative percentage and dB error for the H_z magnetic field component, measured by the HP 11941A probe, in the coaxial orientation, lateral and angular misalignments, as generated by the printed circular spiral TX coil PCS1. The current I_{TXrms} circulating in the TX coil is 160mA.*

At this stage it should be noted that the theoretical H_z magnetic field strength for the circular and square spirals is computed based on the approximation of the coils are composed of concentric loops of infinitesimal conductor width. Clearly, the construction of the prototype coils is somehow different which is expected to cause some discrepancies between the experimental and the analytical results. Hence, this should be taken into consideration when interpreting the results.

4.5.2 Results of coupling measurements

Following the magnetic field measurements the results from the coupling experiments can be now discussed. This section is organised in three subsections, which include the results of the experiments for the solenoid, flat spiral, printed circular and square spiral coils.

4.5.2.1 Power transfer between solenoid coils

Fig. 4.38 shows the results of the power transfer measurements for the short solenoid coils B and C, when the coils are situated in a coaxial orientation and for a lateral displacement and angular tilt of the RX coil. The blue solid line represents the analytical power transfer functions (3.83,3.87,3.90) derived in chapter 4. The red line illustrates the experimental data from the coupling test. The rectified voltage (V) induced at the RX coil is measured by a digital multimeter as discussed in section 4.3. For each RX coil the load resistance is decided by the impedance matching technique using equation (4.7). Hence, for a known input power at the TX coil considered as the transmitted power (P_{TX}) the received power at the RX side can be easily derived as:

$$P_{RX} = \frac{V_{\text{meas}}^2}{R_{\text{Load}}} \tag{4.46}$$

Referring to the coaxial measurements in Fig. 4.38, it is evident that as the RX coil approaches the TX, the mutual coupling between the coils has a significant effect on the power transfer. It can be seen from Fig. 4.38 that for the dimensions of the prototype coils used in the measurements, the assumption of poorly coupled coils employed in the development of a theoretical model, is not valid for a small coil separation distance. As the RX coil approaches the TX its presence detunes the TX coil. This is caused by an increased coupling coefficient for the link. Under these circumstances the poor coupling scenario is not valid. In addition, the TX coil is a very high Q coil which exhibits a very sharp resonance. Consequently, stray capacitances from

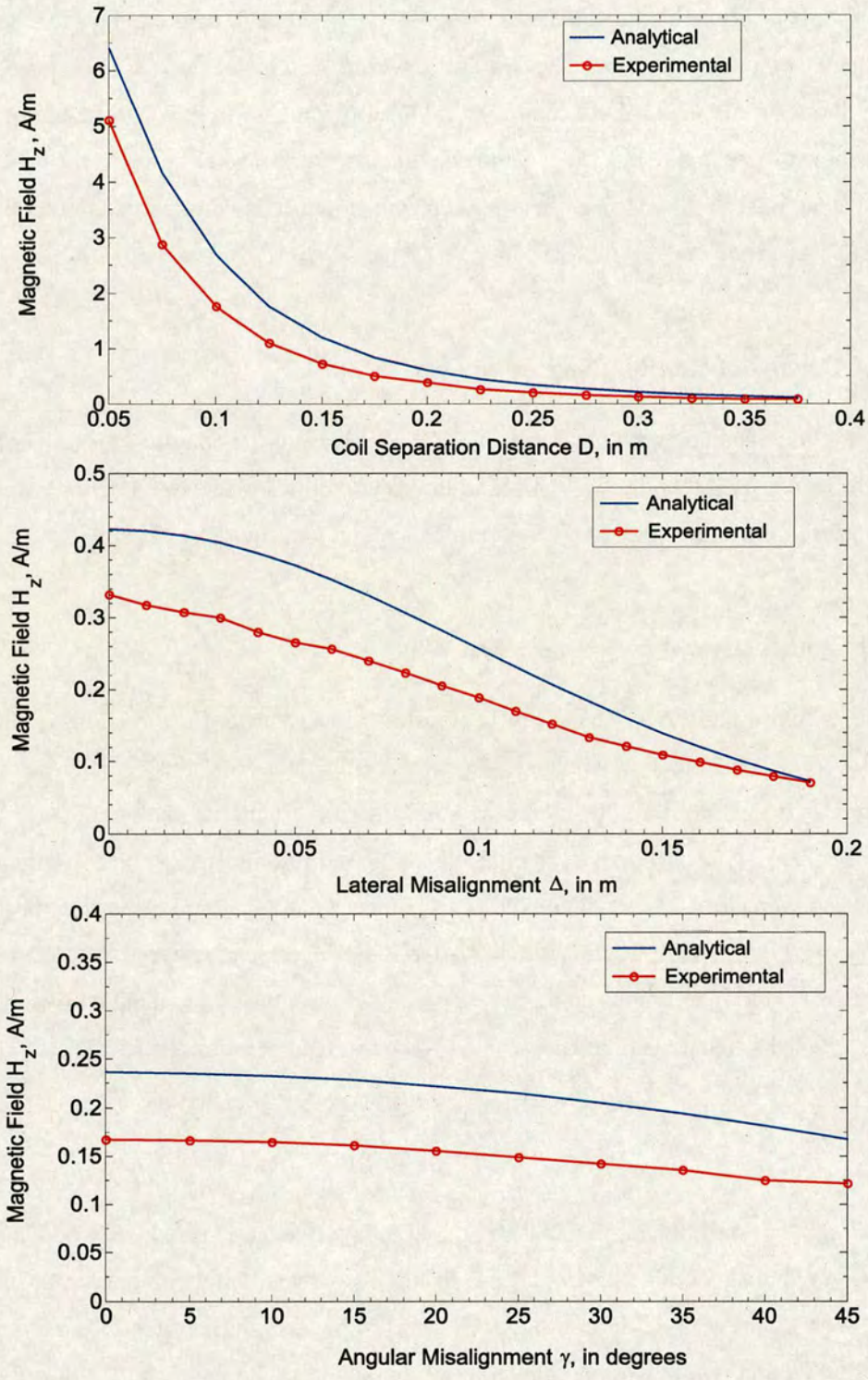

Figure 4.36: *H_z magnetic field component, measured by the HP 11941A probe, in the coaxial orientation, lateral and angular orientations, as generated by the PSS1 printed square spiral TX coil. The current I_{TXrms} circulating in the TX coil is 350mA.*

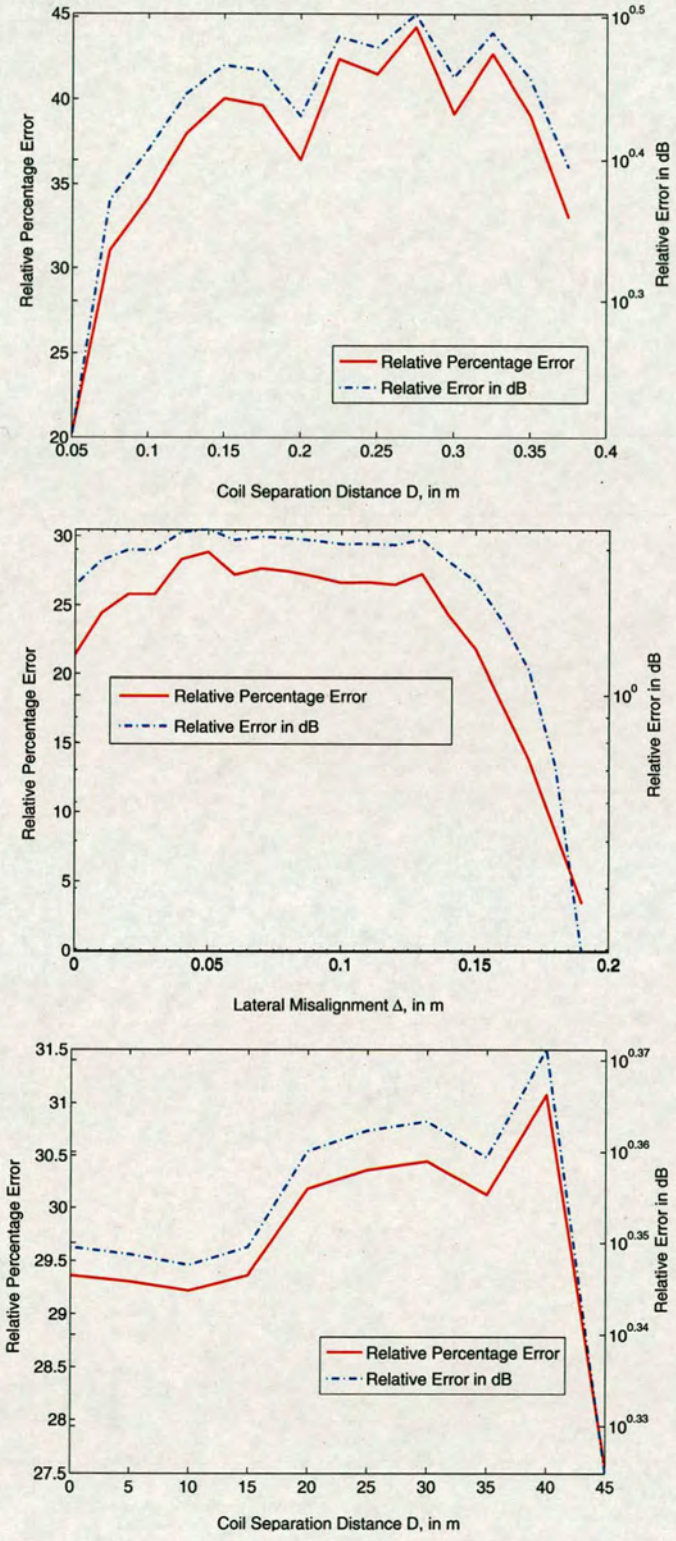

Figure 4.37: *Relative percentage and dB error for the H_z magnetic field component, measured by the HP 11941A probe, in the coaxial orientation, lateral and angular misalignments, as generated by the printed square spiral TX coil PSS1.*

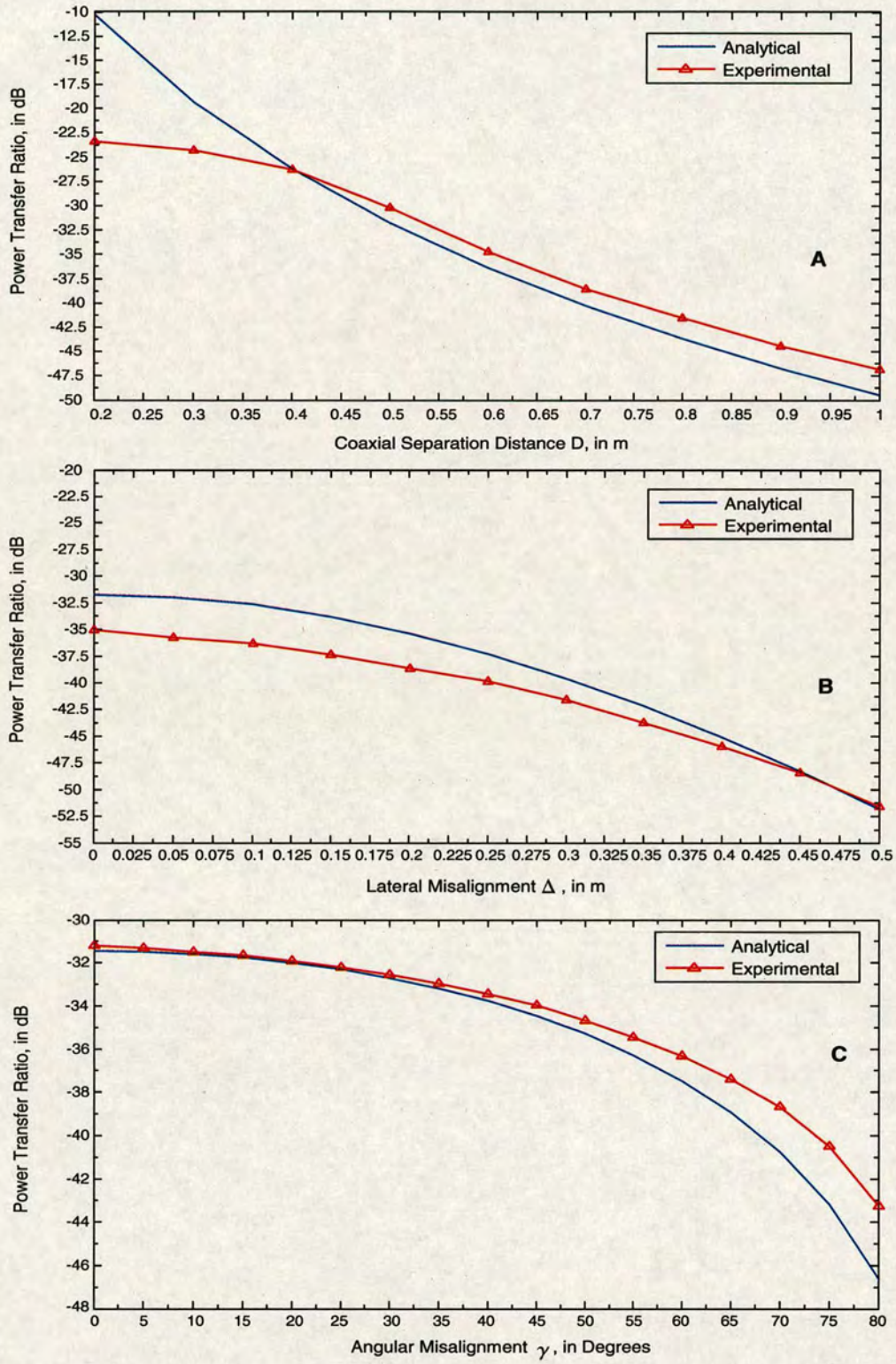

Figure 4.38: *Power transfer ratio* (P_{RX}/P_{TX})*, for the short solenoid TX, RX coil system depicted in Fig. 4.15. A - Power transfer for coils situated in the coaxial orientation, B - Power transfer in the lateral misalignment case for a vertical separation between the coils of 40 cm, C - Power transfer in the angular misalignment case for a vertical separation between the coils of 30 cm.*

nearby objects can easily detune the coil. Therefore, as the RX coil moves closer to the TX coil, it may well introduce some stray capacitance which can change the effective reactance of the tank circuit and alter the resonant frequency.

In order to ensure that the TX coil was matched to the power amplifier and all the output power from the amplifier was fed into the TX coil, the reflected power at the power amplifier was constantly being monitored. Observing the analog dial indicator at the power amplifier revealed that as the RX coil approached the TX at a distance of less than 40cm the reflected power indicator moved from a zero value to 0.5Watts. This supports the opinion that the presence of the RX coil detunes the TX for small separation distances. A closer investigation of coupling measurements in the coaxial orientation, as shown in Fig. 4.39(b) indicates that for the RX coil C with a radius of 34mm, a coil separation of at least one TX coil radius is necessary to ensure that the RX coil has no effect on the TX coil. The poor coupling approximation discussed in section 2.11 of chapter 2 suggests that for coaxial solenoid coils a separation distance of two TX coil diameters is required for a RX coil half the size of the TX for poor coupling to hold. Since the power coupling functions developed in chapter 4 are only valid for a poorly coupled system, a large error is expected for measurements very close to the TX coil. Hence, for the dimensions of the prototype coils used, this factor should be considered when interpreting the results. In view of this, measurements for the lateral and angular misalignment where conducted at a separation distance of at least 30cm to ensure poor coupling.

The general trend of the experimental data follows closely the theoretical model for the power transfer in all three orientations studied. This fact suggests that the predominant error is of a systematic nature. The random error present in the measurements is very small and it is masked by the systematic error present. Fig. 4.40 illustrates the relative error in the measurements compared with the analytic solution as a percentage and dB. A comparison of the predicted and measured power coupling data across the inductive link can be easily expressed as a relative percentage error using expression (4.44). The relative percentage error for the power transfer measurements can be converted into a dB error as follows:

$$e_r(\text{dB}) = 10 \cdot \log \left[\frac{100 + e_r}{100} \right] \tag{4.47}$$

Fig. 4.40 reveals that the maximum relative percentage error in the coaxial measurements is in the order of 5%, 12% in the lateral misalignment and 7% in the angular misalignment. This amount of error is expected and well justified by the limitations of the instrumentation used.

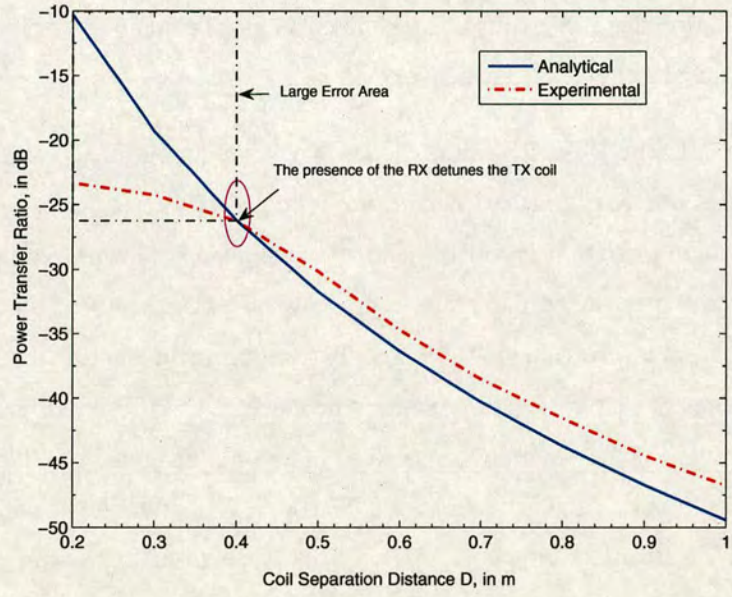

(a)

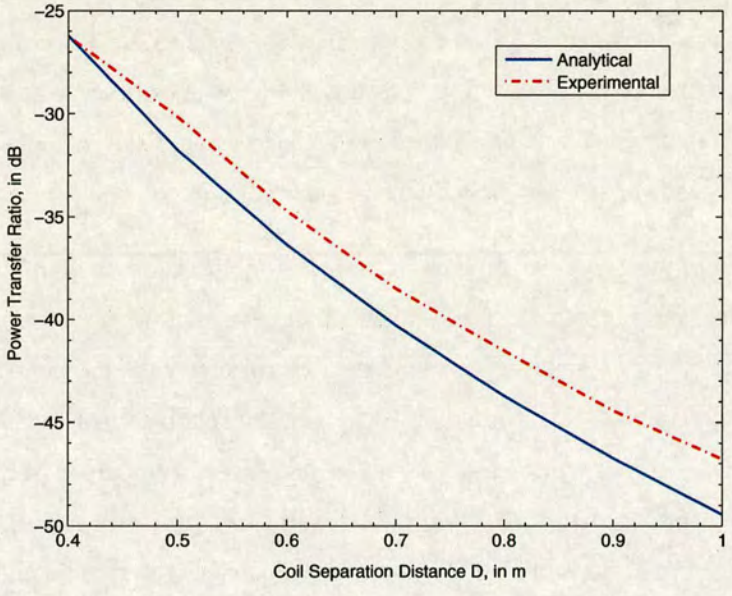

(b)

Figure 4.39: *Plots of the analytical and experimental power transfer ratios for solenoid coils: (a) Graph shows the effect of RX coil as it approaches the TX, discussed in section 2.11. For a separation distance less than the TX coil diameter the poor coupling approximation is no longer valid, which results in a larger error. (b) Analytical and experimental results for the power coupling across the inductive link versus the coil separation distance D where the poor coupling approximation is valid.*

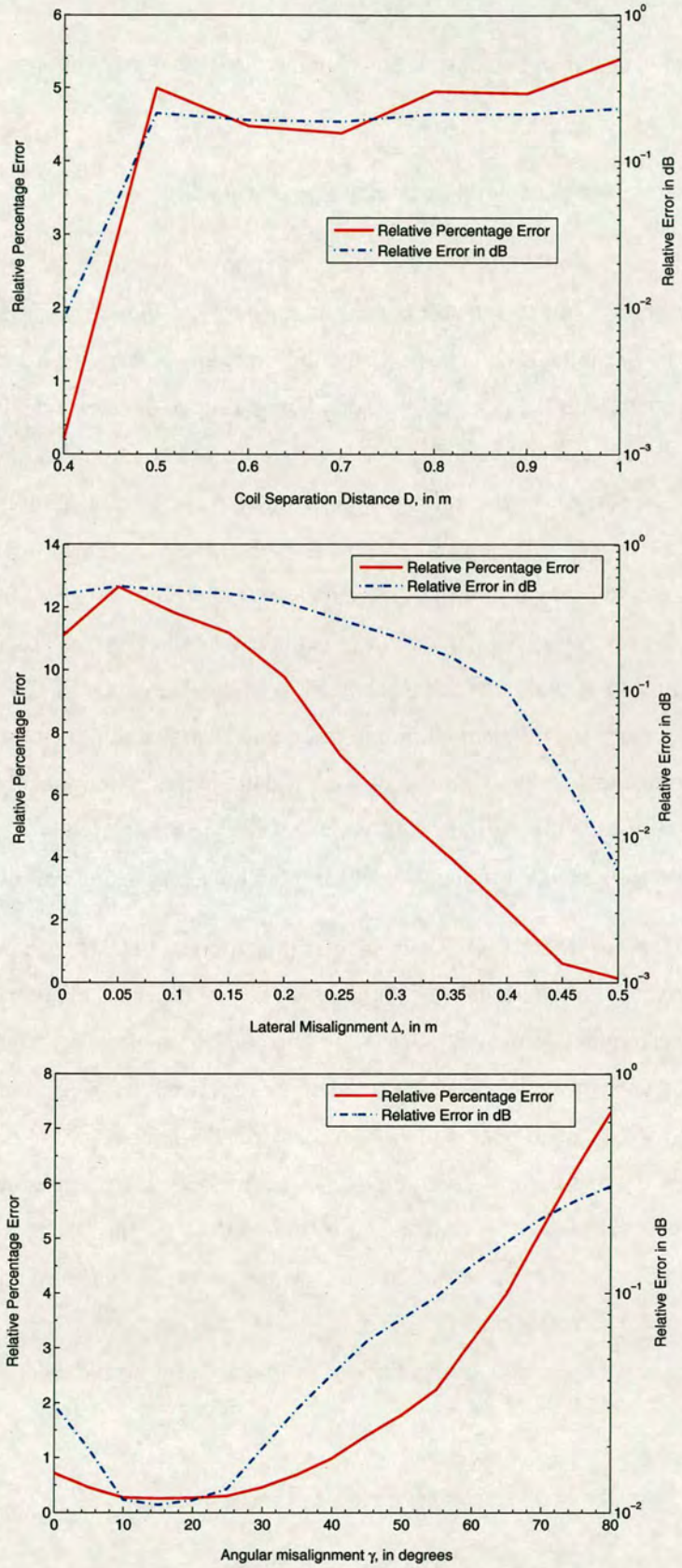

Figure 4.40: *Relative percentage and dB error for the power transfer measurements between coils B and C in the coaxial orientation, lateral and angular misalignment.*

The experimental data show good agreement with the theoretical predictions.

4.5.2.2 Power transfer between planar circular spiral coils

In a similar manner, Fig. 4.41 shows the results of the power transfer measurements between two flat circular spirals. In this case the experiments were conducted using the prototypes FCS1 and FCS2 as TX and RX coils respectively. For this type of coils the experimental results show good agreement with the analytical model. The presence of some random error is more pronounced for the coaxial and lateral measurements in the flat spiral case in comparison to the solenoid coil. Nevertheless, the influence of the random error is not significant with respect to the systematic errors as discussed in section 4.6. An interesting phenomenon that should be addressed here is the crossing of the theoretical and experimental curves in the lateral and angular cases as shown in Fig. 4.42. This can be explained as a three stage process based on the schematic diagram of Fig. 4.42. As the RX coil moves from the center of the TX coil radially in the direction of the y-axis it passes through three different stages. Since the magnetic field is more concentrated around the windings of the TX coil, as the RX crosses that boundary the mutual coupling between the coils increases, which results in an increase in the measured power transfer that is not accounted for in the theoretical model whereby a uniform field is assumed.

In practical applications for RX coils much smaller than the TX, the field can be assumed to be uniform. However, due to the limitations in the sensitivity of the instrumentation used, a much larger RX coil was required to provide sensible readings. Nevertheless, it is worth noticing that even for a RX coil as large as the FCS2 the trend of the experimental measurements indicates a close correlation with the analytical model. A similar behaviour can be observed as the plane of the RX rotates for the angular misalignment measurements. The crossing of the experimental and analytical curves in this case is attributed to the fact that as the RX rotates some of the effective area of the coil moves closer into the TX, which results in increased coupling between the coils. Fig. 4.43 indicates that the percentage error between the experimental data and theoretical predictions for the power transfer is very low even for non-ideal coil dimensions.

4.5.2.3 Power transfer between printed circular spiral coils

In this section the results from the experimental measurements of power transfer efficiency between the printed circular spiral coils PCS1 and PCS2 are presented. A comparison follows

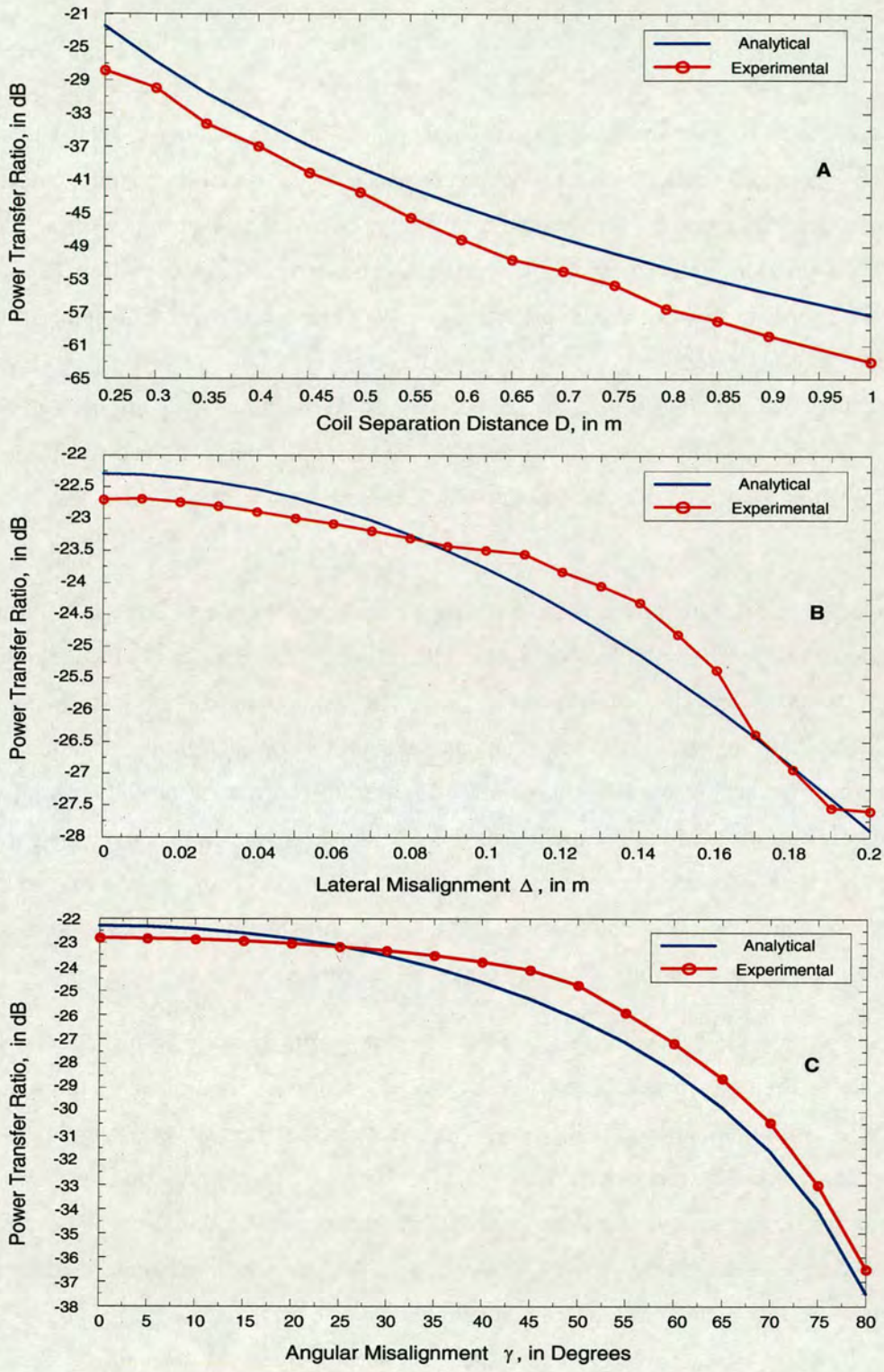

Figure 4.41: *Power transfer ratio (P_{RX}/P_{TX}), for the flat circular spiral TX, RX coil system depicted in Fig. 4.15. A - Power transfer for coils situated in the coaxial orientation, B - Power transfer in the lateral misalignment case for a vertical separation between the coils of 40 cm, C - Power transfer in the angular misalignment case for a vertical separation between the coils of 30 cm.*

between the experimental data and the theoretical link efficiency calculated by expressions (3.84), (3.88) and (3.91), derived in chapter 3. It is evident from Fig. 4.44 that there is a close correlation between the experimental and the analytical data in all the coaxial, lateral and angular orientations studied. The relative percentage error for the coaxial configuration is in the order of 20% neglecting the area close to the TX coil where the accuracy of the loosely coupling approximation is compromised. As the RX coil moves further away from the TX the error is reduced suggesting the coils are again loosely coupled. It is expected that the accuracy of the theoretical model is improved as the separation distance of the coils increases. However, the sensitivity of the voltage meter is not adequate to detect the low voltage induced across the RX at large separation distances. Therefore, the measuring range in the coaxial oriention was limited in 1m with a minimum separation distance between the coils of at least one TX diameter.

In the lateral configuration the relative percentage error is in the order of 20%. It is illustrated in Fig. 4.45 that for the lateral displacement of the RX coil, the error steadily increases until it reaches its maximum value when the center of the RX coil is situated at the circumferance of the TX coil. In the lossely coupled assumption used in the theoretical formulation of the model, the magnetic field across the RX coil is assumed uniform. However, for the coil separation and the coil dimensions used in the experiments this is not always true. In fact, the magnetic field maximises at the circumference of the TX coil hence an increased error can be observed where the analytical model expects a uniform field. The separation distance in this case is 40cm, twice the maximum diameter of the TX to limit the coupling coefficient.

In conjunction to the flat spiral coil of round wire, the results from the printed circular spiral coils exhibit a higher error rate. The discrepancy between measured and calculated power transfer efficiency for this particular coil geometry can be attributed to the fact that the printed spiral coils are not so closely wound as the flat spiral of round wire. Therefore, secondary effects such as the difference between the ideal close turn approximation, assumed in the analytical model, and the design of the prototype coils shown in Fig. 4.15 introduce additional measurement uncertainties. Finally, in the angular orientation the relative percentage error is in the order of 16%, which is very resonable given the placement uncertainty of the apparatus. Overall, the experimental results indicate a strong corellation with the analytical model discussed in chapter 3.

4.5.2.4 Power transfer between printed square spiral coils

This section is dedicated to the printed square spiral coils and concludes the discussion on the experimental results. This geometry exhibits very similar characteristics to the printed circular coils discussed in the previous section.

In a similar fashion to the previous sections, Fig. 4.46 consists of a set of graphs for the power transfered across a typical inductive link composed of two resonant printed square spiral coils. The experimental data were plotted against the theoretical link efficiency expressions derived in chapter 3 for the coaxial, lateral and angular coil displacements given by expression (3.85), (3.89) and (3.92) respectively. Referring to Fig. 4.47 in the coaxial orientation, the relative percentage error for the measurements of Fig. 4.46 is approximated to 22%. In the lateral misalignment the relative percentage error seen is 33% and finally for the rotational misalignment it is 19% . Overall, the experimental data provides a reasonable match to the measurement results given the size of the coils.

4.6 Quantifying the Experimental Error

One of the primary concerns in any measurement technique is a reliable estimate of errors and uncertainty factors influencing the accuracy of the experimental results. This is especially true of a method involving a significant level of mathematical analysis as is the case of the near-field model suggested in chapter 3. A complete and general error analysis requires a combination of approaches, both analytical and experimental, to identify all possible error sources and estimate their individual contribution to the final calculated results. In the current approach the errors in the experimental procedure can be divided in two parts:

- Magnetic near-field strength errors during H_z measurement
- Errors in power transfer measurement between the TX and RX coils

These are studied independently in sections 4.6.1 and 4.6.2, which follow.

Measurement uncertainty reflects the quality and accuracy of the measured data as compared to the theoretical value. All possible errors can be divided into three broad categories: theoretical, numerical calculations, and measurement. Theoretical errors include approximations made during the development of the theoretical model and can ultimately limit the accuracy of

the results. This type of error is accounted for both in the magnetic field and power transfer measurements. However, from a careful study of the theoretical development, one is able to show that such errors due to theoretical approximations are either of negligible magnitude or can be treated as measurement errors. For instance, the close turn approximation in the modelling of spiral coils can introduce some error. In fact, the first assumption is generally valid to within negligible error and infinitesimally thin wire conductor approximations can be viewed as measurement errors. The contribution of these factors will be studied both for the near-field and power transfer measurements. It is possible that the influence of some of these assumptions, such as the magneto-static approximation, can be treated as negligible or converted to a measurement error and included as such in the final error budget. Alternatively, correction factors can be extrapolated based on methods of near-field error correction published by Brunett et al., Iskra et al. and Joseph et al. in [142, 152, 154]. Finally, numerical errors arising from the computation of special functions such as the elliptic integrals in the magnetic field solutions and power transfer functions, derived in chapter 4, are considered to be insignificant. This is attributed to the fact that roundoff errors in modern computers are considered to have a minor impact compared to measurement errors.

Usually uncertainties are calculated using the tolerances of the instrumentation, the experimental set-up variability and the technique used in performing the test. While not generally included in error analysis, in the experimental technique adopted in this thesis, the geometrical parameters and the variability of the coils under test will also be considered. Another component contributing to the overall uncertainty is based on the deviation of the repeated measurements. This means that the tests reported in this chapter had to be repeated several times. By taking down the setup and resetting it, a statistically significant number of repeat measurements was guaranteed, identifying this very important aspect of measurement uncertainty. The combination of the error parameters yields the overall measurement uncertainty.

In view of this, the focus of the error analysis that follows is on the non-ideal character of the measurement system and not on the mathematics. Hence, the errors due to the instrumentation uncertainties are the primary contributors in this work and will be the focus of the remaining discussion. All the individual error sources are itemized in Tables 4.7 and 4.8 for each measurement procedure. Each of these factors is described in detail in the following sections. It is important to note that all the errors listed in Tables 4.7 and 4.8 are primarily systematic. It is possible that a small random error component is present but this will be omitted for the sake

of simplicity, since it is unlikely that it will significantly influence the final error estimation. Consequently, due to its systematic nature each of the errors is assumed independent and uncorrelated with any other error. This means that they can be treated separately and combined using their independent character. Finally, a very important topic that needs to be properly addressed, is the combination of errors that reveal the overall estimate of the accuracy of the experimental results. There is no obvious solution available to this problem and various viewpoints have evolved concerning this topic. The selection of an appropriate method for combining all the systematic errors requires some knowledge about their error distribution, [188]. However, this information is generally not available from experimental tests and it can only be obtained merely through an educated guess. According to Newell in [189], the method of combinations of systematic errors should not be a primary concern if the estimates for each error source are tabulated and the formula used in the combined estimate is stated explicitly. Based on Newell's method the systematic uncertainties (e_i) listed in Tables 4.7 and 4.8 are considered to be independent and normally distributed with (e_i) corresponding to 3σ. According to the central limit theorem, the combined probability distribution will approach a Gaussian. Hence, the total estimated error is given by:

$$e_T = \sqrt{3\sigma_R^2 + \sum_i e_i^2} \tag{4.48}$$

where e_T represents the total error, e_i are the estimates of the worst-case systematic components, and σ_R is the standard deviation of the random component.

4.6.1 Factors affecting the measured magnetic near-field field strength

A magnetic near-field error analysis follows and it is performed for the RF source, the TX coil and the HP 11941A near-field probe. As commonly recognized in electromagnetic measurement techniques, the key parameters that are identified as potential sources of systematic error are summarised below:

- Finite probe size
- The influence of the measurement probe - Field perturbation and averaging effects
- Mutual coupling between the measuring instrument and the source
- Reflections or field distortion caused by local foreign objects
- Instrumentation tolerance/limitation

- Coil dimension error effects
- Theoretical errors - approximations in the theoretical model
- Positioning accuracy

Each of the factors mentioned here will be introduced briefly in the following sections. Furthermore, the individual contribution to the overall error budget, of each uncertainty factor, will be accessed and recorded in Table 4.7.

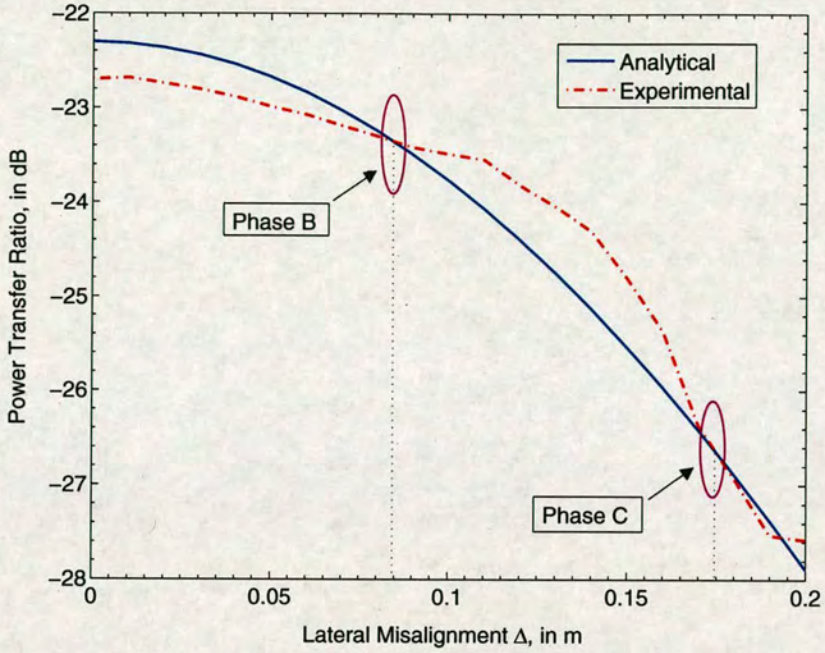

(a)

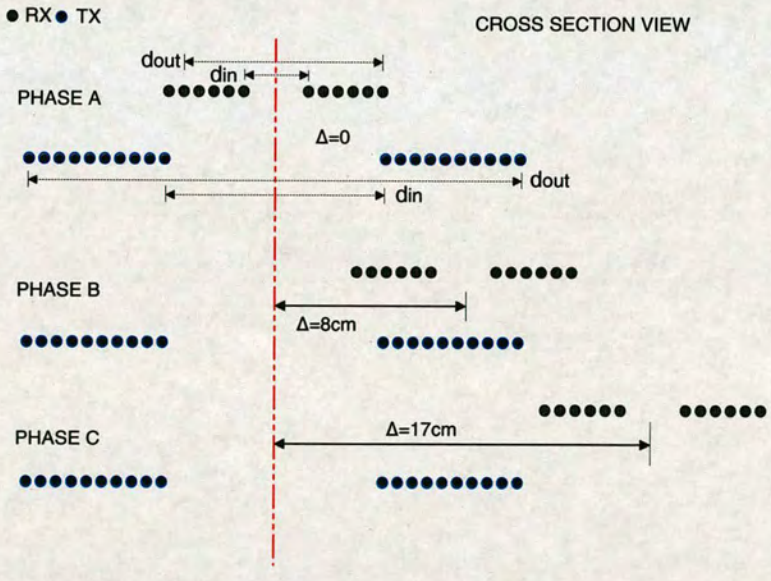

(b)

Figure 4.42: *(a) Power transfer ratio expressed in dB for FCS2 RX coil laterally displaced with respect to the TX coil. (b) Cross-sectional schematic diagram describing the y-axis translation of the spiral RX coil with respect to a stationary spiral TX coil.*

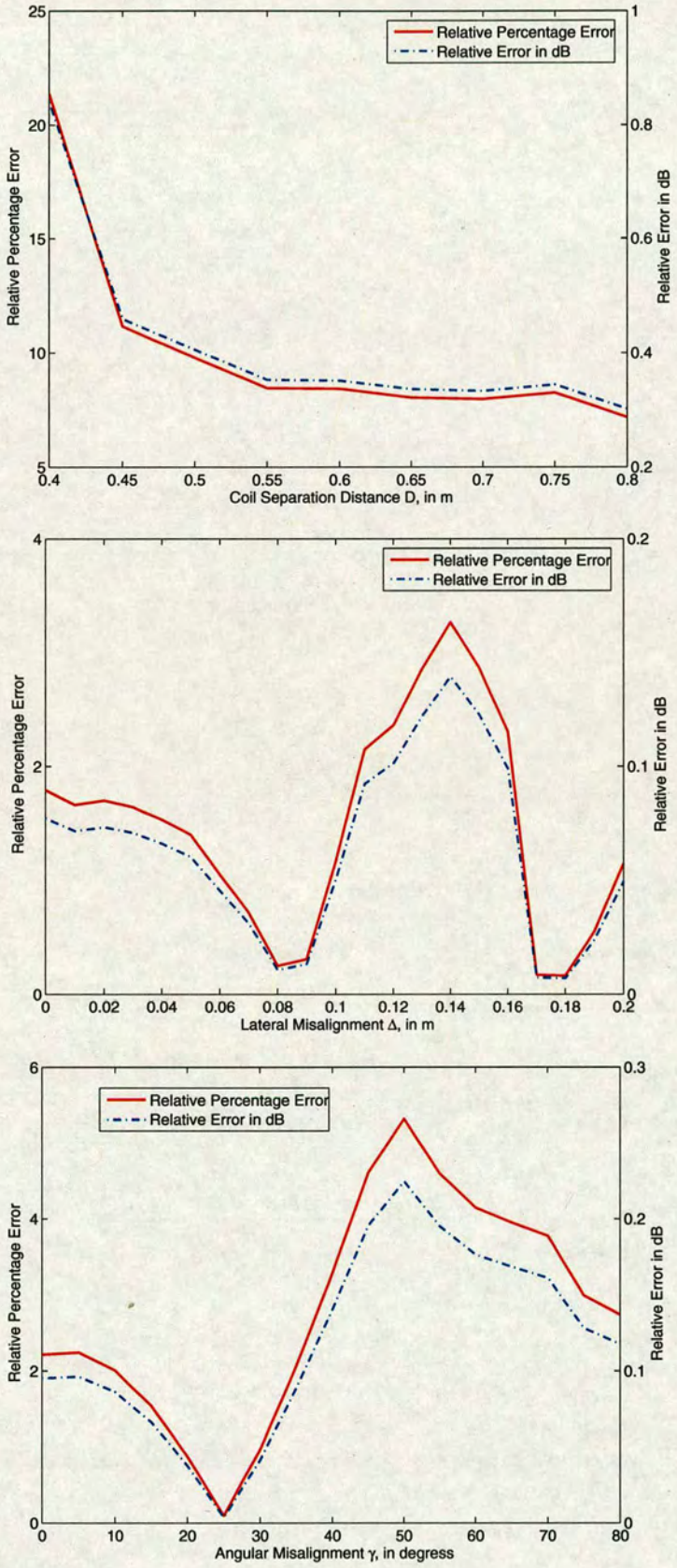

Figure 4.43: *Relative percentage and dB error for the power transfer measurements between coils FCS1 and FCS2 in the coaxial orientation, lateral and angular misalignment.*

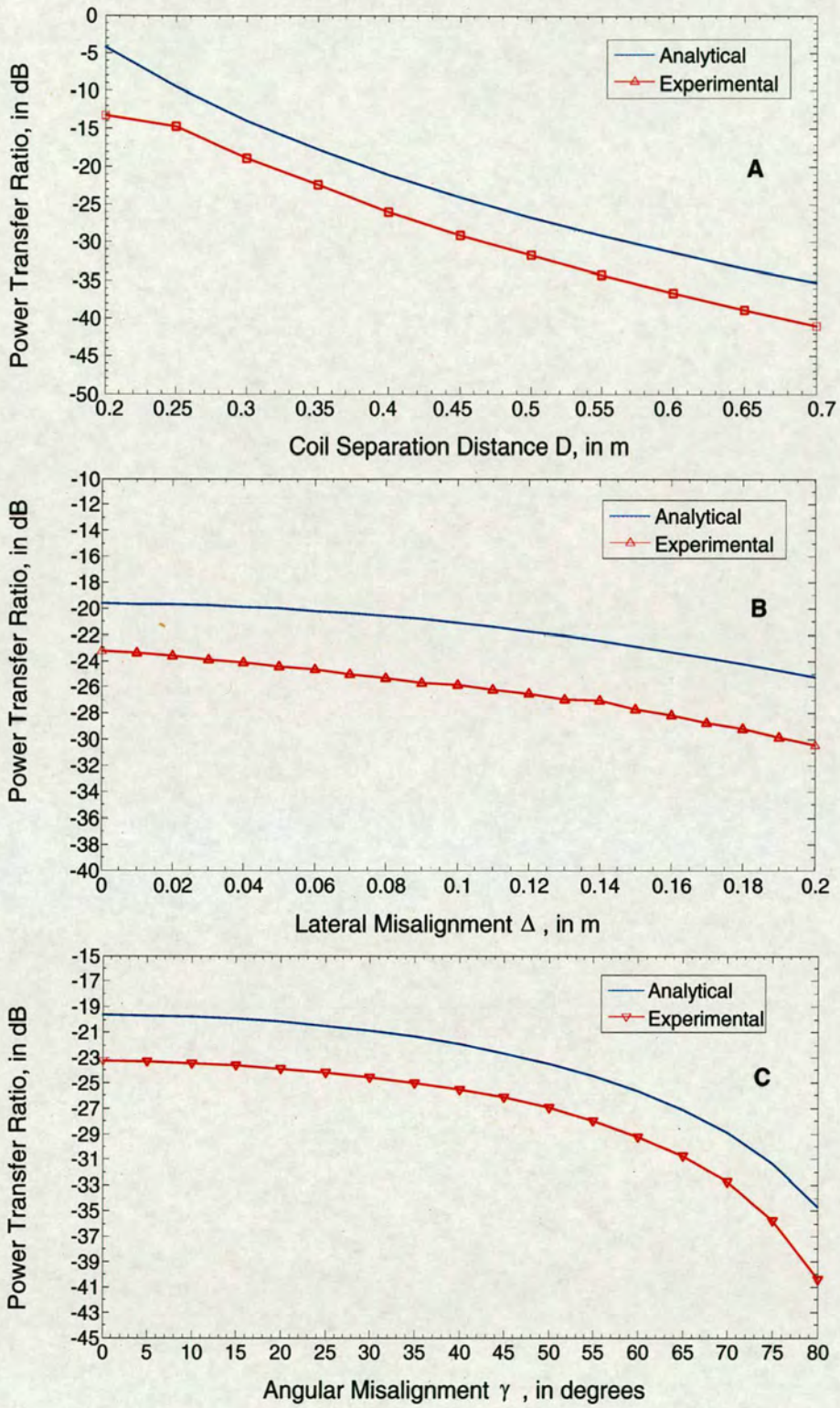

Figure 4.44: *Power transfer ratio (P_{RX}/P_{TX}), for the printed circular spiral TX, RX system depicted in Fig. 4.15. A - Power transfer for coils situated in the coaxial orientation, B - Power transfer in the lateral misalignment case for a vertical separation between the coils of 40 cm, C - Power transfer in the angular misalignment case for a vertical separation between the coils of 40 cm.*

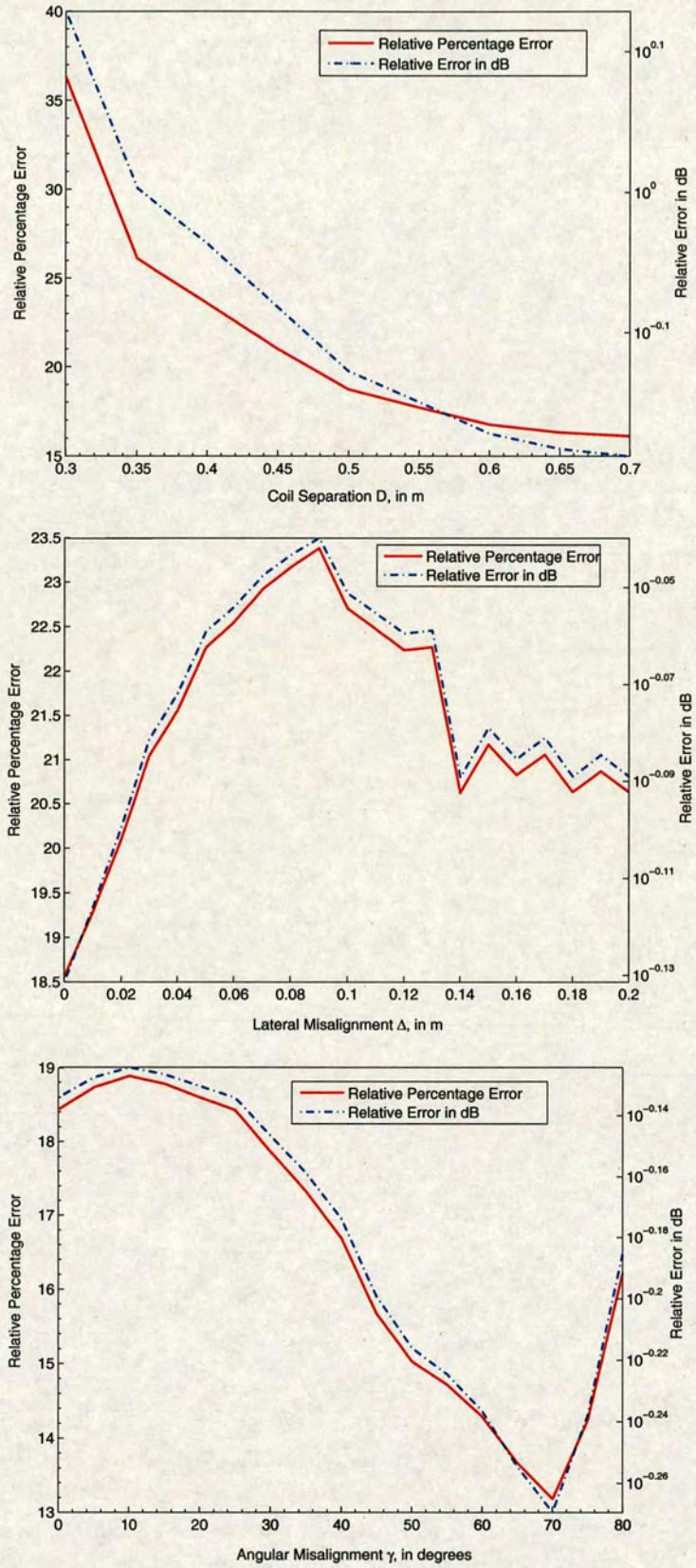

Figure 4.45: *Relative percentage and dB error for the power transfer measurements between coils PCS1 and PCS2 in the coaxial orientation, lateral and angular misalignment.*

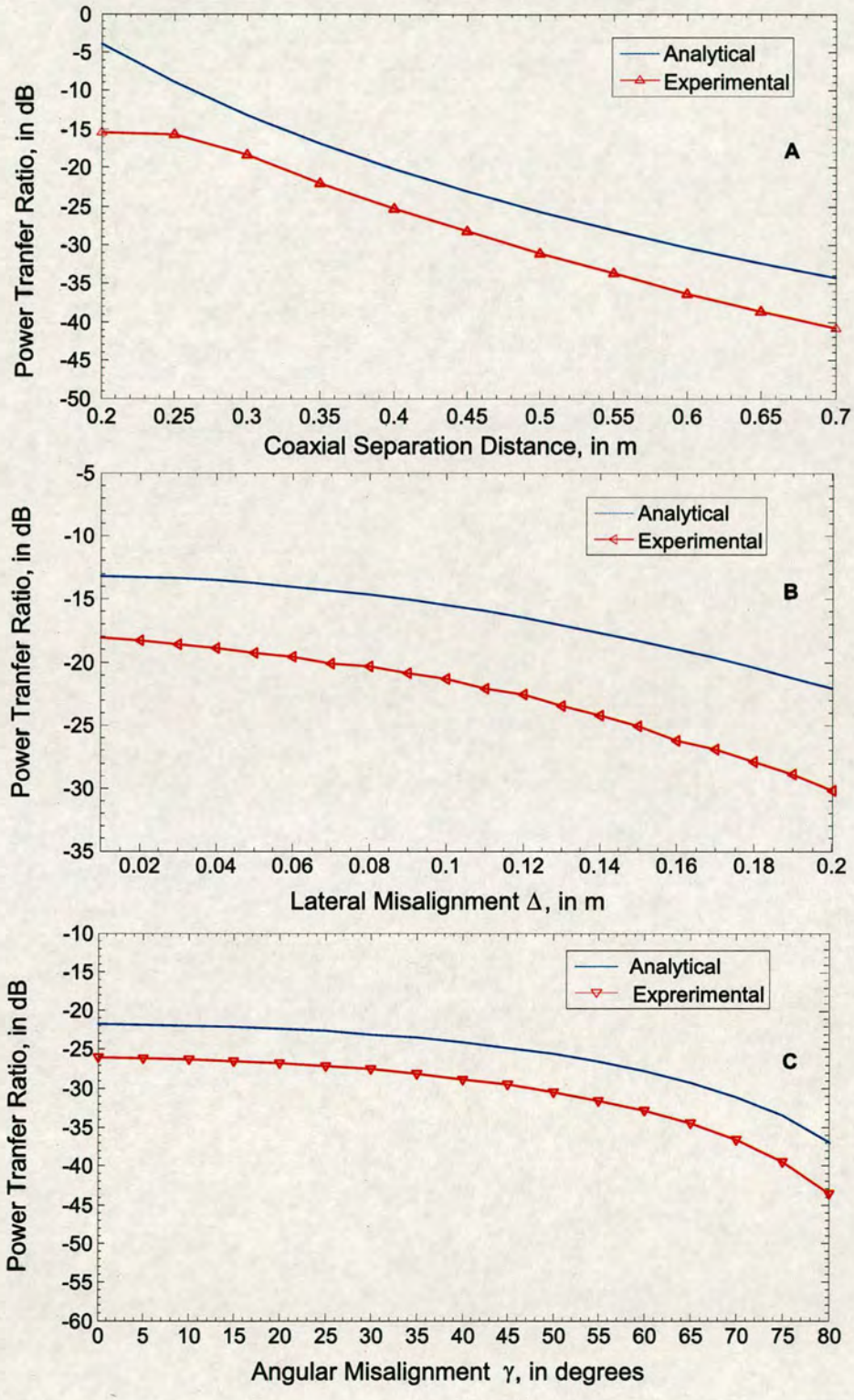

Figure 4.46: *Power transfer ratio (P_{RX}/P_{TX}), for the printed square spiral TX, RX system depicted in Fig. 4.15. A - Power transfer for coils situated in the coaxial orientation, B - Power transfer in the lateral misalignment case for a vertical separation between the coils of 30 cm, C - Power transfer in the angular misalignment case for a vertical separation between the coils of 40 cm.*

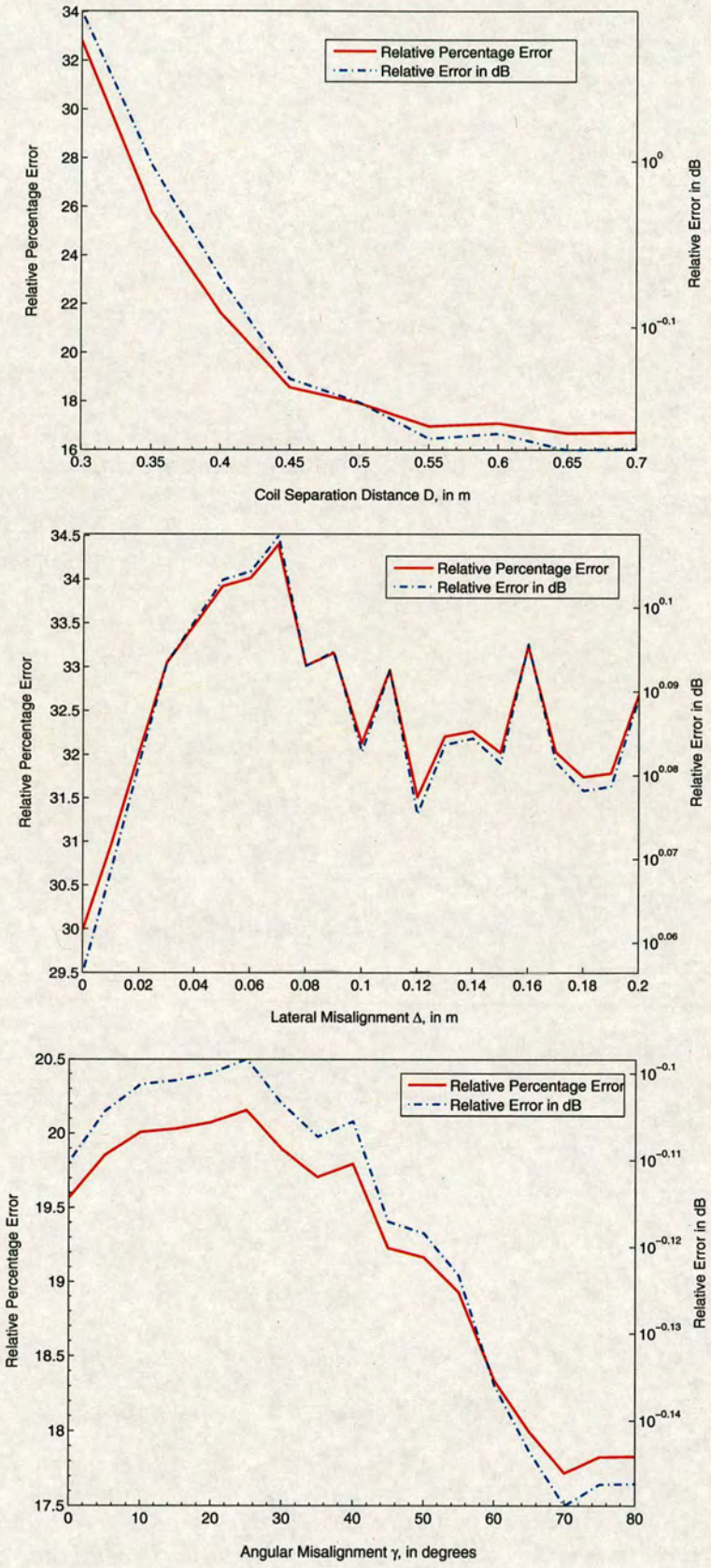

Figure 4.47: *Relative percentage and dB error for the power transfer measurements between coils PSS1 and PSS2 in the coaxial orientation, lateral and angular misalignment.*

ERROR BUDGET FOR H-FIELD MEASUREMENTS			
Source of Error	Uncertainty (dB)	Type	Source of Information
RF Reflections	0.8	Tolerance	section 4.3.1 (reflections $\leq -20dB$), [190, 191]
Field Probe Conversion Factor	2	Tolerance	Manufacturer Data
Current Probe Tolerance	0.13	Tolerance	Manufacturer Data
Spectrum Analyzer Sensitivity	0.265	Tolerance	Manufacturer Data
Probe Dimension	1	Tolerance	According to [152]
Positioning Accuracy - TX Coil		Tolerance	Misalignment Apparatus $\pm 2mm$, $\pm 1°$ Uncertainty
Solenoid (A)	0.08(Coaxial), 0.15(LM), 0.12(AM)	Average	Relative % Error
Flat Spiral (FCS1)	0.12(Coaxial), 0.16 (LM), 0.10 (AM)	Average	Relative % Error
Printed Circular Spiral (PCS1)	0.1(Coaxial), 0.05(LM), 0.1(AM)	Average	Relative % Error
Printed Square Spiral (PSS1)	0.21(Coaxial), 0.16(LM), 0.07(AM)	Average	Relative % Error
System Repeatability	0.5	Standard Deviation	Estimate
ERROR ESTIMATE (dB)	2.46 (Coaxial), 2.46(LM), 2.45(AM)		

Table 4.7: *Error budget for primary uncertainty factors in near-field H_z measurements for the coaxial, lateral (LM) and angular (AM) orientations.*

The influence of the measurement probe

Of the aforementioned factors affecting the accuracy of the field measurements the most critical one is the influence of the measuring probe itself. Joseph et al. suggested in [154] that during measurements, the electromagnetic field will be disturbed by the measurement probe itself. Consequently, the disturbed field will be captured instead of the true free-space value. In the same paper, it is noted that in the near-field in particular, this disturbance cannot be fully quantified by the calibration.

In principle, the calibration of the measuring sensor should take into account the effect of the disturbance due to the presence of the probe. This can only be true if the calibration setup is identical to the measurement configuration. However, the calibration of the probe is usually done in the far-field of one or more antennas [191]. Referring to the manual of the HP 11941A probe, the antenna factors are measured for each unit at 0.009, 0.1, 1, 10 and $30MHz$ to within $\pm 2dB$ in a $377 - Ohm$ field impedance. Therefore, this indicates that calibration was carried out by the manufacturer in the far-field, and as a result the $\pm 2dB$ uncertainty factor is inadequate to fully quantify the influence of the probe in near-field measurements which are of interest to this work. In addition, there is a trade off between the disturbance of the field and the sensitivity of the field measurement device. In essence, the disturbance due to the presence of a smaller probe is less pronounced whereas at the same time the sensitivity of the sensor decreases since less flux passes though the measuring magnetic loop. Thus, the shape of the probe itself introduces further issues. A second effect due to the shape and size of the probe is the averaging of the field over the surface of the probe. The adverse effect of averaging conveys that for a larger and theoretically more sensitive probe, the measured value will deviate further form the true free-space field at a point of interest which in this case is the center of the receiving coil.

A theoretical study of the influence of the probe by Joseph et al., reveals that the measurement probe affects the TX impedance for measurements in the close vicinity of the RF source. The interaction of the approaching probe and the TX coil cause an impedance mismatch between the TX and the RF generator. As a result the power coupled in the TX coil is reduced. Effectively, the probe can detune the resonant TX coil by changing its impedance. According to Joseph et al., the relative deviation, denoted Δ_Z, of the TX impedance due to the presence of the coil is expressed as follows:

$$\Delta_Z = 100 \cdot \left| \frac{Z_{in}^{meas} - Z_{in}^{free}}{Z_{in}^{free}} \right| \tag{4.49}$$

where Z_{in}^{free} and Z_{in}^{meas} are the TX coil impedance in free space, with and without the presence of the probe respectively. Simulations by Joseph et al. show that when the coaxial configuration of the probe and TX coil is employed for measurements, the largest change in the impedance occurs due to the TX and probe oriented in the direction of maximum coupling. On the other hand, in the radial TX-probe configuration representing the measurement setup for the lateral misalignment scenario, the effect of mutual coupling is considered negligible. A value of less than 5% for Δ_z is reported in the same paper for distances larger than λ. Moreover, for the case of an electrically larger TX and field probe, an increased coupling is expected leading to the probe delivering higher values of Δ_Z. In order for low values of Δ_Z to be obtained the dimensions of the TX coil and measurement probe need to be equal or less than 0.45λ, which is true for all the TX coils and the probe used in this work.

Brunett et al. [152], presents a near-field measurement correction accounting for extrapolation error due to loop dimension, providing a minimum separation distance parameter. Measurements made within a few dimensions of an electrically loop source such as the TX coil described in 4.4.4 require the magneto-static field relations of the Biot Savart Law. The sensing probe has been calibrated based on a far-field technique where the source is considered to be infinitesimal[1]. In this case, the strength of the magnetic field at small distances from the source is approximated by the dominant inductive terms for the field of a small circular loop derived in appendix E. However, the emissions from the source of finite size in the near-field zone are also dependent on the source structure and do not demonstrate the source point singularity of (2.26) and (2.27) given in chapter 2. The field of the finite TX coil source, in the coaxial, lateral and angular orientations, is derived directly from Biot-Savart Law in chapter 2. As suggested by Brunett et al. the ratio of the field from a finite sized source to that of an infinitesimal source can be considered a measurement error if the field formulations of a source point antenna are used to calibrate the sensor, such as in the case of the HP 11941A.

It is evident from the previous discussion that the probe can have a loading effect on the TX coil. If inserting the probe into the test space causes the coil current to change by more than a few percent, it should be suspected that the field is distorted and may not be accurate even after retuning the coil current to the correct value. The coil current should always be set with the system empty and then reset to the original value after the probe is inserted. If field distortion is

[1]Infinitesimal in the sense used here means that the source dimensions are negligible when compared with measurement distance, sensing loop dimensions, and wavelength.

suspected, a larger set of TX coils should be used, which is the reason for adopting much larger TX coils than the ones employed in practical applications.

RF reflections

The near-field measurement system was discussed in detail in section 4.3.1. A method of holding and moving the probe close to the TX coil was devised using a misalignment jig. All parts of such a misalignment mechanism were constructed from RF-transparent materials to guarantee measurement accuracy. Since the measurements were conducted in the absence of an anechoic chamber, every effort was made to keep metallic objects away from the RF source. Standard ANSIC63.19-2001 advises to keep RF reflecting objects away from the TX coil at a distance of at least 2 wavelengths at the frequency of operation to ensure that the total reflections from these objects are kept 20dB below the desired direct signal. This was not practical since experiments were carried out in a working RF laboratory and not in an isolated room. The influence of near-by conducting objects was tested by placing a copper screen behind the TX coil and monitoring the change in the signal captured by the probe. As mentioned in section 4.3.1 there was no significant influence by the copper screen which suggests that the level of RF reflections present from conducting objects in the close vicinity of the source did not significantly perturb the measurements. Extra care was needed when it was necessary to manually tune the TX coil since the body of the experimentalist introduces stray capacitance which upsets the impedance of the tank circuit and can also introduce reflections. To avoid such implications low dielectric constant plastics where fixed to the tuning capacitors to minimise the effect the hand of the operator has on the capacitance of the system when tuning the coils and during measurements remained at a distance away from the TX source.

Instrumentation tolerance /limitations

Measurement results often vary from the predicted value given by the theoretical estimation of the field due to the measurement uncertainty introduced by the instrumentation used. Typically, the overall uncertainty of the instrumentation is calculated by identifying the individual uncertainties in the instrumentation chain used in performing these measurements. Hence, the tolerance of the current probe and the spectrum analyzer employed in the current experimental set-up, as provided by the manufacturer, is a good indication of the error expected by these instruments. The percentage tolerance of the current probe and the percentage sensitivity of the spectrum analyzer are converted using equation (4.47) to their equivalent dB error and included in Table. 4.6.1.

Coil dimension error effects

Constructional features such as the radii of the coils have a direct effect on the magnetic field strength in the near-field. For points situated on the z-axis of the coil, equal and opposite errors in the radius of the coils offset each other and do not have an effect on the magnetic field. However, for field computation radially off the z-axis, the field uniformity is no longer symmetrical either side of the center of the coil set. According to ANSI-C63.19-2001 [150] in practice when the dimensions of a coil are measured using a ruler an error as large as 2% in coil radius is common. In order to minimise the impact of this kind of errors the diameter of the coil can be calculated by measuring the diameter from the center of the winding through the center of the coil to the center of the winding at the other end of the diameter and divide by two.

4.6.2 Evaluating the error in the power transfer verification

In RF measurements there are many sources of measurement uncertainty. In the previous section, the main factors which can introduce a level of uncertainty between the experimental and theoretical field strength were identified. In a similar manner, the factors affecting the accuracy of the experimental data for the coil coupling measurements can be now discussed. The possible uncertainty factors in the power transfer measurements are listed below:

- Field uniformity
- Coil radius and spacing error effects
- Positioning accuracy
- Measurement instrumentation tolerances
- The influence of the *thin-wire* approach
- Limitations of coil modelling - Close turn approximation
- Validity issues of the linear representation of embedded electronics. For example, the rectifier equivalent circuit and the impedance of the load.

All the factors mentioned above contribute in one way or another to the overall uncertainty in the power transfer measurements. However, the key parameters include the field uniformity, positioning accuracy, impedance matching and instrumentation tolerance. In power transfer

measurements in particular, the largest errors are usually connected to the mismatch between the source and the load. In the rest of this section these critical uncertainty factors will be briefly introduced. Then an estimate of the dB percentage error that each one of these factors introduces is calculated and an overall error budget is given at the end of this section.

Field Uniformity

The coupling measurements described in this chapter were performed for three different relative orientations of the RX coil with respect to the source TX coil. In the near field region, the electric E and H field components in this region essentially exhibit a quadrature time-phase relative relationship. The voltage induced in a small-loop sensor is proportional to the time rate of change of the total magnetic flux cutting the RX coil.

The open-circuit voltage developed at the terminals of an electrically small RX coil immersed in an electromagnetic field can be deduced from the Faraday-Maxwell relation:

$$\oint E \cdot dl = -\frac{\partial}{\partial t} \int_S \mu \mathbf{H} \cdot d\mathbf{S} \tag{4.50}$$

The integral in the previous expression, (4.50), is evaluated along the small-loop RX coil which yields the open-circuit voltage V_{IND} at its terminals as follows:

$$V_{IND} = -j\omega \int_A \mu \mathbf{H} \cdot \mathbf{dS} \tag{4.51}$$

The total induced emf results from the summation of the normal components of the magnetic field, which act over the surface area A of the RX coil. Assuming field uniformity, (4.51) reduces to:

$$V = -j\omega\mu HA \tag{4.52}$$

This is the familiar, classical form for the expression of the induced open-circuit voltage in a uniform field as employed in chapter 3. In the near field, the assumption of a uniform field distribution is invalid unless the dimensions of the RX coil are significantly smaller than the TX coil and the coil separation distance. The analysis presented in chapter 3 tacitly assumed both of these conditions to be true and the mutual coupling between the TX and RX coils to be minimal. In effect for the applications considered in this work the inductive link is asymmetrical. This can be illustrated by considering the following scenario; a RX, RFID tag or sensor node coil is implanted or embedded and therefore must be small and low power, whereas the TX or reader coil is not subject to the same size constraints. In essence, for these applications the TX and RX coils are very loosely coupled. Under these conditions our original assumption of

minimal coupling remains valid and thus the field strength across the RX coil can be considered uniform. However, for the reasons discussed in section (4.3.1), a larger RX coil compared to the dimensions of coils employed in typical RFID applications was used in the measurements. It is possible that the discrepancy between the measured and the theoretical results in the power transfer efficiency can be partially credited to the size of the RX coil.

It is convenient to define a near-field error expression such that it is an indication of the effect of the quasi-static nonuniform magnetic field distribution over the area of the RX coil on the measured open-circuit voltage. Iskra et al. in [142] developed near-field error expressions for the open circuit voltage at the RX coil with respect to the coil separation distance (D) and the radius of the RX coil (b). For the prototype coil dimensions employed in the power transfer measurements the ratio b/D is defined by the inequality $0.06 < b/D < 0.35$. Referring to Iskra et al., for the ratio b/D defined as $0.06 < b/D < 0.35$, the relative percentage error e_V expected for the induced open circuit voltage is in the range $1\% < e_V < 13\%$. The variation in the value of e_V is justified since an increased error is expected when the coil separation distance is small. In return, the measurement uncertainty decreases when the coils are further apart. Although the analysis presented by Iskra et al. is focused on the single turn loops it can be used as a first approach to the problem. It is expected that the error percentage derived by Iskra is conservative for multiturn coils. However, an exact mathematical derivation of the relative percentage error level in multiturn coils is both tedious and does not facilitate further insight into the problem. Nevertheless, even for the multiturn prototype coils used in the measurements, based on the study by Iskra et al. [142], an average error of 10% is expected for all three orientations.

Positional Accuracy

The positional accuracy of the coils is an additional parameter that affects the accuracy of the measurements. For the misalignment jig employed in the experiments it is safe to assume a vertical and lateral coil displacement accuracy of $\pm 2mm$. In the case of the rotational misalignment a placement uncertainty of $\pm 1^\circ$ is predicted. Based on the construction of the apparatus the values given here are realistic estimates.

Impedance Matching

Another important error factor that needs to be considered is the matching accuracy between the impedance of the RX coil and the corresponding impedance of the receiving electronics. In section (4.2.2) it was shown that equivalent impedance of receiving electronics is comprised of the shunt combination of the rectifier and the load impedances respectively. The accuracy with

which the received power can be measured is limited by any mismatch error present. In the power measurements complex conjugate matching was implemented between the impedance of the RX coil and the receiving electronics. Despite the fact that conjugate matching was used, small drifts in the resonant frequency of the tuned tank RX circuit, can result in impedance mismatch. Hence, for the receiving circuit configuration used in the power transfer measurements it is not uncommon to experience a power reflection coefficient in the order of 0.2 as discussed in a recent paper by Nikitin et al. [192]. Therefore, the maximum mismatch uncertainty denoted as M_u, can be calculated by the following formula, as discussed in [193]:

$$M_{u\,max} = 10\log\left(1+\tau\right)^2 \tag{4.53}$$

where τ is the power reflection coefficient between the RX coil and the resistive load.

The possible error sources affecting the accuracy of the measurements were identified and discussed in the previous sections. Table 4.8 that follows presents the final error budget for the coupling measurements. The contribution of each uncertainty factor is listed and an overall dB error estimate is provided.

ERROR BUDGET FOR POWER TRANSFER MEASUREMENTS			
Source of Error	Uncertainty (dB)	Type	Source of Information
Field Uniformity	0.4	Estimate	Iskra et al. [142]
Multimeter Tolerance	0.03	Tolerance	Manufacturer Data
Impedance Matching	0.2	Estimate	$\tau \approx 0.2$
Positioning Accuracy - TX Coil		Tolerance	Misalignment Apparatus $\pm 2mm$, $\pm 1°$ Uncertainty
Solenoid (A)	0.08(Coaxial), 0.08(LM), 0.2(AM)	Average	Relative % Error
Flat Spiral (FCS1)	0.09(Coaxial), 0.06 (LM), 0.2 (AM)	Average	Relative % Error
Printed Circular Spiral (PCS1)	0.1(Coaxial), 0.06(LM), 0.2(AM)	Average	Relative % Error
Printed Square Spiral (PSS1)	0.10(Coaxial), 0.09(LM), 0.2(AM)	Average	Relative % Error
ERROR ESTIMATE (dB)	0.5	0.5	0.5

Table 4.8: *Error budget for primary uncertainty factors in power transfer measurements*

4.7 Chapter Summary

This chapter presented the experimental procedure and apparatus used to test the theoretical model introduced in chapter 3. In conjunction to the discussion on the experimental procedure adopted, the design and implementation of four sets of prototype coils was presented. The magnetic field strength measurements were carried out prior to the power coupling measurements, primarily to provide information on the field distribution around the RX coil and for testing the modelling assumptions adopted in chapter 3. A direct comparison of the analytical expressions for the magnetic field generated by a short solenoid coil, circular and printed spirals to the measured results for the magnetic field strength indicates a close correlation between measured and analytical data. This seams to suggest that the close turn approximation and the thin wire conductor approximation adopted in the modelling of square spirals are acceptable. In addition to the field-measurements, the results from the power coupling measurements follow closely the analytical model. The error analysis included in this chapter shows that the amount of systematic error observed between the theoretical predictions and the measurement data is well justified. This systematic uncertainty observed is primarily caused by the limitations in experimental accuracy introduced by the instrumentation.

Chapter 5

Optimal Coil Geometry for Efficient Power Transfer

5.1 Introduction

This chapter investigates the power transfer performance of inductively coupled short-solenoid, circular and square spiral coils with respect to coil misalignment and orientation based on the analytical near-field model derived in chapter 3. The fundamental question examined in this chapter is, whether it is possible to improve the misalignment tolerance and power transfer efficiency of a system by adopting a specific coil geometry. Following the power transfer expressions formulated in chapter 3, it is possible to calculate the efficiency of the link for several coil geometries and misalignments in loosely coupled inductive links. The power transfer efficiency achieved using short-solenoid coils is compared with that of printed square and circular spiral coil structures. The results from this analysis indicate that the most efficient coil geometry in terms of power transfer is confirmed to be that of a circular spiral. Initially the magnetic field distribution generated from the different TX coils is investigated. Then the power transfer efficiency between the coil structures is discussed.

5.2 The Analytical Approach to Power Transfer Optimisation

In this thesis, the approach of analytical magnetic field calculations was selected in order to develop a set of novel power transfer functions which predict the effect of coil misalignment on the efficiency of a loosely coupled inductive link. Inductive powering is an established practice, and extensive research has been performed to analyze and optimise the operation of such systems. However, existing literature falls short of properly addressing the coil misalignment problem in applications involving wireless inductive coupling. This thesis attempts to fill this gap by introducing a set of straight-forward analytic design equations that describe the influence of misalignment on the power transfer. For the first time an analytical solution that includes coil

geometrical characteristics for both circular and square coil structures and displacement factors is presented.

An analytical approach is advocated in this thesis as it provides greater insight into the problem. The model suggested in Chapter 3 provides information about the relationships between quantities affecting the efficiency of the inductive link. One can quickly identify trends, in such a manner that a deeper understanding of the problem can be gained. It is difficult to obtain the same information through numerical simulations using the FEM, FDTD methods, since every geometry change demands new meshing, solving and post-processing to take place. Subsequently, numerical methods require repeated simulation runs. In addition, according to the level of accuracy required often a finer grid is necessary which in return demands increased computational time before relationships between quantities and trends can be identified. Given the reasons mentioned here it is clear that a compact analytical model can offer significant advantages. Subsequently, if for a given problem it is possible to converge to an analytic solution that is both mathematically tractable and accurate a compact analytical should be favored over numerical methods.

Inductive links can be classified into two distinguished fields: high power magnetic links and low power magnetic links, [50]. By definition high power inductive links employ closely coupled coils with a coupling coefficient κ of 0.5 or greater, [43]. The operation of such a system resembles a transformer action. In this case the link efficiency is sufficient and does not need to be the main concern in the design. Instead more emphasis is given in optimising the secondary circuit such as the rectifier and voltage regulator. On the contrary, low power links have a coupling coefficient of 0.01 or less and are said to be loosely coupled, [43]. For the applications considered in this thesis such as passive RFID devices and embedded sensors, coils are usually loosely coupled. Due to the very nature of the applications considered, low coupling is often a direct consequence of the geometric constraints imposed by the problem. For example, the unfavorable coil coupling conditions are either caused by a large coil separation or a very small internal coil diameter. To make matters worse, the coupling coefficient can be significantly affected by the relative position of the RX coil, its orientation as well as coil and conductor geometry. Hence, the limiting factor in the overall power transfer efficiency for these devices is the coupling link efficiency. It is precisely this fact that provided the motivation for the approach followed in chapter 3. In the following sections of this chapter the performance of the power transfer between circular solenoid, square and circular spirals will be compared with

respect to the RX orientation and coil dimensions.

5.3 Magnetic Field of Coil Structures

In contrast to the far-field where the TX is considered to be a point source, in the inductive near-field the geometry of the TX coil has a profound effect on the field distribution. Therefore, it is essential to distinguish between circular and square geometries and model each structure independently. This approach is followed in chapter 3 and expressions for the magnetic field strength for coils of this form are given.

Based on the analytical model developed in chapter 3, it is demonstrated that geometrical parameters such as coil dimensions and shape have a direct impact on the magnetic field strength in the near-field. Since the magnitude of the magnetic field is closely related to the efficiency of the inductive link, it is critical to identify a coil structure that maximises the coupling between the TX and the RX. In the present investigation the magnetic field profile of short-solenoid, circular and square spiral coils is studied based on the Biot-Savart principle, as described earlier, in chapter 3. By engaging the expressions for the magnetic field intensity as presented in chapter 3 it is possible to compare the magnetic field intensity profiles for the coils studied at the coaxial orientation, a translation and a rotation.

Initially, it is critical to define the parameters of the coils under consideration in order for a comparison between the three geometries to be valid. It is possible to compare the magnetic field profile of a short solenoid with respect to that generated by planar circular and square spiral structures regarding the effective areas of the coils to be equal, as will be discussed in detail in section 5.4.1 that follows. The dimensions of the coils considered are listed in Table 5.1 below. The strength, shape and uniformity of the field created by the TX coils depend significantly on the coil configuration, and for this purpose square, and circular coils are investigated. The intensity of the z component of the magnetic flux density at an arbitrary point in space when a current is applied to a short-circular solenoid is described in the near-field by expression (3.73). Likewise, equations (3.74) and (3.57) apply for the circular and square spiral coils respectively.

The H_z magnetic field intensity profile at the center of RX coil is depicted in Fig. 5.1(a), Fig. 5.1(b), Fig. 5.3 and Fig. 5.4. The field intensity is represented across the $z - axis$, for a lateral and angular RX displacement. Starting from the axial field profile, as demonstrated in

Coils	radius a [m]	length ℓ [m]	Width (w) [m]	Spacing (s) [m]	Turns
Circular Spiral Coil	0.56	-	0.0015	0.0015	8
Square Spiral Coil	-	0.10	0.0015	0.0015	8
Short Solenoid Coil	0.56	-	-	-	8

Table 5.1: *Dimensions of solenoid, printed circular and square spiral TX coils.*

Fig. 5.1, for distances close to the TX coil the square spiral coil maximises the field intensity. For larger separation distances, which exceed 3cm in this case, the short-solenoid illustrates a higher magnetic field intensity compared to the spiral structures.

An interesting behaviour is demonstrated when considering the radial magnetic field distribution along the $y-$ axis of the TX coil. It is worth noticing that the curves of the magnetic field strength as illustrated in Fig. 5.1(b) and Fig. 5.3 exhibit two local extrema. Between the local maximum and minimum of the magnetic field strength, which vary for each geometry, the magnetic field strength declines rapidly. The curves for the lateral field strength eventually become negative reaching the local minimum point and start increasing again until the field strength approaches zero. This trend can by explained since the direction of the magnetic flux line reverses through the coil, as indicated in Fig. 5.2 below.

In order to compare the different coil topologies, surface plots above the transmitting coils are created as shown in Fig. 5.5, Fig. 5.6 and Fig. 5.7 for the short-solenoid, circular and square spiral coils respectively. The surface plots illustrate the variation of the magnetic field intensity for the component perpendicular to the receiver coil, H_z at several distances from the source transmitting coil. The surface plots of the magnetic field distribution indicate that the magnetic field profile is closely related to the coil geometry for distances close to the coil. Eventually, all the coils create the same bell shaped field profile which tends to become more uniform with increasing distance from the surface of the TX coil. This illustrates that all the coils show similar magnetic field profiles at the distance of operation considered in this work.

Hence, we can conclude that the data for the magnetic field profile alone cannot sufficiently explain the diverse trends in the link efficiency observed for the coil structures investigated in this thesis. Clearly, as already indicated from the analytical model for the power transfer, derived in Chapter 3, the geometry of the RX coil plays an equally critical role to the TX coil in defining the power transfer efficiency of the inductive link. The influence of the coils geometries is also concealed in the ohmic losses of both the TX and RX coils, which are a

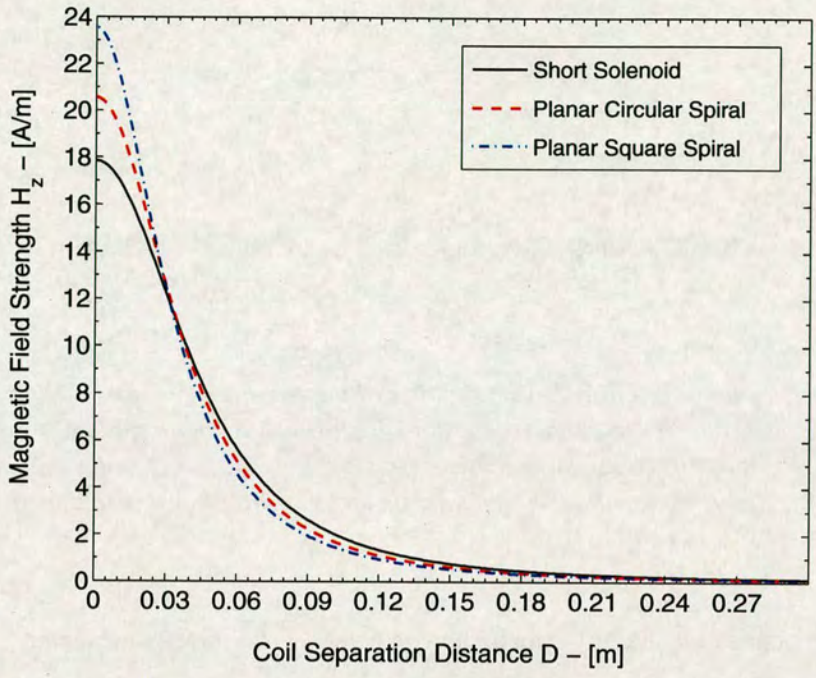

(a)

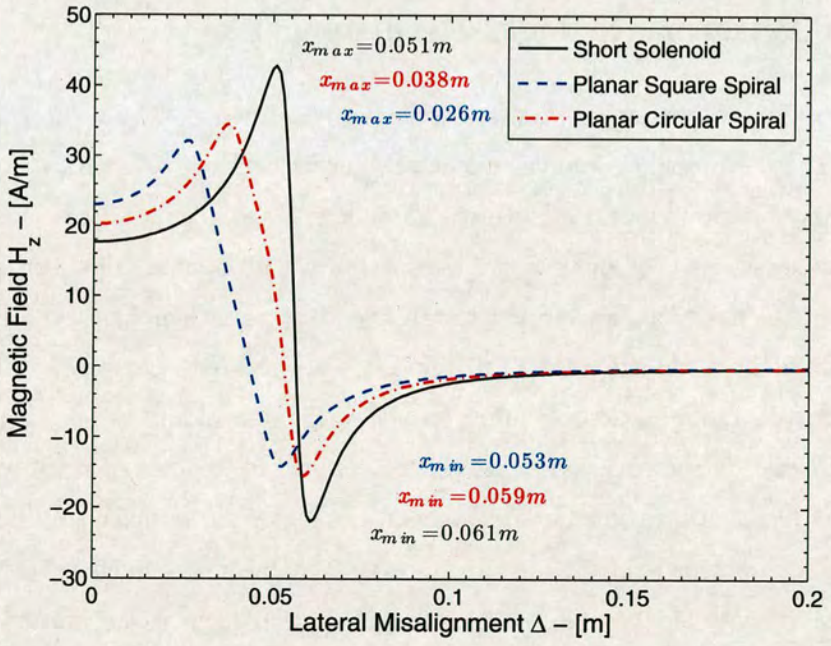

(b)

Figure 5.1: *H_z magnetic field profile for three coils geometries, that of a short solenoid, planar circular and square spiral coils. (a) Axial magnetic field, along the $z-$axis, (b) Radial magnetic field distribution on the $x-y$ plane at a distance of 0.005m from the surface of the coil.*

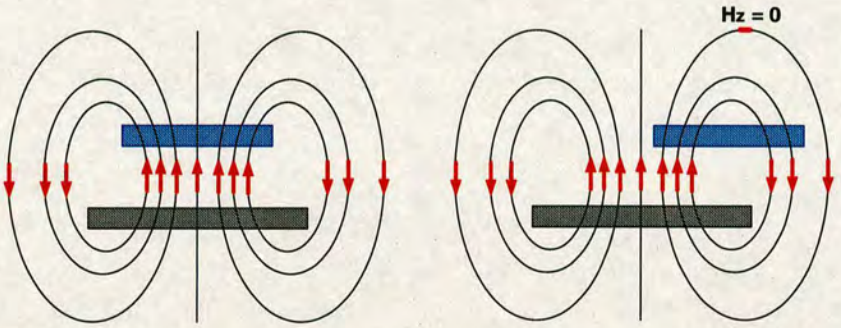

Figure 5.2: *Diagram depicting the distribution of the magnetic flux lines. When the RX coil (blue) is coaxial to the TX coil (red), the direction of the magnetic flux lines point upwards. As the RX shifts laterally to the circumference of the TX, it intersects some magnetic flux lines pointing in the opposite direction. Eventually the net flux vanishes due to the curvature of the field.*

direct consequence of the coils geometrical parameters, as discussed in Chapter 4.

5.4 Coil Performance under Misalignment

A set of novel power transfer equations has been derived in sections 3.6.1, 3.6.2 and 3.6.3 of this thesis. These expressions compute the power transfer between TX and RX resonant coils of an inductive link in the ideal orientation, under lateral and angular displacement for four different coil structures. By employing these functions it is possible to predict the coupling between short-solenoid, flat circular wire spirals as well as printed circular and square spirals. Therefore, different combinations of TX/RX coils are possible to be compared with respect to the power delivered to the load both in the coaxial orientation and under misalignment. This section is focused on short solenoids and printed spirals. Flat spirals of round wire are not discussed here since printed structures are currently more popular for the applications targeted in this thesis. By implementing the analytic expressions for the power efficiency in MATLAB it is possible to compute and plot the efficiency of the link when the coils are situated in the ideal orientation, lateral and angular cases. The results of this analysis are presented in this chapter.

Before proceeding any further, it is important to define the term efficiency as it is employed in this chapter. The power transfer efficiency of an inductive link denoted, η_{link}, describes the ratio of the power that reaches the load of the RFID tag or embedded sensor expressed as P_{RX}, to the input power of the driving TX coil given by, P_{TX}. Hence, the link efficiency is equivalent

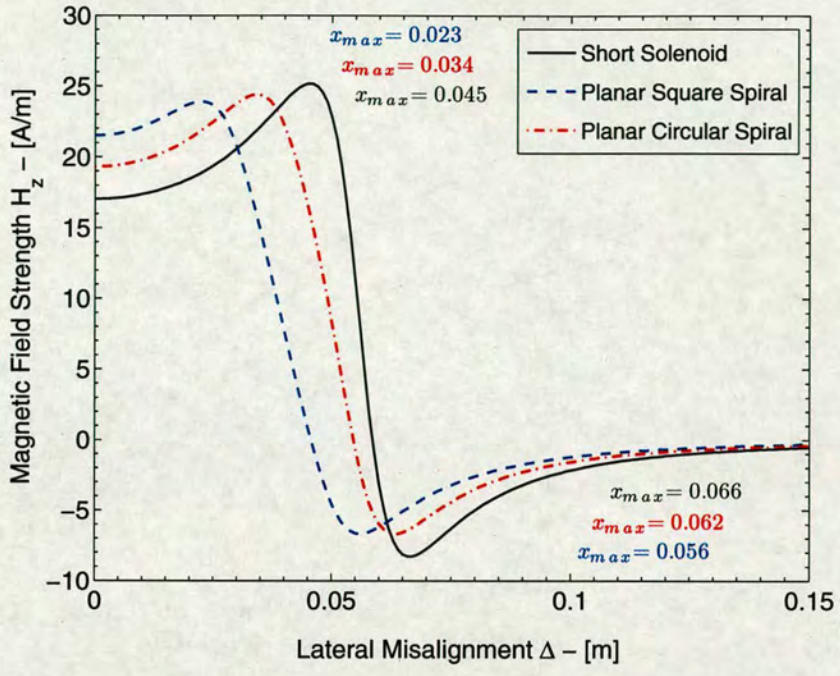

(a)

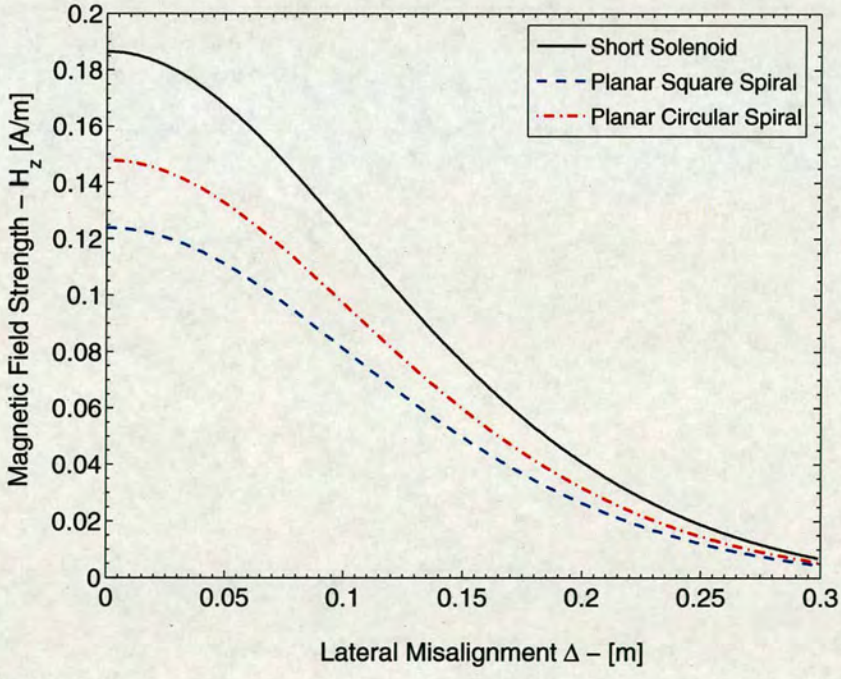

(b)

Figure 5.3: *Hz radial magnetic field component profile at a distance of (a) 0.01m and (b) 0.25m above in the $x - y$ plane, for three coils geometries, that of a short solenoid, planar circular and square spiral coils.*

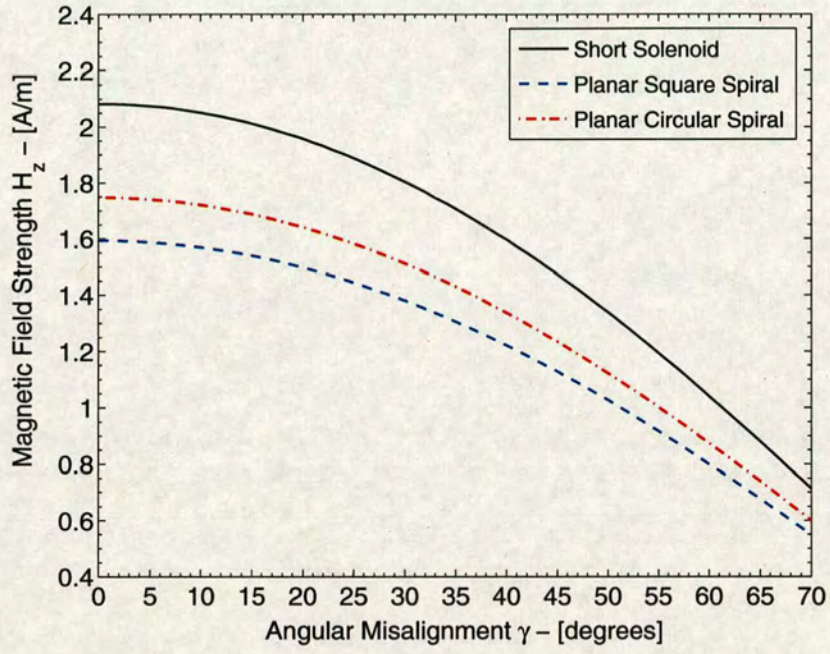

(a)

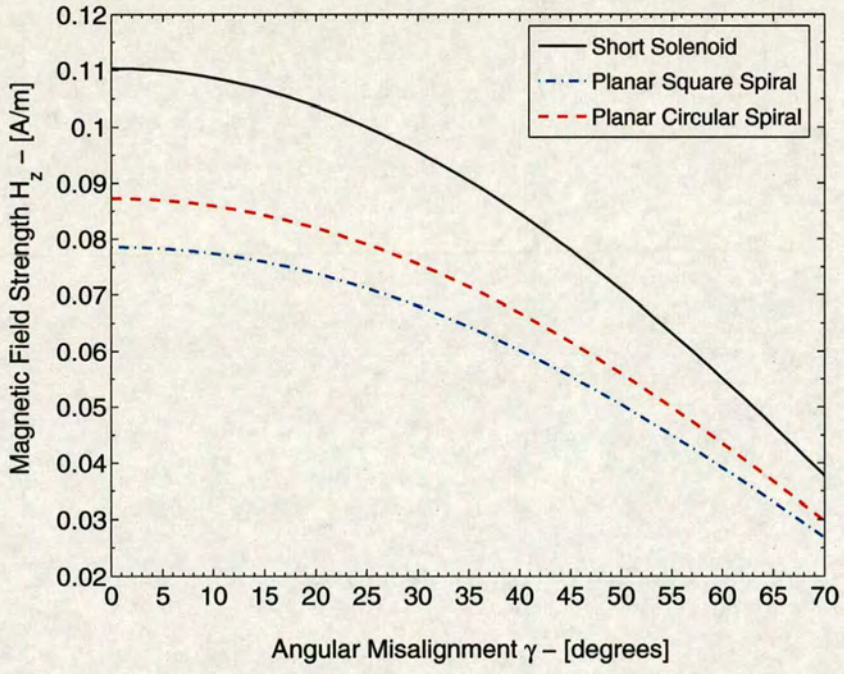

(b)

Figure 5.4: *Hz radial magnetic field component profile at a distance of (a) 0.10m and (b) 0.30m above in the $x - y$ plane, for three coils geometries, that of a short solenoid, planar circular and square spiral coils.*

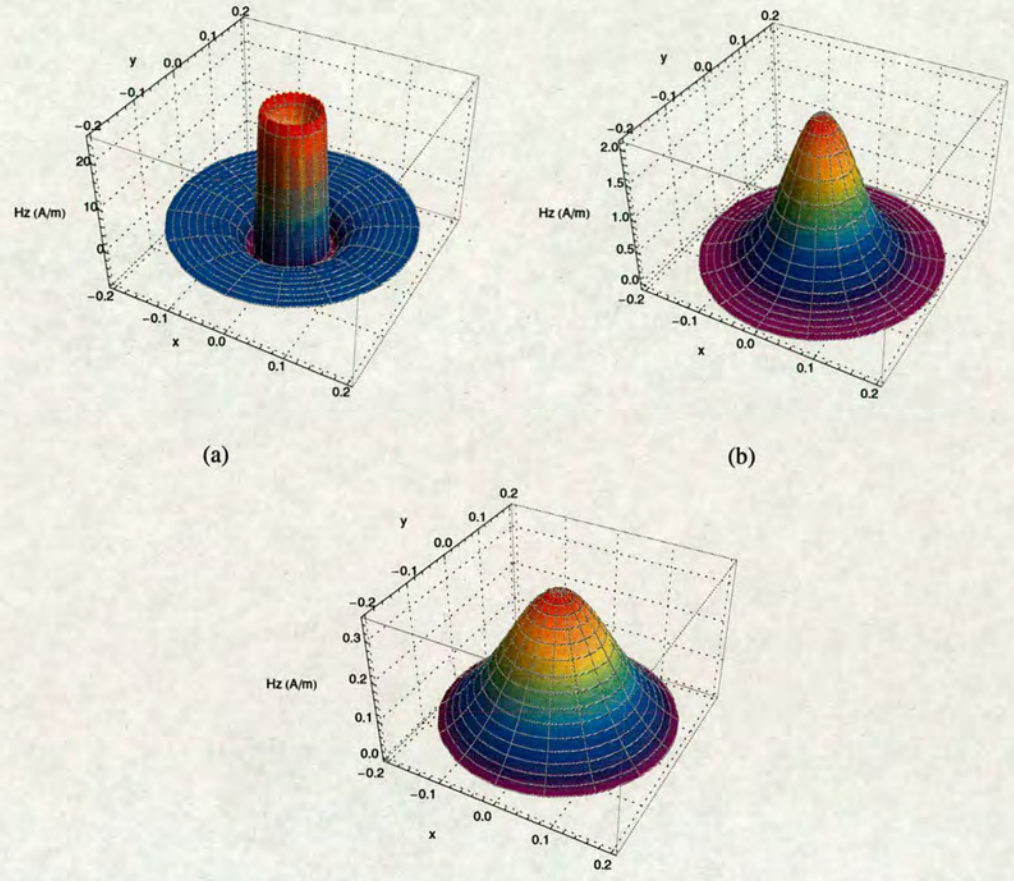

Figure 5.5: *Magnetic field distribution of the H_z component above the TX coil parallel to the $x-y$ plane. The short-solenoid TX source coil is listed in Table 6.2 and a theoretical current of 250mA is considered in the coil: (a) At a distance of 0.01m from the origin of the coil, (b) At a distance of 0.10m from the origin of the coil, (c) Magnetic field profile at a distance of 0.30m from the origin of the coil.*

to the power transfer ratios presented in chapter 3:

$$\eta_{link} = \frac{P_{RX}}{P_{TX}} \tag{5.1}$$

The link efficiency as referred to in this chapter should not be confused with the efficiency of the whole system, which is the link efficiency multiplied by the efficiency of the driving circuit. A key distinguishing factor between the link efficiency and the efficiency of the complete system is that the latter depends on the input impedance of the inductive link and internal impedance of the power supply.

The coils investigated are assumed to have the same cross-sectional area and number of turns for

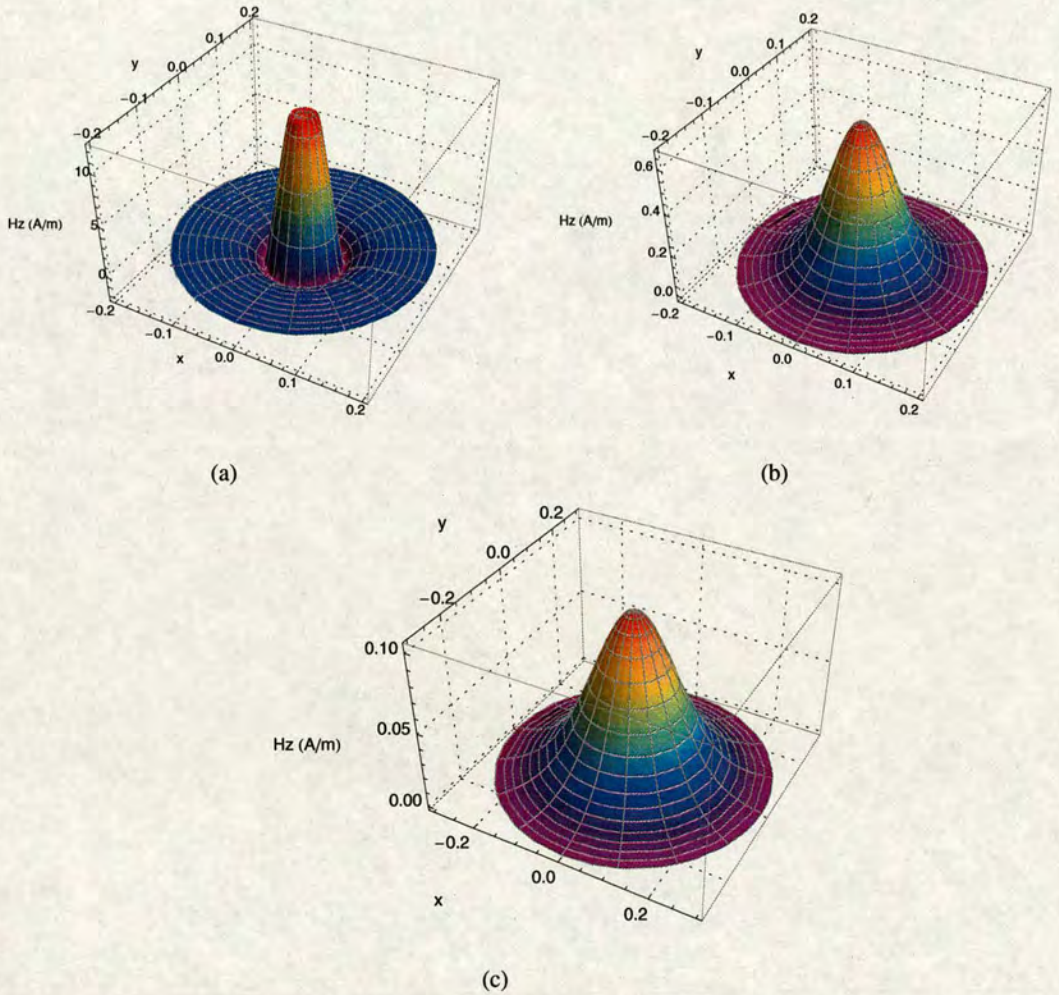

Figure 5.6: *H_z magnetic field map parallel to the $x-y$ plane at a distance from the surface of the TX coil. The dimensions of the circular spiral TX source coil is listed in Table 6.2 and a current of 250mA is considered in the coil:(a) at a distance of 0.01m from the origin of the coil, (b) Field distribution at a distance of 0.10m from the origin of the coil, (c) Magnetic field profile at a distance of 0.30m from the origin of the coil.*

a comparison to be viable. Thus the dimensions of the circular and square spirals are chosen so that the cross-sectional area of the solenoid is the same as the cross-sectional area of the spirals. The coils involved in this scenario are considered to be air-cored and situated in air. In order to investigate the performance of the TX and RX coils under misalignment it is critical to decide upon the dimensions of the coils being compared. The set of equations derived in chapter 3 that compute the efficiency of the power transfer across the inductive link can only describe a loosely coupled system. Consequently, the dimensions for the sets of TX, RX coils to be compared, need to satisfy the requirements of a loosely coupled approximation adopted

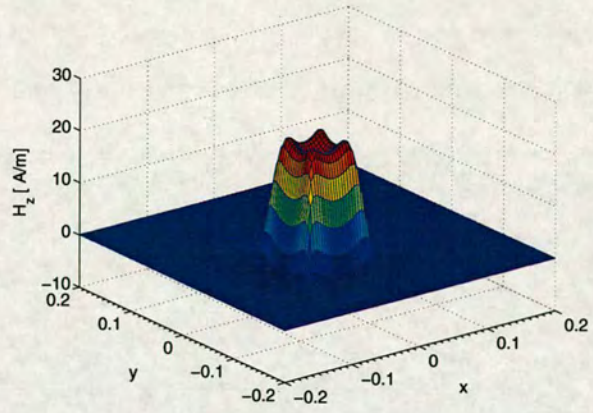

(a)

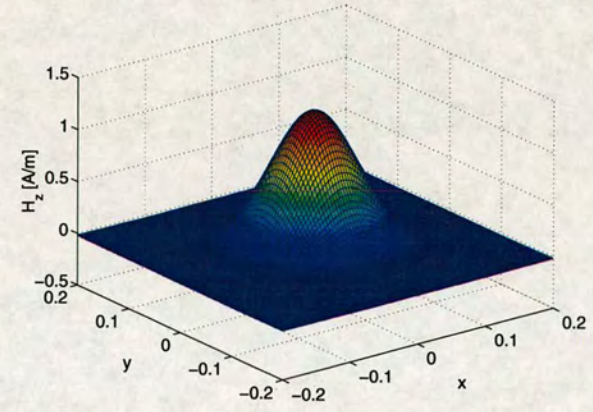

(b)

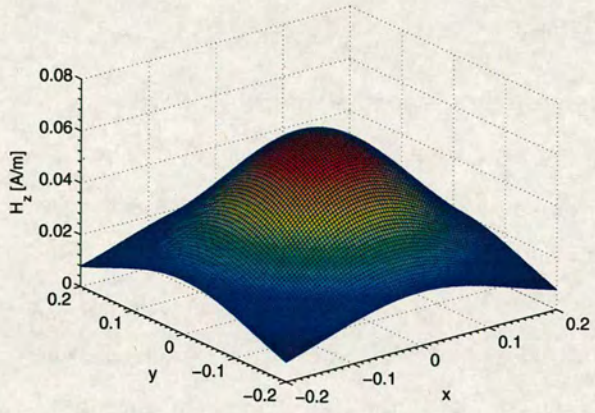

(c)

Figure 5.7: *Magnetic field distribution of the H_z component above the TX coil parallel to the $x-y$ plane. The square spiral TX source coil is listed in Table 6.2 and a theoretical current of 250mA is considered in the coil: (a) At a distance of 0.01m from the origin of the coil, (b) At a distance of 0.10m from the origin of the coil, (c) Magnetic field profile at a distance of 0.30m from the origin of the coil.*

in the model. A contour plot of the coupling coefficient between two coaxial circular loops is shown in Fig. 5.8, as computed in MATLAB based on expression (2.60).

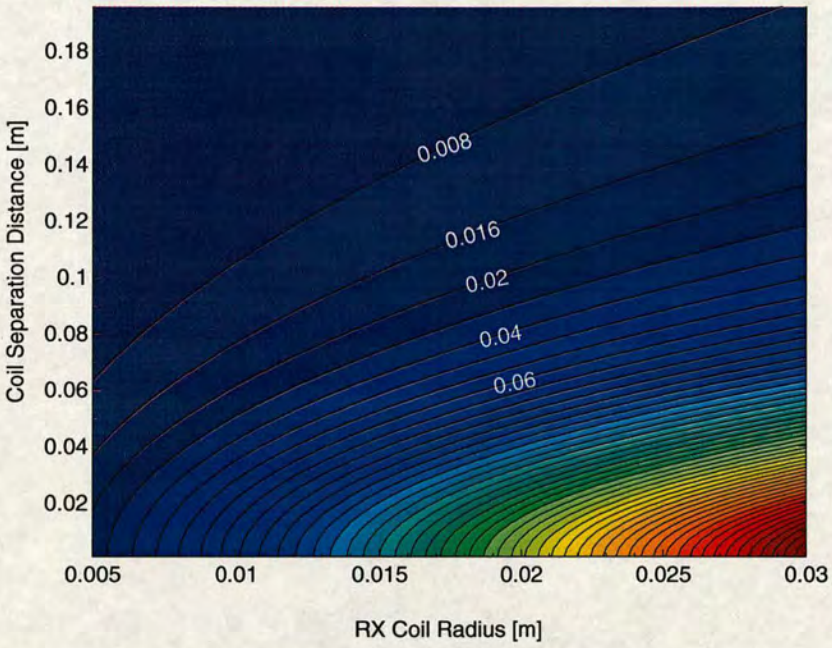

Figure 5.8: *Contour plot of the coupling coefficient between two coaxial short-solenoid coils versus coil separation distance and RX radius. The radius of the TX coil is* $0.056m$ *and the radius of the RX coil varies from* 0.005 *to* $0.025cm$.

5.4.1 Coil dimensions

Based on Fig. 5.8 it is possible to set an empirical ratio between the dimensions of the TX and RX coils for which a loosely coupled approximation is valid. Therefore, it can be shown from Fig. 5.8 that for a TX to RX coil radius ratio of 3 denoted as, $\frac{a}{b} = 3$, the minimum coil separation distance necessary for a loosely coupled link with $\kappa \leq 0.01$ should be equal to the TX coil diameter. The dimensions of the coils have been selected to comply with the loosely coupled criteria. Initially a TX square spiral with a maximum side length of 0.10m is selected. Therefore, the radius of the circular spiral and solenoid coils needs to be selected for the cross-sectional area of these structures to be equal with the cross-sectional area of the square spiral. Hence, for a square spiral side length denoted as a_{SS} the cross-sectional area of the square structure, A_{SS}, is given by:

$$A_{SS} = a_{SS}^2 \tag{5.2}$$

In the same manner given that the radius of the TX short-solenoid, a_S, is equal to the outer radius of the TX circular spiral, a_{CS}, the area of the coils can be written as:

$$A_S = \pi \cdot a_S^2 \tag{5.3}$$

$$A_{CS} = \pi \cdot a_{CS}^2 \tag{5.4}$$

By equating (5.2) to (5.3) and (5.4) and solving for a_S, it yields the dimensions of the solenoid and circular spirals. Therefore, for a square spiral with maximum length of 0.10m the circular structures will have an equivalent cross-sectional area when $a_S = a_{CS} \approx 0.056$m. Once the dimensions of the TX coils are established the size of the RX coils can be selected to satisfy the loosely coupled approximation. Hence, for the circular coil geometries the radius of the RX coils should be one third of the radius of the TX coils which is equal to 0.0186cm. Following the same procedure for the square spiral the length of the outermost turn is calculated to be 0.033cm. For the inductor geometries investigated in this section, 8-turn coils are considered in both the TX and RX coils. The conductor in the case of the short-solenoid coils is considered to be 19SWG and 25SWG copper enamelled wire for the TX and RX coils respectively. Referring to Table G in appendix G a conductor size of 19SWG and 25SWG corresponds to a conductor diameter $d_{TX} = 0.001$m and $d_{RX} = 0.0005$m for the TX and RX coils respectively. In the case of printed spirals copper was selected as the conductive material, with a track thickness of 35μm. The thickness of 35μm is chosen for the conductive material since it is readily used in PCB fabrication of planar magnetic devices, [111]. In addition, according to [194] for Aluminium and Copper coils a track thickness of $t > 30\mu$m is required to achieve a sufficient quality factor, $Q > 60$ even for a small track width. Based on the discussion of the losses in a planar inductor given in section 4.4.2.2, for printed coils the track thickness should be chosen as high as possible in order to achieve high quality factors. It is evident from expressions (4.33) and (4.35) that the track width (w) and interwinding spacing (s) will also influence the losses in the printed coils. In fact the quality factor of the inductor deteriorates as the track width reduces. Shah et al. studied the effect of various w to s ratios on the coil Q, [111]. According to this study, the coils with $w/s > 1$ can achieve greater Q factors than coils with $w/s < 1$. Moreover, Shah et al. demonstrated experimentally that the lowest series ohmic loss in the coils (R_s) is achieved when the track width is twice the interwinding spacing, at the optimum value of $w/s = 1.94$.

Further, every effort should be made to concentrate the turns of the coil on the outline of the spiral essentially creating coils with small fill ratios in order to maximise the effective area of

the coils. This implies that the track width should be small. Clearly, there is a trade-off between maximising the quality factor of the coils and augmenting the amount of magnetic flux that passes through the enclosed collective area of the turns in the spiral. However, according to Mohan et al. in [176], a smaller spacing improves the inter-winding magnetic coupling which in return increases the inductance of the spiral and reduces the area consumed by the spiral. In essence, the only reason supporting a large spacing originates from the need to reduce the inter-winding capacitance. However, Yue et al. in [178] demonstrates that this is not a major concern as the inter-winding capacitance is shadowed by the underpass capacitance. The coils inter-turn capacitance is dependent upon the manufacturing technology of the coils and for printed coils it is estimated in the region of $2 - 4$pF. Subsequently, a track width of 0.002m and 0.0005m with an equal track spacing are selected for the TX and RX coils respectively.

Both solenoid and spiral coils are considered to consist of approximately the same length of conductor. For convenience, MATLAB notation in the form of arrays is employed to describe the coil configuration. The set of TX/RX spiral coils can be described as:

$$a = [a_{min} : d : a_{max}] \tag{5.5}$$

$$b = [b_{min} : d : b_{max}] \tag{5.6}$$

In this representation a_{min}, b_{min} and a_{max}, b_{max} denote the radii in the circular geometry, and the side lengths in the square geometry, for the innermost and outermost concentric loops respectively. The increment d between the radii of the circular spiral is given as $d = w+s$ where w is the track width and s is the inter-turn spacing of the spirals. Referring to the discussion of the previous paragraph for the spirals selected in this scenario $w = s$. In the case of the square spiral, it can be shown from Fig. 3.7 that the increment d between each consecutive loop is $d = 2\ (w + s)$. Therefore, the printed square spiral TX/RX coils with side length of each concentric loop, denoted a_{SS} and b_{SS} are defined as:

$$a_{\text{ss}} = [0.10 : 0.006 : 0.058] \tag{5.7}$$

$$b_{\text{ss}} = [0.033 : 0.002 : 0.019] \tag{5.8}$$

In addition, the set of circular spiral coils with radii for each concentric loop, denoted a_{CS} and b_{CS} can be expressed as:

$$a_{\text{cs}} = [0.056 : 0.003 : 0.040] \tag{5.9}$$

$$b_{\text{cs}} = [0.018 : 0.001 : 0.11] \tag{5.10}$$

Note that the TX and RX coils of both the square and circular shapes are composed of 8 turns represented by 8 concentric loops. The resonant frequency is chosen to be a common ISM frequency band used in HF RFID systems, that of 13.56 MHz.

5.4.2 Power transfer efficiency in coaxial orientation

Equations (3.83), (3.84) and (3.85) allow the computation of the power transfer efficiency for the inductive link between reader and tag coils in the ideal orientation for solenoid, circular and square spiral coils. Therefore, different combinations of reader/tag coils are possible to be compared with respect to the power delivered to the tag. The geometries studied in this thesis are the short solenoid, circular and square spirals. Using code written in MATLAB we can compute and plot the power transfer function in the ideal orientation, lateral and angular cases. The coils investigated are assumed to have the same effective area, for the results to be valid. Thus, the dimensions of the circular spiral are chosen so that the cross - sectional area of the short solenoid is the same as the area of the circular spiral.

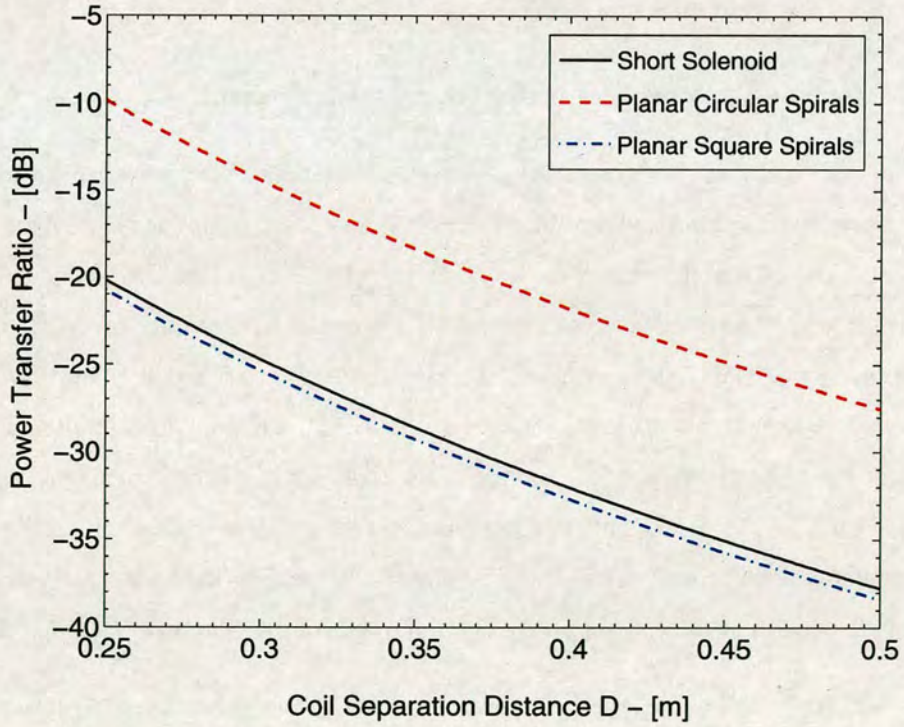

Figure 5.9: *Plot of Power Gain across the Inductive Link versus Coil Separation D, for three Combinations of TX and RX Coil Geometries.*

Referring to Fig. 5.9 it is evident that the combination of TX, RX circular spiral coils does in-

deed improve the coupling between TX and RX in the ideal orientation, when the tag is situated directly on top of the reader. In this configuration the read range of the RFID device can be significantly improved by using circular spiral coils. The plots in Fig. 5.9 clearly show that the planar circular spiral reader coil exhibits stronger coupling with the RX/transponder coil than that of the solenoid design in the coaxial orientation. The difference in the power transfer ratio remains constant as the separation distance of the coils increases. This effect can be understood since a more concentrated magnetic H-field is expected at the same point by arranging the TX coil's conductor loops at the same plane. This was demonstrated in the previous section, where the field strength of different coil geometries were compared. As a result, stronger magnetic coupling is expected and consequently higher read range can be achieved.

Overall the least efficient geometry appears to be the square spiral coil. In the design of RFID systems it is critical to identify the antenna/coil geometry which improves the coupling between reader and tag. It is evident from the results presented that the spiral coils attain almost the same performance as the conventional solenoid with the added advantage that they can be easily mounted to RFID devices, and minimize the size of the tag.

5.4.3 Power transfer efficiency under lateral misalignment

Fig. 5.10 comprises of a set of graphs for power transfer efficiency across a typical inductive link for transcutaneous power and data transfer. Equations (3.87), (3.88) and (3.89), introduced in chapter 3, allow the computation of the link efficiency for short-solenoid, circular and square spiral coils respectively. Based on these expressions, the MATLAB code that produces plot 5.10 is included in section D.3 of the appendix. Representative TX and RX coil dimensions for the applications studied in this work were selected as illustrated in the previous section. For each set of TX, RX coils the variation in coupling efficiency with respect to lateral misalignment is plotted in Fig. 5.10. It is evident from the plots that the efficiency of the link reduces with increasing lateral displacement of the RX. The power efficiency drops significantly as the RX moves from the center of the TX toward the circumference of the TX coil.

The unexpected trough observed at the efficiency plots in Fig. 5.10(a) is caused by the curvature of the magnetic field lines at the periphery of the coil. Due to this curvature, the z component of the magnetic field is zero at the point where the magnetic flux lines are parallel to the plane of the transmitter. Hence, this results in a steep drop in the link efficiency as indicated in Fig. 5.10(a). Naturally, due to the distribution of the magnetic flux lines responsible for the curva-

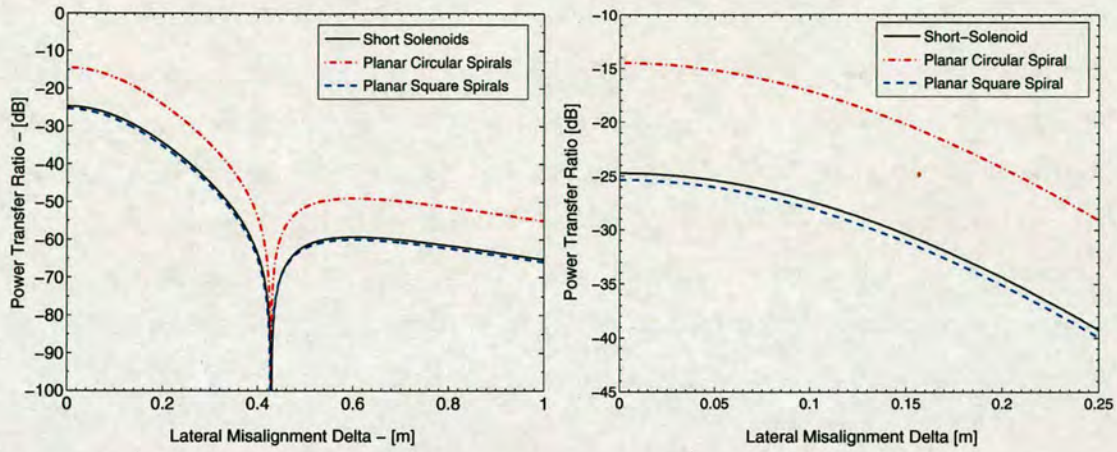

(a) (b)

Figure 5.10: *Plots of Power Gain across the Inductive Link versus Lateral Displacement* Δ*, for three Combinations of TX and RX Coil Geometries.*

ture of the field, the point of local minimum for the link efficiency moves closer to the origin as the coil separation distance decreases. Eventually, the efficiency drops to zero for large lateral misalignments. In addition, it is evident form Fig. 5.10(a) that for small lateral misalignments the system exhibits excellent misalignment tolerance. This is one of the advantages enjoyed by an asymmetrical system where the receiver coil is smaller than the transmitter. Therefore, such an implementation enjoys both the advantage of a smaller receiver coil which is very important in implanted systems and makes the link efficiency insensitive to lateral displacements for misalignment distances that do not exceed the maximum diameter of the transmitter coil.

5.4.4 Power transfer efficiency under angular misalignment

The power transfer efficiency when the plane of the RX coil is tilted is expressed by equations (3.90), (3.91) and (3.92) for the coil geometries studied in this chapter. All calculations have been performed using MATLAB. The MATLAB code that computes the coupling efficiency according to expressions (3.90), (3.91) and (3.92) is included in section D.4 of the appendix.

In the design of inductive coupled systems, it is of interest to determine the impact the orientation angle has on the magnetic coupling. Hence, based on this information it is possible to conclude a RX deployment which will maintain an adequate coupling. In the applications targeted in this thesis, the RX coil is unlikely to remain in a perfect coaxial alignment with the

TX coil.

Fig. 5.11 presents a set of plots for typical TX, RX coil dimensions for the applications studied, as discussed in section 5.4.1, that represent the variation in coupling efficiency under angular misalignment conditions. It is evident from Fig. 5.11 that the link efficiency is substantially reduced with increasing tilt from 0° (coaxial) of the RX and finally it becomes zero at 90° (perpendicular). The coupling efficiency is maximised when the two coils are placed in a coaxial configuration and it starts to decrease with increasing angular tilt of the transponder coil.

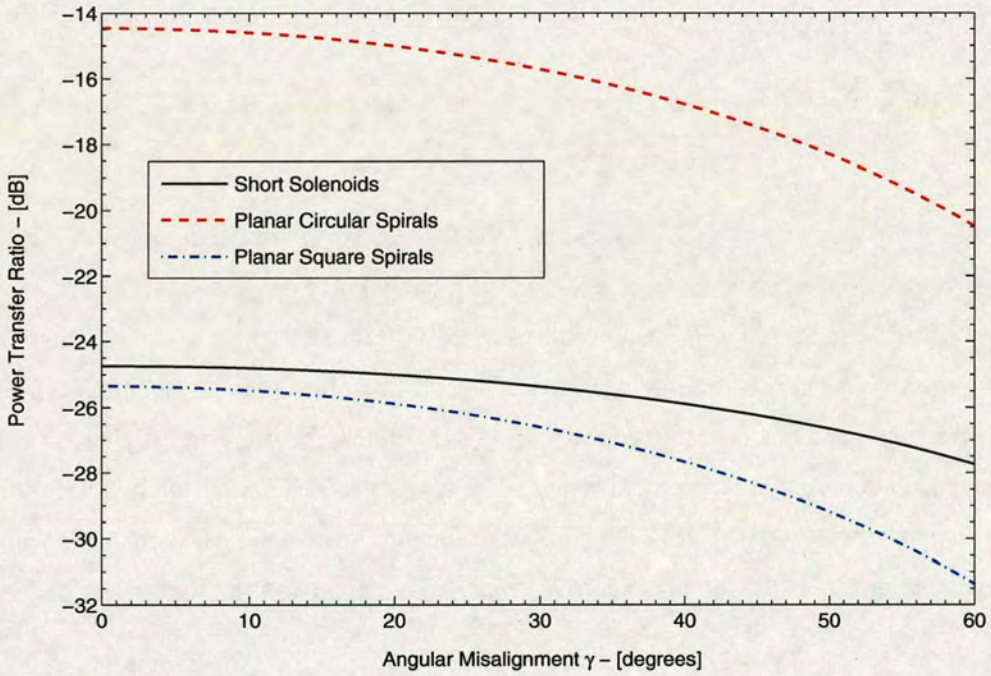

Figure 5.11: *Plot of Power Gain across the Inductive Link versus Angular Displacement γ, for three Combinations of TX and RX Coil Geometries.*

However, an interesting response on the power transfer efficiency with increasing angular misalignment is demonstrated in Fig. 5.11 above. The short solenoid coil, exhibits a more linear power distribution with increasing misalignment than that of spiral coils. This indicates that the short-solenoid acquires an increased angular misalignment tolerance that can benefit applications where the receiving coil is subjected to large angular tilt. Nevertheless, the most efficient topology is the circular spiral, as was the case for the coaxial and lateral orientations.

5.5 Discussion

It is demonstrated in chapter 3 that the link efficiency is directly related to the ohmic losses in the coils, the frequency of operation and geometrical characteristics of the link. In general terms such geometrical characteristics include the coils shape and fill factor, their relative distance, orientation and number of turns. The frequency range targeted in this thesis is in the region of 1-40MHz. The frequency window selection is governed by the following considerations: radio license regulations, absorption in the conductive tissue and size constraints for the implant. To obtain reasonably compact and flat induction coils of a high quality factor, frequencies above 5 to 10 MHz are to be preferred. The majority of passive near-field RFID systems operate in the HF bands with the most popular being that of 13.56MHz. However, for biomedical applications the upper frequency is limited to 40MHz because tissue power absorption can become significant for higher frequencies. It is possible to extend this upper frequency limit if the power level being transmitted is very small, in the order of micro to a few milliwatts. On the other hand, it is common for inductive links to operate at allocated ISM frequency bands. Usually the operating frequency is predefined to comply with the radio license regulations and safety standards. Therefore, optimisation of the link efficiency with respect to the resonant frequency is not considered critical. Hence, we can conclude that in the design of efficient inductive coupled systems the coils geometries are the most important factors in defining the link efficiency.

Despite the importance of the coils geometry in inductive link design, there has been little research on optimizing the geometry of these coils in order to maximise their power transmission efficiency. Shah et al. in [111] derived some general guidelines from experimental data. However, this study stopped short from identifying the performance behaviour of different coil shapes under misalignment. It is evident from the results presented in the previous sections that for similar numbers of turns, frequency and w and s dimensions, the dependence of the coil's Q factor of circular spiral coil are similar to those measured for the square spiral. Nevertheless, the consequences of misalignment between transmitting and receiving coils were more severe for square spiral coils than for circular spiral coils and short solenoids.

The square spirals exhibit poorer performance when compared to their circular counterparts. This can be attributed to the fact that numerous sharp corners in square inductors introduce crowding series resistance which degrades the quality factor of the coil significantly. Segments that couple most strongly tend to be parallel and closely spaced in a typical spiral. In the circular

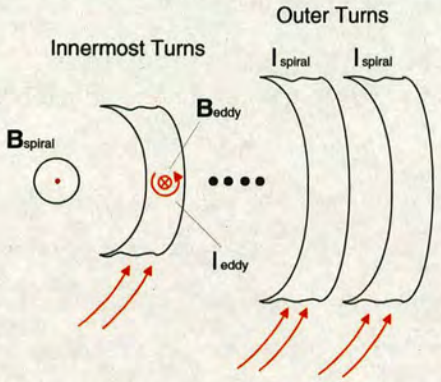

Figure 5.12: *Current distribution in spiral coil conductor.*

layout the current flows in the same direction in all the turns, as shown in Fig. 5.12, which helps to boost the overall mutual inductance. One of the advantages of a square geometry arises from the fact that because a circle has a minimum circumference for a given spacing between the inner edges of the coil, a square spiral coil provides more area in the center of the coil as well as more inductance compared to a circular spiral coil of similar dimensions. However, the consequences of misalignment between transmitting and receiving coils are greater for square spiral coils than for the circular geometry as seen in Fig. 5.10 and Fig. 5.11. Thus, it would be preferable to adopt circular spiral coils rather than square spirals for a loosely coupled inductive powering system.

5.6 Chapter Summary

This chapter presented a performance comparison for three common coil geometries with respect to the efficiency of inductive power transfer in the coaxial orientation, lateral and angular misalignment. To date, there has been no published performance comparison between short solenoid coils, circular and square spirals under misalignment conditions. The examination of the influence of geometrical parameters such as the shape of the coils and their relative position on the link efficiency was conducted in two parts. In the first part of this chapter the axial and radial H_z magnetic field component generated from the transmitting coils was studied at several distances form the source coils. It was demonstrated that the magnetic field profiles for the coils studied are different at very small distances from the coil surface. At larger distances from the TX coil, where poor coupling takes place, the field behaviour becomes more uniform and the field map is similar for all the coil structures investigated. The main distinction in the

magnetic field style between the coil geometries considered, is the fact that the short-solenoid produces the higher magnetic field strength compared to the other structures. Finally, the most efficient coil structure in terms of power transferred across an inductive link was proved to be a circular spiral coil for all the three receiver orientations investigated.

Chapter 6
RFID Design Example

6.1 Introduction

An RFID design example is presented in this chapter, based on an ASIC for specialised HF passive RFID label tag applications. Focusing on passive systems, the majority of tag antennas, suited for on-body application, implants or RFID tags operating in close proximity to metallic surfaces, conventionally work in the HF band of 13.56MHz. At this frequency the performance of the antenna is acceptable in close proximity with conducting media. Usually, these devices are typically fabricated as multi-turn coils. Due to the nature of the application considered in this chapter spiral coils are favored. Considering practical coils for RFID applications, the coil structures studied are restricted to planar coils which can be easily attached to items being monitored. The contribution of this chapter is a demonstration of a misalignment sensitivity analysis for a practical HF passive RFID device, using the theoretical model suggested in Chapter 3. A design example is presented, based on the Philips ICODE Label IC range, for a set of printed circular and square spiral coils. The position tolerance of the system is determined by plotting contours of constant received power as a function of coil position and orientation.

6.2 RFID Design Example

In this section the efficacy of the power transfer functions introduced in this thesis is demonstrated via a practical RFID design example. A design procedure is presented for coils of circular and square spiral shape factors, with respect to the power transfer efficiency, under misalignment conditions.

A general purpose typical RFID integrated circuit for label application in retail and logistics is adopted for this investigation. The performance of the SL1ICS3101 I-CODE1 Philips semiconductors label IC is demonstrated below using equations (3.88,3.89,3.91,3.92). The choice of this tag is well-justified due to its popularity among high-frequency smart label solutions. Owing to the passive nature of the ICODE1 label IC no internal power supply is required. A

contact-less interface generates the power supply and the system clock via the resonant circuitry by inductive coupling to the reader. The electrical and operational characteristics of the SL1ICS3101 are listed in Table 6.1.

6.2.1 Electrical characteristics of the IC label

An equivalent circuit of the RFID label integrated circuit is illustrated in Fig. 6.1. The receiver coil is connected across the pads LA and LB as shown in the diagram of Fig. 6.1(a). Together with the label coil, the input capacitance of the label IC (C_{res}), forms a parallel resonant circuit with a target resonant frequency of 13.56MHz. According to the following calculation a label IC input capacitance of 97pF leads to an inductance of approximately 1.5 μH. The resonant frequency of the device is expressed as:

$$f_{res} = \frac{1}{2\pi\sqrt{L_c C_{\text{res}}}} \tag{6.1}$$

SYMBOL	PARAMETER	RATING	UNIT
C_{res}	Input Capacitance between LA - LB	97	pF
R_{label}	Label Input Resistance	65	$k\Omega$
P_{min}	Minimum Operating Supply Power	450	μW
V_{LA-LB}	Threshold Voltage	2	V_{rms}
f_{res}	Operating Frequency	13.56	MHz

Table 6.1: *Characteristics of HF SL1ICS3101 RFID tag according to [36].*

The key factors which influence the design of the RX coil are the electrical characteristics of the ICODE IC. However, the typical behaviour of the capacitance and modulating resistance of the IC varies according to the applied voltage across the terminals LA and LB denoted $V_{\text{LA-LB}}$. Therefore, the operating frequency of $13.56MHz$ is defined as a threshold frequency by the manufacturer for the minimum operating voltage of the IC. According to the manufacturer specifications given in [36] the minimal supply voltage for ICODE label IC operation is 2V_{rms}. Hence, Table 6.1 summarises the electrical properties of the label IC which are of interest for the coil design. These characteristics are measured at the point of interest, for an applied threshold voltage, $V_{\text{LA-LB}} = 2\text{V}_{\text{rms}}$. In addition, the minimum operating power consumed by the IC is 450μW including the losses in resonant capacitor and rectifier.

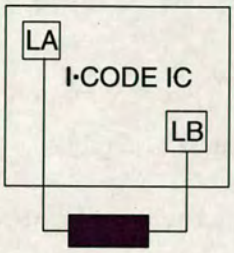

(a)

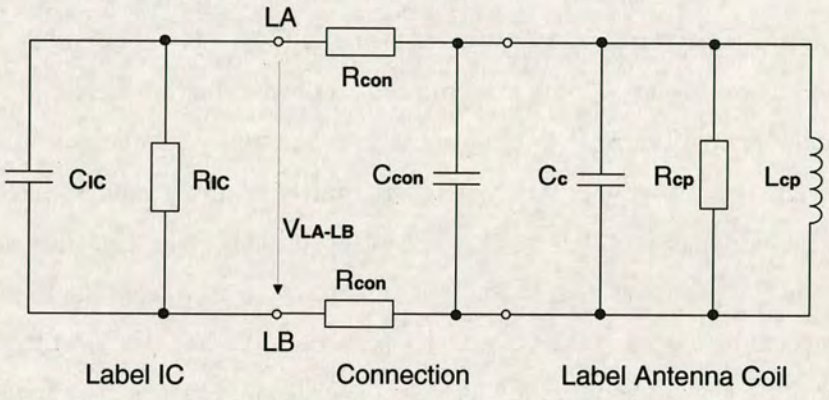

(b)

Figure 6.1: *Equivalent circuits of the Philips Semiconductors ICODE1 Label IC: (a) ICODE label IC showing the coil connection pads, (b) Equivalent circuit of the label including the RX coil, [36, 194].*

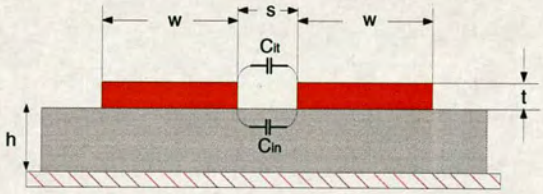

Figure 6.2: *Cross-section of adjacent conductors in a printed spiral coil depicting the parasitic components withing the insulator and substrate.*

6.2.2 Equivalent circuit of the label IC

Upon establishing the electrical characteristics of the label the focus shifts to the equivalent circuit of the label shown in Fig. 6.1. In Fig. 6.1, R_{con} and C_{con} signify the ohmic losses of the wire connection and the stray connection capacitance between the IC and the RX coil. Attention is required to minimise the ohmic losses in the connection resistance. Practically, R_{con} should

be kept as low as possible in order to have a minimal impact on the total parallel equivalent resistance of the label. Moreover, a relatively high connection resistance will degrade the total quality factor of the label and result in a reduced transmission range. A connection resistance in the order of $R_{\text{con}} << 1\Omega$ is considered negligible.

The connection capacitance represented as C_{con} describes the increase of the total label capacitance due to dielectric changes in the connection area when the chip is applied to the coil. This type of parasitic capacitance is influenced by the size of the IC and the value varies between different devices in the ICODE range. This capacitance is difficult to estimate, so it is recommended by the manufacturer to select a value in the range $C_{\text{con}} = 0.5 - 2\text{pF}$. In the early stages of the design process for the RX coil it is critical to know the correct value for the inductance of the RX coil, required for the ICODE device to resonate at the optimum resonant frequency of 13.56MHz. In order to achieve this goal it is imperative to have a good estimate of the parallel equivalent capacitance of the label IC. The total capacitance of the device consists of the stray capacitance of the connections, discussed previously, the input capacitance for threshold condition denoted as C_{ICT} and the parasitic capacitance of the RX coil itself represented as C_{c}. The parasitic capacitance of the coil includes the inter-turn capacitance, C_{it}, the additional capacitance due to a possibly integrated bridge, C_{br}, and finally an inlet capacitance, C_{in}, as shown in Fig. 6.2. It is recommended by the manual of the RFID device that such an inlet capacitance should be measured since it is difficult to estimate theoretically. Apropos, C_{in}, cannot be considered in the theoretical example presented here. Hence the total equivalent capacitance of the label is given as:

$$C_{label} = C_{\text{c}} + C_{\text{con}} + C_{\text{ICT}} \tag{6.2}$$

Based on the previous equation (6.2), the total capacitance of the label IC is equal to $C_{label} = 102.5\text{pF}$. Consequently, it follows from expression (6.1) that the necessary inductance of the RX coil for the label to resonate at the frequency of 13.56MHz is equal to $L = 1.34\mu\text{H}$.

The efficiency of the RFID label will be investigated henceforth based on two different RX coil geometries that of a square and circular printed spirals. Therefore, the main challenge is to design the RX spiral coils in order to achieve an objective inductance of $1.34\mu\text{H}$. The degree of coupling for two inductive links using printed square and circular spiral TX (Reader) and RX (tag) coils can be predicted from the power transfer expressions (3.88, 3.89) and (3.91, 3.92) with respect to the lateral and angular tilts of the tag coil respectively. It is important to identify the context in which expressions (3.88, 3.89) and (3.91, 3.92) can be applied to predict

the read range and the misalignment tolerance of the system. Consequently, the SL1ICS3101 RFID device must comply with the following operating conditions:

- For the present HF passive RFID application the inductively coupled reader and tag coils must be loosely coupled. This suggests a coupling coefficient of $\kappa < 0.01$ and a separation distance $D >> S_{\text{max}}$ much greater than the maximum size of the transponder S_{max}.
- Typically, a minimum power reflection coefficient (τ) between the antenna and chip is desired. Consequently, the complex impedance of the RX coil should be matched to the impedance of the load, which is represented by the label IC electronics.

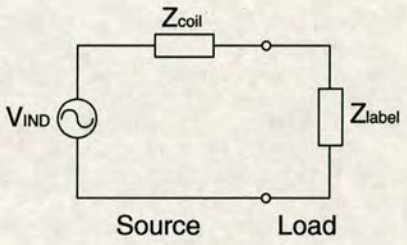

Figure 6.3: *Generator-load circuit with two complex impedances.*

6.2.3 Impedance matching

In order to maximise the reading range of the system it is crucial to optimise the amount of power transfered to the load, which is represented by the internal impedance of the label IC. Maximum power transfer can be achieved by conjugate impedance matching the RX coil to the impedance of the label IC. This principle is demonstrated through Fig. 6.3. As discussed earlier the label tag exhibits a complex impedance:

$$Z_{\text{label}} = R_{\text{in}} - \frac{j}{\omega C_{\text{IC}}}$$

According to the data sheet of the ICODE SL1ICS3101 RFID tag given in [194] at the operating resonant frequency of 13.56MHz, corresponding to a threshold voltage $V_{\text{LA-LB}} = 2\text{V}$, the capacitance of the SL1ICS3101 ICODE label IC is specified as $C_{IC} = 97pF$, [194]. Furthermore, the input resistance of the label is interpolated from the SL1ICS3101 datasheet to be equal to $65k\Omega$. Finally, from expression (6.2.3) the corresponding impedance of the label IC can be expressed as follows:

$$Z_{\text{label}} = 65k\Omega - j\ 121.5\Omega$$

The microchip exhibits a strongly capacitive input reactance which can be justified from the fact that the microchip includes an energy storage stage. RFID tag antennas are typically designed for an application specific integrated circuit (ASIC) and thus, chip impedance is usually given to an antenna designer. The RFID label tag in the receiving mode can be represented by Fig. 6.3, where Z_{label} is the chip impedance, Z_{coil} is the antenna impedance, and V_{IND} is the open-circuit RF voltage developed across the terminals of the tag antenna. Once the target impedance of the label is known the primary design concern is impedance matching the coil to the label IC. The input impedance of the SL1ICS3101 RFID microchip is largely dictated by the junction capacitance of the rectification diode and as a result the input impedance of the device is primarily capacitive. Therefore, in order to meet the requirements of maximum power transfer and ensure optimum tag performance, the RX coil impedance should be a conjugate match of the impedance presented by the IC. Hence, the impedance of the antenna coil should be inductive in order to achieve conjugate matching. The power transmission coefficient (τ) accounts for the impedance mismatch between the antenna ($Z_{coil} = R_{coil} + jZ_{coil}$) and the microchip ($Z_{label} = R_{label} + jZ_{label}$) and is expressed as, [195]:

$$\tau = \frac{4R_{label}R_{coil}}{|Z_{label} + Z_{coil}|^2} \leq 1 \tag{6.3}$$

In order to minimise the power reflection coefficient it is imperative to achieve an equivalent parallel resistance, R_{P}, for the RX coil equal to the real part of the label's impedance. At the resonant frequency of 13.56MHz the following expression must hold:

$$R_P = R_{\mathrm{IC}} = Q_{\mathrm{RX}}^2 \cdot R_S \tag{6.4}$$

$$= \left(\frac{\omega L_{\mathrm{RX}}}{R_S}\right)^2 \cdot R_S \tag{6.5}$$

where Q_{RX} is the quality factor for the RX coil, R_P and R_S represent the parallel and series resistance of the receiver coil respectively and L_{RX} is the self inductance of the RX coil. Substituting for $R_{\mathrm{IC}} = 65k\Omega$ and solving for R_S in the previous expression, it yields the target series AC resistance for both the square and circular printed spiral coils to be $R_S = 0.2\Omega$.

6.2.4 Coil design

The dimensions of the RX printed spiral coil must be decided first. A performance comparison between the circular and square coil geometries demands the effective areas of the coils considered to be equal. Starting with a printed RX square spiral coil with a maximum side length

equal to $a_{PSS} = 0.045$m, the radius, of the RX circular coil, denoted as a_{PCS}, is calculated as follows:

$$a_{PCS} = \sqrt{\frac{a_{PSS}^2}{\pi}} \tag{6.6}$$

Hence, the outer radius of the RX circular spiral coil is derived from the previous expression to be $a_{PCS} = 0.0254$m. Once the dimensions of the RX spiral are set, the rest of the dimensional parameters such as the number of turns N, the conductor track width, w, the inter-turn separation distance s, and the track thickness t of the coils can be decided. Such parameters are critical in the design of coils as they influence the total inductance and the quality factor of the structure. The challenge is to choose, for a given technology with a fixed metal thickness t, the optimum combination of N, w, s and fill factor φ in order to converge to an optimum but tangible Q for the desired frequency.

At the same time the specifications for the receiver coil design call for square and circular spiral coils with an inductance of $1.34\mu H$ and an AC resistance, that represents the real part of the coil's impedance, equal to $R_{coil} = 0.2\Omega$. The remaining geometrical parameters of N, w, s determine the AC resistance through their influence on eddy and current crowding effects in the turns of the spiral. Furthermore, the area occupied by the inductor should be maximised in order to improve the sensitivity of the RFID device and increase its operational range. It becomes clear that a trade-off exists between the aforementioned parameters and maximising Q. Ohmic losses in the coil arising from current crowding or proximity effects are best minimised by making the coil conductor narrow, as discussed by Kuhn et al. in [196]. However, although a narrow track reduces the proximity effect, the structure will suffer from an increased coil resistance. Subsequently, it is possible to overcome this dilemma by using a thicker conductor. Consequently, the surface area of the coil can be increased by concentrating the turns in the circumference of the coil without compromising the quality factor of the inductor.

Several closed-form equations have been proposed by researchers to approximate the self-inductance of printed spiral coils, such as in [42, 176, 181]. Simple and accurate analytic expressions for the self inductance of square and printed spirals developed by Mohan et al. [176] were introduced earlier in section 4.4.2. Expressions (4.27) and (4.28) were used for the design of the prototype coils used in the experimental phase and are adopted for the design of the printed spirals discussed in this section. Given the number of factors involved in the design of spiral coils, an iterative method is usually employed. This method is implemented in the design of the spiral coils considered in this chapter, and is better illustrated with reference to

the design flowchart of Fig. 6.4. The results of the iterative design method are presented in Table 6.2 where the characteristics of the spiral coils are listed.

Coils	d_{in} [mm]	d_{out} [mm]	φ	w [mm]	s [mm]	t [μm]	N
TX Circular Spiral - CS	152	124	0.10	2.5	1	30	5
RX Circular Spiral - CS	50	23	0.37	2.5	1	30	5
TX Square Spiral - PSS	135	107	0.12	2.5	1	40	5
RX Square Spiral - PSS	45	17	0.45	2.5	1	40	5

Table 6.2: *Dimensions of printed circular and square spiral inductive coupled coils.*

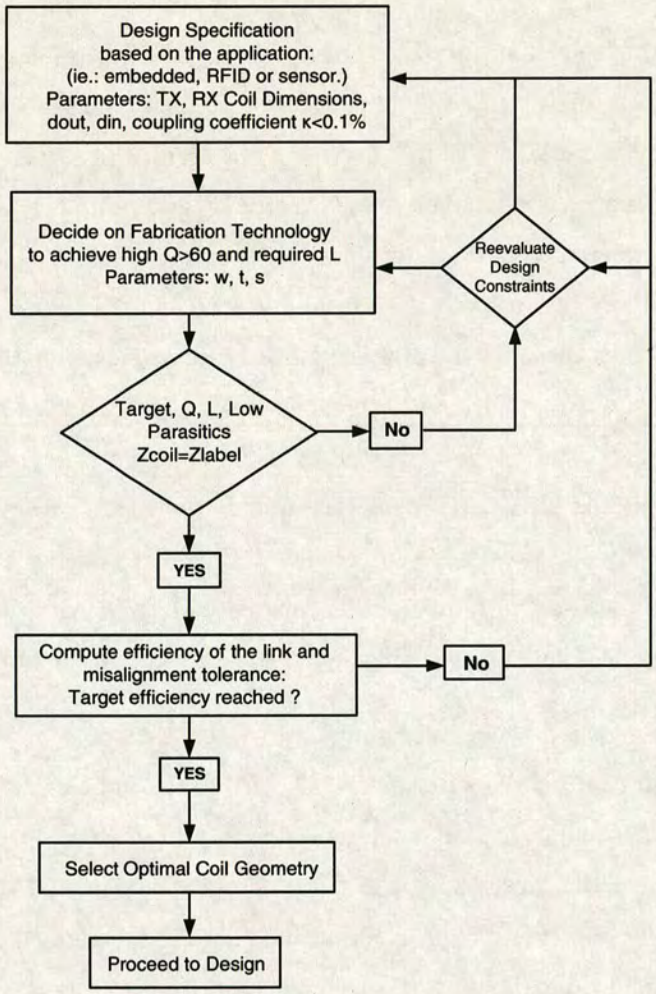

Figure 6.4: *Iterative TX, RX printed spiral coil design flowchart for passive RFID applications.*

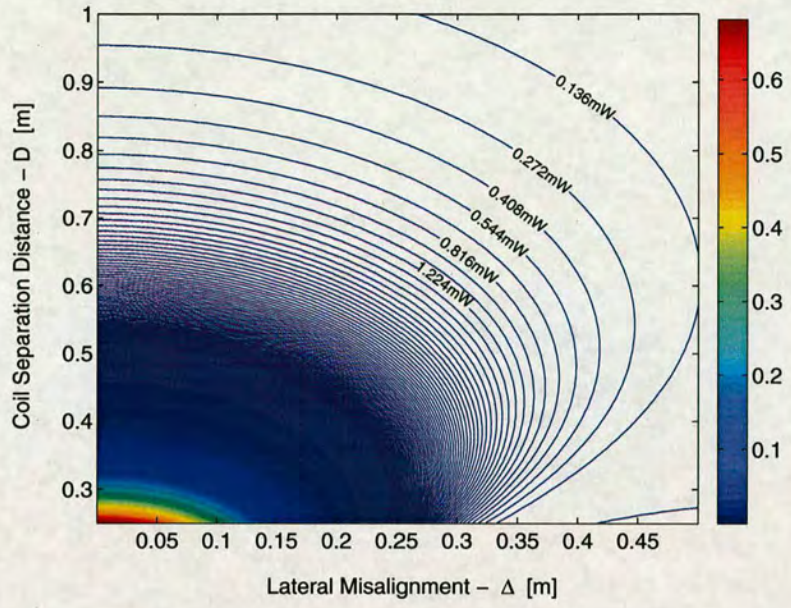

(a)

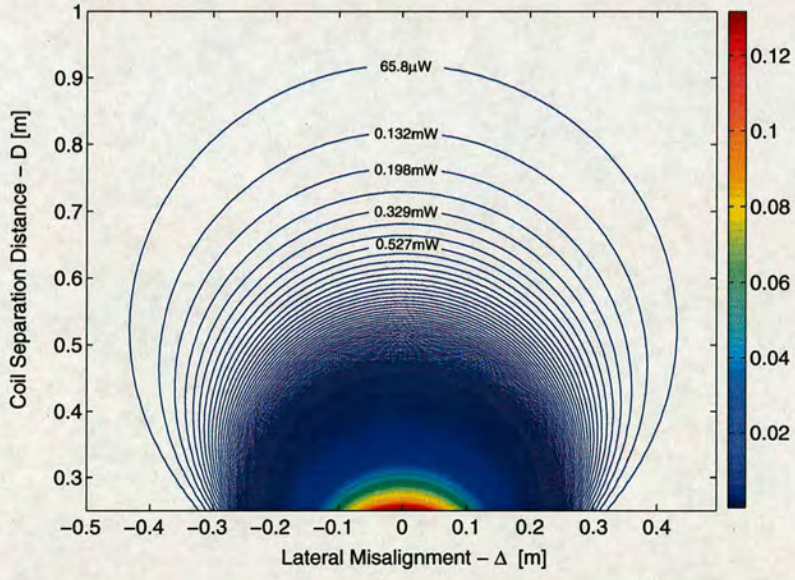

(b)

Figure 6.5: *Contours of constant received power (P_{RX}) versus coil separation distance and lateral displacement for the HF passive Philips ICODE SL1ICS3101 RFID label tag IC. The system is operating at the frequency of 13.56MHz with an input power in the reader coil of 1Watt: (a) The RX coil is a 5-turn printed circular spiral coil, (b) The RX coil is a 5-turn printed square spiral coil. The colour-bar depicts power intensity in Watts.*

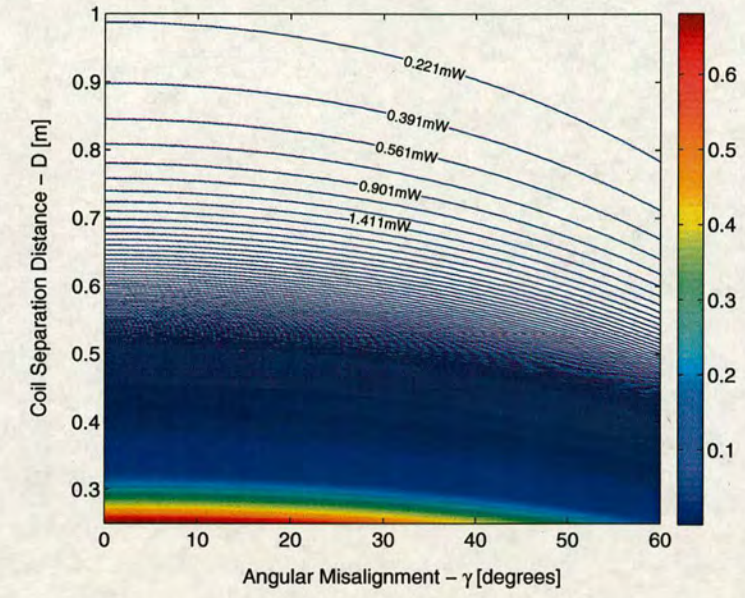

(a)

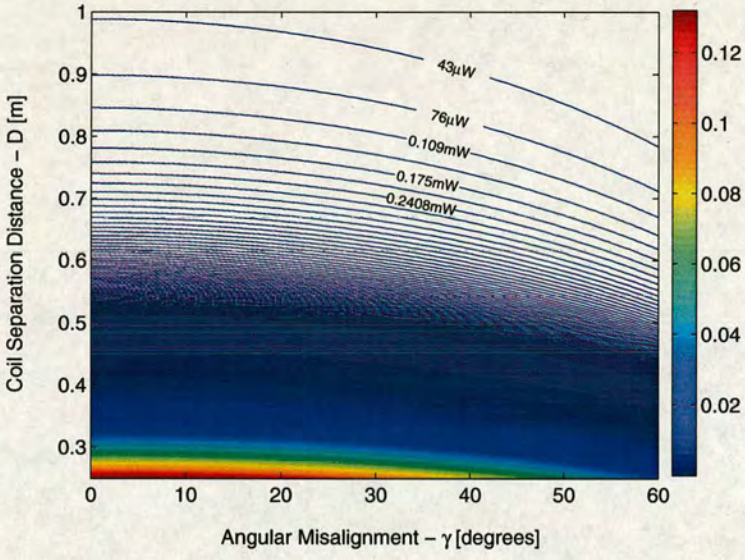

(b)

Figure 6.6: *Contours of constant received power (P_{RX}) versus coil separation distance and angular misalignment for the HF passive Philips ICODE SL1ICS3101 RFID label tag IC. The system is operating at the frequency of 13.56MHz with an input power in the reader coil of 1Watt: (a) The RX coil is a 5-turn printed circular spiral coil, (b) The RX coil is a 5-turn printed square spiral coil. The colour-bar depicts power intensity in Watts.*

6.2.5 Operating range and misalignment sensitivity

The positional tolerance of the system is found by plotting contours of constant received power (P_{RX}) as a function of RX coil lateral displacement and angular tilt, as is shown in Fig. 6.5 and Fig. 6.6. The analysis presented in this section is performed for the two sets of spiral circular and square coils with dimensions given in Table 6.2. In the lateral misalignment case, it is possible to predict the received power at the RFID tag device by solving for P_{RX} in expressions (3.88) and (3.89), which can then produce the contour plots given in Fig. 6.5 and Fig. 6.6. Consequently, referring to Fig. 6.5 and Fig. 6.6 it is possible to set upper bounds of permissible misalignment. This principle is demonstrated in Fig. 6.8 and Fig. 6.8. The inscribed squares indicate possible operating regions for the SL1ICS3101 RFID tag, for a minimum operating power of $450\mu W$, in the radial and angular misalignment regimes. Figs. 6.7(a) and Fig. 6.8(a) depict possible operating areas for the set of inductively coupled circular spiral coils listed in Table 6.2. Finally, Fig.6.7(b) and Fig.6.8(b) show an acceptable operating area for the set of square spiral coils presented in Table 6.2.

6.3 Chapter Summary

This chapter illustrated a practical RFID design example based on the analytical power transfer expressions introduced in Chapter 3. A misalignment sensitivity analysis for the SL1ICS3101 HF passive RFID label IC was presented for two sets of planar inductive coupled coils popular in HF RFID label applications. Contour plots of constant received power under lateral and angular misalignment conditions were produced based on the analytical model suggested in this thesis. In this chapter it was demonstrated that the analytical model can be used to predict upper bounds of misalignment tolerance for a specific design. Finally, acceptable areas of operation for the ICODE SL1ICS3101 label IC were suggested for designs employing both square and circular spiral coils under misalignment conditions.

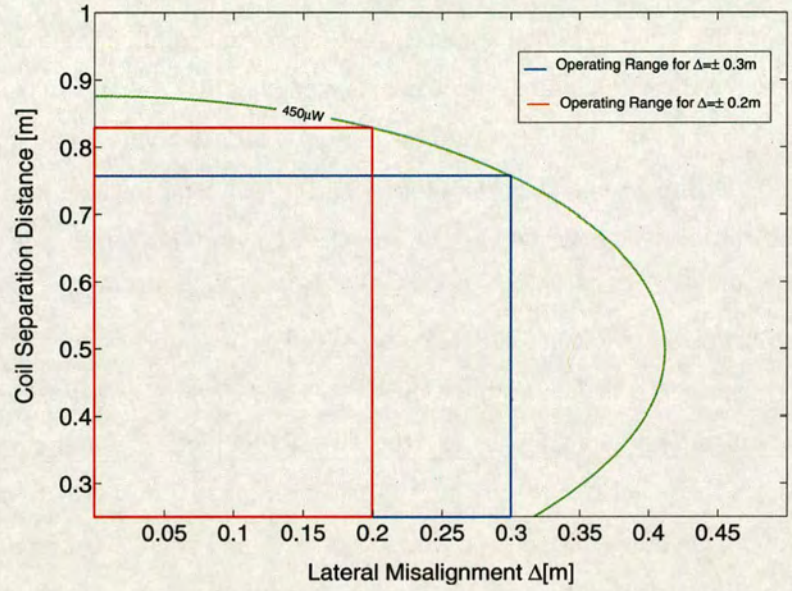

(a)

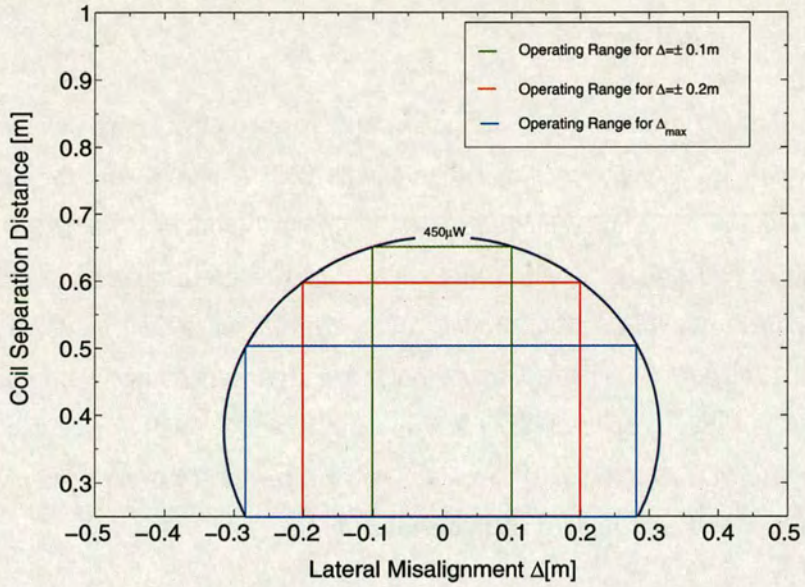

(b)

Figure 6.7: *Optimal operating region for the SL1ICS3101 RFID tag with minimal operating power of* $450\mu W$ *and transmitted power of 1W: (a) Circular spiral coils under lateral misalignment (b) Square spiral coils under lateral misalignment.*

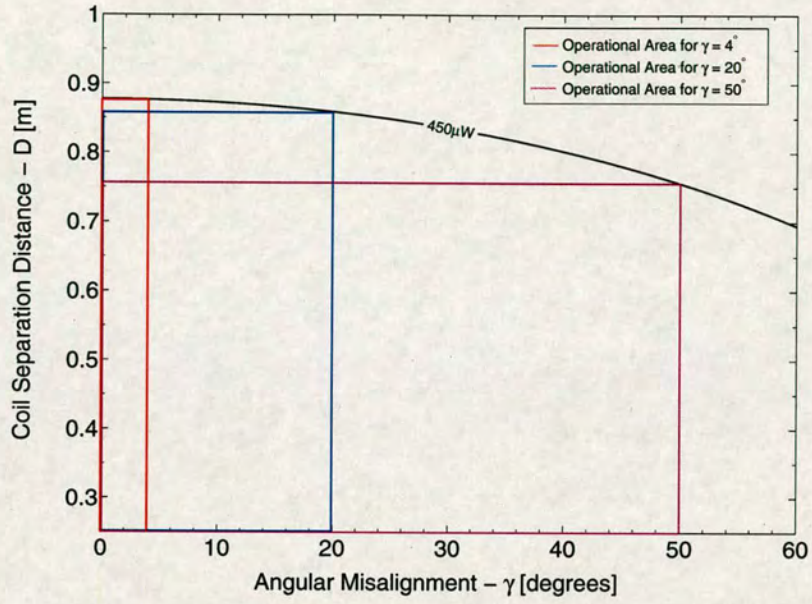

(a)

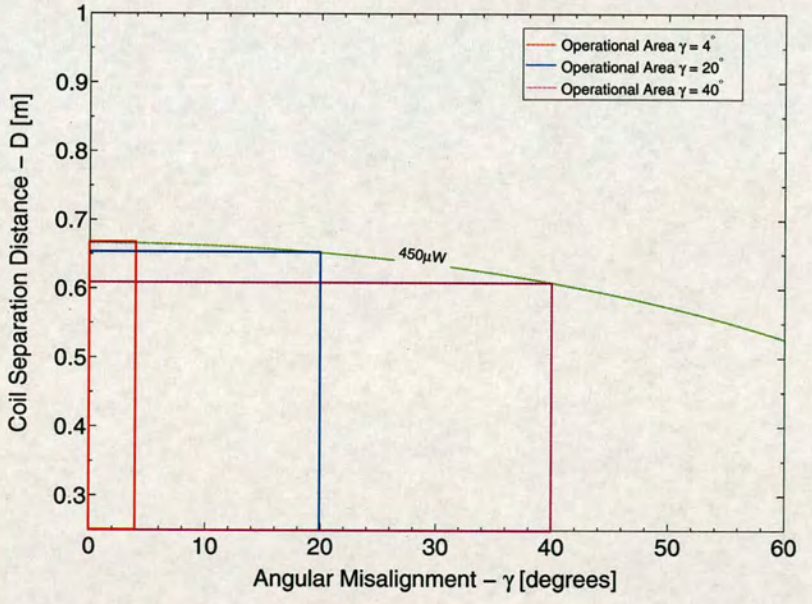

(b)

Figure 6.8: *Optimal operating region for the SL1ICS3101 RFID tag with minimal operating power of* $450\mu W$ *and transmitted power of 1W: (a) Circular spiral coils under angular misalignment, (b) Square spiral coils under angular misalignment.*

Chapter 7
Conclusion

7.1 Summary

Low power RF inductive links are used extensively for wireless powering of passive near-field RFID systems, and in applications involving embedded devices and biomedical sensors. This thesis studies the effect of coil misalignment and geometry on the power transfer efficiency of a loosely coupled link. For the first time a novel analytical model for the inductive link power transfer efficiency is presented, which incorporates both coil misalignment effects and geometrical characteristics.

Chapter 1 introduced inductive coupling to the reader and addressed its advantages over conventional powering schemes. Emphasis was given to applications employing loosely coupled links such as passive HF RFID and embedded biomedical devices. In the absence of an accurate and cohesive analytical model in the literature, the design of loosely coupled inductive links is a challenge for design engineers. This thesis attempts to fill this gap by introducing an analytical model that predicts the influence of coil misalignment and geometry on the power transfer efficiency. The model developed can serve as a tool for power transfer optimisation studies in real implementations.

The work presented in this thesis is organised in four parts. The first part is included in Chapter 2 which serves as an introduction to the background theory of inductive links. Misalignment is identified in this chapter as being one of the most critical parameters that affect the link efficiency. The operation of a typical inductive link was described using transformer action, where energy is coupled from the primary to the secondary by induction. Once a circuital representation for the loosely coupled transformer was established the key electromagnetic theory of the near-field was discussed. An aspect central to the novelty of the approach presented in this thesis, lies in the combination of circuital and electromagnetic perspectives employed in the description of inductive power transfer. Chapter 2 concluded with a discussion of the effect of the surrounding tissue in the case of implanted medical devices. A method for accounting for the power losses was suggested based on the attenuation constant principle. However, it was

shown that these losses can be neglected if the operating frequency is limited to the range of HF RFID devices, below 30MHz.

Chapter 3 constitutes the core of this thesis and is where the novel analytical model for the power transfer efficiency of loosely coupled inductive links is presented. The efficiency of a magnetic link was studied under coil misalignment conditions for a number of coil geometries used in practical RFID applications. The model suggested, incorporates misalignment effects between two inductively coupled coils of solenoidal, circular and square spiral type.

Chapter 4 is dedicated to the experimental verification of the analytical power transfer expressions developed in Chapter 3. The experimental work was carried out in two parts. In the first part the magnetic field of the TX coils was investigated as a means of checking the assumptions adopted in the modelling phase. In the second part measurements of the level of power transfered across the inductive link were carried out to test the accuracy of the power transfer functions. Experimental results indicate a close correlation between measured data and theoretical predictions.

A power transfer performance analysis was carried out in Chapter 5, comparing the efficiency and misalignment tolerance of the coil structures studied in this thesis. It is now possible to compare the performance of different coupled coil geometries such as short solenoids, circular and rectangular planar and printed spirals with respect to the power delivered to the load, with the aid of the equations derived in chapter 3. To the author's knowledge a comparison of this type has not been performed in previous studies. Finally, it is possible to identify the optimum coil structure, in terms of power transfer and immunity to misalignment in order to comply with the requirements of a specific design.

Chapter 6 merged the analytical methods devised in Chapter 3 and the coil performance comparison presented in Chapter 5 into a design algorithm that identifies the misalignment tolerance of the system for efficient inductive power coupling. This design algorithm is implemented into a case study for a passive RFID label. Upper bounds of efficient operating range and misalignment tolerance are set for both circular and square spiral structures.

Finally, this chapter provides an opportunity to summarize the work discussed in the thesis and places the research presented into perspective. A discussion of the contribution and implications of this research project follows. Finally, areas of future research that can enhance the ideas suggested in this thesis are proposed.

7.2 Conclusions and Thesis Contribution

This section presents the main conclusions drawn from this thesis. The contribution to knowledge of this thesis is classified into five main categories, based on the objectives set in Chapter 1:

- A novel analytical model for the power transfer efficiency across a loosely coupled link was presented, for circular and square TX and RX solenoid and spiral coils positioned in non-optimal orientations. The model introduced in this work combines the electromagnetic theory of a loop antenna in the near-field with the circuital principle of a loosely coupled transformer. The synergy of the magnetic field modelling of the coils and the nodal equations of a loosely coupled inductive link result in a set of novel power transfer equations for each coil (circular, square spiral coils and short solenoids). This methodology gives the engineer a direct perspective into the problem. With the aid of this analytical model it is now possible to combine in the same expression geometrical parameters of the problem such as the coil shape and configuration as well as the electrical properties of the coils (quality factor) and operating frequency. Each set of equations define the trend of the link efficiency for different coil geometries and misalignment configurations. In this manner the model can provide valuable insight into the design of loosely coupled inductive links which until now has been mostly empirical. In addition, this method can also be applied in optimisation studies for a number of design implementations.

- Based on the novel analytical model described in this thesis it is now possible to identify the most critical parameters that affect the link efficiency in low power loosely coupled inductive links. It is evident from the novel power transfer equations derived in section 3.6 that a number of factors can influence the efficiency of the link. Both the numerator and denominator, in the power transfer expressions of section 3.6, increase with the number of turns, the effective area of the coils as well as the frequency. However, the numerator increases more quickly and hence determines the overall trend in power transfer. Based on this observation it is possible to conclude that the most influential parameters are misalignment and coil geometry. In addition, the efficiency of the link decreases with increasing ohmic losses in the coil. It is worth noticing that the value of the resistive losses in the coupled coils is also concealed in the geometrical parameters in the numerator of the power transfer equations. Thus, in order to meet the design specifications for an inductive coupled system an iterative approach is more suitable as was demonstrated

in Fig. 6.4.

- The proposed theoretical model was evaluated experimentally with very good agreement with the analytical predictions. The maximum relative percentage error observed between the experimental and the analytical data was of the order of 20%. It follows from the discussion presented in section 4.6.2 that a discrepancy of this order is well justified given the limited accuracy of the experimental set-up employed in the measurements. Hence, for loosely coupled links where the RX coil satisfies the loosely coupled approximation as discussed in section 2.11, confidence should be placed in the accuracy of the model.

- A systematic approach to the design of loosely coupled inductive links for RFID and embedded devices is proposed using the analytical model discussed in this thesis. An RFID design example is given in chapter 6 where an iterative methodology is introduced. In chapter 6 operating bounds for the coil permissible misalignment were set for a 13.5MHz RFID tag using the analytical power transfer model developed.

- An optimum coil geometry for efficient power transfer and misalignment tolerance that meets the design criteria was identified. It was demonstrated that the most optimal design employs a circular spiral receiver coil which exhibits both maximum coupling and misalignment tolerance. A single exception to this rule is observed for the short solenoid which indicates a more linear performance with increased angular misalignment compared to its spiral counterparts.

The aim of the work presented in this thesis is twofold. First, emphasis is given to the development and experimental validation of a novel compact model for near-field inductive coupling. The model presented in this thesis includes misalignment effects and geometric characteristics of the RF coil system. The analytical model proposed is experimentaly verified, in the second phase of the project and it is used to compare the performance of different coil structures.

The advantage of this new approach lies is the fact that it provides a clear and direct perspective into the parameters that affect the power transfer efficiency of the inductive link. For instance, the trend of the link efficiency as a result of a variation in a specific parameter in the model can be quickly identified. This provides the designer with vital data on the response of the system under several misalignment configurations and different coil geometries without the need of repeated and costly simulation runs.

Due to the fact that inductive coupling is advantageous for a number of different applications, it has attracted a lot of interest from the research community. This topic has been well studied during the last few decades and numerous publications exist that offer several different approaches to link optimisation. Although, the bulk of the available work proposes new techniques for specific scenarios, it targets the same optimisation problems. The majority of the studies available target closely coupled systems with a focus on steady state circuital analysis. At this point is important to stress that a steady state analysis can be useful for certain implementations. Nevertheless, for the applications targeted in this thesis, a steady state approach cannot describe the impact of geometric aspects on the inductive link efficiency. Subsequently, a very challenging aspect of link efficiency, that of misalignment in the system of coils has been systematically overlooked in literature. In loosely coupled systems in particular, the coupling coefficient is directly related to the geometry of the coils and their position. In particular, for loosely coupled systems targeted in this dissertation, the effect of coil displacement, orientation and position has a significant adverse effect on the transmission characteristics. It is fair to say that for loosely coupled inductive links, the overall power transfer efficiency is dominated by the efficiency of the magnetic link. It should be pointed out that the link efficiency is also related to the operating frequency. Usually, inductive links for RFID and embedded electronic systems all operate at allocated ISM frequency bands, thus, optimisation with respect to frequency was not considered crucial in this work. Instead among the most important parameters affecting link efficiency are the coupling coefficient and the quality factors of the coils. As is well known from electromagnetic theory both of these critical parameters are dependent on the geometric characteristics of the coils.

It is evident that for the design of coupled coils the coupling coefficient is of paramount importance. Ultimately, the coupling coefficient determines the power efficiency of the link and the tolerance of the system to lateral and angular misalignment. The degree of coupling is directly related to the mutual inductance between the RF coils. However, the calculation of the mutual inductance under misalignment can become very convoluted for complex coil structures such as spirals. It is difficult to extract useful information from complicated solutions since they tend to obfuscate the effects of coil parameters on the link efficiency. Consequently, by approaching the problem from a different perspective, straight from basic principles, can provide a more direct solution. This alternative approach is based on the calculation of the magnetic field generated from the TX coil using the Biot-Savart law in the magnetostatic scenario. Since, the magnetic field strength is linked to the geometry of the source it is possible to see how the

shape of the TX coil can be optimised to generate the maximum possible uniform field strength. Information about the RX coil geometry and position can be supplied through the use of Faraday's law, that determines the induced voltage at the RX coil. Based on this technique, and referring back to the equivalent circuit for a loosely coupled transformer, power transfer ratios are presented in the second part of this work. The functions developed can directly express the efficiency of the link for different coil structures and misalignment conditions.

The experimental verification of the theoretical model is presented in chapter 4. It was shown that the model developed gives accurate results as long as the dimensions of the coils comply with the loosely coupled approximation. The results of the comparison between theoretical and measured data presented, show that the uncertainty in the model increases as the coil separation distance decreases. It is clear from the experimental results presented that the analytical model derived, is both cohesive and computationally efficient in estimating the power transfer efficiency in real conditions.

The fourth part of this thesis presents an optimisation study based on the analytical model developed earlier. The critical question examined is whether it is possible to improve the coupling and misalignment tolerance of the system by adopting a specific coil geometry. It is demonstrated in this thesis that the coupling coefficient of two magnetically coupled coils can be significantly enhanced by circular spiral coil structures. However, although circular spiral structures performed significantly better than the solenoid coils, the efficiency of the square spirals was lower. Overall, the most effective geometry seems to be the circular shape which surprisingly significantly outperforms the square spirals. This behaviour is evident for both the coaxial, lateral and angular orientations. Nevertheless, in angular misalignment, the coupling coefficient of solenoid coils remains relatively stable even for large misalignment angles. Hence, for applications where large angular misalignments are common solenoid coils should be favored. An application specific study is illustrated in chapter 5 for a 13.56 MHz passive RFID tag. The two coil structures chosen are the circular and square printed spiral coils usually employed as antenna coils in this type of applications.

7.3 Directions for Further Research

A number of possible directions for further study have emerged from the research presented in this thesis. Among the potential fields of future research are the following topics:

- **Experimental evaluation of the losses due to tissue absorption**

  Concerning the experimental procedure followed in this work, it is important to note that measurements were performed in air and did not account for the presence of conductive media. The scale of the experimental apparatus made any such measurements extremely non-practical and very challenging considering that the RX coil needs to be completely submerged in a uniform volume of liquid that simulates the conductive tissue of the human body. Furthermore, the electrical characteristics of the biomedical specimen simulated, such as its complex permittivity and conductivity, are exceptionally diverse between different tissue types. Consequently, the only plausible solution is to conduct repeated experiment for several values of permittivity representing different tissue categories, and keep a record of the accuracy shown by the model. Additional complications can be introduced from stray capacitances caused by the presence of the liquid which will tend to detune the coil and reduce its Q factor. Effects like this add to the experimental complexity and should be properly addressed and minimised to guarantee a successful experimental procedure.

- **Conduct experiments to scale**

  Regarding the experimental procedure followed in this thesis, a scaled up experimental set-up was employed for the reasons discussed in Chapter 4. The decision to use a scaled up model is well justified and it was adopted to combat measurement errors primarily linked to instrumentation sensitivity. However, it might be useful to test the analytical model developed in Chapter 3 using smaller and more realistic receiver coil sizes that approach in size of coils employed in practical RFID applications. Of course such a configuration poses unique challenges itself since a more sensitive instrumentation is required compared to the conventional scaled up model. Provided that more sensitive instrumentation is secured and the influence of external noise sources is minimised, it would be interesting to see if a smaller coil size can reduce some of the systematic errors encountered in the current set-up.

- **Evaluation of the model using numerical methods**

  The research presented in this thesis addresses the need for an efficient analytical model that will play an integral role in the design and analysis of wireless inductive power transfer, as an alternative to repetitive design prototyping and measurements. In the modelling approach followed in this thesis analytical methods were favored. However, a possible interesting extension of this work would be to implement the model using efficient numerical methods like the Finite-Difference Time-Domain (FDTD) approach. Then the analytical model can be effectively tested against the results from simulations carried out using numerical techniques. The advantage of a numerical modelling would be that complex coil structures could be studied as well as the effect of inhomogeneous dispersive media which is traditionally solved using FDTD methods. Consequently, a double verification of the analytical model using both experimental and numerical methods will guarantee its accuracy and convince the design community to implement the method as an industry standard.

- **In depth model of the ohmic losses in the coils**

  One of the critical parameters included in the expressions for the power transfer ratio developed in Chapter 3 are the AC ohmic losses in the transmitting and receiving coils. Currently, the accuracy of existing expressions for the ohmic losses of coil structures investigated in this work is unknown. Uncertainty introduced from the ohmic resistance can introduce a domino effect and compromise the accuracy of the calculated value of the power transfer efficiency. Therefore, in order for the power transfer functions to be implemented properly it is important to have an in-depth knowledge of the losses of the TX and RX coils. Existing analytical methods for the computation of coil AC resistance are focused on integrated inductors and the accuracy of these formulae for the RFID coil dimensions is not clear. Consequently, there is scope for further research of this topic both from a theoretical and experimental perspective that will ultimately converge into an accurate analytical expression evaluating the resistive and capacitive losses for coils through a lumped element model format.

- **Extend the model for more coil geometries**

  In the analytical model presented in this thesis the coil geometries investigated are the circular short-solenoid as well as circular and square spirals constructed of conductor with rectangular and circular cross-sections. It was demonstrated that the power transfer efficiency of an inductive link is directly related to the coil geometrical characteristics

and critically affected by coil position and orientation. It would be possible to expand the analytical model and investigate the power transfer performance of more coil geometries, such as polygonal spirals, figure 8 shaped coils, rectangular solenoids of both circular and round wire. It may also be useful to test whether implementing double layer coils will have an improvement on the coupling efficiency despite the fact that the ohmic losses may increase.

Appendix A
Coordinate Systems and Vector Relations

In this appendix we present the three coordinate systems utilized in this Thesis, these being rectangular coordinates, circular cylindrical coordinates and spherical coordinates. In addition, coordinate transformation techniques are introduced briefly.

A.1 Rectangular - Cartesian Coordinates

A rectangular coordinate system is depicted in Fig. A.1(a), where the three planes $x = x_1$, $y = y_1$ and $z = z_1$ intersect at a point designated by the coordinates x_1, y_1, $z1$. The elements of length in the three coordinate directions are dx, dy and dz, the elements of area $dxdy$, $dydz$ and $dzdx$, and the element of volume is $dxdydz$, [56].

In the rectangular coordinate system we express a $\mathbf{A}$ as

$$\mathbf{A} = \hat{\mathbf{a}}_x A_x + \hat{\mathbf{a}}_y A_y + \hat{\mathbf{a}}_z A_z \tag{A.1}$$

where $\hat{\mathbf{a}}_x$, $\hat{\mathbf{a}}_y$, $\hat{\mathbf{a}}_z$ are the unit vectors and A_x, A_y and A_z are the components of the vector $\mathbf{A}$ in the rectangular coordinate system.

The coordinate transformation from rectangular (x, y, z) to cylindrical (ρ, ϕ, z) is given, referring to Fig. A.1(b) by the following matrix, [56]:

$$\begin{pmatrix} A_\rho \\ A_\phi \\ A_z \end{pmatrix} \begin{pmatrix} \cos\phi & \sin\phi & 0 \\ -\sin\phi & \cos\phi & 0 \\ 0 & 0 & 1 \end{pmatrix} = \begin{pmatrix} A_x \\ A_y \\ A_z \end{pmatrix} \tag{A.2}$$

A.2 Cylindrical Coordinates

In the circular cylindrical coordinate, the coordinate surfaces are defined as a set of circular cylinders (r = constant), a set of planes all passing through the axis and finally a set of planes

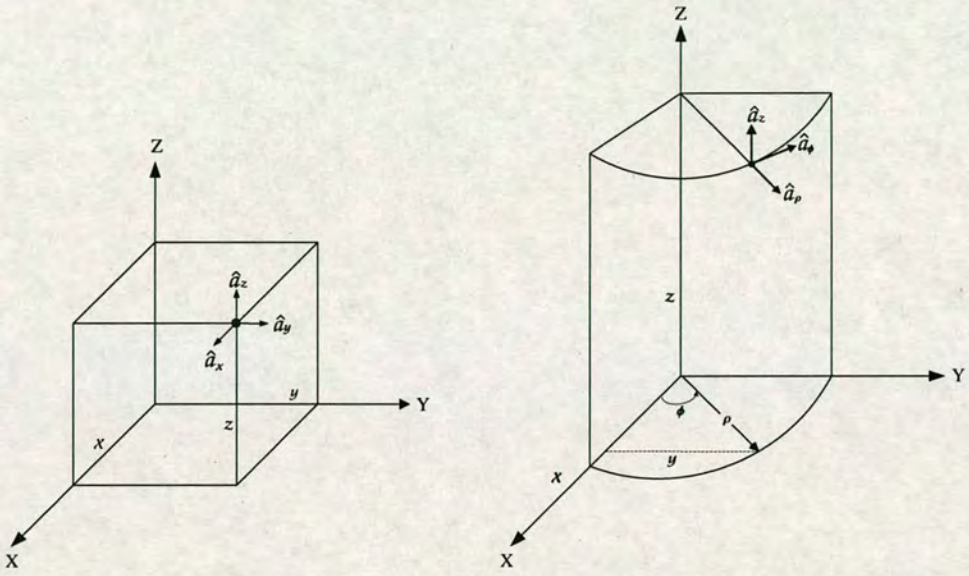

(a) System of rectangular coordinates.

(b) System of circular cylindrical coordinates.

normal to the axis (z = constant), [53]. Thus, the coordinates of a particular point are given as r_1, ϕ_1 and z_1, where the r, ϕ and z are known as the radius, the azimuthial angle and the distance along the axis respectively. The elements of lentgh are represented as dr, $r\ d\phi$, dz and the element of volume is given by $r\ dr\ d\phi\ dz$, [53]. Referring to Fig. A.1, the cylindrical-to-spherical transformation of vector components is given in matrix form as follows:

$$\begin{pmatrix} A_r \\ A_\theta \\ A_\phi \end{pmatrix} = \begin{pmatrix} \sin\theta & 0 & \cos\theta \\ \cos\theta & 0 & -\sin\theta \\ 0 & 1 & 0 \end{pmatrix} \begin{pmatrix} A_\rho \\ A_\phi \\ A_z \end{pmatrix} \tag{A.3}$$

A.3 Spherical Coordinates

In a spherical coordinate system illustrated in Fig. A.1, the surfaces can be defined as a set of spheres (radius$r$from the origin = constant), a set of cones about the axis (θ = constant) and a set of planes passing through the polar axis (ϕ = constant). The point with coordinates r_1, θ_1 and ϕ_1, lies at the intersection of sphere $r = r_1$, cone $\theta = \theta_1$, and plane $\phi = \phi_1$. r is the radius, θ the polar angle or colatitude, and ϕ is the azimuthial angle of longitude. The elements of distance are expressed by dr, $r\ d\theta$ and $r\ \sin\theta$, elements of area are given as

$r\ dr\ d\theta$, $r^2\ \sin\theta\ d\theta\ d\phi$ and $r\sin\theta\ d\phi\ dr$. Finally, the element of volume is defined as $r^2\ \sin\theta\ dr\ d\theta\ d\phi$.

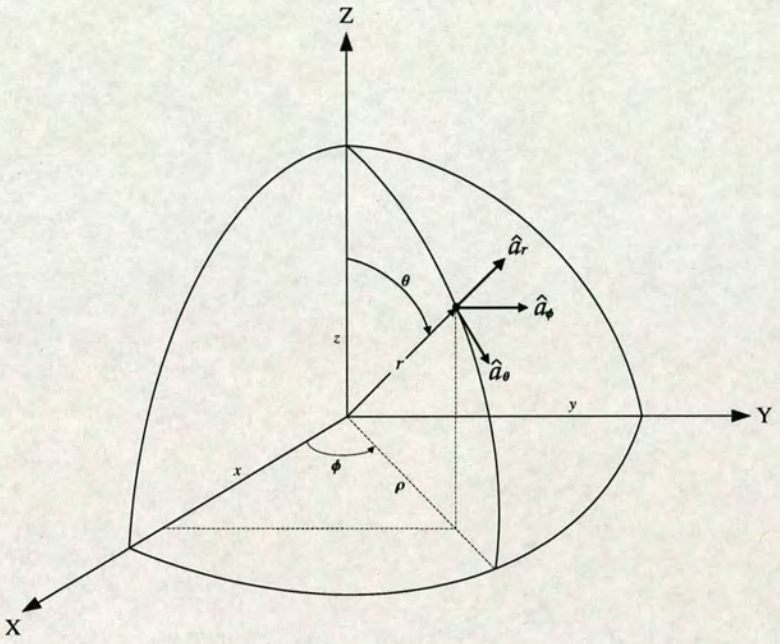

Figure A.1: *System of spherical coordinates*

Referring to Fig. A.1 the rectangular-to-spharical transformation can be expressed in the following matrix form:

$$\begin{pmatrix} A_r \\ A_\theta \\ A_\phi \end{pmatrix} = \begin{pmatrix} \sin\theta\ \cos\phi & \sin\theta\sin\phi & \cos\theta \\ \cos\theta\ \cos\phi & \cos\theta\sin\phi & -\sin\theta \\ -\sin\phi & \cos\phi & 0 \end{pmatrix} \begin{pmatrix} A_x \\ A_y \\ A_z \end{pmatrix} \tag{A.4}$$

Appendix B
Special Functions

B.1 Incomplete Elliptic Integral of the First Kind

The *incomplete elliptic integral* of the *first kind* is defined as

$$F(m,\phi) = \int_0^{\phi} \frac{d\theta}{\sqrt{1-m^2\sin\theta^2}}\,, \quad where\, 0 \prec m \prec 1 \tag{B.1}$$

where ϕ is the *amplitude* of $F(m,\phi)$ or u, written $\phi = \text{am}u$, and m is its *modulus*, written $m = \text{mod}u$. The form of the integral in (B.1) is also called *Legendre's form* of the elliptic integral of the first kind. If $\phi = \pi/2$ the integral is called the complete elliptic integral of the first kind and is denoted by $K(m)$ or simply K. For all purposes it will be assumed that m is a given constant.

B.2 Incomplete Elliptic Integral of the Second Kind

The *incomplete elliptic integral* of the *second kind* is defined by

$$E(m,\phi) = \int_0^{\phi} \sqrt{1-m^2\sin\theta^2}\, d\theta\,, \quad where\, 0 \prec m \prec 1 \tag{B.2}$$

(B.2) is also referred to as *Legendre's form* for the elliptic integral of the second kind. If $\phi = \pi/2$ the integral is called the complete elliptic integral of the second kind and is denoted by $E(m)$ or simply E. For all purposes it will be assumed that m is a given constant.

B.3 Derivatives of KelvinBei and KelvinBer Functions

On a different note, the derivatives of the Ber and Bei functions introduced in Chapter 2 are given as follows:

$$Ber'(q) = \frac{\partial Ber(q)}{\partial q} = \frac{Bei_1(q) + Ber_1(q)}{\sqrt{2}} \tag{B.3}$$

$$Bei'(q) = \frac{\partial Bei(q)}{\partial q} = \frac{Bei_1(q) - Ber_1(q)}{\sqrt{2}} \tag{B.4}$$

Appendix C
Misalignment Apparatus Drawings

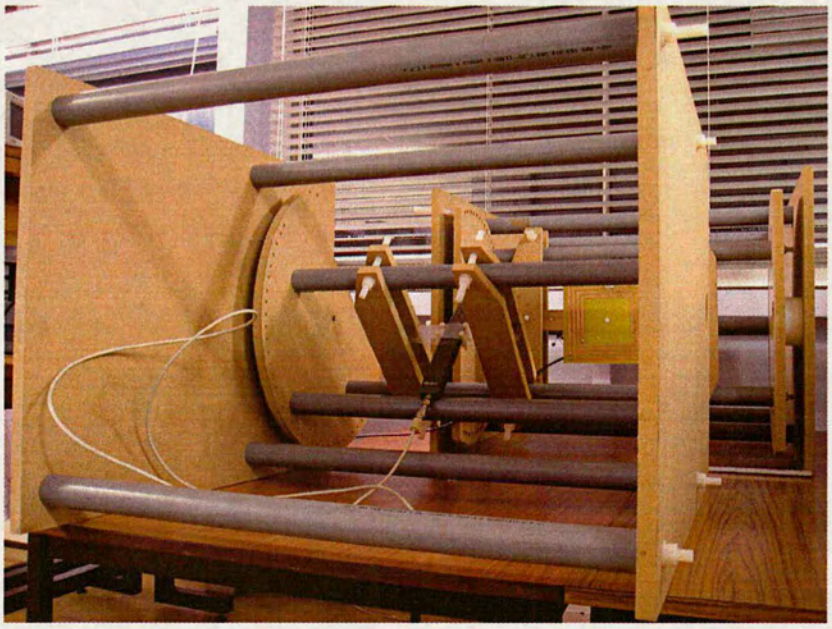

Figure C.1: *Photograph of the misalignment apparatus including the TX coil under test and the measurement probe.*

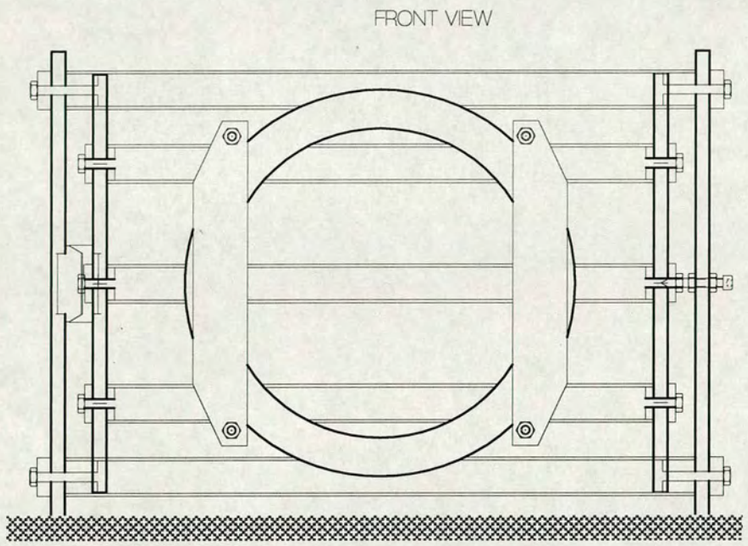

TABLE TOP SURFACE

GENERAL ASSEMBLY

TRANSMITTER-RECEIVER MISALIGNMENT SYSTEM

DESIGN BY: KYRIAKI FOTOPOULOU, PROF. STEPHEN SALTER
PHD PROJECT SUPERVISOR: DR BRIAN FLYNN

DATE OF LAST EDIT: 10/10/2006
EMAIL: K.Foto@ed.ac .uk

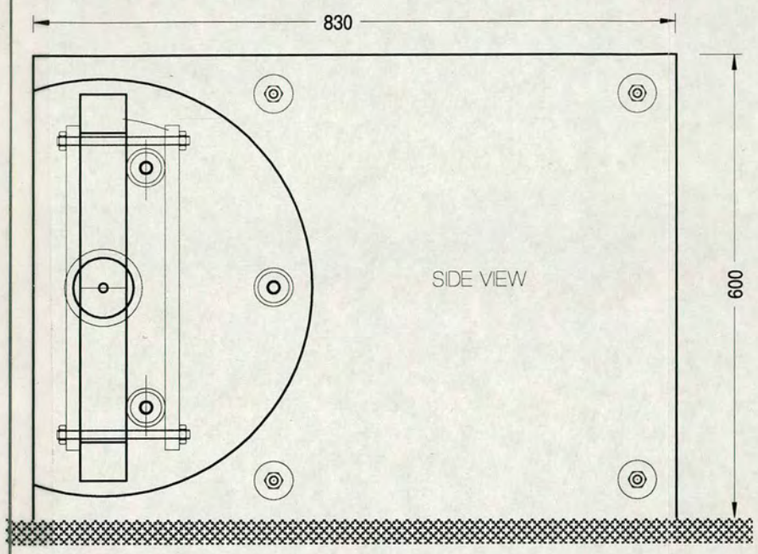

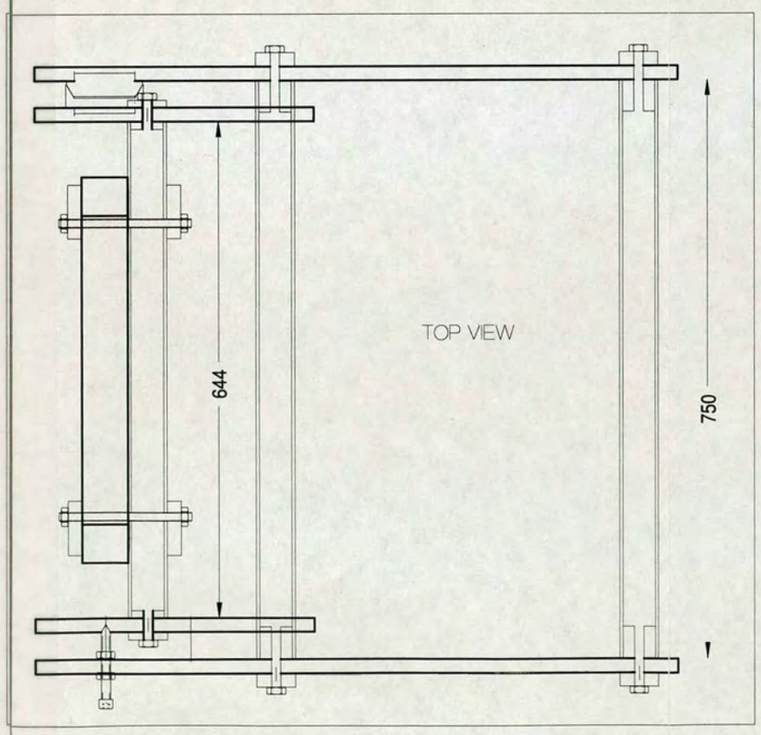

Figure C.2: *Mechanical drawing of the general assembly of the misalignment apparatus.*

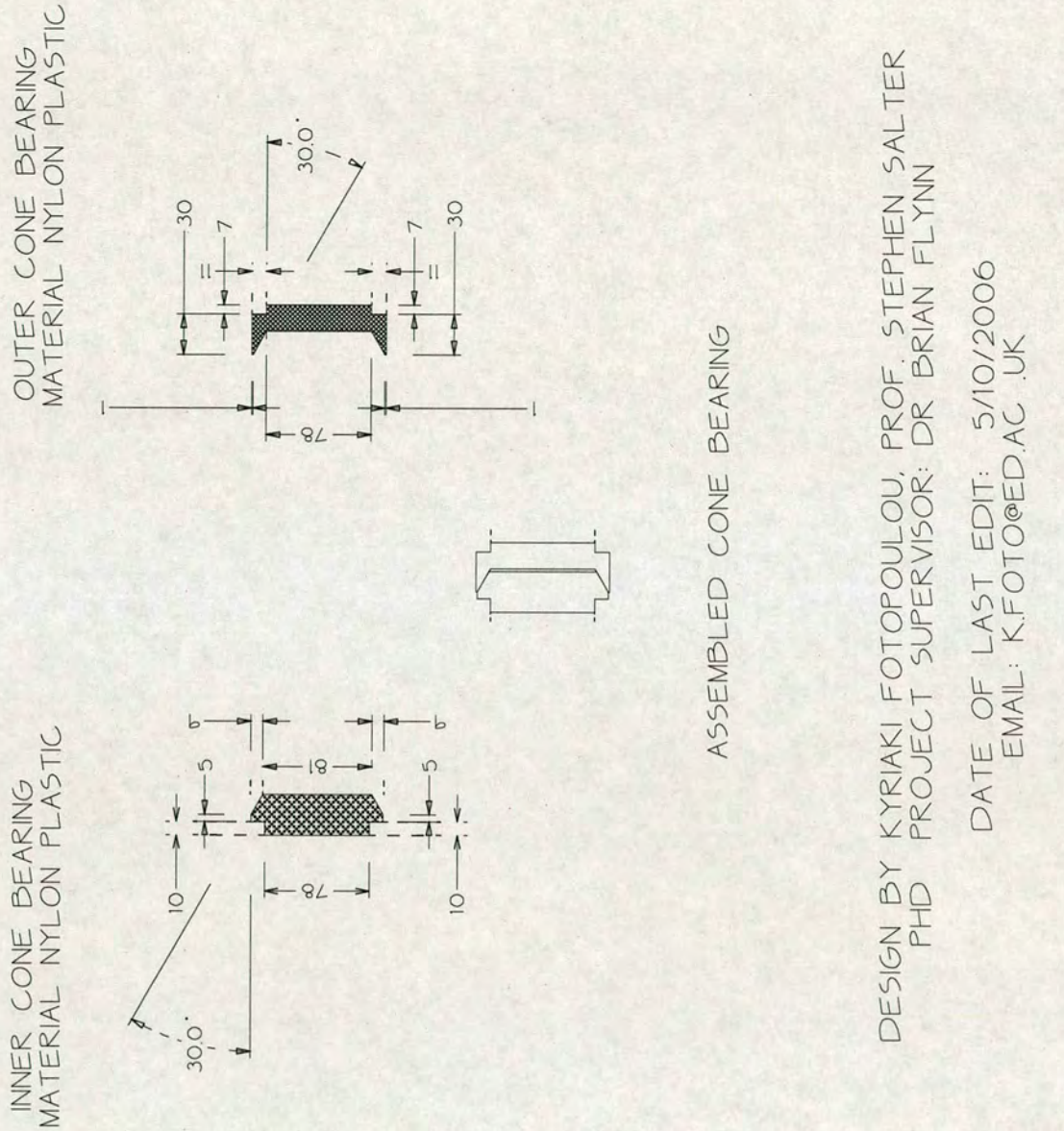

Figure C.3: *Design of the cone bearing of the misalignment apparatus.*

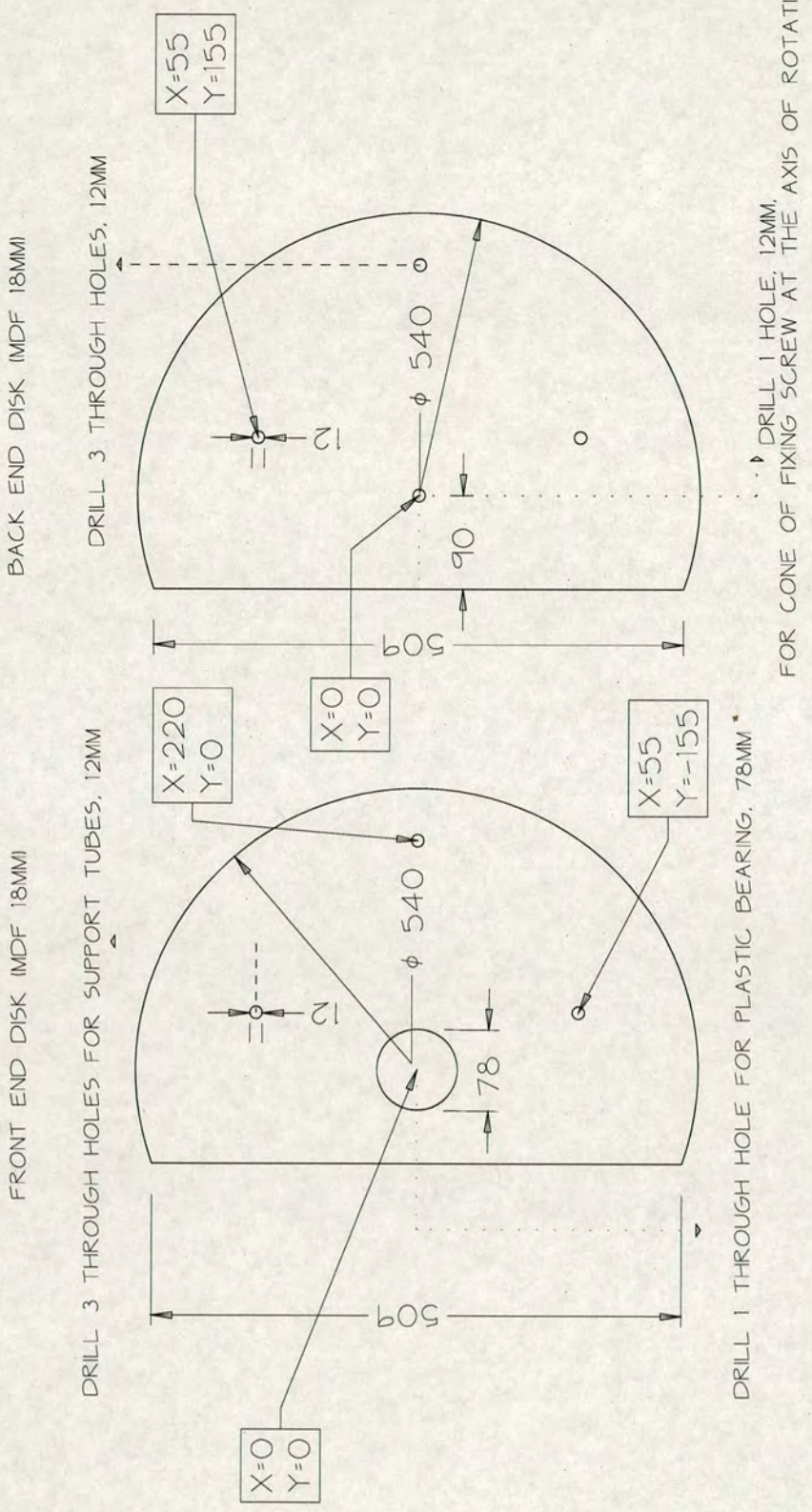

Figure C.4: *Design of the end disks of the misalignment apparatus.*

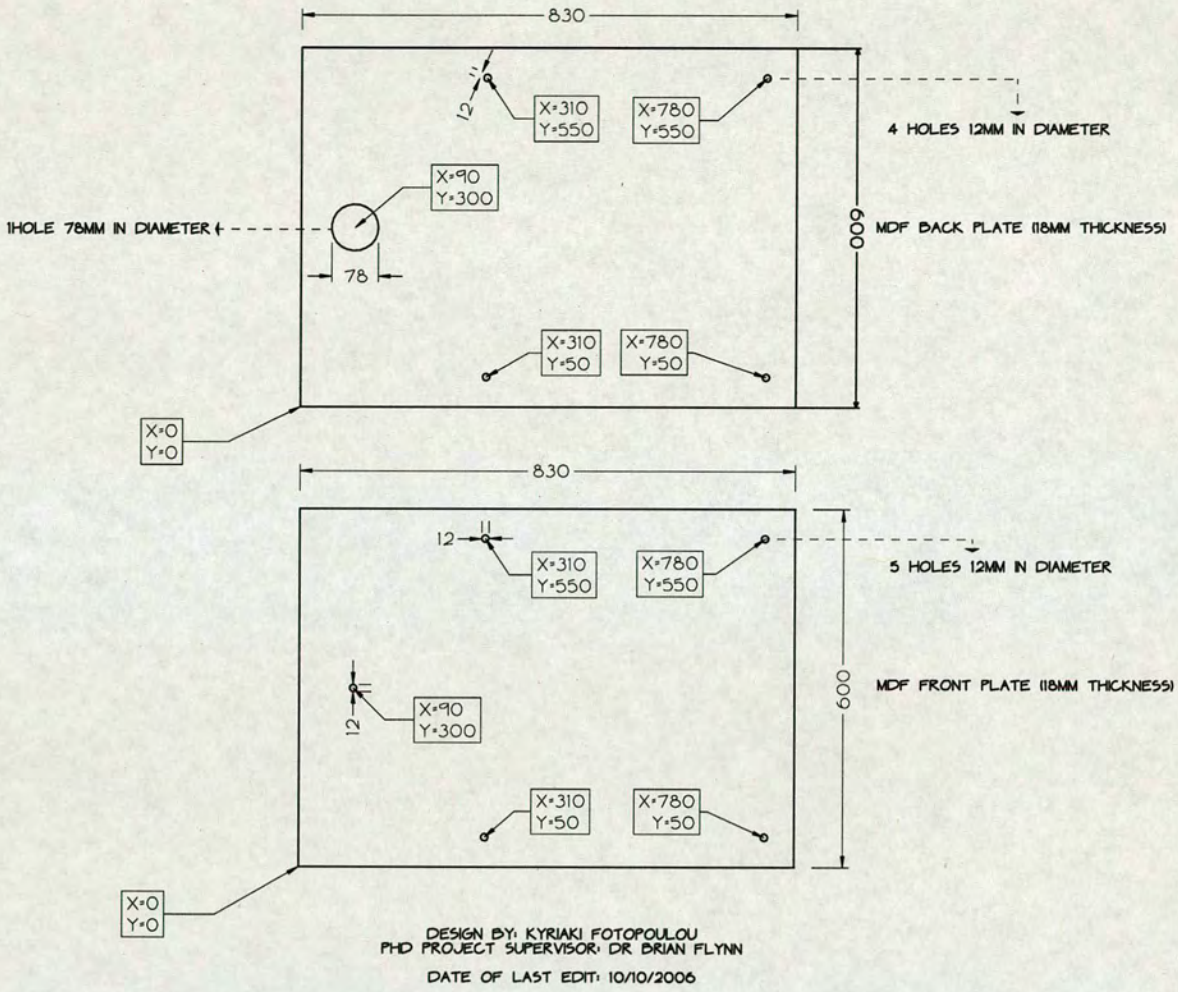

Figure C.5: *Design of the support plates of the misalignment apparatus.*

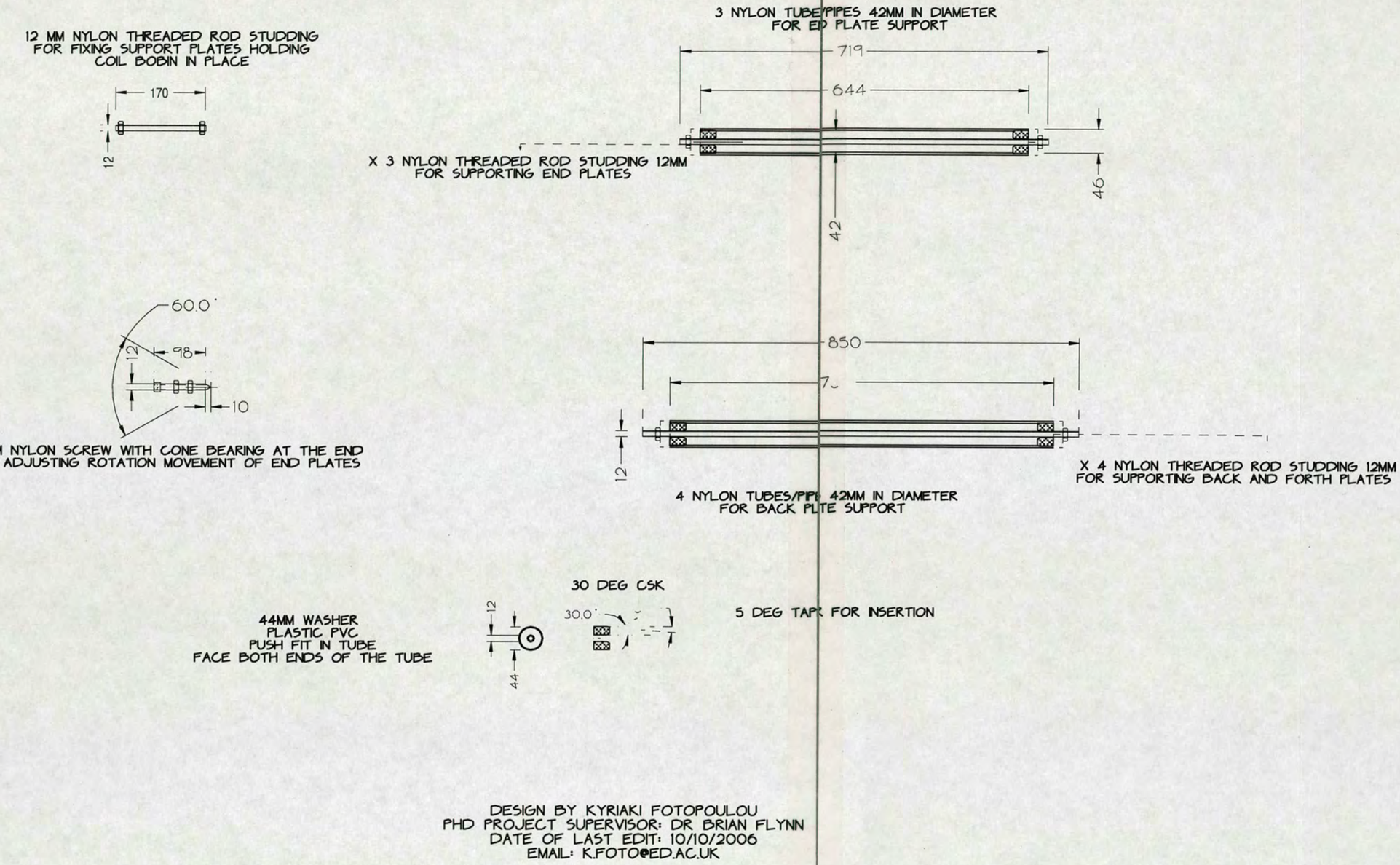

Figure C.6: *Design of the fasteners of the misalignment apparatus.*

Appendix D
MATLAB Scripts

D.1 Modified AC resistance computation based on Rodriguez method

```
% Author: Kyriaki Fotopoulou
% Date of Last Revision: 5/10/2007
%-------------------------------------------------------------------------%
% MATLAB script that computes the AC resistance of N-turn close wound
% air-core circular spiral coils of circular wire (copper enameled wire).
% Method based on the function introduced by Rodriguez et al.
% ------------------------------------------------------------------------%
% Reference:
% R. Rodriguez et al. "Modeling of two dimensional spiral inductors",
% IEEE Transactions on Components, Hybrids and Manufacturing Technology,
% vol. 3, no. 4, pp. 5345-541
%-------------------------------------------------------------------------%
%magnetic Permeability of free space
mo=4*pi*10^(-7);
%Resonant Frequency
f=1*10^6;
%Conductivity of copper
sigma=5.7*10^7;
rho=1./sigma;
%Conductor Radius
a=0.00045;
TempRPE=[];
TempR1=[];
%Arrays M,N defining the radii the concentric loops
%comprising the windings of the TX spiral coil
L=[0.03:0.0015:0.06]
M=[0.03 0.033 0.036 0.039 0.042 0.045 0.048 0.051 0.054 0.057]
N=[0.0315 0.0345 0.0375 0.0405 0.0435 0.0465 0.0495 0.0525 0.0555 0.0585]
%Compute the DC and skin effect resistance of the coil
%taking into account all the turns
sumRDCSE=0;
for  i=1:length(L)
    RDCSE(i)=L(i)*(1.25+a/2*sqrt((pi*f*mo)/rho));
    sumRDCSE=sumRDCSE+RDCSE(i);
end
RDCSEtot=(2*rho/a^2)*sumRDCSE
%Compute the proximity effect resistance consider only adjacent turns
```

```
A=M.*N
B=M+N
C=M-N
          k=2.*(sqrt(A)./(B))
%Compute the elliptic integrals K, E of the first kind
           [K,E]=ellipke(k);
           RPE=(K./B)+ (E./(-0.0015));
  TempRPE=[TempRPE;RPE];
 sum(TempRPE)^2
for j=1:length(M)
    R1=M(j)*(sum(TempRPE)^2)
 TempR1=[TempR1;R1]
end
 sum(TempR1)
  R2tot=((((pi*mo*f)^2)*a^4)/(2*rho))*sum(TempR1)
%R_tot is the total AC resistance of the spiral coil
Rtot=RDCSEtot+R2tot
```

D.2 Calculation of power transfer for solenoid, square and circular spiral coils in coaxial orientation

```
%Author: Kyriaki Fotopoulou
%Date of Last Revision: 9/02/2008
%Scipt computes and plots the power transfer between short-solenoid, square
%and circular spiral inductively coupled TX, RX coils in the coaxial
%orientation with respect to the coils separation distance D.
clear all;
%%%%%%%%%%%%%%Constant Initialization%%%%%%%%%%%%%%%%%%%%%%%%%%
%Solenoid Tx coil radius, denoted a_S
a_S=0.056;
%Solenoid Rx coil radius, denoted b_S
b_S=0.018;
%Printed Circular Spiral Tx coil radius, denoted a_S
a_CS=[0.056 0.053 0.055 0.052 0.049 0.046 0.043 0.040];
%Printed Circular Spiral Rx coil radius, denoted b_S
b_CS=[0.019 0.017 0.016 0.015 0.014 0.013 0.012 0.11];
%Printed Square Spiral Tx coil side length of each concentric loop
a_PSS=[0.10 0.094 0.088 0.082 0.076 0.07 0.064 0.058];
%Printed Square Spiral Rx coil side length of each concentric loop
b_PSS=[0.033 0.031 0.029 0.027 0.025 0.023 0.021 0.019];
%Coil separation distance in m
D=[0.25:0.001:0.5];
%Number of Turns of Sholenoid TX coil
N_TX=8;
%Number of Turns of Solenoid RX coil
```

```
N_RX=8;
%%%%
x=0;
y=0;
%Resonant frequency f=13.5MHz
f=13.5*10^(6);
%omega is the angular frequency of operation
omega=2*pi*f;
TempB_PCS=[];
TempHz_PCS=[];
TempHz_PSS=[];
TempB_PSS=[];
TempA1=[];
TempB1=[];
TempC1=[];
TempD1=[];
%------------Calculate the series resistance of the coils-----------------
%%%%%%%%%%%%%%%%%%Losses in the Short-Solenoids%%%%%%%%%%%%%%%%%%%%%%%%
%------TX Short solenoid - 19SWG Copper enamelled wire------%
d_TX=0.001
%------TX Short solenoid - 25SWG Copper enamelled wire------%
d_RX=0.0005
%Conductivity of copper at 25 degrees Celcius%
sigma=5.9*10^(7);
%Resistivity of copper at 25 degrees Celcius%
rho=(1./sigma);
%mu is the absolute permeability of the conductor
%mu_o is the permeability of free space
%mu_r is the relative permeability of the conductor
%for copper mu_r=1
mu_o=4*pi*10^(-7)
mu_r=1;
mu=mu_o.*mu_r;
%Skin depth in the copper conductor
delta=sqrt(1./(sigma.*pi.*mu.*f));
%%%%%%%%%Losses in the Short Solenoid Coils%%%%%%%%%%%%%%%%%%%
A_w_TX=pi.*((d_TX.^2)./4);
A_w_RX=pi.*((d_RX.^2)./4);
L_S_TX=N_TX.*2*pi*a_S;
L_S_RX=N_RX.*2*pi*b_S;
R_DC_TX=(rho.*L_S_TX)./A_w_TX;
R_DC_RX=(rho.*L_S_RX)./A_w_RX;
Xi_Tx=(d_TX.^2)./(4.*(d_TX.*delta-delta.^2));
Xi_Rx=(d_RX.^2)./(4.*(d_RX.*delta-delta.^2));
%Medhurst experimental constant for the proximity effect
Phi_Tx=5.31;
Phi_Rx=5.45;
R_Tx_S=R_DC_TX.*Xi_Tx.*Phi_Tx.*((N_TX-1)./N_TX);
```

```
R_Rx_S=R_DC_RX.*Xi_Rx.*Phi_Rx.*((N_RX-1)./N_RX);
%%%%%%%%%Losses in the Circular Printed Spirals%%%%%%%%%%%%%%%
t=35.*10^(-6);
w_Tx=0.002;
w_Rx=0.0005;
x_w_Tx=sqrt(2.*f.*sigma.*mu.*w_Tx.*t);
x_w_Rx=sqrt(2.*f.*sigma.*mu.*w_Rx.*t);
L_Tx_CS=2.*pi.*sum(a_CS);
L_Rx_CS=2.*pi.*sum(b_CS);
R_Tx_CS=(L_Tx_CS./(sigma*w_Tx*t)).*(((0.43093*x_w_Tx)./...
(1+0.004.*(w_Tx./t).^(1.19)))+ ((1.1147+(1.268.*x_w_Tx))./...
(1.2296+(1.287.*x_w_Tx.^(3))))+(0.0035.*((w_Tx./t)-1).^(1.8)));

R_Rx_CS=(L_Rx_CS./(sigma.*w_Rx.*t)).*(((0.43093*x_w_Rx)./...
    (1+0.004.*(w_Rx./t).^(1.19)))+ ((1.1147+(1.268.*x_w_Rx))./...
    (1.2296+(1.287.*x_w_Rx.^(3))))+(0.0035.*((w_Rx./t)-1).^(1.8)));
%%%%%%%%%Losses in the Square Printed Spirals%%%%%%%%%%%%%%%%
L_Tx_PSS=4.*sum(a_PSS);
L_Rx_PSS=4.*sum(b_PSS);
t_eff=delta.*(1-exp(-t./delta));
R_Tx_PSS=(rho.*L_Tx_PSS)./(w_Tx.*t_eff);
R_Rx_PSS=(rho.*L_Rx_PSS)./(w_Rx.*t_eff);
%%%%%%%%%%%%%%%%Theoretical Power Gain Values%%%%%%%%%%%%%%%%%%
%Define Power Transfer function P_TX/P_RX, denoted G(P)
%for Short-Solenoid TX, RX coils
G_P_S=((mu_o^(2)*N_TX^(2)*N_RX^(2)*a_S.^(4)*b_S^(4)*omega^(2)*pi^(2))./...
(16*R_Rx_S*R_Tx_S*(a_S.^(2)+ D.^(2)).^(3)));
GP_S=10.*log10(G_P_S);
%Define Power Transfer function P_TX/P_RX, denoted G(P)
%for Circular Spiral TX, RX coils
for i=1:length(a_CS)
%Define the z-component of the magnetic field, which induces
%flux across the RX coil
Hz_PCS=(a_CS(i)^(2))./((sqrt(a_CS(i)^(2)+D.^(2))).^(3));
TempHz_PCS=[TempHz_PCS;Hz_PCS]
end
HZ=sum(TempHz_PCS)
%Effective area of the circular spiral RX coil
 for j=1:length(b_CS)
B1_PCS=b_CS(j).^(2)
TempB_PCS=[TempB_PCS;B1_PCS]
end
B_PCS=sum(TempB_PCS)
%Theoretical Power Ratio Computation
G_P_CS=((mu_o^(2)*pi^(2)*omega^(2))./(16*R_Rx_CS*R_Tx_CS)).*...
    HZ.^(2).*B_PCS.^(2);
GP_PCS=10.*log10(G_P_CS);
%Define Power Transfer function P_TX/P_RX, denoted G(P) for
```

```
%Square Spiral TX, RX coils
for i=1:length(a_PSS)
%Define the z-component of the magnetic field, which induces
%flux across the RX coil
A1=(((y-(a_PSS(i)./2))./((y-(a_PSS(i)./2)).^2 + D.^2)).*...
    ((((a_PSS(i)./2)+x)./(sqrt(((a_PSS(i)./2)+x).^2 +...
    (y-(a_PSS(i)./2)).^2 + D.^2)))+(((a_PSS(i)./2)-x)./...
    sqrt((((a_PSS(i)./2)-x).^2+(y-(a_PSS(i)./2)).^2 + D.^2)))))
TempA1=[TempA1;A1]
B1=((((a_PSS(i)./2) + x)./((x+(a_PSS(i)./2)).^2 + D.^2)).*...
    ((((a_PSS(i)./2)+y)./(sqrt(((a_PSS(i)./2)+y).^2 +...
    (x+(a_PSS(i)./2)).^2 + D.^2)))+(((a_PSS(i)./2)-y)./...
    (sqrt(((a_PSS(i)./2)-y).^2 +(x+(a_PSS(i)./2)).^2 + D.^2)))))
TempB1=[TempB1;B1]
C1=(((y+(a_PSS(i)./2))./((y+(a_PSS(i)./2)).^2 + D.^2)).*...
    ((((a_PSS(i)./2)-x)./(sqrt(((a_PSS(i)./2)-x).^2+...
    (y+(a_PSS(i)./2)).^2 + D.^2)))+ (((a_PSS(i)./2)+x)./...
    (sqrt(((a_PSS(i)./2)+x).^2 +(y+(a_PSS(i)./2)).^2 + D.^2)))))
TempC1=[TempC1;C1]
D1=(((x-(a_PSS(i)./2))./((x-(a_PSS(i)./2)).^2 + D.^2)).*...
    ((((a_PSS(i)./2)-y)./(sqrt(((a_PSS(i)./2)-y).^2+...
    (x-(a_PSS(i)./2)).^2 + D.^2)))+ (((a_PSS(i)./2)+y)./...
    (sqrt(((a_PSS(i)./2)+y).^2 +(x-(a_PSS(i)./2)).^2 + D.^2)))))
TempD1=[TempD1;D1]
end
Hz_total_PSS=(-TempA1 + TempB1 + TempC1 - TempD1);
 Hz_PSS=sum(Hz_total_PSS)
%Effective area of the square spiral RX coil
 for j=1:length(b_PSS)
B1_PSS=b_PSS(j).^(2)
TempB_PSS=[TempB_PSS;B1_PSS]
end
B_PSS=sum(TempB_PSS)
%Theoretical Power Ratio Computation
G_P_PSS=((mu_o^(2)*omega^(2))./(64*pi^(2)*R_Rx_PSS*R_Tx_PSS)).*...
Hz_PSS.^(2).*B_PSS.^(2)
GP_PSS=10.*log10(G_P_PSS);
%%%%%%%%%%%%%%%%%Plot Results%%%%%%%%%%%%%%%%%%%%%%%%%%%%%%%%%%%%
plot(D,GP_S,'k-', D,GP_PCS,'r-',D,GP_PSS,'b-')
     xlabel('Coil Separation Distance D [m]');
     ylabel('Power Transfer Ratio [dB]');
```

D.3 Calculation of power transfer for solenoid, square and circular spiral coils in lateral misalignment scenario

```
%Author: Kyriaki Fotopoulou
%Date of Last Revision: 9/02/2008

%Scipt computes and plots the power transfer between short-solenoid,
%square and circular spiral TX, RX coils. The RX is lateraly misaligned
%with respect to the TX coil.
%%%%%%%%%%%%%%Constant Initialization%%%%%%%%%%%%%%%%%%%%%%%%%%
%Solenoid Tx coil radius, denoted a_S
a_S=0.056;
%Solenoid Rx coil radius, denoted b_S
b_S=0.018;
%Printed Circular Spiral Tx coil radius, denoted a_S
a_CS=[0.056 0.053 0.055 0.052 0.049 0.046 0.043 0.040];
%Printed Circular Spiral Rx coil radius, denoted b_S
b_CS=[0.019 0.017 0.016 0.015 0.014 0.013 0.012 0.11];
%Printed Square Spiral Tx coil side length of each concentric loop
a_PSS=[0.10 0.094 0.088 0.082 0.076 0.07 0.064 0.058];
%Printed Square Spiral Rx coil side length of each concentric loop
b_PSS=[0.033 0.031 0.029 0.027 0.025 0.023 0.021 0.019];
%Coil separation distance in m
D=0.3;
%Lateral misalignment Delta
Delta=[0.00001:0.001:1]
%Number of Turns of Sholenoid TX coil
N_TX=8;
%Number of Turns of Solenoid RX coil
N_RX=8;
%%%%
x=0;
%Resonant frequency f=13.5MHz
f=13.5*10^(6);
%omega is the angular frequency of operation
omega=2*pi*f;
TempB_PCS=[];
TempHz_PCS=[];
TempHz_CS=[];
TempHz_PSS=[];
TempB_PSS=[];
TempA1=[];
TempB1=[];
TempC1=[];
TempD1=[];
%------------Calculate the series resistance of the coils-----------------%
%%%%%%%%%%%%%%%%%%%%Losses in the Short-Solenoids%%%%%%%%%%%%%%%%%%%%%%%%%%
```

```
%------TX Short solenoid - 19SWG Copper enamelled wire------%
d_TX=0.001
%------TX Short solenoid - 25SWG Copper enamelled wire------%
d_RX=0.0005
%Conductivity of copper at 25 degrees Celcius%
sigma=5.9*10^(7);
%Resistivity of copper at 25 degrees Celcius%
rho=(1./sigma);
%mu is the absolute permeability of the conductor
%mu_o is the permeability of free space
%mu_r is the relative permeability of the conductor
%for copper mu_r=1
mu_o=4*pi*10^(-7)
mu_r=1;
mu=mu_o.*mu_r;
%Skin depth in the copper conductor
delta=sqrt(1./(sigma.*pi.*mu.*f));
%%%%%%%%%Losses in the Short Solenoid Coils%%%%%%%%%%%%%%%%%%
A_w_TX=pi.*((d_TX.^2)./4);
A_w_RX=pi.*((d_RX.^2)./4);
L_S_TX=N_TX.*2*pi*a_S;
L_S_RX=N_RX.*2*pi*b_S;
R_DC_TX=(rho.*L_S_TX)./A_w_TX;
R_DC_RX=(rho.*L_S_RX)./A_w_RX;
Xi_Tx=(d_TX.^2)./(4.*(d_TX.*delta-delta.^2));
Xi_Rx=(d_RX.^2)./(4.*(d_RX.*delta-delta.^2));
%Medhurst experimental constant for the proximity effect
Phi_Tx=5.31;
Phi_Rx=5.45;
R_Tx_S=R_DC_TX.*Xi_Tx.*Phi_Tx.*((N_TX-1)./N_TX)
R_Rx_S=R_DC_RX.*Xi_Rx.*Phi_Rx.*((N_RX-1)./N_RX)
%%%%%%%%%Losses in the Circular Printed Spirals%%%%%%%%%%%%%%%
t=35.*10^(-6);
w_Tx=0.002;
w_Rx=0.0005;
x_w_Tx=sqrt(2.*f.*sigma.*mu.*w_Tx.*t);
x_w_Rx=sqrt(2.*f.*sigma.*mu.*w_Rx.*t);
L_Tx_CS=2.*pi.*sum(a_CS);
L_Rx_CS=2.*pi.*sum(b_CS);
R_Tx_CS=(L_Tx_CS./(sigma*w_Tx*t)).*(((0.43093*x_w_Tx)./(1+0.004.*...
    (w_Tx./t).^(1.19)))+ ((1.1147+(1.268.*x_w_Tx))./...
    (1.2296+(1.287.*x_w_Tx.^(3))))+(0.0035.*((w_Tx./t)-1).^(1.8)))
R_Rx_CS=(L_Rx_CS./(sigma.*w_Rx.*t)).*(((0.43093*x_w_Rx)./...
    (1+0.004.*(w_Rx./t).^(1.19)))+ ((1.1147+(1.268.*x_w_Rx))./...
    (1.2296+(1.287.*x_w_Rx.^(3))))+(0.0035.*((w_Rx./t)-1).^(1.8)))
%%%%%%%%%Losses in the Square Printed Spirals%%%%%%%%%%%%%%%%%
L_Tx_PSS=4.*sum(a_PSS);
L_Rx_PSS=4.*sum(b_PSS);
```

```
t_eff=delta.*(1-exp(-t./delta));
R_Tx_PSS=(rho.*L_Tx_PSS)./(w_Tx.*t_eff)
R_Rx_PSS=(rho.*L_Rx_PSS)./(w_Rx.*t_eff)
%%%%%%%%%%%%%%%%Theoretical Power Gain Values%%%%%%%%%%%%%%%%%%
%modulus of elliptic integrals
m_S=((4.*a_S.*Delta)./((a_S+Delta).^2 + D^2))
%EllipticK - Complete elliptic integral of the first kind
%EllipticE - Complete elliptic integral of the first kind
[K1,E1]=ellipke(m_S)
Hz_S=magfieldz_S(a_S,m_S,Delta,K1,E1)
%Define Power Transfer function P_TX/P_RX, denoted G(P) for Short-Solenoid
%TX, RX coils
G_P_S=((mu_o^(2)*N_TX.^(2)*N_RX^(2)*b_S.^(4)*omega^(2))./...
    (16*R_Rx_S*R_Tx_S)).*Hz_S.^(2);
GP_S=10.*log10(G_P_S);
for i=1:length(a_CS)
%modulus of elliptic integrals
m_CS =((4*a_CS(i).*Delta)./((a_CS(i)+Delta).^2 + D^2));
%EllipticK - Complete elliptic integral of the first kind
%EllipticE - Complete elliptic integral of the first kind
[K2,E2]=ellipke(m_CS);
Hz_CS=(magfieldz_CS(a_CS(i),m_CS,Delta,K2,E2));
TempHz_CS=[TempHz_CS;Hz_CS];
end
HZ=sum(TempHz_CS)
%Effective area of the circular spiral RX coil
for j=1:length(b_CS)
B1_PCS=b_CS(j).^(2);
TempB_PCS=[TempB_PCS;B1_PCS];
end
B_PCS=sum(TempB_PCS)
%Theoretical Power Ratio Computation for Circular Spiral
G_P_CS=((mu_o^(2)*omega^(2))./(16*R_Rx_CS*R_Tx_CS)).*HZ.^(2).*B_PCS.^(2);
GP_PCS=10.*log10(G_P_CS);
%Define Power Transfer function P_TX/P_RX, denoted G(P) for Square Spiral
%TX, RX coils
for i=1:length(a_PSS)
%Define the z-component of the magnetic field, which induces flux across
%the RX coil
A1=(((Delta-(a_PSS(i)./2))./((Delta-(a_PSS(i)./2)).^2 + D.^2)).*...
    ((((a_PSS(i)./2)+x)./(sqrt(((a_PSS(i)./2)+x).^2 +...
    (Delta-(a_PSS(i)./2)).^2 + D.^2)))+(((a_PSS(i)./2)-x)./...
    sqrt((((a_PSS(i)./2)-x).^2+(Delta-(a_PSS(i)./2)).^2 + D.^2)))));
TempA1=[TempA1;A1];
B1=((((a_PSS(i)./2) + x)./((x+(a_PSS(i)./2)).^2 + D.^2)).*...
    ((((a_PSS(i)./2)+Delta)./(sqrt(((a_PSS(i)./2)+Delta).^2 +...
    (x+(a_PSS(i)./2)).^2 + D.^2)))+(((a_PSS(i)./2)-Delta)./...
    (sqrt(((a_PSS(i)./2)-Delta).^2 +(x+(a_PSS(i)./2)).^2 + D.^2)))));
```

```
TempB1=[TempB1;B1];
C1=(((Delta+(a_PSS(i)./2))./((Delta+(a_PSS(i)./2)).^2 + D.^2)).*...
    ((((a_PSS(i)./2)-x)./(sqrt(((a_PSS(i)./2)-x).^2 +...
    (Delta+(a_PSS(i)./2)).^2 + D.^2)))+ (((a_PSS(i)./2)+x)./...
    (sqrt(((a_PSS(i)./2)+x).^2 +(Delta+(a_PSS(i)./2)).^2 + D.^2)))));
TempC1=[TempC1;C1];
D1=(((x-(a_PSS(i)./2))./((x-(a_PSS(i)./2)).^2 + D.^2)).*...
    ((((a_PSS(i)./2)-Delta)./(sqrt(((a_PSS(i)./2)-Delta).^2 +...
    (x-(a_PSS(i)./2)).^2 + D.^2)))+ (((a_PSS(i)./2)+Delta)./...
    (sqrt(((a_PSS(i)./2)+Delta).^2 +(x-(a_PSS(i)./2)).^2 + D.^2)))));
TempD1=[TempD1;D1];
end
Hz_total_PSS=(-TempA1 + TempB1 + TempC1 - TempD1);
Hz_PSS=sum(Hz_total_PSS);
%Effective area of the square spiral RX coil
for j=1:length(b_PSS)
B1_PSS=b_PSS(j).^(2);
TempB_PSS=[TempB_PSS;B1_PSS];
end
B_PSS=sum(TempB_PSS)
%Theoretical Power Ratio Computation
G_P_PSS=((mu_o^(2)*omega^(2))./(64*pi^(2)*R_Rx_PSS*R_Tx_PSS)).*...
    Hz_PSS.^(2).*B_PSS.^(2);
GP_PSS=10.*log10(G_P_PSS);
%%%%%%%%%%%%%%%%%%Plot Results%%%%%%%%%%%%%%%%%%%%%%%%%%%%%%%%%%%%
%plot(Delta,GP_PCS,'b-')
plot(Delta,GP_S,'k-', Delta,GP_PCS,'r-',Delta,GP_PSS,'b-')
     xlabel('Lateral Misalignment Delta [m]');
     ylabel('Power Transfer Ratio [dB]');
```

D.4 Calculation of power transfer for solenoid, square and circular spiral coils in the angular misalignment scenario

```
clear all;
%Author: Kyriaki Fotopoulou
%Date of Last Revision: 9/02/2008
%Scipt computes and plots the power transfer between short-solenoid, square
%and circular spiral TX, RX coils in the coaxial orientation with respect
%to the coils separation distance D.

%%%%%%%%%%%%%%%Constant Initialization%%%%%%%%%%%%%%%%%%%%%%%%%%%%
%Solenoid Tx coil radius, denoted a_S
a_S=0.056;
%Solenoid Rx coil radius, denoted b_S
b_S=0.018;
```

```
%Printed Circular Spiral Tx coil radius, denoted a_S
a_CS=[0.056 0.053 0.055 0.052 0.049 0.046 0.043 0.040];
%Printed Circular Spiral Rx coil radius, denoted b_S
b_CS=[0.019 0.017 0.016 0.015 0.014 0.013 0.012 0.11];
%Printed Square Spiral Tx coil side length of each concentric loop
a_PSS=[0.10 0.094 0.088 0.082 0.076 0.07 0.064 0.058];
%Printed Square Spiral Rx coil side length of each concentric loop
b_PSS=[0.033 0.031 0.029 0.027 0.025 0.023 0.021 0.019];
%Coil separation distance in m
D=0.3;
%Number of Turns of Sholenoid TX coil
N_TX=8;
%Number of Turns of Solenoid RX coil
N_RX=8;
%%%%
gamma=[0:1:60]
gamma_rad=((pi.*gamma)./180);
x=0;
y=0;
%Resonant frequency f=13.5MHz
f=13.5*10^(6);
%omega is the angular frequency of operation
omega=2*pi*f;
TempB_PCS=[];
TempHz_PCS=[];
TempHz_PSS=[];
TempB_PSS=[];
TempA1=[];
TempB1=[];
TempC1=[];
TempD1=[];
%------------Calculate the series resistance of the coils-----------------%
%%%%%%%%%%%%%%%%%%%%Losses in the Short-Solenoids%%%%%%%%%%%%%%%%%%%%%%%%%%%%
%------TX Short solenoid - 19SWG Copper enamelled wire------%
d_TX=0.001
%------TX Short solenoid - 25SWG Copper enamelled wire------%
d_RX=0.0005
%Conductivity of copper at 25 degrees Celcius%
sigma=5.9*10^(7);
%Resistivity of copper at 25 degrees Celcius%
rho=(1./sigma);
%mu is the absolute permeability of the conductor
%mu_o is the permeability of free space
%mu_r is the relative permeability of the conductor
%for copper mu_r=1
mu_o=4*pi*10^(-7)
mu_r=1;
mu=mu_o.*mu_r;
```

```
%Skin depth in the copper conductor
delta=sqrt(1./(sigma.*pi.*mu.*f));
%%%%%%%%%Losses in the Short Solenoid Coils%%%%%%%%%%%%%%%%%%
A_w_TX=pi.*((d_TX.^2)./4);
A_w_RX=pi.*((d_RX.^2)./4);
L_S_TX=N_TX.*2*pi*a_S;
L_S_RX=N_RX.*2*pi*b_S;
R_DC_TX=(rho.*L_S_TX)./A_w_TX;
R_DC_RX=(rho.*L_S_RX)./A_w_RX;
Xi_Tx=(d_TX.^2)./(4.*(d_TX.*delta-delta.^2));
Xi_Rx=(d_RX.^2)./(4.*(d_RX.*delta-delta.^2));
%Medhurst experimental constant for the proximity effect
Phi_Tx=5.31;
Phi_Rx=5.45;
R_Tx_S=R_DC_TX.*Xi_Tx.*Phi_Tx.*((N_TX-1)./N_TX);
R_Rx_S=R_DC_RX.*Xi_Rx.*Phi_Rx.*((N_RX-1)./N_RX);
%%%%%%%%%Losses in the Circular Printed Spirals%%%%%%%%%%%%%%%
t=35.*10^(-6);
w_Tx=0.002;
w_Rx=0.0005;
x_w_Tx=sqrt(2.*f.*sigma.*mu.*w_Tx.*t);
x_w_Rx=sqrt(2.*f.*sigma.*mu.*w_Rx.*t);
L_Tx_CS=2.*pi.*sum(a_CS);
L_Rx_CS=2.*pi.*sum(b_CS);
R_Tx_CS=(L_Tx_CS./(sigma*w_Tx*t)).*(((0.43093*x_w_Tx)./...
    (1+0.004.*(w_Tx./t).^(1.19)))+ ((1.1147+(1.268.*x_w_Tx))./...
    (1.2296+(1.287.*x_w_Tx.^(3))))+(0.0035.*((w_Tx./t)-1).^(1.8)));
R_Rx_CS=(L_Rx_CS./(sigma.*w_Rx.*t)).*(((0.43093*x_w_Rx)./...
    (1+0.004.*(w_Rx./t).^(1.19)))+ ((1.1147+(1.268.*x_w_Rx))./...
    (1.2296+(1.287.*x_w_Rx.^(3))))+(0.0035.*((w_Rx./t)-1).^(1.8)));
%%%%%%%%%Losses in the Square Printed Spirals%%%%%%%%%%%%%%%%
L_Tx_PSS=4.*sum(a_PSS);
L_Rx_PSS=4.*sum(b_PSS);
t_eff=delta.*(1-exp(-t./delta));
R_Tx_PSS=(rho.*L_Tx_PSS)./(w_Tx.*t_eff);
R_Rx_PSS=(rho.*L_Rx_PSS)./(w_Rx.*t_eff);
%%%%%%%%%%%%%%%%Theoretical Power Gain Values%%%%%%%%%%%%%%%%%%
%Define Power Transfer function P_TX/P_RX, denoted G(P)
%for Short-Solenoid TX, RX coils
G_P_S=((mu_o^(2).*N_TX^(2).*N_RX^(2).*a_S.^(4).*b_S^(4).*omega^(2).*...
    pi^(2).*cos(gamma_rad))./(16*R_Rx_S*R_Tx_S*(a_S.^(2)+ D.^(2)).^(3)));
GP_S=10.*log10(G_P_S);
%Define Power Transfer function P_TX/P_RX, denoted G(P)
%for Circular Spiral TX, RX coils
for i=1:length(a_CS)
%Define the z-component of the magnetic field, which induces flux
%across the RX coil
Hz_PCS=((a_CS(i)^(2))./((sqrt(a_CS(i)^(2)+D.^(2))).^(3))).*cos(gamma_rad);
```

```
TempHz_PCS=[TempHz_PCS;Hz_PCS]
end
HZ=sum(TempHz_PCS)
%Effective area of the circular spiral RX coil
 for j=1:length(b_CS)
B1_PCS=b_CS(j).^(2)
TempB_PCS=[TempB_PCS;B1_PCS]
end
B_PCS=sum(TempB_PCS)
%Theoretical Power Ratio Computation
G_P_CS=((mu_o^(2)*pi^(2)*omega^(2))./(16*R_Rx_CS*R_Tx_CS)).*HZ.^(2).*...
    B_PCS.^(2);
GP_PCS=10.*log10(G_P_CS);
%Define Power Transfer function P_TX/P_RX, denoted G(P) for Square Spiral
%TX, RX coils
for i=1:length(a_PSS)
%Define the z-component of the magnetic field, which induces flux across
%the RX coil
A1=(((y-(a_PSS(i)./2))./((y-(a_PSS(i)./2)).^2 + D.^2)).*...
    ((((a_PSS(i)./2)+x)./(sqrt(((a_PSS(i)./2)+x).^2 +...
    (y-(a_PSS(i)./2)).^2 + D.^2)))+(((a_PSS(i)./2)-x)./...
    sqrt((((a_PSS(i)./2)-x).^2+(y-(a_PSS(i)./2)).^2 + D.^2))))).*...
    cos(gamma_rad)
TempA1=[TempA1;A1]
B1=((((a_PSS(i)./2) + x)./((x+(a_PSS(i)./2)).^2 + D.^2)).*...
    ((((a_PSS(i)./2)+y)./(sqrt(((a_PSS(i)./2)+y).^2 +...
    (x+(a_PSS(i)./2)).^2 + D.^2)))+(((a_PSS(i)./2)-y)./...
    (sqrt(((a_PSS(i)./2)-y).^2 +(x+(a_PSS(i)./2)).^2 + D.^2))))).*...
    cos(gamma_rad)
TempB1=[TempB1;B1]
C1=(((y+(a_PSS(i)./2))./((y+(a_PSS(i)./2)).^2 + D.^2)).*...
    ((((a_PSS(i)./2)-x)./(sqrt(((a_PSS(i)./2)-x).^2 +...
    (y+(a_PSS(i)./2)).^2 + D.^2)))+ (((a_PSS(i)./2)+x)./...
    (sqrt(((a_PSS(i)./2)+x).^2 +(y+(a_PSS(i)./2)).^2 + D.^2))))).*...
    cos(gamma_rad)
TempC1=[TempC1;C1]
D1=(((x-(a_PSS(i)./2))./((x-(a_PSS(i)./2)).^2 + D.^2)).*...
    ((((a_PSS(i)./2)-y)./(sqrt(((a_PSS(i)./2)-y).^2 +...
    (x-(a_PSS(i)./2)).^2 + D.^2)))+ (((a_PSS(i)./2)+y)./...
    (sqrt(((a_PSS(i)./2)+y).^2 +(x-(a_PSS(i)./2)).^2 + D.^2))))).*...
    cos(gamma_rad)
TempD1=[TempD1;D1]
end
Hz_total_PSS=(-TempA1 + TempB1 + TempC1 - TempD1);
 Hz_PSS=sum(Hz_total_PSS)
%Effective area of the square spiral RX coil
 for j=1:length(b_PSS)
B1_PSS=b_PSS(j).^(2)
```

```
TempB_PSS=[TempB_PSS;B1_PSS]
end
B_PSS=sum(TempB_PSS)
%Theoretical Power Ratio Computation
G_P_PSS=((mu_o^(2)*omega^(2))./(64*pi^(2)*R_Rx_PSS*R_Tx_PSS)).*...
    Hz_PSS.^(2).*B_PSS.^(2)
GP_PSS=10.*log10(G_P_PSS);
%%%%%%%%%%%%%%%%%Plot Results%%%%%%%%%%%%%%%%%%%%%%%%%%%%%%%%%%%
plot( gamma, GP_S,'k-',gamma,GP_PCS,'r-',gamma,GP_PSS,'b-')
%plot(D,GP_S,'k-')
%plot(D,GP_PCS,'b-')
%plot(D,GP_PSS,'r-')
     xlabel('Angular Misalignment \gamma - [degrees]');
     ylabel('Power Transfer Ratio - [dB]');
```

D.5 Function magfieldz

```
%Author: Kyriaki Fotopoulou
%Date of Last Revision: 9/02/2008

function [H_z] = magfieldz(a,m,Delta,K,E)
% Computes the z-component of the magnetic field at the
% center of the receiver coil, where a, b are the radii
% of the TX, RX coils respectively. Delta is the Lateral displacement
% and K, E are the elliptic integrals of the first and second kind.
H_z=((a.*sqrt(2.*m))./((2*a.*Delta).^(3/2))).*((Delta.*K + (((a.*m)-(2-m)...
.*Delta)./(2-2*m)).*E));
return
```

Appendix E

Radiated Field of Small Circular Loop

In this appendix we present the evaluation of the radiated fields from an electrically small circular loop following the magnetic vector potential approach as shown in [56], [59].

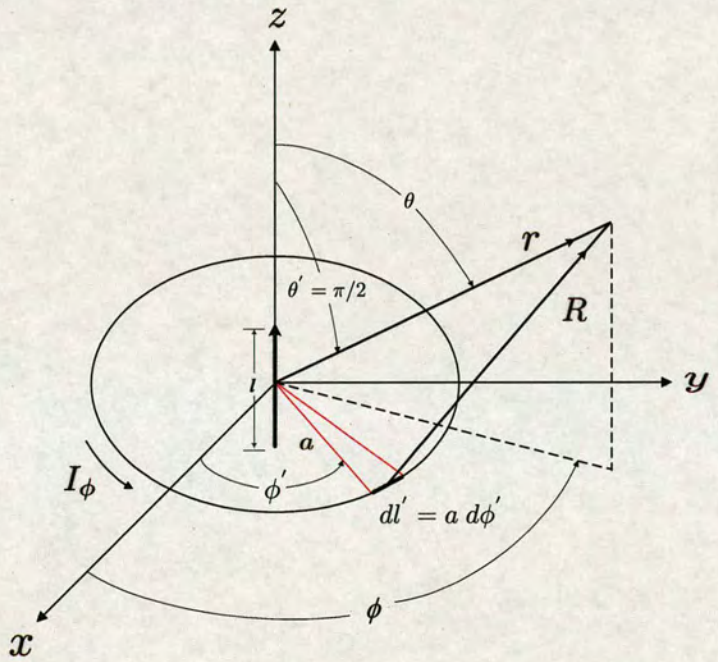

Figure E.1: *Geometrical arrangement for loop antenna analysis [56].*

Based on the geometry of Fig. E.1 the magnetic vector potential $\mathbf{A}$ is first evaluated as, [56]:

$$\mathbf{A}(x,y,z) = \frac{\mu}{4\pi}\int_C \mathbf{I}_e(x',y',z')\,\frac{e^{-jkR}}{R}\,dl' \tag{E.1}$$

In general, the current distribution $\mathbf{I}_e(x',y',z')$ can be written as:

$$\mathbf{I}_e(x',y',z') = \hat{\mathbf{a}}_x I_x(x',y',z') + \hat{\mathbf{a}}_x I_y(x',y',z') + \hat{\mathbf{a}}_x I_z(x',y',z') \tag{E.2}$$

For a circular loop antenna of Fig. E.1, the current is directed along a circular path. hence, it is more convenient to transform the expression in (E.2) in cylindrical components using the

following transformation:

$$\begin{bmatrix} I_x \\ I_y \\ I_z \end{bmatrix} = \begin{bmatrix} \cos\phi' & -\sin\phi' & 0 \\ \sin\phi' & \cos\phi' & 0 \\ 0 & 0 & 1 \end{bmatrix} \begin{bmatrix} I_\rho \\ I_\phi \\ I_z \end{bmatrix} \tag{E.3}$$

Expanding the previous matrix transformation yields:

$$\left.\begin{aligned} I_x &= I_\rho \cos\phi' - I_\phi \sin\phi' \\ I_y &= I_\rho \sin\phi' + I_\rho \cos\phi' \\ I_z &= I_z \end{aligned}\right\} \tag{E.4}$$

Since the radiated fields are usually determined in spherical components, the rectangular unit vectors of (E.2) need to be transformed to spherical coordinates:

$$\left.\begin{aligned} \hat{\mathbf{a}}_x &= \hat{\mathbf{a}}_r \sin\theta\cos\phi + \hat{\mathbf{a}}_\theta \cos\theta\cos\phi - \hat{\mathbf{a}}_\phi \sin\phi \\ \hat{\mathbf{a}}_y &= \hat{\mathbf{a}}_r \sin\theta\sin\phi + \hat{\mathbf{a}}_\theta \cos\theta\sin\phi + \hat{\mathbf{a}}_\phi \cos\phi \\ \hat{\mathbf{a}}_z &= \hat{\mathbf{a}}_r \cos\theta - \hat{\mathbf{a}}_\theta \sin\theta \end{aligned}\right\} \tag{E.5}$$

By substituting (E.4) and (E.5) into (E.2) yields the expression for the current in the loop. This can be simplified by noting that the current circulating in the loop antenna is flowing in the ϕ direction (I_ϕ), hence the expression can be reduced as:

$$\mathbf{I}_e = \hat{\mathbf{a}}_r I_\phi \sin\theta\ \sin(\phi - \phi') + \hat{\mathbf{a}}_\theta I_\phi \cos\theta\ \sin(\phi - \phi') + \hat{\mathbf{a}}_\phi I_\phi \cos(\phi - \phi') \tag{E.6}$$

The distance R, from the point of the loop to the observation point, can be written as:

$$R = \sqrt{r^2 + a^2 - 2ar\sin\theta\ \cos(\phi - \phi')} \tag{E.7}$$

By reffering to Fig. 5.7(c), the differential element length is given by

$$dl' = a\, d\phi' \tag{E.8}$$

It follows from (E.1), that the ϕ component of the magnetic vector potential is of the form:

$$A_\phi = \frac{a\mu I_o}{4\pi} \int_0^{2\pi} \cos\phi' \frac{e^{-jk\sqrt{r^2+a^2-2ar\sin\theta\cos\phi'}}}{\sqrt{r^2+a^2-2ar\sin\theta\cos\phi'}}\, d\phi' \tag{E.9}$$

The integration of the previous expression, (E.9), cannot be carried out without any approximations. However, for small loops, the function:

$$f = \frac{e^{-jk\sqrt{r^2+a^2-2ar\sin\theta\cos\phi'}}}{\sqrt{r^2+a^2-2ar\sin\theta\cos\phi'}} \tag{E.10}$$

of the integrand in (E.9), can be expanded in a Maclaurin series in a as:

$$f = f(0) + f^{'}(0)a + \frac{1}{2!}f^{''}(0)a^2 + \cdots + \frac{1}{(n-1)!}f^{(n-1)}(0)a^{n-1} + \cdots \tag{E.11}$$

where $f^{'}(0) = \partial f/\partial a\Big|_{a=0}$, $f^{''}(0) = \partial^2 f/\partial^2 a\Big|_{a=0}$. Taking into account only the first two terms of the Maclaurin series in (E.11), or

$$f(0) = \frac{e^{-jkr}}{r} \tag{E.12}$$

$$f^{'}(0) = \left(\frac{jk}{r} + \frac{1}{r^2}\right) e^{-jkr} \sin\theta \ \cos\phi^{'} \tag{E.13}$$

$$f \simeq \left[\frac{1}{r} + a\left(\frac{jk}{r} + \frac{1}{r^2}\right) \sin\theta \ \cos\phi^{'}\right] \ e^{-jkr} \tag{E.14}$$

Therefore, the (E.1) reduces to

$$A_\phi \simeq \frac{a\mu I_o}{4\pi} \int_0^{2\pi} \cos\phi^{'} \left[\frac{1}{r} + a\left(\frac{jk}{r} + \frac{1}{r^2}\right) \sin\theta\cos\phi^{'}\right] \ e^{-jkr} \ d\phi^{'} \tag{E.15}$$

$$A_\phi \simeq \frac{a\mu I_o}{4} \ e^{-jkr} \left(\frac{jk}{r} + \frac{1}{r^2}\right) \sin\theta \tag{E.16}$$

In a similar manner, the r and θ components of the magnetic vector potential can be written as:

$$A_r \simeq \frac{a\mu I_o}{4\pi} \sin\theta \int_0^{2\pi} \sin\phi^{'} \left[\frac{1}{r} + a\left(\frac{jk}{r} + \frac{1}{r^2}\right) \ \sin\theta \ \cos\phi^{'}\right] = 0 \tag{E.17}$$

$$A_\theta \simeq -\frac{a\mu I_o}{4\pi} \cos\theta \int_0^{2\pi} \sin\phi^{'} \left[\frac{1}{r} + a\left(\frac{jk}{r} + \frac{1}{r^2}\right) \ \sin\theta \ \cos\phi^{'}\right] = 0 \tag{E.18}$$

Consequently, only the ϕ component of the magnetic vector potential remains:

$$\begin{aligned} \mathbf{A} &\simeq \hat{\mathbf{a}}_\phi A_\phi = \hat{\mathbf{a}}_\phi \ \frac{a^2\mu I_o}{4} \ e^{-jkr} \left[\frac{jk}{r} + \frac{1}{r^2}\right] \ \sin\theta \\ &= \hat{\mathbf{a}}_\phi j\frac{k\mu a^2 I_o \sin\theta}{4r} \left[1 + \frac{1}{jkr}\right] \ e^{-jkr} \end{aligned} \tag{E.19}$$

The magnetic flux $\mathbf{B}$ is always solenoidal hence, $\nabla \bullet \mathbf{B} = 0$. Therefore, it can be represented as the curl of the magnetic vector potential since it obeys the vector identity:

$$\nabla \bullet \nabla \times \mathbf{A} = 0 \tag{E.20}$$

Consequently, referring to the original Maxwell's equations as presented in [197], we can define the magnetic flux as:

$$\mathbf{B} = \mu \, \mathbf{H} = \nabla \times \mathbf{A} \tag{E.21}$$

or

$$\boxed{\mathbf{H} = \frac{1}{\mu} \nabla \times \mathbf{A}} \tag{E.22}$$

$$\begin{aligned} \text{Curl } \nabla \times \mathbf{A} = & \frac{1}{r \sin\theta} \left[\frac{\partial}{\partial_\theta} (A_\phi \sin\theta) - \frac{\partial A_\theta}{\partial \phi} \right] \hat{\mathbf{r}} + \\ & \frac{1}{r} \left[\frac{1}{\sin\theta} \frac{\partial A_r}{\partial \phi} - \frac{\partial}{\partial r} (r\, A_\phi) \right] \hat{\boldsymbol{\theta}} + \\ & \frac{1}{r} \left[\frac{\partial}{\partial r} (r\, A_\theta) - \frac{\partial A_r}{\partial \theta} \right] \hat{\boldsymbol{\phi}} \end{aligned} \tag{E.23}$$

Substituting the remaining ϕ component of the magnetic vector potential in (E.22) and computing the curl in the spherical coordinates by (E.23) and rearranging, yields the field components for a small circular loop are given by Balanis [56] as follows:

$$H_r = j \frac{ka^2 I_o \cos\theta}{2r^2} \left[1 + \frac{1}{jkr} \right] e^{-jkr} \tag{E.24}$$

$$H_\theta = -\frac{(ka)^2 I_o \sin\theta}{4r} \left[1 + \frac{1}{jkr} - \frac{1}{(kr)^2} \right] e^{-jkr} \tag{E.25}$$

$$H_\phi = 0 \tag{E.26}$$

Again from Maxwell's equations:

$$\boxed{\nabla \times \mathbf{H} = \mathbf{J} + j\omega\epsilon E} \tag{E.27}$$

and neglecting the electric current density ($\mathbf{J} = 0$), reveals the corresponding electric field components written as:

$$E_r = E_\theta = 0 \tag{E.28}$$

$$E_\phi = \eta \frac{(ka)^2 I_o \sin\theta}{4r} \left[1 + \frac{1}{jkr} \right] e^{-jkr} \tag{E.29}$$

Appendix F
Radiation Resistance of a Small Loop with Uniform Current

A magnetic dipole of length l and magnetic moment $I_m\ l$ is equivalent to a small electric loop of radius a and a constant electric current I_o provided that:

$$I_m\ l = jA\omega\mu I_o \quad \text{where } A = \pi a^2 \text{ is the area of the loop}$$

It follows that for simplification purposes, the electrically small loop can be replaced by a small linear magnetic dipole of constant current. Fig. E.1 illustrates this equivalence where the magnetic dipole is directed along the z-axis which is also perpendicular to the plane of the loop.

The power in the near-field ($k\ r << 1$) of the antenna is predominantly reactive whereas in the far-field ($k\ r >> 1$) is predominantly real. To illustrate this for the loop, initially the complex power density is formed as:

$$\begin{aligned}\mathbf{W} &= \frac{1}{2}\left(\mathbf{E}\times\mathbf{H}^*\right) = \frac{1}{2}\left[\left(\hat{\mathbf{a}}_\phi\ E_\phi\right)\times\left(\hat{\mathbf{a}}_r\ H_r^* + \hat{\mathbf{a}}_\theta\ H_\theta^*\right)\right] \\ &= \frac{1}{2}\left(-\hat{\mathbf{a}}_r\ E_\phi\ H_\theta^* + \hat{\mathbf{a}}_\theta\ E_\phi\ H_r^*\right) \end{aligned} \tag{F.1}$$

Reffering to Balanis, [56], when the power density as expressed in F.1 is integrated over a closed sphere, only its radial component is given by:

$$W_r = \eta\frac{(ka)^4}{32}\left|I_o\right|^2\frac{sin^2\theta}{r^2}\left[1 + j\frac{1}{(kr)^3}\right] \tag{F.2}$$

contributes to the complex power P_r. As a result,

$$P_r = \mathbf{W}\cdot d\mathbf{s} = \eta\frac{(ka)^4}{32}\left|I_o\right|^2\int_0^{2\pi}\int_0^{2\pi}\left[1 + j\frac{1}{(kr)^3}\right]\sin^3\theta\ d\theta\ d\phi \tag{F.3}$$

which reduces to

$$P_r = \eta\left(\frac{\pi}{12}\right)(ka)^4\left|I_o\right|^2\left[1 + j\frac{1}{(kr)^3}\right] \tag{F.4}$$

and whose real part is equal to

$$P_{rad} = \eta\left(\frac{\pi}{12}\right)(ka)^4\left|I_o\right|^2 \tag{F.5}$$

In the near-field ($kr << 1$), the imaginary term within the brackets of (F.4) is dominant which makes the power mainly reactive. In the far-field ($kr >> 1$), the second term within the brackets diminishes and as a result the power is considered to be real. The complex power for an infinitesimal dipole is given by the following expression, [56], [59]:

$$P = \eta \frac{\pi}{3} \left| \frac{I_o l}{\lambda} \right|^2 \left[1 - j \frac{1}{(kr)^3} \right] \tag{F.6}$$

Hence, a comparison between the expression of the radiated power for the infinitesimal dipole (F.6), and the electrically small loop (F.4), yields a change in sine in the bracketed expression. This indicates that the radial power density is capacitive for the infinitesimal dipole and inductive for the loop. Consequently, we can conclude that the radial magnetic energy is larger than the electric energy for the small loop, a characteristic that makes loop antennas popular in the inductive power transfer applications. In order to calculate the radiation resistance we need to equate expression (F.4) to $|I_o| \ R_r/2$ and solve for R_r, as follows:

$$R_r = \eta \left(\frac{\pi}{6} \right) \left(k^2 a^2 \right)^2 = \eta \frac{2\pi}{3} \left(\frac{kS}{\lambda} \right)^2 = 20\pi^2 \left(\frac{C}{\lambda} \right)^4 \tag{F.7}$$

where $S = \pi\alpha^2$ is the area and $C = 2\pi a$ is the circumference of the loop. For a multi-turn loop antenna of N turns the magnetic loop passes through all the loops. Hence, the radiation resistance is proportional to the square of the number of turns ($R_r \propto N^2$) as follows:

$$R_r = N^2 \, 20\pi^2 \left(\frac{C}{\lambda} \right)^4 \tag{F.8}$$

Appendix G
S.W.G British Imperial Wire Gauge

No.	Size inches	No.	Size inches	No.	Size inches	No.	Size inches
7/0	0.500	9	0.144	24	0.022	39	0.0052
6/0	0.464	10	0.128	25	0.020	40	0.0048
5/0	0.432	11	0.116	26	0.018	41	0.0044
4/0	0.400	12	0.104	27	0.0164	42	0.0040
3/0	0.372	13	0.092	28	0.0148	43	0.0036
2/0	0.348	14	0.080	29	0.0136	44	0.0032
0	0.324	15	0.072	30	0.0124	45	0.0028
1	0.300	16	0.064	31	0.0116	46	0.0024
2	0.276	17	0.056	32	0.0108	47	0.0020
3	0.252	18	0.048	33	0.0100	48	0.0016
4	0.232	19	0.040	34	0.0092	49	0.0012
5	0.212	20	0.036	35	0.0084	50	0.0010
6	0.192	21	0.032	36	0.0076		
7	0.176	22	0.028	37	0.0068		
8	0.160	23	0.024	38	0.0060		

Table G.1: *Table of S.W.G numbering for wire diameter. For dimensions in millimeters multiply the size in inches by* 25.4.

	Coil Length/Coil Diameter (ℓ/D)											
p/d	0	0.2	0.4	0.6	0.8	1.0	2	4	6	8	10	∞
1	5.31	5.45	5.65	5.80	5.80	5.55	4.10	3.54	3.31	3.20	3.23	3.41
1.11	3.73	3.84	3.99	4.11	4.17	4.10	3.36	3.05	2.92	2.90	2.93	3.11
1.25	2.74	2.83	2.97	3.10	3.20	3.17	2.74	2.06	2.60	2.62	2.65	2.81
1.429	2.12	2.20	2.28	2.38	2.44	2.47	2.32	2.27	2.29	2.34	2.27	2.51
1.667	1.74	1.77	1.83	1.89	1.92	1.94	1.98	2.01	2.03	2.08	2.10	2.22
2	1.44	1.48	1.54	1.00	1.64	1.67	1.74	1.78	1.80	1.81	1.83	1.93
2.5	1.20	1.29	1.33	1.38	1.42	1.45	1.50	1.54	1.56	1.57	1.58	1.65
3.333	1.16	1.19	1.21	1.22	1.23	1.24	1.28	1.32	1.34	1.34	1.35	1.40
5	1.07	1.08	1.08	1.10	1.10	1.10	1.13	1.15	1.16	1.16	1.17	1.19
10	1.02	1.02	1.03	1.03	1.03	1.03	1.04	1.04	1.04	1.04	1.04	1.05

Table G.2: *Experimental values of the ratio of the high-frequency coil resistance to the resistance at the same frequency of the same length of straight wire, [93].*

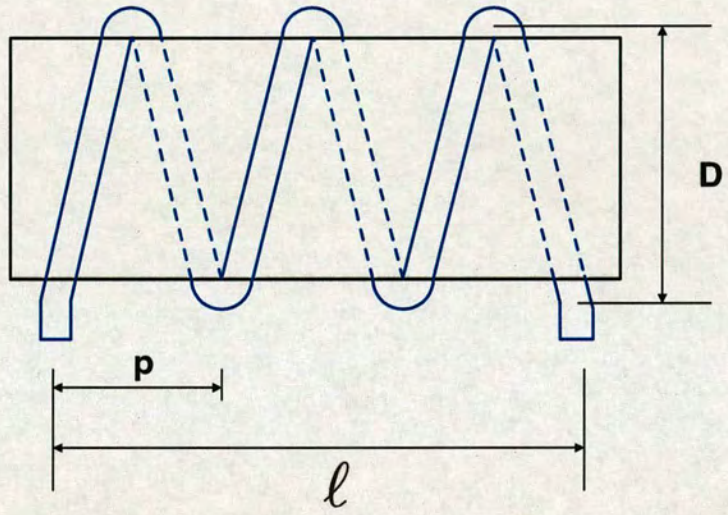

Figure G.1: *A solenoid coil of diameter D and length ℓ, with a winding pitch (turn spacing) of p.*

Appendix H
Publications

- K. Fotopoulou and B. W. Flynn, *Wireless Powering of Implanted Sensors using RF inductive Coupling*, in Proceedings of the IEEE International Conference on Sensors (IEEE Sensors), Daegu, South Korea, October, 2006

- K. Fotopoulou and B. W. Flynn, *Optimum Antenna Coil Structure for Inductive Powering of Passive RFID Tags*,in Proceedings of the IEEE International Conference on Radio Frequency Identification (IEEE RFID), Dallas, Texas USA, March, 2007

References

[1] H. Hertz, "Ueber sehr schnelle electrische schwingungen," *Annalen der Physik und Chemie*, vol. 267, no. 7, pp. 421–448, 1887.

[2] W. Brown, "The history of power transmission by radio waves," *Microwave Theory and Techniques, IEEE Transactions on*, vol. 32, no. 9, pp. 1230–1242, 1984.

[3] N. Tesla, "Apparatus for transmission of electrical energy," U.S. Patent 649621, May 1900.

[4] N. Tesla, "Method of utilizing effects transmitted through natural media," U.S. Patent 685954, November 1901.

[5] W. J. Heetderks, "Rf powering of millimeter and submillimeter sized neural prosthetic implants," *Biomedical Engineering, IEEE Transactions on*, vol. 35, no. 5, pp. 323–327, 1988.

[6] L. Wang, T. B. Tang, E. Johannessen, A. Astaras, M. Ahmadian, A. Murray, J. Cooper, S. Beaumont, B. Flynn, and D. Cumming, "Integrated micro-instrumentation for dynamic monitoring of the gastro-intestinal tract," in *Proc. IEEE-EMBS Annual International Special Topic Conference on Microtechnologies in Medicine & Biology*, pp. 219 – 222, 2002.

[7] W. Liu, K. Vichienchom, M. Clements, S. C. DeMarco, C. Hughes, E. McGucken, M. Humayun, E. de Juan, J. Weiland, and R. Greenbery, "A neuro-stimulus chip with telemetry unit for retinal prosthetic device," *IEEE Journal of Solid-State Circuits*, vol. 35, no. 10, pp. 1487–1497, 2000.

[8] J. Scuder, "Powering an artificial heart: Birth of the inductively coupled-radio frequency system in 1960," *Artificial Organs*, vol. 26, no. 11, pp. 909–915, 2002.

[9] Z. Hamici, R. Itti, and J. Champier, "A high-efficiency power and data transmission system for biomedical implanted electronic devices," *Measurement Science and Technology.*, vol. 7, pp. 192–201, 1996.

[10] J. E. McGray, "Theoretical foundation for real-time prostate localization using an inductively coupled transmitter and a superconducting quantum interference device (SQUID) magnetometer system," *Journal of Applied Clinical Medical Physics*, vol. 5, no. 4, pp. 29–45, 2004.

[11] J. D. Bronzino, *The Biomedical Engineering Handbook*. New York: IEEE Press, 1995.

[12] J. Wu, V. Quinn, and G. H. Bernstein, "A simple, wireless powering scheme for mems devices," *Proceedings of SPIE*, vol. 4559, pp. 43–52, 2001.

[13] D. Jeutter, "Overview of biomedical telemetry techniques," *Engineering in Medicine and Biology Magazine*, vol. 2, pp. 17–24, 1983.

[14] K. Murakawa, M. Kobayashi, O. Nakamura, and S. Kawata, "A wireless near-infrared energy system for medical implants," *IEEE Engineering in Medicine and Biology Magazine*, vol. 18, no. 6, pp. 70–72, 1999.

[15] K. Goto, T. Nakagama, O. Nakamura, and S. Kawata, "An implantable power supply with an optically rechargable lithium battery," *Biomedical Engineering, IEEE Transactions on*, vol. 48, no. 7, pp. 830–833, 2001.

[16] M. Sawan, Y. Hu, and J. Coulombe, "Wireless smart implants dedicated to multichannel monitoring and microstimulation," *Proc. IEEE International Conference on Pervasive Computing*, vol. 5, no. 1, pp. 21–39, 2005.

[17] P. Walter, Z. Kisvarday, G. Roessler, N. Alteheld, M. Goertz, T. Stieglitz, and U. Eysel, "Optimal activation via an implanted wireless retinal prosthesis," *Investigative Ophthalmology & Visual Science*, vol. 46, no. 5, pp. 1780–1785, 2005.

[18] H. Stockman, "Communication by means of reflected power," *Proceedings of the IRE*, vol. 36, no. 10, pp. 1196–1204, 1948.

[19] K. S. Rao, P. Nikitin, and S. Lam, "Antenna design for uhf rfid tags: A review and a practical application," *Antennas and Propagation, IEEE Transactions on*, vol. 53, no. 12, pp. 3870–3876, 2005.

[20] K. Foster and J. Jaeger, "RFID inside - the murky ethics of implanted chips," *IEEE Spectrum*, vol. 44, no. 3, pp. 8–29, 2007.

[21] A. Graafstra, "Hands on - How Radio-Frequency identification and I got personal," *IEEE Spectrum*, vol. 44, no. 3, pp. 18–23, 2007.

[22] S. Chen and V. Thomas, "Optimization of inductive RFID technology," pp. 82–87, May 2001.

[23] R. Weinstein, "RFID: A technical overview and its application to the enterprise," *IT Professional*, vol. 7, no. 3, pp. 27–33, 2005.

[24] M. Philipose, J. Smith, B. Jiang, A. Mamishev, S. Roy, and K. Sundara-Rajan, "Battery-free wireless identification and sensing," *IEEE Pervasive Computing*, vol. 4, no. 1, pp. 37–45, 2005.

[25] T. Wiechert, F. Thiesse, F. Michahelles, P. Schmitt, and E. Fleisch, "Connecting mobile phones to the internet of things - A discussion of compatibility issues between EPC technology and NFC technology," tech. rep., Auto-ID Lab Switzerland, 2008.

[26] W. Mokwa, "Medical implants based on microsystems," *Measurement Science and Technology*, vol. 18, no. 5, pp. 47–57, 2007.

[27] M. Baker and R. Sarpeshkar, "Feedback analysis and design of RF power links for low-power bionic systems," *Biomedical Circuits and Systems, IEEE Transactions on*, vol. 1, no. 1, pp. 28–38, 2007.

[28] S. Smith, T. Tang, J. Terry, J. Stevenson, B. Flynn, H. Reekie, A. Murray, A. Gundlach, D. Renshaw, B. Dhillon, A. Ohtori, Y. Inone, and A. J. Walton, "Development of a miniaturised drug delivery system with wireless power transfer and communication," *IET Nanobiotechnology*, vol. 1, no. 5, pp. 80–86, 2007.

[29] N. Neihart and R. Harrison, "Micropower circuit for bidirectional wireless telemetry in neural recording applications," *Biomedical Engineering, IEEE Transactions on*, vol. 52, no. 11, pp. 1950–1959, 2005.

[30] T. Akin, K. Najafi, and R. M. Bradley, "A wireless implantable multichannel digital neural recording system for a micromachined sieve electrode," *IEEE Journal of Solid-State Circuits*, vol. 33, no. 1, pp. 109–118, 1998.

[31] Q. Huang and M. Oberle, "A 0.5-mW passive telemetry IC for biomedical applications," *IEEE Journal of Solid-State Circuits*, vol. 33, no. 7, pp. 937–946, 1998.

[32] J. Parramon, P. Doguet, D. Marin, M. Verleyssen, R. Munoz, L. Leija, and E. Valderrama, "Asic-based battery less implantable telemetry microsystem for recording purposes," in *Proc. IEEE 19th Annual International Conference of Engineering in Medicine and Biology Society*, vol. 5, pp. 2225–2228, 1997.

[33] U. Kaiser and W. Steinhagen, "A low-power transponder IC for high-performance identification systems," *IEEE Journal of Solid-State Circuits*, vol. 30, pp. 306–310, 1995.

[34] C. Sauer, M. Stanaćević, G. Cauwenberghs, and N. Thakor, "Power harvesting and telemetry in CMOS for implanted devices," *Circuits and Systems-I: Regular Papers, IEEE Transactions on*, vol. 52, no. 12, pp. 2605–2613, 2005.

[35] M. Suster, D. Young, and W. Ko, "Micro-power wireless transmitter for high-temperature MEMS sensing and communication applications," in *Proc. IEEE International Conference on Microelectromechanical Systems*, pp. 641–644, 2002.

[36] "SL1ICS3101 I-CODE1 Label IC," Data Sheet, Product Specification Rev. 1.3, Philips Semiconductors, January 2005.

[37] P. R. Troyk, "Injectable electronic identification, monitoring, and stimulation systems," *Annual Review of Biomedical Engineering*, vol. 1, pp. 177–209, 1999.

[38] N. N. Donaldson and T. A. Perkins, "Analysis of resonant coupled coils in the design of radio frequency transcutaneous links," *Medical & Biological Engineering & Computing*, vol. 21, no. 5, pp. 612–627, 1983.

[39] D. C. Galbraith, M. Soma, and R. L. White, "A wide-band efficient inductive transdermal power and data link with coupling insensitive gain," *Biomedical Engineering, IEEE Transactions on*, vol. 34, no. 4, pp. 265–275, 1987.

[40] S. L. W. Ko and C. Fung, "Design of radio-frequency powered coils for implant instruments," *Medical and Biological Engineering and Computing*, vol. 15, no. 6, pp. 634–640, 1977.

[41] S. Schmidt and G. Lazzi, "Use of FDTD thin-strut formalism for biomedical telemetry coil designs," *Microwave Theory and Techniques, IEEE Transactions on*, vol. 52, no. 8, pp. 1952–1956, 2004.

[42] F. W. Grover, *Inductance Calculations, Working Formulas and Tables*. New York: D. Van Nostrand Company, Inc., second ed., 1946.

[43] F. Terman, *Radio Engineers Handbook*. New York: McGraw-Hill, 1943.

[44] M. Soma, C. D. Galbraith, and R. White, "Radio-frequency coils in implantable devices: Misalignment analysis and design procedure," *Biomedical Engineering, IEEE Transactions on*, vol. BME-34, no. 4, pp. 276–282, 1987.

[45] E. S. Hochmair, "System optimization for improved accuracy in transcutaneous signal and power transmission," *Biomedical Engineering, IEEE Transactions on*, vol. BME-31, no. 2, pp. 177–186, 1984.

[46] K. Finkenzeller, *RFID Handbook - Radio-Frequency Identification Fundamentals and Applications*. John Wiley & Sons Ltd., 1999.

[47] D. C. Yates, A. S. Holmes, and A. J. Burdett, "Optimal transmission frequency for ultralow-power short range radio links," *Circuits and Systems I: Regular Papers, IEEE Transactions on*, vol. 51, no. 7, pp. 1405–1413, 2004.

[48] J. B. Earnshaw, *An introduction to AC circuit theory*. New York: Macmillan & Co. Ltd., 1960.

[49] P. Basset, A. Kaiser, B. Legrand, D. Collard, and L. Buchaillot, "Complete system for wireless powering and remote control of electrostatic actuators by inductive coupling," *Mechatronics, IEEE Transactions on*, vol. 12, no. 1, pp. 23–31, 2007.

[50] G. Vandevoorde and R. Puers, "Wireless energy transfer for stand-alone systems: a comparison between low and high power applicability," *Sensors and Actuators A: Physical*, vol. 92, no. 1, pp. 305–311, 2001.

[51] B. Jiang, J. Smith, M. Philipose, S. Roy, K. Sundara-Rajan, and A. Mamishev, "Energy scavenging for inductively coupled passive RFID systems," *Instrumentation and Measurement, IEEE Transactions on*, vol. 56, no. 1, pp. 118–125, 2007.

[52] W. R. Smythe, *Static and Dynamic Electricity*. McGraw-Hill Book Company, second ed., 1950.

[53] S. Ramo, J. R. Whinnery, and T. VanDuzer, *Fields and Waves in Communication Electronics*. John Wiley & Sons, Inc., third ed., 1994.

[54] E. C. Snelling, *Soft Ferrites: Properties and Applications*. Butterworths, second ed., 1988.

[55] S. F. Pichorim and P. J. Abatti, "Design of coils for millimeter- and submillimeter-sized biotelemetry," *Biomedical Engineering, IEEE Transactions on*, vol. 51, no. 8, pp. 1487–1489, 2004.

[56] C. Balanis, *Antenna theory : analysis and design*. New York: Wiley, second ed., 1997.

[57] G. S. Smith, *Loop Antennas*. New York: McGraw-Hill, in antennas engineering handbook ed., 1984.

[58] C. A. Balanis, "Antenna theory: A review," *Proceedings of the IEEE*, vol. 80, no. 1, pp. 7–23, 1992.

[59] J. D. Kraus, *Antennas*. McGraw-Hill, Inc., second edition ed., 1988.

[60] G. S. Smith, *An introduction to classical electromagnetic radiation*. New York: Cambridge University Press, 1997.

[61] D. H. Werner, "An exact formulation for the vector potential of a cylindrical antenna with uniformly distributed current and arbitrary radius," *Antennas and Propagation, IEEE Transactions on*, vol. 41, no. 8, pp. 1009–1018, 1993.

[62] D. H. Werner, "An exact integration procedure for vector potentials of thin circular loop antennas," *Antennas and Propagation, IEEE Transactions on*, vol. 44, no. 2, pp. 157–165, 1996.

[63] P. L. Overfelt, "Near fields of the constant current thin circular loop antenna of arbitrary radius," *Antennas and Propagation, IEEE Transactions on*, vol. 44, no. 2, pp. 166–171, 1996.

[64] L. Li, M.-S. Leong, P. Kooi, and T. Yeo, "Exact solutions of electromagnetic fields in both near and far zones radiated by thin circular-loop antennas: A general representation," *Antennas and Propagation, IEEE Transactions on*, vol. 45, no. 12, pp. 1741–1748, 1997.

[65] F. M. Greene, "The near-zone magnetic field of a small circular-loop antenna," *Journal of Research of the National Bureau of Standards-C*, vol. 71C, no. 4, pp. 319–325, 1967.

[66] R. King, "The rectangular loop antenna as a dipole," *Antennas and Propagation, IEEE Transactions on*, vol. 7, no. 1, pp. 53–61, 1959.

[67] R. C. Fenwick and W. L. Weeks, "Submerged antenna characteristics," *Antennas and Propagation, IEEE Transactions on*, vol. 11, no. 3, pp. 296–305, 1963.

[68] R. C. Hansen, "Radiation and reception with buried and submerged antennas," *Antennas and Propagation, IEEE Transactions on*, vol. 11, no. 3, pp. 207–216, 1963.

[69] R. K. Moore, "Effects of surrounding conducting medium on antenna analysis," *Antennas and Propagation, IEEE Transactions on*, vol. 11, no. 2, pp. 216–225, 1963.

[70] P. Kennedy, "Loop antenna measurements," *IRE Transactions on Antennas and Propagation*, vol. 4, no. 4, pp. 610–618, 1956.

[71] J. D. Kraus and D. A. Fleisch, *Electromagnetics with Applications*. McGraw Hill International Editions, fifth ed., 1999.

[72] B. Levin, "Field of a rectangular loop," *Antennas and Propagation, IEEE Transactions on*, vol. 52, no. 4, pp. 948–952, 2004.

[73] E. Lou, N. Durdle, V. Raso, and D. Hill, "Measurement of the magnetic field in the near-field region and self-inductance in free space due to a multiturn square loop," *IEE Proceedings Science Measurement and Technology*, vol. 144, no. 6, pp. 252–256, 1997.

[74] "IEEE standard definitions of terms for antennas," IEEE Std. 145-1993, March 1993.

[75] G. Wang, W. Liu, M. Sivaprakasam, and G. Kendir, "Design and analysis of an adaptive transcutaneous power telemetry for biomedical implants," *Circuits and Systems - I: Regular Papers, IEEE Transactions on*, vol. 52, no. 10, pp. 2109–2117, 2005.

[76] O. Chevalerias, T. O'Donnell, D. Power, N. O'Donnovan, G. Duffy, G. Grant, and S. C. O'Mathuna, "Inductive telemetry of multiple sensor modules," *IEEE Pervasive Computing*, vol. 4, no. 1, pp. 46–52, 2005.

[77] J. Paradiso and T. Starner, "Energy scavenging for mobile and wireless electronics," *IEEE Pervasive Computing*, vol. 4, no. 1, pp. 18–27, 2005.

[78] M. Ahmadian, B. Flynn, A. Murray, and D. Cumming, "Data transmission for implantable microsystems using magnetic coupling," *IEE Proceedings Communications*, vol. 152, no. 2, pp. 247–250, 2005.

[79] A. Richtscheid, "Calculation of the radiation resistance of loop antennas with sinusoidal current distribution," *Antennas and Propagation, IEEE Transactions on*, vol. 24, no. 6, pp. 889–891, 1976.

[80] E. H. Newman, P. Bohley, and C. H. Walter, "Two methods for the measurement of antenna efficiency," *Antennas and Propagation, IEEE Transactions on*, vol. 23, no. 4, pp. 457–461, 1975.

[81] G. S. Smith, "Efficiency of electrically small antennas combined with matching networks," *Antennas and Propagation, IEEE Transactions on*, vol. 25, no. 3, pp. 369–373, 1977.

[82] G. S. Smith, "Radiation efficiency of electrically small multiturn loop antennas," *Antennas and Propagation, IEEE Transactions on*, vol. 20, no. 5, pp. 656–657, 1972.

[83] R. Pettengill, H. Garland, and J. Meindl, "Receiving antenna design for miniature receivers," *Antennas and Propagation, IEEE Transactions on*, vol. 25, no. 4, pp. 528–530, 1977.

[84] T. Roz and V. Fuentes, "Using low power transponders and tags for RFID applications," pp. 1–8.

[85] F. C. Flack, E. D. James, and D. M. Schlapp, "Mutual inductance of air-cored coils: Effect on design of radio-frequency coupled implants," *Medical & Biological Engineering & Computing*, vol. 9, pp. 79–85, 1971.

[86] Z. Tang, B. Smith, J. Schild, and P. Peckham, "Data transmission from an implantable biotelemeter by load-shift keying using circuit configuration modulator," *Biomedical Engineering, IEEE Transactions on*, vol. 42, no. 5, pp. 524–528, 1995.

[87] C. Liang, J. Chen, C. Chung, C. Cheng, and C. Wang, "An implantable bi-directional wireless transmission system for transcutaneous biological signal recording," *Physiological Measurement*, vol. 26, no. 1, pp. 83–97, 2005.

[88] J. P. Daniel, "Mutual coupling between antennas for emission of reception - application to passive and active dipoles," *Antennas and Propagation, IEEE Transactions on*, vol. 22, no. 2, pp. 347–349, 1974.

[89] H. A. Wheeler, "Small antennas," *Antennas and Propagation, IEEE Transactions on*, vol. 23, no. 4, pp. 462–469, 1975.

[90] H. A. Wheeler, "Fundamental limitations of small antennas," *Proceedings of the IRE*, vol. 35, no. 12, pp. 1479–1484, 1947.

[91] S. Butterworth, "Note on the alternating current resistance of single layer coils," *Physical Review*, vol. 23, pp. 752–755, 1924.

[92] S. Butterworth, "On the alternating current resistance of solenoidal coils," *Proceedings of the Royal Society of London. Series A, Containing Papers of a Mathematical and Physical*, vol. 107, no. 744, pp. 693–715, 1925.

[93] R. G. Medhurst, "H.F. resistance and self-capacitance of single layer solenoids - Part I," *Wireless Engineer*, vol. 24, no. February, pp. 35–43, 1947.

[94] R. G. Medhurst, "H.F. resistance and self-capacitance of single layer solenoids - Part II," *Wireless Engineer*, vol. 24, no. March, pp. 80–92, 1947.

[95] G. S. Smith, "Proximity effect in systems of parallel conductors," *Journal of Applied Physics*, vol. 43, no. 5, pp. 2196–2203, 1972.

[96] C. Gabriel, S. Gabriel, and E. Corthout, "The dielectric properties of biological tissues: I. literature survey," *Physics in Medicine and Biology*, vol. 41, no. 11, pp. 2231–2249, 1996.

[97] S. Gabriel, R. Lau, and C. Gabriel, "The dielectric properties of biological tissues: III parametric models of the dielectric spectrum of tissues," *Physic in Medicine and Biology*, vol. 41, no. 11, pp. 2271–2293, 1996.

[98] M. Stuchly and T. Dawson, "Interaction of low-frequency electric and magnetic fields with the human body," *Proceedings of the IEEE*, vol. 88, no. 5, pp. 643–664, 2000.

[99] P. Bottomley and E. Andrew, "RF magnetic field penetration, phase shift and power dissipation in biological tissue: Implications for NMR imaging," *Physics in Medicine and Biology*, vol. 23, no. 4, pp. 630–643, 1978.

[100] W. H. Ko, R. Plonsey, and S. R. Kang, "The radiation from an electrically small circular wire loop implanted in a dissipative homogeneous spherical medium," *Annals of Biomedical Engineering*, vol. 1, no. 135-145, pp. 135–145, 1972.

[101] M. Zborowski, B. Kligman, R. Midura, A. Wolfman, T. Patterson, M. Ibiwoye, and M. Grabiner, "Decibel attenuation of pulsed electromagnetic field (PEMF) in blood and cortical bone determined experimentally and from the theory of ohmic losses," *Annals of Biomedical Engineering*, vol. 34, no. 6, pp. 1030–1041, 2006.

[102] R. M. Dunbar, "The performance of a magnetic loop transmitter-receiver system submerged in the sea," *The Radio and Electronic Engineer*, vol. 42, no. 10, pp. 457–463, 1972.

[103] C. Johnson and A. Guy, "Nonionizing electromagnetic wave effects in biological materials and systems," *Proceedings of the IEEE*, vol. 60, no. 6, pp. 692–718, 1972.

[104] J. Dellinger, "Principles of radio transmission and reception with antenna and coil aerials," *Proceedings of the IEEE*, vol. 87, no. 5, pp. 894–921, 1999.

[105] P. Nikitin, K. Rao, and S. Lazar, "An overview of near-field UHF RFID," in *Proc. IEEE-EMBS*, pp. 167–174, 2007.

[106] A. C. Ludwig and R. A. Norman, "A new-method for calculating correction factors for near-field gain measurements," *Antennas and Propagation, IEEE Transactions on*, vol. 21, no. 5, pp. 623–628, 1973.

[107] A. D. Yaghjian, "An overview of near-field antenna measurements," *Antennas and Propagation, IEEE Transactions on*, vol. 34, no. 1, pp. 30–45, 1986.

[108] N. Gerbaux, J. Glowacki, M. Ammann, and V. Thorne, "Investigation of the near-field behaviour and SAR for the resonant loop antenna operating at 434 MHz for medical applications," *Microwave and Optical Technology Letters*, vol. 47, no. 6, pp. 597–599, 2005.

[109] P. Zalud and J. Schepps, "Radio frequency identification tag having an inductively coupled antenna," U.S. Patent 2006/0012482 A1, January 2006.

[110] K.-H. Hsu, S. S. Nagarajan, and D. M. Durand, "Analysis of efficiency of magnetic stimulation," *Biomedical Engineering, IEEE Transactions on*, vol. 50, no. 11, pp. 1276–1285, 2003.

[111] M. R. Shah, R. P. Phillips, and R. A. Norman, "A study of printed spiral coils for neuroprosthetic transcranial telemetry applications," *Biomedical Engineering, IEEE Transactions on*, vol. 45, no. 7, pp. 867–876, 1998.

[112] T. Bergeman, G. Erez, and H. J. Metcalf, "Magnetostatic trapping fields for neutral atoms," *Physical Review A*, vol. 35, no. 4, pp. 1535–1546, 1987.

[113] B. Azzeroni, E. Cardelli, M. Raugi, and A. Tellini, "Magnetic field evaluation for thick annular conductors," *Magnetics, IEEE Transactions on*, vol. 29, no. 3, pp. 2090–2094, 1993.

[114] S. Babic and C. Akyel, "Improvement in calculation of the self- and mutual inductance of thin-wall solenoids and disk coils," *Magnetics, IEEE Transactions on*, vol. 36, no. 4, pp. 1970–1975, 2000.

[115] A. Aydmer and E. Yanmaz, "Numerical calculation of trapped magnetic field for square and cylindrical superconductors," *Superconductor Science and Technology*, vol. 18, no. 7, pp. 1010–1015, 2005.

[116] A. O. Rodriguez, R. Amador, R. Rojas, and F. A. Barrios, "Magnetic field visualisation and inductance calculation of a simple configuration surface coil at low magnetic field," *Revista Mexicana de Fisica E*, vol. 52, no. 1, pp. 1–12, 2006.

[117] O. Mohammed, W. Batina, and L. Gipson, "Electromagnetic field modeling of implantable telemetry systems," *Magnetics, IEEE Transactions on*, vol. 21, no. 5, pp. 2068–2070, 1985.

[118] W. A. Perkins and J. C. Brown, "MAFCO - a magnetic field code for handling general current elements in three dimensions," *Journal of Applied Physics*, vol. 35, no. 11, pp. 3337–3343, 1964.

[119] Z. Feng, "The treatment of singularities in calculation of magnetic field by using integral method," *Magnetics, IEEE Transactions on*, vol. 21, no. 6, pp. 2207–2210, 1985.

[120] S. R. Marandi, "The magnetic near-field of a solenoid," in *Proc. Canadian Conference on Electrical and Computer Engineering*, pp. 1–4, May 1996.

[121] M. W. Garrett, "Calculation of fields, forces, and mutual inductances of current systems by elliptic integrals," *Journal of Applied Physics*, vol. 34, no. 9, pp. 2567–2573, 1963.

[122] L. K. Urankar, "Vector potential and magnetic field of current-carrying finite arc segment in analytical form, part I: Filament approximation," *Magnetics, IEEE Transactions on*, vol. 16, no. 5, pp. 1283–1288, 1980.

[123] L. K. Urankar, "Compact extended algorithms for elliptic integrals in electromagnetic field and potential computations part II: Elliptic integral of third kind with extended integration range," *Magnetics, IEEE Transactions on*, vol. 30, no. 3, pp. 1236–1241, 1994.

[124] A. I. Rusinov, "High precision computation of solenoid magnetic fields by Garrett's method," *Magnetics, IEEE Transactions on*, vol. 30, no. 4, pp. 2685–2688, 1994.

[125] M. Abramowitz and I. Stegun, *Handbook of mathematical functions*. Washington, D.C. 20402, USA: National Bureau of Standards, second ed., 1972.

[126] S. Y. Leung and D. C. Lam, "Performance of printed polymer-based RFID antenna on curvilinear surface," *Electronics Packaging Manufacturing, IEEE Transactions on*, vol. 30, no. 3, pp. 200–205, 2007.

[127] VeriChip Corporation, *http://www.verichipcorp.com*, 2007.

[128] UPM Raflatac, *http://www.upmraflatac.com/*, 2007.

[129] C. M. Zierhofer and E. S. Hochmair, "Geometric approach for coupling enhancement of magnetically coupled coils," *Biomedical Engineering, IEEE Transactions on*, vol. 43, no. 7, pp. 708–714, 1996.

[130] R. Rodriguez, J. Dishman, F. Dickens, and E. Whelan, "Modeling of two-dimensional spiral inductors," *Components, Hybrids and Manufacturing Technology, IEEE Transaction on*, vol. 3, no. 4, pp. 535–541, 1980.

[131] S. Eroglu, G. Friedman, and R. L. Magin, "Estimate of losses and signal-to-noise ratio in planar inductive micro-coil detectors used for NMR," *Magnetics, IEEE Transactions on*, vol. 37, no. 4, pp. 2787–2789, 2001.

[132] K. Bartusek, Z. Dokoupil, and E. Gescheidtova, "Mapping of magnetic field around small coils using the magnetic resonance method," *Measurement Science and Technology*, vol. 18, no. 7, pp. 2223–2230, 2007.

[133] H. Lee, "A high-bandwidth induction sensor coil," *Journal of Physics E: Scientific Instruments*, vol. 15, no. 10, pp. 1017–1019, 1982.

[134] R. H. Good, "Elliptic integrals, the forgotten functions," *European Journal of Physics*, vol. 22, pp. 119–126, 2001.

[135] P. F. Byrd and M. D. Friedman, *Handbook of Elliptic Integrals for Engineers and Physicists*. Springer-Verlag, 1954.

[136] Y. Rahmat-Samii, "Useful coordinate transformations for antenna applications," *Antennas and Propagation, IEEE Transactions on*, vol. 27, no. 4, pp. 571–574, 1979.

[137] T. Leuerer and W. Mokwa, "Planar coils with magnetic layers for optimized energy transfer in telemetric systems," *Sensors and Actuators - Physical A*, vol. 116, no. 3, pp. 410–416, 2004.

[138] R. DeVore and P. Bohley, "The electrically small magnetically loaded multiturn loop antenna," *Antennas and Propagation, IEEE Transactions on*, vol. 25, no. 4, pp. 496–505, 1977.

[139] C. Neagu, H. Jansen, A. Smith, J. Gardeniers, and M. Elwenspoek, "Characterization of a planar microcoil for implantable microsystems," *Sensors and Actuators A: Physical*, vol. 62, no. 1-3, pp. 599–611, 1997.

[140] I. Sasada, T. Yamaguchi, K. Harada, and Y. Notohara, "Planar inductors using nizn ferrite thin plates and the application to high-frequency dc-dc converters," *Magnetics, IEEE Transactions on*, vol. 29, no. 6, pp. 3231–3233, 1993.

[141] W. Hurley, M. Duffy, S. O'reilly, and S. C. O. Mathuna, "Impedance formulas for planar magnetic structures with spiral windings," *Industrial Electronics, IEEE Transactions on*, vol. 46, no. 2, pp. 271–277, 1999.

[142] S. Iskra and I. Macfarlane, "H-field sensor measurement errors in the near-field of a magnetic dipole source," *Electromagnetic Compatibility, IEEE Transactions on*, vol. 31, no. 3, pp. 306–311, 1989.

[143] "IEEE standard methods for measuring electromagnetic field strength of sinusoidal continuous waves," IEEE Std.291-1991, April 1991.

[144] H. Beverage, S. Bowhill, H. Fine, and F. Greene, "IEEE standard methods for measuring electromagnetic field strength for frequencies below 1000 MHz in radio wave propagation," IEEE Std. 302-1969, May 1981.

[145] "IEEE standard definitions of terms for radio wave propagation," IEEE Std. 211-1997, December 1997.

[146] K. Fujii, Y. Yamanaka, Y. Nakajima, and A. Sugiura, "A novel standard loop antenna for antenna calibration in the MF and HF bands," in *Proc. IEEE International Symposium on Electromagnetic Compatibility*, pp. 86–89, 2005.

[147] J. McLean, R. Sutton, and R. Hoffman, "Interpreting antenna performance parameters for EMC applications - part 1: Radiation efficiency and input impedance match," tech. rep., TDK RF Solutions Inc.

[148] H. Whiteside and R. W. King, "The loop antenna as a probe," *Antennas and Propagation, IEEE Transactions on*, vol. 12, no. 3, pp. 291–297, 1964.

[149] J. McLean, R. Sutton, and R. Hoffman, "Interpreting antenna performance parameters for EMC applications - part 3: Antenna factor," tech. rep., TDK RF Solutions Inc.

[150] "American national standard for methods of measurement of compatibility between wireless communication devices and hearing aids," ANSI C63.19-2001, October 2001.

[151] S. G. Allen, "Radio-frequency field measurements and hazard," *Journal of Radiological Protection*, vol. 11, no. 1, pp. 49–62, 1991.

[152] J. D. Brunett, V. Liepa, and D. L. Sengupta, "Extrapolating near-field emissions of low-frequency loop transmitters," *Electromagnetic Compatibility, IEEE Transactions on*, vol. 47, no. 3, pp. 635–641, 2005.

[153] H. R. Kucia, "Accuracy limitation in measurements of HF field intensities for protection against radiation hazards," *Electromagnetic Compatibility, IEEE Transactions on*, vol. IM-21, no. 4, pp. 412–415, 1972.

[154] W. Joseph and L. Martens, "The influence of the measurement probe on the evaluation of electromagnetic fields," *Electromagnetic Compatibility, IEEE Transactions on*, vol. 43, no. 2, pp. 339–349, 2003.

[155] S. Roleson, "Field probes as EMI diagnostic tools," *Conformity Magazine*, vol. November, pp. 18–25, 2002.

[156] D. C. Smith, "Signal and noise measurement techniques using magnetic field probes," in *Proc. IEEE International Symposium on Electromagnetic Compatibility*, pp. 559–563, 1999.

[157] *HP 11941A Close-Field Probe*, July 1987.

[158] S. Kopparthi and P. K. Ajmera, "Power delivery for remotely located microsystems," in *Proc. IEEE Region 5 Conference: Annual Technical and Leadership Workshop*, pp. 31–39, 2004.

[159] R. W. Erickson, *Fundamentals of Power Electronics*. Massachusetts, USA: Kluwer Academic Publishers, 1999.

[160] A. Ghahary and B. H. Cho, "Design of a transcutaneous energy transmission system using a series resonant converter," *Power Electronics, IEEE Transactions on*, vol. 7, no. 2, pp. 261–269, 1992.

[161] G. B. Joung and B. H. Cho, "An energy transmission system for an artificial heart using leakage inductance compensation of transcutaneous transformer," *Power Electronics, IEEE Transactions on*, vol. 13, no. 6, pp. 1013–1022, 1998.

[162] "IEEE recommended practice for the measurements of potentially hazardous electromagnetic fields RF and microwave," IEEE Std. C95.3-1991, May 1992.

[163] *HP 8753C Network Analyzer*, May 1989.

[164] G. Grandi, M. Kazimierczuk, A. Massarini, and U. Reggiani, "Stray capacitances of single-layer solenoid air-core inductors," *Industry Applications, IEEE Transactions on*, vol. 35, no. 5, pp. 1162–1168, 1999.

[165] C. Bowick, *RF Circuit Design*. Newnes, second ed., 2008.

[166] W. Hayward, *Introduction to Radio Frequency Design*. USA: The American Radio Relay League (ARRL), Inc., 2000.

[167] J. C. Maxwell, *A Treatise on Electricity and Magnetism*. Oxford University Press, third ed., 1989. vol 1, vol. 2.

[168] M. T. Thompson, "Inductance calculation techniques – part I: Classical methods," *Power Control and Intelligent Motion*, vol. 25, no. 12, pp. 40–45, 1999.

[169] M. T. Thompson, "Inductance calculation techniques – part II: Approximations and handbook methods," *Power Control and Intelligent Motion*, vol. 25, no. 12, pp. 40–45, 1999.

[170] V. J. Bashenoff, "Abbreviated method for calculating the inductance of irregular plane polygons of round wire," *Proceedings of the IEEE*, vol. 15, no. 12, pp. 1013– 1039, 1927.

[171] V. J. Bashenoff, "Supplimentary to abbreviated method for calculating the inductance of irregular plane polygons of round wire," *Proceedings of the IEEE*, vol. 16, no. 11, pp. 1553– 1558, 1928.

[172] H. A. Wheeler, "Simple inductance formulas for radio coils," *Proceedings of the IRE*, vol. 16, no. 10, pp. 1398–1400, 1928.

[173] H. A. Wheeler, "Discussion on simple inductance formulas for radio coils," *Proceedings of the IRE*, vol. 17, no. 3, pp. 580– 582, 1929.

[174] E. B. Rosa and F. W. Grover, "Formulas and tables for the calculation of mutual and self-inductances," *United States Bureau of standards Scientific papers*, no. 169, 1916.

[175] H. Wheeler, "Inductance formulas for circular and square coils," *Proceedings of the IEEE*, vol. 70, no. 12, pp. 149–1450, 1982.

[176] S. Mohan, M. Hershenson, S. Boyd, and T. Lee, "Simple accurate expressions for planar spiral inductances," *IEEE Journal of Solid-State Circuits*, vol. 34, no. 10, pp. 1419–1424, 1999.

[177] R. Lundin, "A handbook formula for the inductance of a single-layer circular coil," *Proceedings of the IEEE*, vol. 73, no. 9, pp. 1428–1429, 1985.

[178] C. P. Yue and S. S. Wong, "On-chip spiral inductors with patterned ground shields for Si-based RF IC's," *IEEE Journal of Solid-State Circuits*, vol. 33, no. 5, pp. 743–752, 1998.

[179] C. P. Yue and S. S. Wong, "Physical modeling of spiral inductors on silicon," *Electron Devices, IEEE Transactions on*, vol. 47, no. 3, pp. 560–568, 2000.

[180] N. A. Talwalkar, C. P. Yue, and S. S. Wong, "Analysis and synthesis of on-chip spiral inductors," *Electron Devices, IEEE Transactions on*, vol. 52, no. 2, pp. 176–182, 2005.

[181] H. M. Greenhouse, "Design of planar rectangular microelectronic inductors," *Parts, Hybrids and Packaging, IEEE Transactions on*, vol. 10, no. 2, pp. 101–109, 1974.

[182] D. Schieber, "On the inductance of printed spiral coils," *Archiv fur Elektrotechnik*, vol. 68, pp. 155–159, 1985.

[183] H. A. Wheeler, "Formulas for the skin effect," *Proceedings of the IRE*, vol. 30, no. 9, pp. 412– 424, 1942.

[184] E. Pettenpaul, H. Kapusta, A. Weisgerber, H. Mampe, J. Luginsland, and I. Wolff, "CAD models of lumped elements on GaAs up to 18GHz," *Microwave Theory and Techniques, IEEE Transactions on*, vol. 36, no. 2, pp. 294–304, 1988.

[185] S. J. Haefner, "Alternating current of rectangular conductors," *Proceedings of the IRE*, vol. 25, pp. 434–447, 1937.

[186] P. H. Smith, *Electronic Applications of the Smith Chart*. Atlanta, GA: Noble Publishing Corporation, second ed., 1995.

[187] L. Youbok, "Antenna circuit design for RFID applications," Tech. Rep. AN710, Microchip, 2003.

[188] M. Pentz and M. Shott, *Handing Experimental Data*. Open University Press, 1994.

[189] A. C. Newell, "Error analysis techniques for planar near-field measurements," *Antennas and Propagation, IEEE Transactions on*, vol. 36, no. 6, pp. 754–768, 1988.

[190] "American national standard for methods of measurement of compatibility between wireless communication devices and hearing aids," ANSIC63.19-2001, 2001.

[191] "American national standard for electromagnetic compatibility - radiated emission measurement in electromagnetic interference (EMI) control - Calibration of antennas (9kHz to 40GHz)," ANSI C63.4-1998, 1998.

[192] P. Nikitin, K. S. Rao, S. Lam, V. Pillai, R. Martinez, and H. Heinrich, "Power reflection coefficient analysis for complex impedances in rfid tag design," *Microwave Theory and Techniques, IEEE Transactions on*, vol. 53, no. 9, pp. 2721–2725, 2005.

[193] "Fundamentals of RF and Microwave Power Measurements," Application Note 64-1B, Agilent Technologies, 2000.

[194] "ICODE Coil Design Guide," Application Note, Product Specification Rev. 3.0, Philips Semiconductors, September 2002.

[195] G. Marroco, "RFID antennas for the UHF remote monitoring of human subjects," *Antennas and Propagation, IEEE Transactions on*, vol. 55, no. 6, pp. 1862–1870, 2007.

[196] W. B. Kuhn and N. M. Ibrahim, "Analysis of current crowding effects in multiturn spiral inductors," *Microwave Theory and Techniques, IEEE Transactions on*, vol. 49, no. 1, pp. 31–38, 2001.

[197] J. Maxwell, "A dynamical theory of the electromagnetic field," *Philosophical Transactions of the Royal Society of London*, vol. 155, pp. 459–512, 1865.

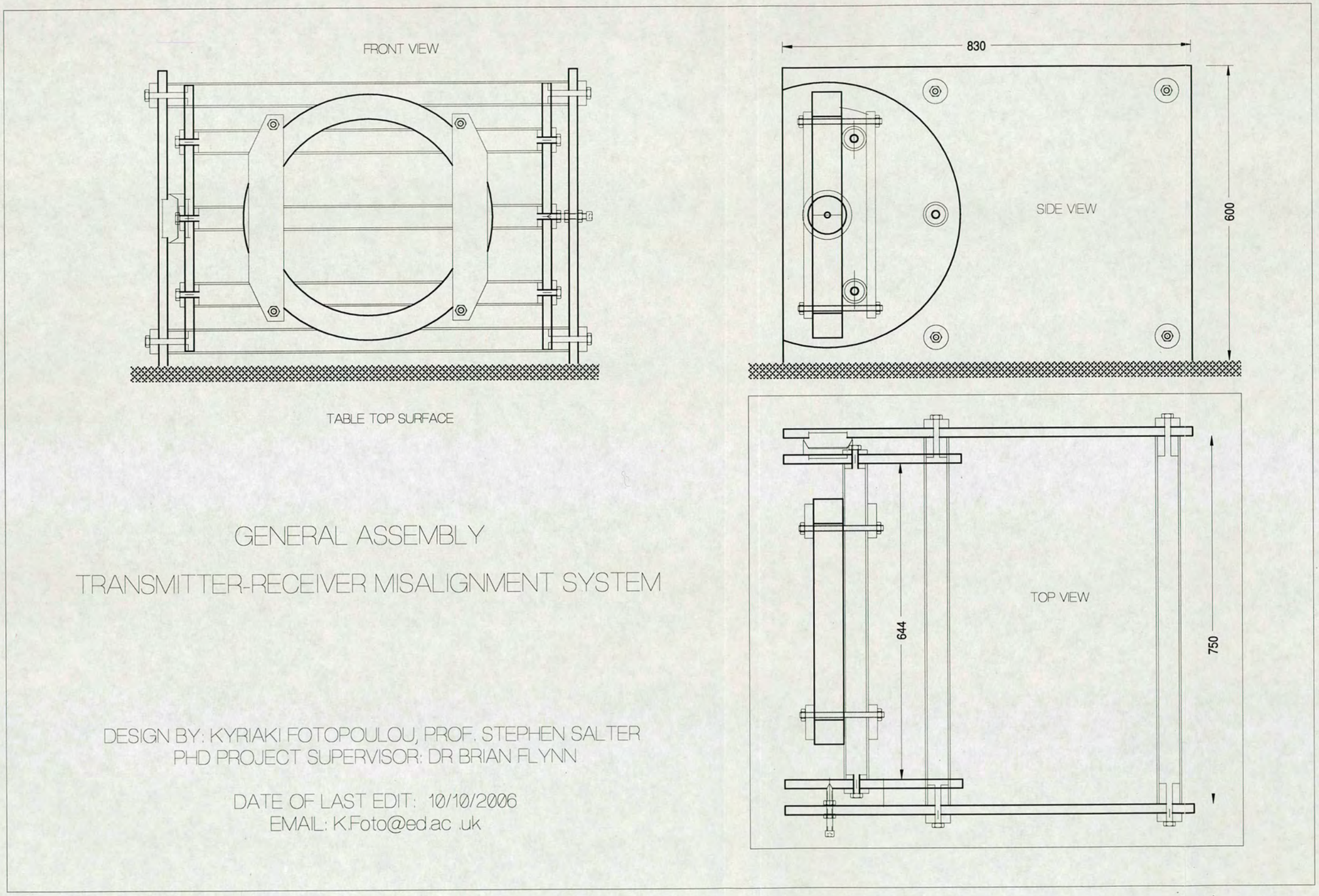

Figure C.2: *Mechanical drawing of the general assembly of the misalignment apparatus.*

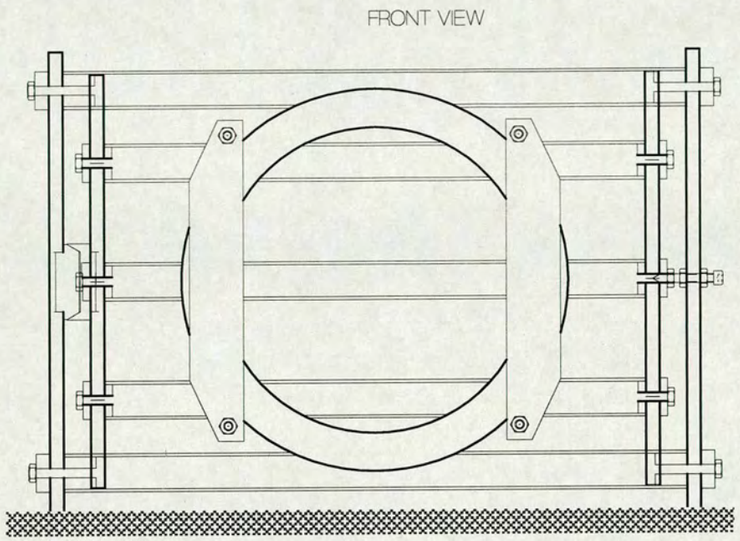

TABLE TOP SURFACE

GENERAL ASSEMBLY

TRANSMITTER-RECEIVER MISALIGNMENT SYSTEM

DESIGN BY: KYRIAKI FOTOPOULOU, PROF. STEPHEN SALTER
PHD PROJECT SUPERVISOR: DR BRIAN FLYNN

DATE OF LAST EDIT: 10/10/2006
EMAIL: K.Foto@ed.ac .uk

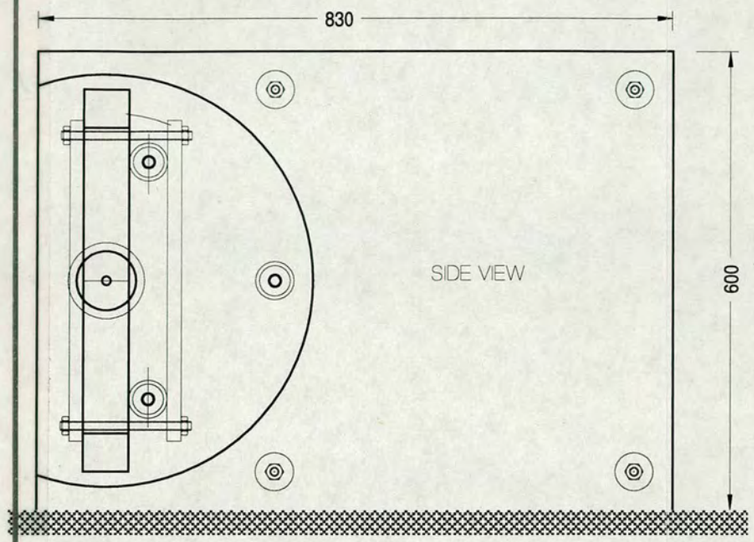

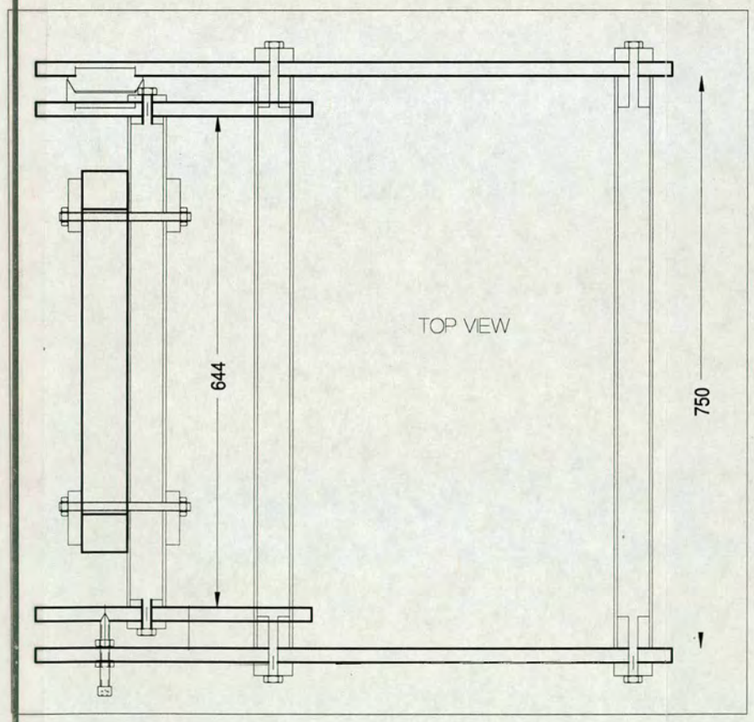

Figure C.2: *Mechanical drawing of the general assembly of the misalignment apparatus.*